DISSERTATION

MODELING OF MAGNETORHEOLOGICAL ELASTOMERS

Submitted by

David Marchfield

Department of Physics

In partial fulfillment of the requirements

For the Degree of Doctor of Philosophy

Colorado State University

Fort Collins, Colorado

Summer 2025

Doctoral Committee:

Advisor: Kristen Buchanan

Martin Gelfand
Hua Chen
Derek Schutt

ABSTRACT

MODELING OF MAGNETORHEOLOGICAL ELASTOMERS

Magnetorheological elastomers (MREs) are composite materials whose mechanical properties can rapidly and reversibly change with the application of a magnetic field. MREs are composed of a non-magnetic polymer matrix embedded with magnetic particles. These materials can also demonstrate magnetostriction, with large strains compared to the magnetostriction seen in crystalline solids. Ultrasoft MREs, with Young's moduli on the order of kPa or less, have characteristic pinched magnetic hysteresis loop shapes that are associated with rearrangement and clustering of magnetic particles within the surrounding polymer matrix. MREs have potential applications as vibration isolators and absorbers, soft actuators, sensors, and applications in biomedical fields. Modeling of these systems at different length and time scales is an important challenge for understanding their complex magnetomechanical behavior, fabricating MREs with desired properties, and designing MRE devices. This dissertation covers efforts centered on creating models of MRE systems at length scales that resolve the micron sized magnetic particles, but not the polymer chains of the surrounding matrix, in order to study the magnetic response, particle motion, polymer deformation, and field-dependent stiffness.

A simple dipole-spring model is developed to investigate the interplay between magnetic and elastic forces in a two particle system. Results from this model show particle motion on the scale of the particle size, the role of particle clustering in magnetic hysteresis in these systems, and a pinched magnetic hysteresis loop shape that qualitatively matches experimentally measured hysteresis loops for ultrasoft MREs. Magnetometry measurements of MRE samples with polymer matrices with varying Young's moduli shows decreasing magnetic hysteresis with increasing polymer stiffness. Similarly, cooling an ultrasoft MRE below a glassy phase transition increases the

elastic modulus, and magnetometry measurements show no magnetic hysteresis when below this temperature.

A more sophisticated model is developed that takes into account the nonlinear magnetic susceptibility and gradual approach to saturation of the carbonyl iron particles, and treats the surrounding polymer matrix as a linearly elastic continuum that surrounds the particles. Results for two particle systems in this model demonstrate non-zero remanent magnetization and switching fields for the magnetization direction. This more sophisticated modeling approach was used to study the combined response of MREs to magnetic fields and strains. Shear strain simulations for two particle systems show the effective shear modulus increases with applied magnetic field up to magnetic saturation, that the relative size of this effect increases with the volume fraction of magnetic particles up to a point, and that particle clustering enhances the stiffening effect. Shear strain simulations for chain-like arrangements of magnetic particles were also done to study the effect of magnetic field orientation on the effective shear modulus. These simulations show that the shear modulus increases with increasing magnetic field when the field is applied parallel to the chain, but the shear modulus decreases with increasing field when the field is applied perpendicular to the chain. Finally, helical arrangements of particles with varying helix radii show the complex relationship between particle geometry and the effective shear modulus, as well as the ability for applied strains to create or break particle clusters.

ACKNOWLEDGEMENTS

I would like to thank my advisor, Dr. Kristen Buchanan, without whom this would not have been possible. I would also like to thank my family, for the love and support they've given me, and the things they have taught me. To my brother, Mark, thank you for being an inspiration to me in the pursuit of higher education and becoming a scientist. Daria, your kindness, love, and support has helped me through the long process of a PhD, and you inspire me to grow, change, and become a better person. I would like to thank Prof. Tillotson, who encouraged me to pursue studies in Physics as an undergraduate, and Prof. Grein, who encouraged me to pursue graduate studies in Physics. I would also like to thank Dr. David Ucker for taking me into his lab as an undergraduate, and giving me an opportunity to experience research in a Cell Bio lab, and grow as a scientist and researcher. There are many other teachers and professors who have contributed to my growth, and I am grateful to them, even if I haven't called them out here. I would like to thank Russel Gremel, Doug Sanders, and troop 979 for instilling a set of values, and providing skills and experiences that I carry with me today as an Eagle Scout. To my friends, Sebi, Gerry, Tom, and Rob, thank you for your support, belief, the good memories, and the different experiences and points of view that have helped me grow into more than I could be by myself. I also need to thank my friends and cohort members, Ryan, Justin, and Derek, for helping me prepare for my defense, and sharing the experience of graduate school at CSU with me. You made the good and the bad days more enjoyable, and it was a great pleasure to grow and learn with you.

Work at CSU is supported by National Science Foundation DMR Grant Number 1709525. We also thank Dr. Marty Gelfand for helpful discussions on modeling.

DEDICATION

I would like to dedicate this thesis to my family, and my partner Daria.

TABLE OF CONTENTS

LIST OF TABLES

LIST OF FIGURES

Chapter 1

Introduction

1.1 Introduction

This dissertation is focused on modeling of magnetrheological elastomers (MREs), specifically ultrasoft polymers embedded with micron-sized magnetic particles that are magnetically soft. The introduction of magnetic particles into a non-magnetic viscoelastic matrix results in complex magnetomechanical coupling and behaviors. These materials can demonstrate large magnetostriction (tens of percent or greater tensile strains), changes to stiffness and damping, and shape memory under the effect of an external magnetic field. Their complex behaviors make them interesting subjects of research across numerous fields, including polymer science, magnetism, elasticity, rheology, and engineering. These behaviors also make MREs intriguing for numerous engineering applications.

The complexity of MRE systems makes them challenging to model. Decisions need to be made regarding which aspects are of interest, and at what length scales one wants to simulate behavior. While it is technically possible to write down equations governing the system at an atomistic level, solving these equations would be intractable. Instead, simplifying assumptions have to be made, where the goal is to preserve the consequences of the underlying structure and to capture the larger scale behaviors.

In this dissertation, the magnetic particles are treated as isotropic magnetic dipoles that are saturable with either a linear susceptibility up to saturation (see Section 2.4), or a nonlinear susceptibility with a gradual approach to saturation (see Section 4.1). In both cases the magnetic dipoles are at the center of spherical rigid bodies, and the particles are mutually magnetizing. The viscoelastic behavior of the polymer matrix will be reduced to elastic behavior modeled by linearly elastic springs, or a linearly elastic continuum that is modeled using cubic volume elements and linearly elastic springs.

Our modeling efforts are first focused on the magnetic reversal process of ultrasoft magnetoactive polymers using the simplified linear dipole model and elastic springs (Chapter 2, Chapter 3). This model qualitatively reproduces a pinched magnetic hysteresis loop shape observed experimentally (see Chapter 3 Figure 3.1a)), which is not observed in the carbonyl iron magnetic filler (see Chapter 3 Figure 3.7) or polydimethylsiloxane polymer when considered individually. We then discuss experimental results demonstrating the effect of the polymer stiffness on the magnetization behavior of MREs utilizing different polymer matrices and temperature dependent phase transitions for polymer stiffness, complemented by modeling work using the simplified dipole-spring model. This work validates the assumption that the observed magnetic hysteresis is a consequence of particle motion and clustering within the polymer matrix, which can be blocked by stiffening the matrix.

Later, we discuss a more complex 3D model that treats the polymer as a continuum and the embedded magnetic particles as rigid bodies (Chapter 4). The system is discretized into cubic volume elements and uniformly distributed nodes connected by linearly elastic springs. The approach taken uses experimentally measurable stiffness and incompressibility of the polymer as inputs. This modeling effort includes the more realistic but still simplified nonlinear saturable magnetic dipole model. The use of dipole based models in MRE modeling simplifies the computational effort, but ignores details like non-uniform magnetization and their impact on interactions at distances close to the particle size. With this more complex model we investigate the magnetization behavior of ultrasoft magnetoactive polymer systems, as well as the field dependent stiffness of systems under simple shear conditions. We explore the impact of the volume fraction of magnetic particles from $\Phi \approx 1\%$ to 20%, and of the underlying microstructure/particle arrangement. The magnetic hysteresis results differ from the linear magnetization model in significant ways. A non-zero remanent magnetization is found for particles that cluster together in the 3D nonlinear magnetization model, along with clustered particles showing switching behavior at critical fields, and the hysteretic behavior differs from the pinched hysteresis loop shape seen experimentally and in the linear magnetization dipole-spring model. The importance of the choice of magneti-

zation response model and numerical method is discussed. Modeling results show an increasing stiffening response with increased volume fraction of magnetic particles. The impact of varying combinations of magnetic field, anisotropy of particle arrangement, and strain directions was also studied. Effective shear moduli results for a more realistic particle arrangement consisting of 8-particle helical chains showcase the complicated relationship between particle microstructure and mechanical properties.

In this chapter we will introduce background information on magnetism, elasticity theory, and magnetoactive polymers which will be necessary for understanding the work in the following chapters. Chapter two covers the simple dipole-spring model, and the interplay between particle motion and the magnetization response of the system. Chapter three is a published paper covering experimental and modeling results studying the impact of polymer stiffness on the magnetization response of ultrasoft magnetorheological elastomers. Chapter four covers a more complex and realistic 3D modeling approach. This model better captures the behavior of magnetically soft particles embedded in an elastic matrix, and was used to study magnetization behavior and field dependent shear strain stiffness of small systems.

1.2 Magnetoactive Polymers

Magnetorheological (MR) materials are a class of composite smart materials that change in response to an applied magnetic field. Magnetorheological elastomers (MREs), magnetoactive polymers (MAPs), ferrogels, and magnetoactive elastomers (MAEs) are terms used somewhat interchangeably for solid materials that belong to this class. Magnetorheological fluids (MRFs) also fall under the umbrella of magnetorheological materials. For this dissertation, the terms magnetoactive polymers and magnetorheological elastomers will be used interchangeably. These materials can show rapid, reversible changes in stiffness [2] or shape [3] in the presence of an applied magnetic field. They are also capable of demonstrating shape memory, preserving shapes when deformed in the presence of a magnetic field, so long as the magnetic field is maintained [4–6]. MAPs have also been fabricated that demonstrated piezoresistivity and magnetoresistivity [7], that

is, changes to electrical resistance under an applied strain or magnetic field, respectively, enabled by conduction through magnetic particle contacts and chains. These behaviors, especially adjustable dynamic moduli and large magnetostriction, make MR materials attractive for a variety of applications. Devices making use of the above behaviors have been proposed and investigated, including tuneable vibration isolators [8] (adjustable moduli), soft actuators and artificial muscles (magnetostriction) [9, 10], sensors [8], and haptic feedback devices [11]. To my knowledge, the only commercial applications of magnetorheological materials are magnetorheological fluids in vibration damping [12]. These composites are also used in biomedical settings as growth substrate for cell tissue studies [13, 14], as artificial tissues, as biosensors, and for drug delivery devices.

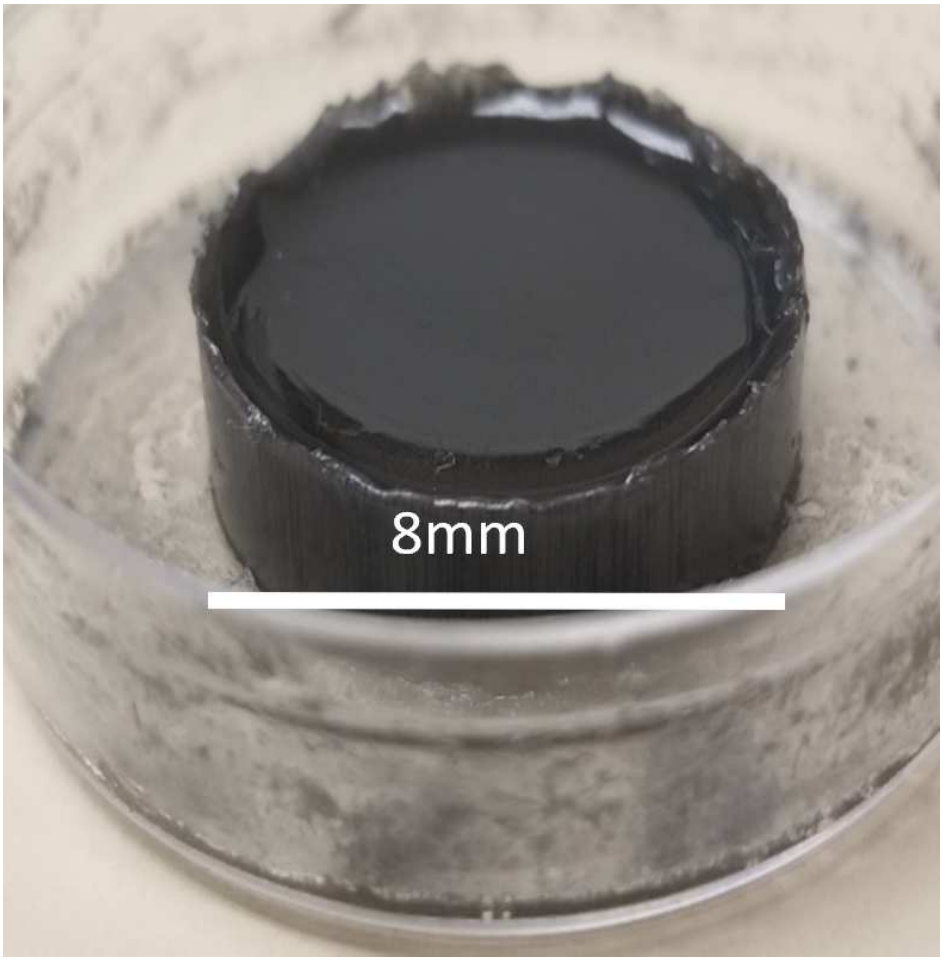

Figure 1.1: A macroscopic MRE sample fabricated with PDMS-527 and carbonyl iron. Image courtesy of Andy Clark.

It is useful to explore aspects of polymers and polymer behavior that will be relevant to understanding the behavior of these composites, and then discuss magnetomechanical coupling in magnetoactive polymers. Readers can refer to texts [15, 16] for background information on polymers and polymer physics, which have been used to inform the following section.

Elastomers are polymers that are elastic over a large range of strain values, up to tens or hundreds of percent of tensile strain. Examples include natural rubber, and polydimethylsiloxane (PDMS). The material response is not necessarily linear over the range of strains before failure, but can be approximated as linear for small strains. These materials also exhibit viscous effects, and so are considered viscoelastic. They return to their original shape when deformed, but viscoelastic materials also exhibit hysteretic stress-strain responses, and their stiffness depends on the rate at which they are stressed or strained. Viscoelastic behavior plays an important role in the performance of these materials in real applications. In this dissertation the focus will be on static properties of magnetoactive elastomers in response to applied magnetic fields and strains, and the dynamic and time dependent response of the material is neglected.

The origin of elasticity in these materials comes from cross-links among polymer chains, and entropy driven restoring forces. Cross-links between polymer chains are covalent bonds that enhance the stiffness of the polymer, and these provide structure that allows a polymer to return to its original shape after deformation. Other non-covalent interactions between chains contribute to the viscous effects in polymers, causing friction-like interactions as the chains are stretched and move past one another. In addition to cross-links, the elastic force in polymers is entropic in origin. Long polymer chains tend to coil, rather than remain straight, resulting in end-to-end distances that are less than the length of the polymer chain. Under tension the polymer is deformed and the chains are stretched, and they arrange themselves into low energy configurations. The tension reduces the number of available configurations of the chain and decreases the entropy of the system, leading to an increase in the Helmholtz free energy.

$$F = U - TS \tag{1.1}$$

Where U is the internal energy of the system, F is the Helmholtz free energy, T is the tmemperature, and S is the entropy. The system evolves to decrease its energy and increase entropy (second law of thermodynamics, for any closed system in thermodynamic equilibrium undergoing a process, $\Delta S \geq 0$), which drives it towards configurations with coiled polymer chains and generates a restoring force.

With some understanding of the behavior of polymers, we can now address magnetomechanical coupling in magnetoactive polymers. The rearrangement of magnetic particles in the polymer matrix leads to stiffness changes, shape changes, and shape memory in these materials. Magnetic particles interact with the external magnetic field and with each other, resulting in forces that push, pull, and rotate the magnetic particles. The surrounding matrix is distorted by the displacement of the magnetic particles, resisting the rearrangement and restricting how the magnetic particles can move. The magnetic particles rearrange to minimize their magnetic energy, but the rearrangement is balanced by the energy cost of deforming the matrix. The local distortions can cause visible changes to the macroscopic shape of the MAP, a form of magnetostriction distinct from the small strains associated with magnetostriction in crystalline materials. From a continuum perspective the MAP should elongate along the applied field direction in order to minimize the magnetostatic energy [17]. An applied magnetic field has been shown experimentally to cause elongation or compression along the applied field direction depending on the details of the microstructure and shape magnetostriction on the macro-scale [17, 18] .

Along with magnetostriction, MAPs demonstrate field-dependent stiffness, or elastic moduli, as shown in Figure 1.2 where the shear modulus increases with increasing magnetic field for isotropic MRE samples with varying volume fraction of iron particles. Stiffness is a measure of the energy or force required to strain or deform the object. Magnetic interaction energies and the energy stored in the polymer deformation can cause changes in the stiffness of the composite. Applied strains will alter the arrangement of the magnetic particles as well as deforming the polymer matrix. By including additional magnetic energies, which may increase or decrease with the applied strain, the stiffness of the composite varies from the zero-magnetic field case. The details

of the microstructure, the applied magnetic field magnitude and direction, and the applied strain all impact the effective stiffness of the system.

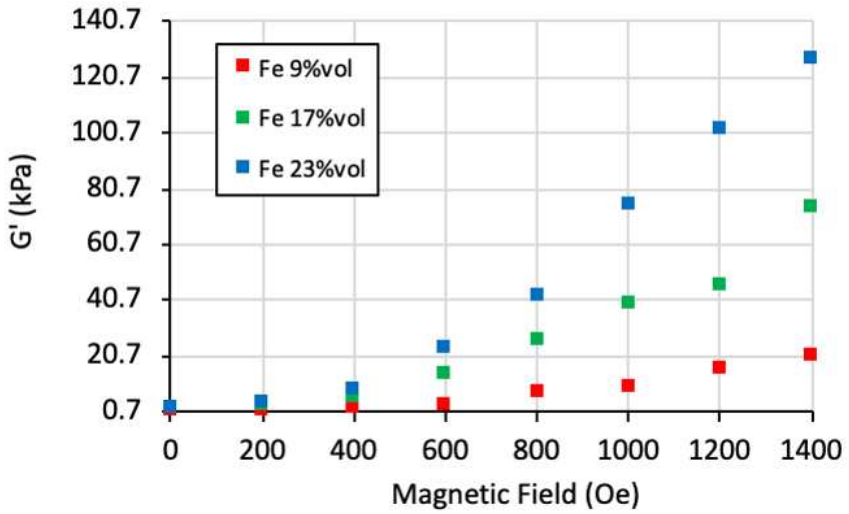

Figure 1.2: Experimental results showing effective shear modulus, G, for isotropic MREs with the magnetic field applied parallel to the axis of torsion with $\Phi = 9, 17,$ and 23%. Polydimethylsiloxane-based MREs fabricated with Sylgard^{TM}-527 elastomer and carbonyl iron particles with 3.9-5.2 μm mean diameter. Figure courtesy of Andy Clark.

Shape memory is another consequence of magnetomechanical coupling in MAPs. Objects with shape memory "remember" a particular configuration or shape. In MAPs the presence of a magnetic field causes rearrangement of magnetic particles. Applying a strain simultaneously can cause particles to rearrange further and achieve configurations that wouldn't be achieved without the strain. With the magnetic field still on, those configurations can be maintained even after the applied strain or force is removed, resulting in the composite "remembering" the shape. Removing the magnetic field causes the elastomer to relax back into its preferred shape, to the extent that no irreversible deformations occurred, such as the breaking or creation of cross-linkages.

Engineering samples with desired properties requires thoughtful selection of materials as well as controlling the internal structure of MAPs due to the dependence of MAP properties on microstructure. MAP properties can be controlled through the choice of polymer, as well as the

addition of any additives like silicone oils or other non-magnetic fillers, and by controlling the amount of cross-linking that occurs. Magnetoactive polymers will also have different properties depending on how the magnetic particlse are distributed. When cured in the presence of an external magnetic field the magnetic filler can arrange itself into chain-like or columnar structures aligned with the magnetic field, resulting in an anisotropic particle structure. Anisotropic MAPs can demonstrate different magnetostrictive and stiffness changing behaviors compared to isotropic MAPs. Figure 1.3 shows micrographs of a cross-section of an isotropic MRE sample with $\Phi = 3\%$, while Figure 1.4 shows a similar set of micrographs for an anisotropic sample with $\Phi = 3\%$.

Full magnetomechanical characterization of a MAP sample requires multiple measurements in different configurations. For isotropic MAPs, two combinations of applied strain direction and magnetic field direction are typically used to characterize the response of the material experimentally under uniaxial tensile strain: magnetic field and strain aligned, or magnetic field and strain perpendicular. Furthermore, the measured response is potentially different from performing the same measurements under uniaxial compression. With anisotropic MAPs, additional combinations of applied strain and magnetic field direction are needed to characterize the response of the material as one must also consider the directionality of the magnetic particle structure. Typical configurations considered are all three of magnetic field, strain, and chain direction parallel, field and chains parallel with strain perpendicular, chains and strain parallel with field perpendicular, field and strain parallel with chains perpendicular, and all three perpendicular. When considering simple shear strains one should also consider the normal to the surface being strained along with the strain direction. The choice of polymer matrix, magnetic inclusions, non-magnetic fillers, and curing with or without a magnetic field allow for significant variation in samples, and provide numerous mechanisms for designing samples with different properties.

There are a number of review articles that provide a view into the background of MAPs, and that cover fabrication, characterization, experimental results and analysis, theoretical models and numerical results, and proposed devices and design considerations. These articles also provide a starting point for branching out further into the literature. Some of the earliest publications refer-

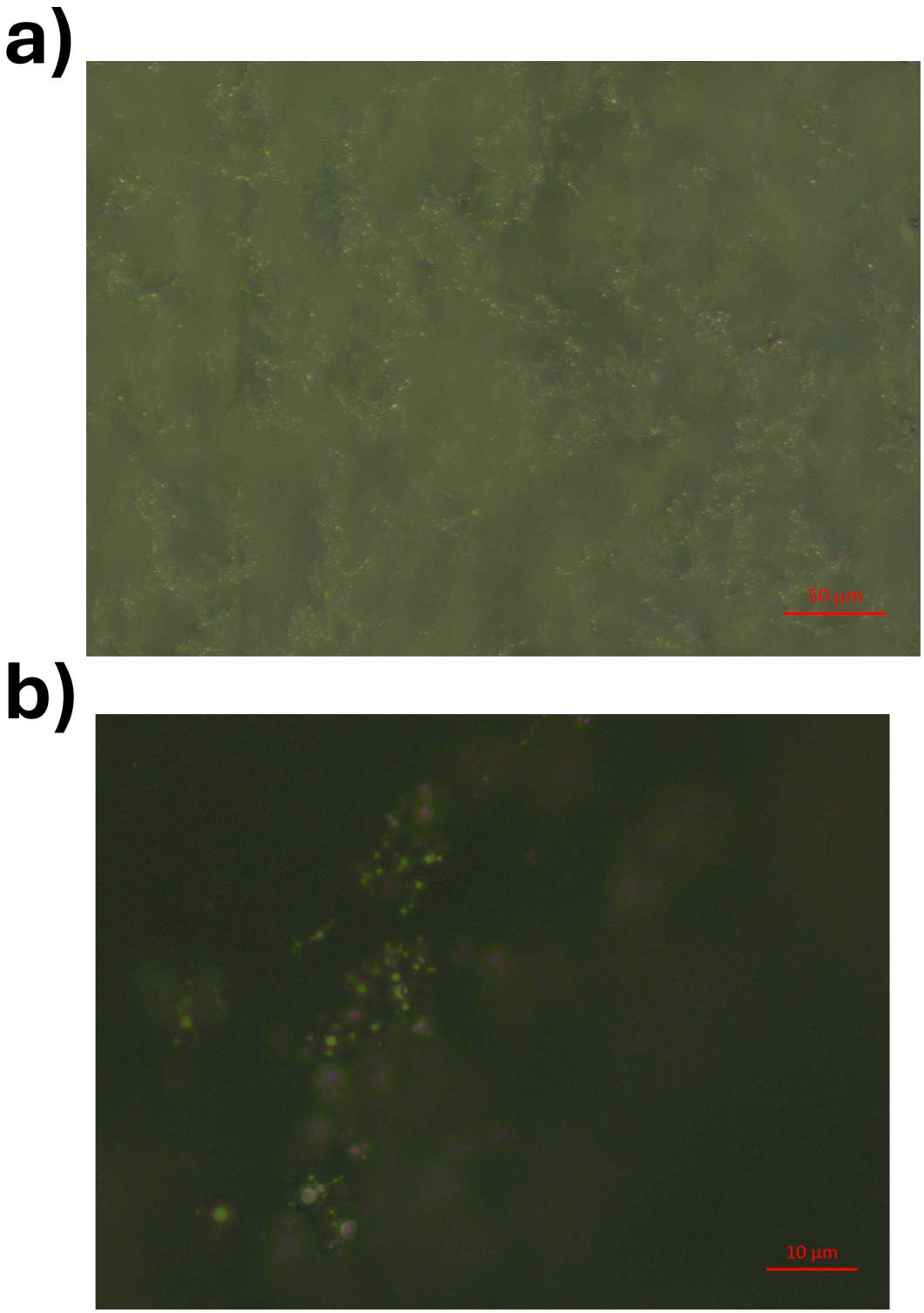

Figure 1.3: Optical micrographs showing a cross section of an isotropic MRE sample with $\Phi = 3\%$ at a) $20\times$ and b) $100\times$ magnification. Images courtesy of Andy Clark.

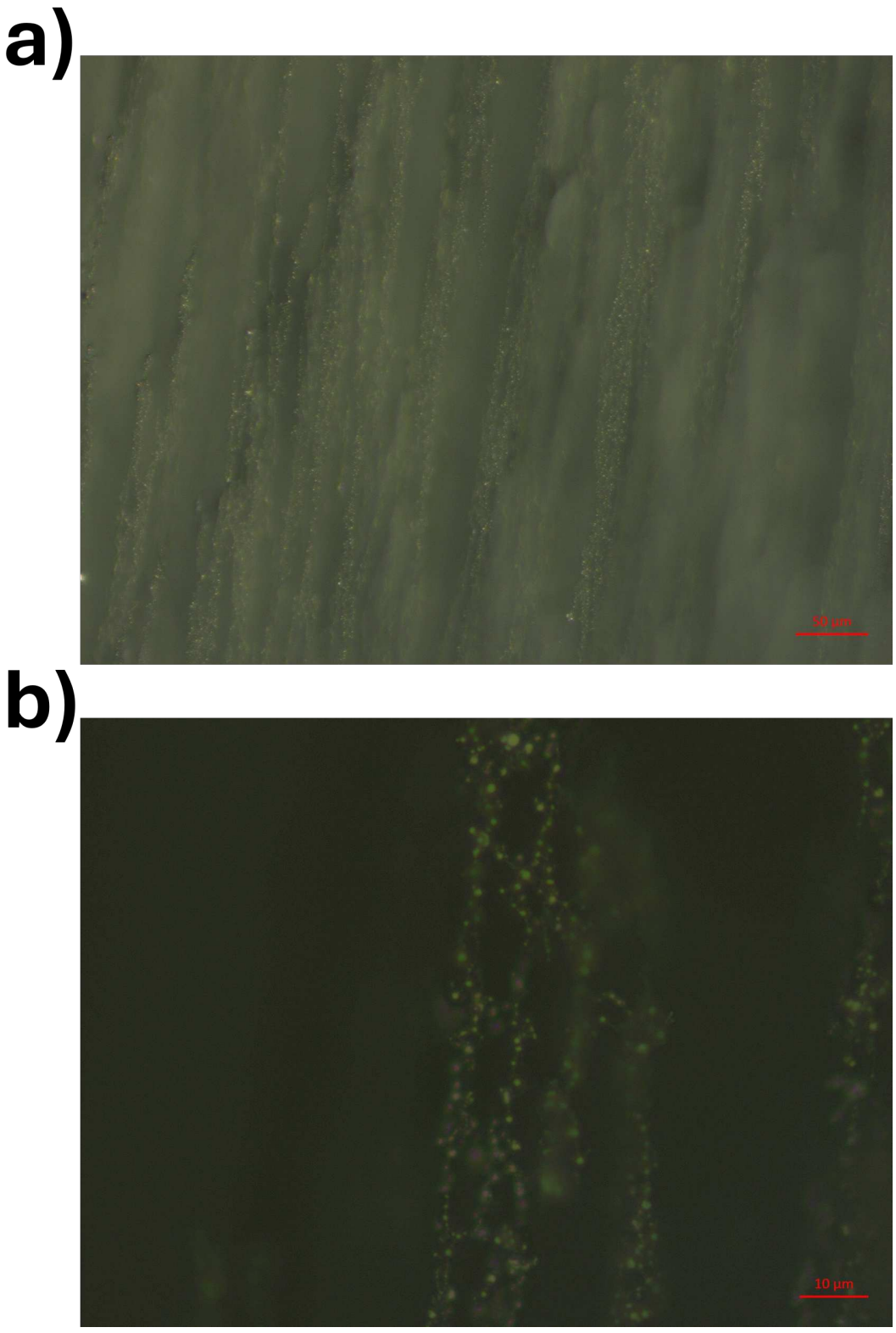

Figure 1.4: Optical micrographs showing a cross section of an anisotropic MRE sample with $\Phi = 3\%$ at a) $20\times$ and b) $100\times$ magnification. Images courtesy of Andy Clark.

encing magnetorheological polymers are early experimental results by Rigbi and Jilken [19], and Rigbi and Mark [20]. Early modeling work includes efforts by Jolly *et al*. [21, 22] and Davis [23] which use dipole models to calculate the change in the shear modulus of an MRE by considering magnetic dipole-dipole interactions in uniform chains of magnetic particles, but note that these are not dipole-spring models.

For a review of polymer-based MR materials, discussing functional behavior, raw material components, fabrication, characterization, current and potential devices and device design, see Ubaidallah *et al*. [12]. Li *et al*. [24] reviews device design and applications, details numerous issues that need to be addressed for engineering applications including: power requirements, size of the MRE, difficulty producing uniform fields for large MREs, the need to standardize testing and characterization, cycling tests, and a better understanding of failure modes. Lopez-Lopez *et al*. [25] provides a review of "magnetopolymer composites", a discussion of a range of experimental results, and analytical models studying the magnetostriction and modulus changing behaviors of these composites. This article also includes a discussion of theoretical and computational results, including finite element methods (FEM), Monte Carlo simulations, and the use of dipole-dipole approximations to study magnetostriction and field dependent moduli, including the impact of the microstructure.

Cantera *et al*. [26] reviews modeling of anisotropic MREs and MRE-based systems, with the focus on variation in stiffness and damping effects, rather than magnetostriction. It categorizes the models as "particle interaction-based, magnetoelastic response-based, magnetoviscoelastic response-based, or models including the effects of environmental conditions and fatigue," and includes analytical, numerical, finite element, and phenomenological models. It includes references to experimental validation of some modeling work, and in its conclusion emphasizes the need for future modeling of long term behavior including creep, fatigue, and fracture, and the inclusion of environmental factors and their effects on the constituent materials.

Weeber *et al*. [27] makes a distinction between magnetic gels and magnetic elastomers and concerns itself mostly with magnetic gels. This paper provides an overview of polymer architectures,

the polymer molecular structure, and discusses fabrication and characterization of ferrogels, as well as introducing theoretical approaches and simulation results. Throughout most of the review, the magnetic particles considered are single domain nanoparticles, which behave quite differently magnetically from multidomain micron-sized particles due to their permanent dipole moment and the mechanisms by which it reorients. Simulation approaches at different length scales are discussed, such as coarse grained continuum approaches, which allow simulating systems at large scales relative to the particle size, and approaches that resolve the magnetic particles, or both the magnetic particles and polymer structure that are restricted to smaller scale systems.

Bastola and Hossain [28] provide a review of MRE fabrication and characterization, with some discussion of the author's own 3D printing method for MRE fabrication. The review article attempts to provide a comprehensive review of characterization methods. Bastola emphasizes the importance of standardizing characterization methods and reporting results to improve comparing results from separate studies. Bastola *et al*. [29] discusses background, materials used in fabrication, and fabrication processes. It also discusses applications, including vibration absorbers, isolators, soft actuators, sensors, a microfluidic device and a peristaltic pump.

Morillas and de Vicente [30] summarizes publications from the period $\approx$ 2010-2020, covering magnetorheological materials, including magnetorheological fluids and elastomers. Morillas also discusses other emerging MR materials such as MR foams, MRF impregnated composites and hybrid MR materials. Hafeez *et al*. [31] focuses on isotropic MREs, discussing fabrication, and properties including: morphology, particle distribution, static and dynamic mechanical properties, frictional response, fatigue response and degradation. Nadzharyan *et al*. [32] reviews theoretical descriptions and modeling attempts for magnetoactive elastomers at different length scales, from the behavior of MAE samples to the behavior of individual magnetic particles. It covers a great deal of modeling efforts, both numerical and analytical. In its conclusions it emphasizes the increasing complexity of fabricated MAEs, and the importance of improving theoretical work that captures the non-linear mechanical and magnetic properties of the constituent materials. Readers are also encouraged to look at *Magneto-Active Polymers* by Pelteret and Steinmann (2020) [33] for

a treatise covering fabrication, characterization, modeling and simulation of magneto-active polymers.

1.3 Magnetism

As magnetic particles are a key constituent of a MRE, magnetism is central to developing a working model. Large portions of this section are condensed from Cullity's *Introduction to Magnetic Materials* [34].

Many people are familiar with magnetism through refrigerator magnets, compass needles, and playing with bar magnets, and have experienced the attraction and repulsion among the poles of bar magnets. A compass needle aligns itself with the magnetic field of the Earth, and iron shavings can reveal the shape of the magnetic field produced by a bar magnet. Our modern electrified and digital world is underpinned by magnetism. To name a few examples: the production of electricity with generators, the transmission of electricity facilitated by transformers, the production of mechanical work with electric motors, and long term data storage with magnetic hard drives.

All matter has a magnetic response to an applied magnetic field, though we classify materials as "magnetic" and "non-magnetic" based on the magnitude and nature of their response to an applied magnetic field. Magnetic fields can be generated from permanent magnets, like bar magnets, or from electromagnets, where the flow of electricity generates a magnetic field. Ignoring the subject of electromagnets and magnetic fields generated by moving charged particles for now, magnetism in matter is quantum mechanical and connected to the angular momentum of fundamental particles, where the dominant contribution is from electron angular momentum.

Electrons have inherent angular momentum, referred to as spin, as well as orbital angular momentum due to motion around a nucleus when bound to an atom, which are both directly proportional to the electron's magnetic moment. A magnetic moment is analogous to a bar magnet, where the strength of the magnet is the magnitude of the magnetic moment, and the magnetic moment is a vector whose components give the orientation. The magnetic moment associated with the nucleus is small in comparison with that of the electron, and is often ignored due to the difference in mag-

nitudes. This nuclear magnetic moment is relevant for the splitting of electronic energy levels as hyper-fine splitting, and is utilized in the experimental technique of nuclear magnetic resonance, and neutron scattering to study magnetic structure, but has a negligible impact on the magnetic response of materials. The magnetic moments of atoms are then the sum of the magnetic moments of the electrons. For bulk matter, the magnetization, $\vec{M}$, is defined as the magnetic moment per unit volume of material, and the maximum value that can be achieved is called the saturation magnetization, M_s. When the magnetic moments of the electrons are oriented so that they cancel, the atom has no net magnetic moment and is diamagnetic. Unpaired electron magnetic moments in atoms are the origin of magnetism in paramagnets and ferromagnets.

1.3.1 Paramagnetism

In the classical theory of paramagnetism, paramagnetic materials are composed of atoms whose magnetic moments are non-zero, but whose orientations in the absence of an applied field are distributed randomly so that the magnetization is zero. When a field is applied, the magnetic moments tend to align with the field, which corresponds to a minimum of the Zeeman energy

$$U_{Zeeman} = -\mu_0 \vec{m} \cdot \vec{H} \tag{1.2}$$

where μ_0 is the vacuum permeability, $\vec{H}$ is the magnetic field, and $\vec{m}$ is the magnetic moment. The magnetic moments of a paramagnet would align with the magnetic field except for thermal motion which opposes the alignment. Thermal motion leads to only partial alignment with the applied field, and a linear relationship between the magnetization and the applied magnetic field with a small positive susceptibility. The magnetic susceptibility is denoted χ, is defined by

$$\chi = M/H \tag{1.3}$$

There are related terms, such as the differential susceptibility, $\chi_{diff}(H) = dM/dH$, which is the slope of the M-H curve at some field value, and the initial susceptibility χ_0, which is the slope of the M-H curve at $H = 0$.

A detailed quantum mechanical description of paramagnetism (and ferromagnetism) is beyond the scope of this dissertation, but a quantum mechanical theory is necessary to correctly describe magnetic behaviors of atoms by taking into account the discrete nature of the energy of a system, allowing only certain electronic states, including restrictions on the orbital, spin, and total angular momentum.

1.3.2 Diamagnetism

Diamagnets become magnetized in the direction opposite an applied external field, though this effect is so small that objects made of diamagnetic materials are normally considered "non-magnetic". The model that is typically used to describe magnetism involves electrons in the material in orbitals that act like current loops. The effect of an applied magnetic field on the electron orbits is to reduce the effective/bound current, which produces a magnetic moment that opposes the applied field [35]. Due to this effect, diamagnetic materials show a linear relationship between magnetization and applied magnetic field with a small, negative magnetic susceptibility. "Electrons which constitute a closed shell in an atom usually have their spin and orbital moments oriented so that the atom as a whole has no net moment." [35] Matter which has closed-shell electronic structures are mostly diamagnetic. Examples include noble gasses, He, Ne, Ar, many diatomic gasses such as H_2 and N_2, NaCl, and many organic compounds, including most polymers that are used for MREs.

1.3.3 Ferromagnetism

Ferromagnets are materials that have a strong response to an applied magnetic field, orders of magnitude greater than a paramagnet, and that exhibit spontaneous magnetization. The internal structure of a ferromagnet is composed of magnetic domains, where the magnetic moments within a domain are aligned and the volume is hence magnetized at the saturation value M_s. In a de-

magnetized state the orientations of the magnetization of the domains are such that the material has no net magnetization. These domains are separated by domain walls, regions across which the spin/magnetic moment orientation changes from one domain's orientation to the other's.

The structure of these domains and domain walls are a consequence of competition between magnetic dipole-dipole interactions, magetocrystalline anisotropy, which defines a preferred axis, axes, or plane for the magnetic moment orientation, and exchange energy, which causes adjacent magnetic moments to be parallel. The process of magnetizing a ferromagnet causes domain wall motion, leading to the growth of some domains and the shrinkage and eventual disappearance of others, increasing the magnetization parallel to the applied field direction. At high enough fields, the magnetization rotates to align with the applied field and the object is magnetically saturated.

In ferromagnets the atomic or molecular magnetic dipoles are oriented along the same direction within a magnetic domain as a result of the quantum mechanical exchange interaction and magnetocrystalline anisotropy. The exchange interaction, also referred to as spin-spin coupling, acts like a force to align nearby electron spins into parallel orientations in a ferromagnetic material. For a detailed explanation of the exchange interaction, readers are referred to textbooks on quantum mechanics, including Griffiths, Cohen-Tannoudji, or Shankar. As electrons are fermions, and indistinguishable from one another, they cannot exist in the same quantum state. Fermi statistics require that the total quantum mechanical wave functions of electrons are anti-symmetric on exchange of particles. As a consequence of this, electron wavefunction overlap among electrons in multi-electron states with non-zero spin can be lower compared to states where the spin magnetic moments would cancel, and the expectation value of the Coulumb interaction between the negatively charged electrons is lowered. As such the origin of the exchange energy is electron-electron repulsion. Other forms of exchange interactions are possible (such as indirect exchange), and exchange interactions can energetically favor anti-parallel alignment resulting in antiferromagnets and ferrimagnets. Examples of ferromagnetic elements at room temperature are iron, cobalt, and nickel.

A magnetically anisotropic object has different magnetic properties depending on directionality, such as uniaxial anisotropy with a preferred or "easy" axis of magnetization. In contrast, a magnetically isotropic object has magnetic properties that do not depend on the relative orientation of the object and an applied magnetic field. Shape anisotropy, which makes it easier to magnetize a rod-shaped object along the axis of the rod or to magnetize a thin film in the plane of the film, arises due to a difference in the demagnetizing field within an object, where the configuration with the weaker demagnetization field is favored. Magnetoelastic anisotropy can result from non-zero stress on the object influencing its electronic band structure. Magnetocrystalline anisotropy is another form of anisotropy related to the crystal structure of the material. Magnetocrystalline anisotropy arises out of coupling between spin-orbit interactions and the crystal electric field of the underlying lattice [36]. The electric field of the crystal lattice impacts the shape of electron orbitals and tends to restrict the reorientation of the orbital magnetic moment under the effect of an applied magnetic field, which also tends to "quench" [35] the orbital contribution to the magnetic moment of the atom. The spin-orbit interaction between the electron spin and its orbital motion results in an additional energy to rotate a spin from its easy axis which is referred to as the anisotropy energy.

Hysteresis loops are measurements of the magnetization of a material in response to an applied magnetic field. Figure 1.5 shows a simulated example of a hysteresis loop for a magnetically hard ferromagnet. As the applied field increases, the magnetization along the applied field direction increases. When the applied field is decreased, the magnetization of the material can be different than it was on the "upward leg" of the measurement. The value of the magnetization when the applied field returns to zero is called the remanent magnetization, or remanence, M_R, typically slightly less than M_s. Continuing to decrease the field, the value at which the magnetization returns to zero is called the coercive field, B_c, or the coercivity of the material. The difference between the magnetization measured for the upward and downward legs of the measurement is the magnetic hysteresis. The area between the curves of the upward and downward legs is proportional to the energy loss associated with irreversibility in the magnetization process. Ferromagnets can be broadly classified as magnetically hard or soft. Magnetically hard ferromagnets have significant coercivity,

B_c, and remanence, M_R. Magnetically soft materials have low coercivity and remanence, and little hysteresis. Magnetically soft materials are useful in applications that involve rapid switching of the magnetization, in order to minimize energy losses, such as transformers. The carbonyl iron magnetic particles that are frequently used in MREs are magnetically soft.

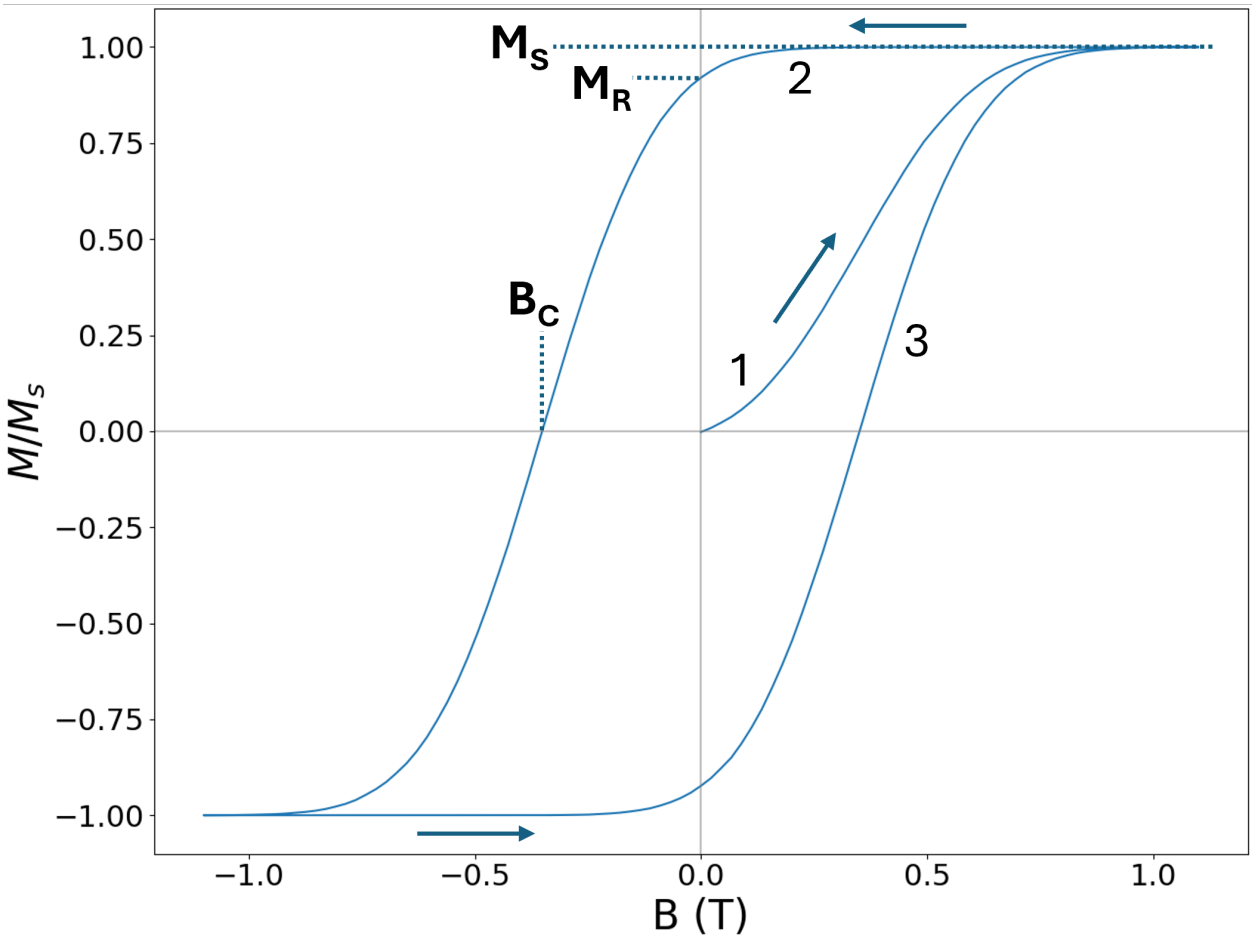

Figure 1.5: Simulated hysteresis loop for a magnetically hard ferromagnet showing M/M_s as a function of the applied field B. The line marked 1 is the initial upward leg, line 2 is the downward leg, and line 3 is the final upward leg. The saturation magnetization, M_s, coercive field, B_c, and remanent magnetization, M_r, are marked. Results generated using the Preisach model of hysteresis [37] with 1×10^5 relays, switching fields generated using a normal distribution around -0.35 and 0.35 T respectively, with a standard deviation of 0.2 T, with relay weights normally distributed around 5, with a standard deviation of 2.5, with weights clipped to a minimum value of 0.01, and then normalized to get a normalized magnetization of the system of relays.

Two models of magnetization response are used in this dissertation. The first is a linear response model with clipped maximum magnitude of M_s.

$$\vec{M} = \chi \vec{H} \tag{1.4}$$

Where $\vec{M}$ is the magnetization, assumed to be uniform throughout the spherical particle, and collinear with $\vec{H}$, the total magnetic field at the center of the particle, and χ is the magnetic susceptibility. Though this response is more in line with a paramagnetic material, it allows the use of well understood methods for solving linear systems of equations to determine the magnetization response of the particles. The other magnetization response model used is the Froelich-Kenelly law,

$$\vec{M} = \frac{M_s \chi_0 \vec{H}}{M_s + \chi_0 |H|}, \tag{1.5}$$

where again $\vec{M}$ is the magnetization, assumed to be uniform throughout the spherical particle, and collinear with $\vec{H}$, the total magnetic field at the center of the particle, $|H|$ is the Euclidean norm of the magnetic field, χ_0 is the initial susceptibility, and M_s is the saturation magnetization. The Froelich-Kenelly magnetization law is a phenomenological model of a nonlinear, saturable, anhysteretic magnetization response. At low fields, when $\chi_0 |H| << M_s$, the response is approximately linear (1.4), at intermediate fields the curve begins to flatten out, and at high fields the curve asymptotically approaches M_s. The use of this magnetization response model does have increased computational cost, and requires more complex methods to solve the nonlinear system of equations that results. Those methods are not guaranteed to converge to a solution, and depend on having an initial guess for the solution that is close to an actual solution.

In both models the magnetization response of the magnetic particles is assumed to be isotropic, there is no preferred direction for the magnetization. The magnetic particles being modeled are on the order of microns and polycrystalline. The result of this polycrystalline nature is that each crystal grain has its own magnetic anisotropy and spontaneous magnetization, but averaging over the volume of the particles leads to a net isotropic magnetization response and zero magnetization

at zero field. This is seen in experimental measurements of the magnetization response of carbonyl iron particles in Figure 3.7, which justifies the use of the Froehlich-Kenelly magnetization law. Smaller particles would be monocrystals, having permanent magnetic moments, and magnetic anisotropy, and require a different magnetization model, but will not be treated here.

In order to more accurately capture the magnetically soft but ferromagnetic response of the magnetic particles, the Froehlich-Kenelly law is used in Chapter 4, which allows us to better qualitatively match the experimentally observed magnetization curve. An example magnetization curve for a magnetically soft material can be seen in Figure 1.6, which is calculated using the Froehlich-Kenelly magnetization law (1.5).

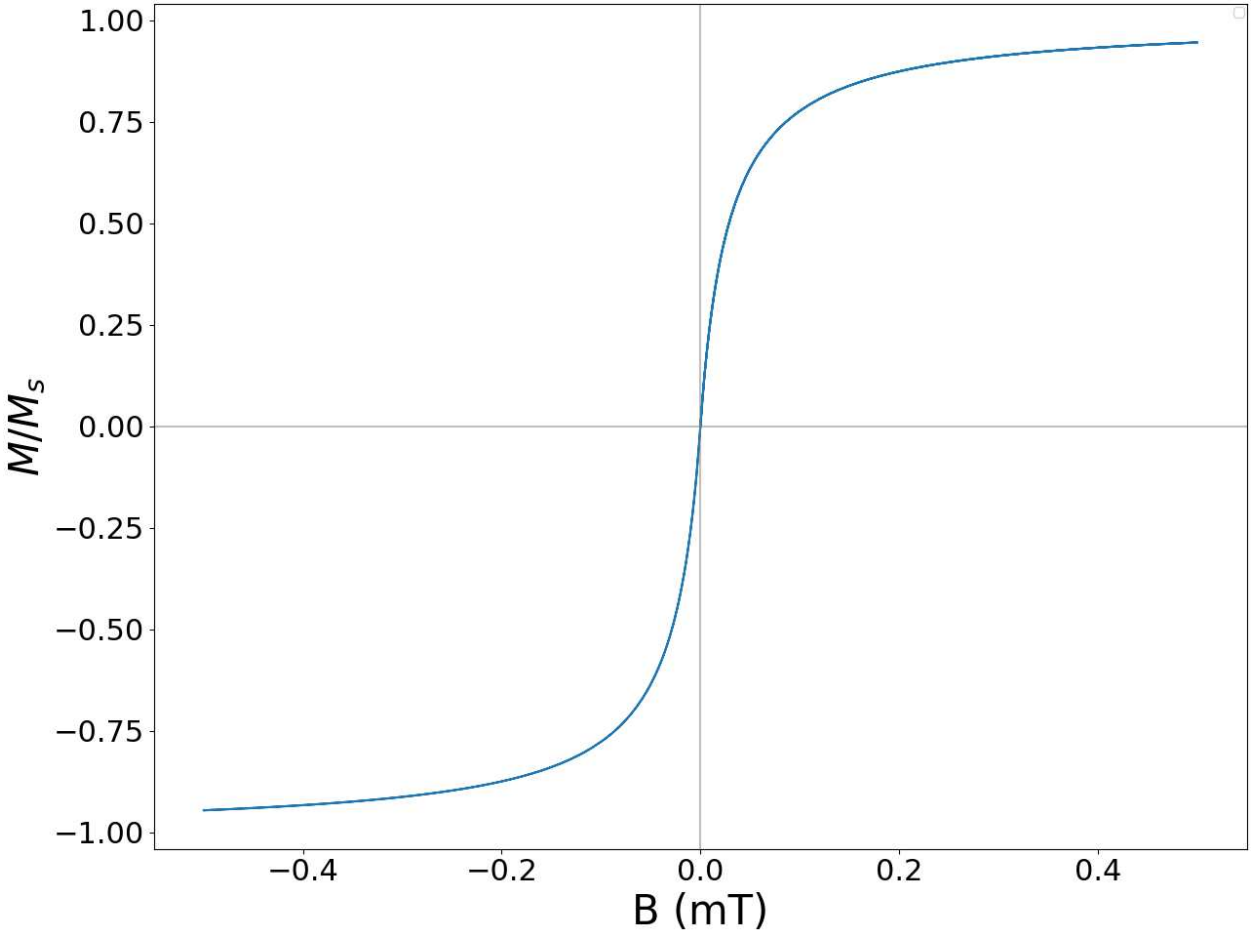

Figure 1.6: Simulated hysteresis loop for a magnetically soft ferromagnet showing M/M_s as a function of applied field B. Results generated using the Froehlich-Kennelly magnetization law, with $\chi = 70$ and $M_s = 1.6 \times 10^6$ A/m. The response is initially linear, but quickly turns nonlinear and levels off, asymptotically approaching saturation, with no remanence or coercivity.

Micromagnetics simulations were also used to help inform the choice of magnetization response models. Micromagnetics studies magnetic behaviors at sub-micrometer length scales, but large enough that atomic structure is ignored. Micromagnetics simulations of a spherical particle with exchange stiffness constant values $A_{ex} = 2 \times 10^{-11}$ J/m and $M_s = 1.7 \times 10^6$ A/m, corresponding to iron, demonstrated a complex internal magnetization texture, see Figure 1.7. The system also demonstrated an isotropic, linear and anhysteretic overall magnetization response, which supported the use of the linear magnetization response law with saturation for the dipole-spring modeling done in Chapter 2 and Chapter 3. For the micromagnetics simulations, simplifications for the internal structure were made by replacing the polycrystalline nature with a magnetically isotropic continuum. While the discretization length of 30 nm is too large to resolve domain walls, it isn't necessary to resolve domain walls when there is no magnetic anisotropy or multiple crystal grains. The complex internal magnetization shows that even with simplifying assumptions about the shape of the magnetic particles and their magnetic isotropy the internal magnetization is inhomogeneous. This stands in contrast to the solution for polarization of a dielectric sphere in a uniform electric field, or a paramagnetic sphere in a uniform magnetic field, where the resulting polarization and magnetization are uniform throughout the sphere. This non-uniformity means that the use of dipole-dipole interaction forces and energies as approximations may underestimate the strength of the magnetic interactions at distances that are small compared to the size of the magnetic particles, and that the magnetostatic self-energy is likely underestimated by assuming a uniform internal magnetization. Still, the computational effort of accurately calculating these magnetic energies is too large to justify for our modeling goals.

Atomistic descriptions of the magnetization response of the magnetic particles is computationally expensive. Micromagnetics simulations are also computationally demanding, and not appropriate for handling the number of magnetic particles we are interested in. The use of micromagnetics simulations is warranted in some contexts, particularly with reduced dimensionality and small length scales, e.g. studies of thin films and interfaces. MuMax3 is software developed to perform micromagnetic calculations using dynamics to evolve the Landau-Lifschitz-Gilbert equation.

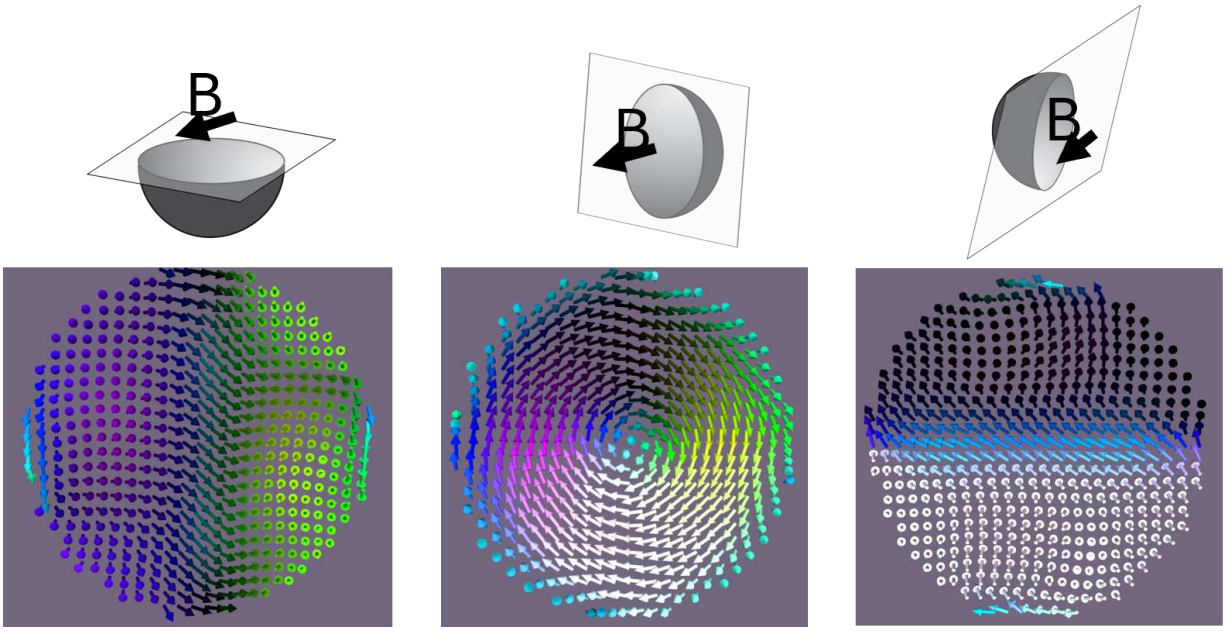

Figure 1.7: Magnetization distributions for a single magnetically soft ferromagnet with applied magnetic field $B = 0.15$ T. Results generated using MuMax3, for a spherical particle of size $R = 1.5$ μm, $A_{ex} = 2\times10-11$ J/m and $M_s = 1.7\times10^6$ A/m, system discretized into cubic elements with side length 30 nm. The net magnetization response is linear with the applied field, but internal magnetization texture is complex, as can be seen in the three cuts through the sphere. Credit to Tori Deng for running the simulation.

It can be used for systems of arbitrary geometry with magnetization vectors with fixed magnitude existing on some grid, and takes into account spatially varying material properties such as M_s, A_{ex} and magnetic anisotropies, dipole-dipole interactions and more [38]. When the magnetic material is fixed in space certain techniques can speed up otherwise expensive calculations like dipole-dipole interactions that are long range and of order N^2, scaling rapidly with the number of magnetic dipoles. Unfortunately, the micromagnetics framework and these techniques for speeding up calculations of magnetic interactions are not easily leveraged for the study of MRE systems with large dimensions and large displacements of magnetic particles.

1.4 Elasticity Theory

Matter is made of atoms, and atomistic models of materials are useful in many contexts. However, we are often interested in the behavior of objects that are large compared to the length scales of atoms and atomic interactions. While it is possible to derive the behavior of large collections

of atoms or molecules in some cases, it is not necessary to begin from this description to create useful and physically reasonable models of material behavior. Continuum mechanics is the study of deformable bodies, and we will begin by examining a small part of the subject before discussing elasticity. The following texts were used to help develop this section, and are potentially useful references, Gurtin for an introduction to continuum mechanics, Truesdell and Noll for nonlinear theories, and Bertram for a modern take on nonlinear theory. [39–41]

Suppose we have a rubber ball or a block of metal, we can imagine that the material is the same throughout, it is homogeneous, and we can cut it into smaller pieces that still contain so many atoms that it would be impossible to account for all the atomic interactions. We can treat the material as continuous, in that we can infinitely divide it. We can define the body of the object Ω, and the surface of the object $\partial\Omega$, and points within the body $\vec{p} \in \Omega$ and on the surface $\vec{p} \in \partial\Omega$ called material points. If the material looks the same in all directions, it is isotropic. If the object does not look the same in all directions, for example if there were rods aligned along some direction, we would say the object is anisotropic. The body is homogeneous if the structure is uniform throughout the body.

A deformation is a transformation of the material points $\vec{p}$ of the body Ω from its reference configuration $\vec{X}(p)$ in 3D Euclidean space, to its current configuration, $\vec{x}(p)$. This deformation can include rigid body translation and rotations, as well as stretching, compressing, and shearing of the material. All of this is contained in the displacement $\vec{u}$ of the material

$$\vec{u}(\vec{X}) = \vec{x}(\vec{X}) - \vec{X}. \tag{1.6}$$

By taking the gradient of the displacement we can retain information about the stretching, compressing, shearing, and rotation of the object while ignoring rigid body translations, for which the gradient of the displacement field would be 0. A closely related object is the deformation gradient, $\mathbf{F} = \mathbf{I} + \nabla\vec{u}$. When $\mathbf{F}$ is constant throughout the body, the deformation is homogeneous.

The determinant of $\mathbf{F}(\vec{X})$, $J =$det$(\mathbf{F}(\vec{X}))$ is a measure of the change in volume of the material at $\vec{X}$ after the deformation. For incompressible materials det$(\mathbf{F}) = 1$. It is possible to perform a

polar decomposition of $\mathbf{F}$ into two tensors, one orthogonal tensor that performs a rotation, and the other a symmetric tensor containing the principal stretches.

$$\mathbf{F} = \mathbf{RU} = \mathbf{VR} \tag{1.7}$$

where $\mathbf{R}$ is an orthogonal tensor, $\mathbf{R}^T = \mathbf{R}^{-1}$, $\mathbf{U}$ is the right stretch tensor, and $\mathbf{V}$ is the left stretch tensor. $\mathbf{U}$ and $\mathbf{V}$ are positive definite, symmetric tensors with the same eigenvalues, called the principal stretches, λ_i, but different eigenvectors defining principal directions. We can also define the right Cauchy-Green strain tensor

$$\mathbf{C} = \mathbf{F}^T\mathbf{F} = \mathbf{I} + \nabla\vec{u} + (\nabla\vec{u})^T + \nabla\vec{u}(\nabla\vec{u})^T + \nabla\vec{u}^T(\nabla\vec{u}) \tag{1.8}$$

The Lagrangian (or Green-Lagrangian) strain tensor, $\mathbf{E}$ is one of multiple strain measures that can be used to describe the way the material is deforming.

$$\mathbf{E} = \frac{1}{2}(\mathbf{C} - \mathbf{I}) = \frac{1}{2}[\nabla\vec{u} + (\nabla\vec{u})^T + \nabla\vec{u}(\nabla\vec{u})^T + (\nabla\vec{u})^T\nabla\vec{u}]. \tag{1.9}$$

The last term is nonlinear in $\nabla\vec{u}$ and so $\mathbf{E}$ is considered geometrically nonlinear. These strain tensors are symmetric and rotation-independent. In the small strain limit this leads to the linear strain tensor.

$$\boldsymbol{\varepsilon} = \frac{1}{2}(\nabla\vec{u} + (\nabla\vec{u})^T). \tag{1.10}$$

The linear strain tensor is not rotation-independent, since a pure rigid body rotation can result in non-zero elements. Since the material response should be unchanged by a rotation of the coordinate system, and since a rigid body rotation of the object should not cause any stress to develop in the material, the use of tensors that are invariant to rotations is important for describing material behavior. In the small-strain limit, the reference and current configurations roughly coincide, and so it is appropriate to use the linear strain tensor.

Balance laws, like the conservation of mass, linear momentum, angular momentum, and energy need to be obeyed in continuum mechanics, but do not uniquely define material behavior. In order to do so, additional constitutive equations need to be assumed that define different classes of materials and material behavior.

An elastic body has a preferred configuration it will maintain unless acted upon. When a force or stress is applied, the body will deform in response, and if the force or stress is removed, the body will return to its initial configuration. This is in contrast to plastic materials or deformations, which are inelastic, and result in deformations that are irreversible. With a plastic deformation the material does not return to its initial configuration even after the force or stress is removed.

In finite strain theory, elastomers and rubber-like polymers are sometimes treated as hyperelastic solids, behaving elastically but nonlinearly over large ranges of strains. These hyperelastic solid models have no dissipative mechanisms, and so can have a strain-energy density constitutive equation relating the energy stored in the deformation of the material to the strain in the material. The stress tensor is then conjugate to the strain-energy density. One simple hyperelastic material constitutive equation is the Neo-Hookean model, where the strain energy density, W, is given in terms of the principal stretches, λ_i:

$$W_{Neo-Hookean} = C_1(\lambda_1^2 + \lambda_2^2 + \lambda_3^2 - 3), \tag{1.11}$$

where λ_i are the principal stretches, and C_1 is a material constant. The second Piola-Kirchoff stress tensor, $\mathbf{S}$ or sometimes $\boldsymbol{\sigma}_{PK2}$, is one stress measure for finite deformations and is energy conjugate to the Green–Lagrange finite strain tensor, $\mathbf{E}$ defined earlier

$$\mathbf{P} = \partial W / \partial \mathbf{E}. \tag{1.12}$$

The second Piola-Kirchoff stress tensor relates the forces acting on a surface at a material point in the current configuration to the area in the reference configuration. The Cauchy stress tensor, $\boldsymbol{\sigma}$,

relates the force on the surface to the are of the current configuration. The two are related by

$$\mathbf{S} = J\mathbf{F}^{-1} \cdot \boldsymbol{\sigma} \cdot \mathbf{F}^{-T} \tag{1.13}$$

where $J = \det(\mathbf{F})$ is a measure of the relative volume change, $\mathbf{F}^{-1}$ is the inverse of the deformation gradient, and $\mathbf{F}^{-T}$ is the inverse transpose of the deformation gradient. Other constitutive equations can be written taking advantage of the invariants of strain tensors, like the right Cauchy-Green deformation tensor:

$$I_1 = tr(\mathbf{C}) = \lambda_1^2 + \lambda_2^2 + \lambda_3^2 \tag{1.14}$$

$$I_2 = tr(\mathbf{C}^2) - tr(\mathbf{C})^2 = \lambda_1\lambda_2 + \lambda_2\lambda_3 + \lambda_1\lambda_3 \tag{1.15}$$

$$I_3 = det(\mathbf{C}) = (\lambda_1\lambda_2\lambda_3)^2 = J^2. \tag{1.16}$$

These are invariants of the tensors, which means that they are independent of the basis or coordinate system in which the tensor is described. By writing constitutive equations in terms of these invariants we ensure material frame indifference. The material behavior should not depend on the observer frame of reference.

A nonlinear theory of elasticity, a theory of finite strains, is needed to describe large deformations, like the large stretches elastomers are capable of. However, the theory of finite strains isn't trivial. While the predictions of infinitesimal strain theory and linear elasticity break down at higher strains, the framework provides a good starting point for modeling elastic material behaviors. In order to do that modeling, we need a constitutive equation that will relate the stress and strain in the system.

In linear elasticity the constitutive equation is analogous to Hooke's law for springs. A linearly elastic material has a linear response, the strain is linearly proportional to the applied stress. Hooke's law for a linear spring says that the restoring force F is proportional to the displacement

from equilibrium, and the constant of proportionality, k is the stiffness.

$$F = -kx. \tag{1.17}$$

In a continuum mechanics framework, Hooke's law takes on a different form due to the three dimensional nature of the problem and the possibility for anisotropic materials, which can still have a linear but different response depending on the direction of the displacement or applied stress. In this case, the stress in the material is linearly proportional to the strain, but due to being tensors they need to be related by a fourth order stiffness tensor, $\mathbf{C}$.

$$\boldsymbol{\sigma} = \mathbf{C} : \boldsymbol{\varepsilon} \tag{1.18}$$

or in component form,

$$\sigma_{ij} = \mathsf{C}_{ijkl}\varepsilon_{kl} \tag{1.19}$$

where repeated indices imply summation.

Due to the symmetries of $\boldsymbol{\sigma}$, $\boldsymbol{\varepsilon}$ and $\mathbf{C}$, at most 21 coefficients of $\mathbf{C}$ are independent. For isotropic media, $\mathbf{C}$ can be reduced to two independent values. The stress tensor is a symmetric 3×3 tensor, and the stress and strain tensors are related to one another by the fourth order stiffness tensor C. This allows us to write down a strain-energy density equation

$$W = \frac{1}{2}\boldsymbol{\varepsilon} : \mathbf{C} : \boldsymbol{\varepsilon} \tag{1.20}$$

or in component form

$$W = \frac{1}{2}\mathsf{C}_{ijkl}\varepsilon_{ij}\varepsilon_{kl} \tag{1.21}$$

We will use this form in Chapter 4 to derive expressions relating the Young's modulus and Poisson ratio of an isotropic material to stiffness constants in our model.

Figure 1.8 shows strain types that are implemented for the model, and that are used in experiments characterizing the mechanical response of MREs, such as uniaxial tension and compression,

and simple shearing. Other configurations are used in mechanical characterization, including indentation measurements, biaxial and triaxial tension, single and double lap shear, and the use of commercial rheometers, which apply torsion.

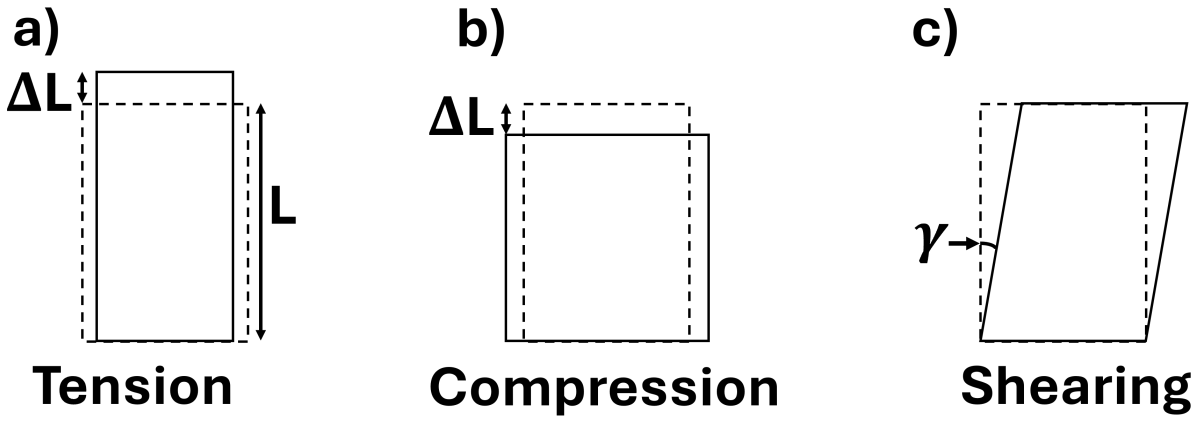

Figure 1.8: Two dimensional diagrams of homogeneous a) tension, b) compression, and c) simple shearing strains. Dashed lines indicate the original shape of the object. In a-b) tension and compression, strain is defined as a percent change in length $\varepsilon = \Delta L/L_0$. In c) shear, strain is defined as $\tan(\gamma)$, where γ is the angle (in radians) opened up by the strain. In the small strain limit $\tan(\gamma) \approx \gamma$, and the shear strain is often given as γ.

Chapter 2

Magnetorheological elastomer modeling: lessons from a two-dipole model

2.1 Context and Contributions

This chapter consists of an article planned for submission titled *Magnetorheological elastomer modeling: lessons from a two-dipole model*, the article was written by D. B. Marchfield in collaboration with K. S. Buchanan (CSU), A. T. Clark and X. M. Cheng (Bryn Mawr). Modeling work was performed by D. B. Marchfield (CSU). This article uses a simple two particle dipole-spring model to understand the connections between mechanical motion and the magnetic response of a MRE.

2.2 Abstract

Magnetorheological elastomers (MREs), composite materials consisting of a polymer matrix with embedded magnetic particles, are attracting interest because their mechanical properties can be tuned via an external magnetic field. Understanding the connection between magnetic particle motion and the magnetic response of MRE materials is key to improving MRE design, and this is especially important for ultrasoft MREs where the particle displacement can be large, on the order of the particle size or much larger depending on the particle concentration. Here we present and analyze results calculated from a simple two-dipole model with parameters appropriate for carbonyl iron-based ultrasoft MREs, and we show how the model provides insight into the mechanisms of MRE magnetization reversal. The model shows that the magnetic field ranges over which magnetic hysteresis is observed are the same as the field ranges where mechanical hysteresis is observed. Furthermore, the attractive particle interactions, which are strongest for smaller angles

between the field and the axis that connects the interacting particles, play a key role in the MRE hysteresis.

2.3 Introduction

Magnetorheological elastomers (MREs) are a class of smart materials whose mechanical properties can be reversibly altered by applying a magnetic field. The dynamically tunable mechanical properties of MREs are attractive for a wide range of applications including actuators, tunable vibrational dampers, and dynamic cell culture substrates [29,42]. MREs typically consist of micron-sized magnetic particles embedded in a resilient polymer matrix. Ultrasoft MREs, that is, MREs with a base Young's modulus (E) of several kPa, have received increased attention recently because they offer an innovative means to study the cellular response to realistic biophysical mechanical cues *in vitro* [13,14,43]. The mechanical behavior of ultrasoft MREs is complex and the motion of the magnetic particles within the polymer matrix can be on the order of micrometers [44]. Recent work shows that the larger scale of the particle motion in ultrasoft MREs compared to that of stiffer MREs also leads to an altered magnetic response where a characteristic pinched hysteresis loop shape is observed in the ultrasoft case [45,46].

Modeling of MREs is important for understanding the underlying mechanisms of the stiffness response to a magnetic field as well as the connections between the particle motion and magnetic response, which are needed to guide the design of new MREs [26]. MRE modeling approaches can be classified based on the scale of the model: micro-, meso-, or macro-scale [47]. Microscopic models follow the details of the positions of individual particles in the MRE and also take the discrete nature of individual polymer chains into account. Mesoscopic models also treat the magnetic particles explicitly but consider the elastic matrix as a continuum using either springs to connect the particles or finite element simulations to describe the response of the particles and elastic matrix to applied magnetic fields. Microscopic and mesoscopic models provide detailed information on the motion of the particles but the volume of the MRE that can be modeled is limited. Macroscopic models, in contrast, use effective continuum parameters to study larger volumes of an MRE, and

utilize the framework of continuum mechanics to predict the macroscopic response. Analytical modeling at the particle scale has also been used to relate the magnetic interaction energies among particles to the magnetorheological response of the MRE [21, 23], but analytical theories require significant simplification and complement rather than replace other modeling approaches.

Mesoscopic modeling is particularly important for MREs because the mesoscopic approaches provide a bridge between the large-scale continuum response and the microscopic, and yield mechanistic insight into MRE behaviors. Mesoscopic particle-based modeling can be combined with finite element method calculations of the elastic matrix [48], but the high computational expense limits the size of the systems that can be studied, whereas models that treat the polymer matrix by connecting the magnetic particles with elastic springs and spring networks can be used to describe larger numbers of particles [5, 49]. Modeling is challenging for ultrasoft MREs ($G, E \approx$ kPa, where G is the shear modulus) compared to rubber-like MREs ($G, E \approx$ MPa) since the particles can rearrange more freely [44]. Particle-spring models that focus on the interaction between pairs of particles, while simple in nature, have served as a useful tool to study the role of particle motion in the magnetization behavior of soft MREs [50–52], and, as we will show, can provide insight into the complex behavior of ultrasoft MREs.

In this work we present and analyze a set of calculations performed using two-particle spring models. We recently showed that a one-spring, two-particle model qualitatively captures the magnetization reversal behavior observed experimentally in ultrasoft MREs and provides insight into the mechanistic connections between particle motion and magnetization reversal [45]. Here we show more detailed two-particle modeling results and examine the effects of the spring stiffness as an analogy to polymer stiffness, the equilibrium spring length as an analogy to volume filling fraction, and the applied field angle on the particle motion and magnetic reversal. These results highlight the important connection between attractive interparticle interactions and magnetic hysteresis.

2.4 Methods

To understand the connection between particle motion and the magnetic response of MREs, we use two simple models: a single-spring model, illustrated in Figure 2.1(a), that involves two point dipoles connected to one another by a spring, and a three-spring model shown in Figure 2.1(b) that includes two additional springs that connect each dipole to its zero-field position. The single-spring model is simpler and can be used to treat two specific cases where the applied magnetic field $\vec{H}$ is applied along and perpendicular to the axis of the two particles, but since it lacks rotational restoring forces it cannot be used to model the particle response for other field angles. The three-spring model, in contrast, provides a realistic restoring force for particle rotation and hence can be used to model the particle response when $\vec{H}$ is applied at an arbitrary angle θ_H [50, 53].

While real MREs are more complex – they contain large numbers of particles and the polymers used to make MREs often exhibit viscoelastic behavior – these simple models have the advantage that they are straightforward to interpret and provide insight into the connection between the mechanical motion of the particles and their magnetic reversal. Furthermore, the magnetic responses of larger ensembles of particles can be approximated by considering averages of two-dipole results weighted by an appropriate distribution of particle pairs with different separations and applied field angles, which provides a qualitative match to experiments in spite of neglecting interactions between pairs and viscoelastic effects [45]. Averaging approaches have been used previously to extend Stoner-Wohlfarth hysteresis models to capture the behaviour of nanoparticle ensembles [54, 55], and the Preisach model similarly uses averaging of many independent units [56].

The models involve two magnetic particles that are treated as spherical dipoles. The net magnetic moment of each sphere is $\vec{m}_i M_s V$, where M_s is the saturation magnetization, $\vec{m}_i$ is the normalized magnetic moment of the sphere, $V = \frac{4}{3}\pi\left(R\right)^3$ is the sphere volume, and R is the radius of the sphere. The magnetic moment of particle i, $\vec{m}_i$, is linearly proportional to the effective

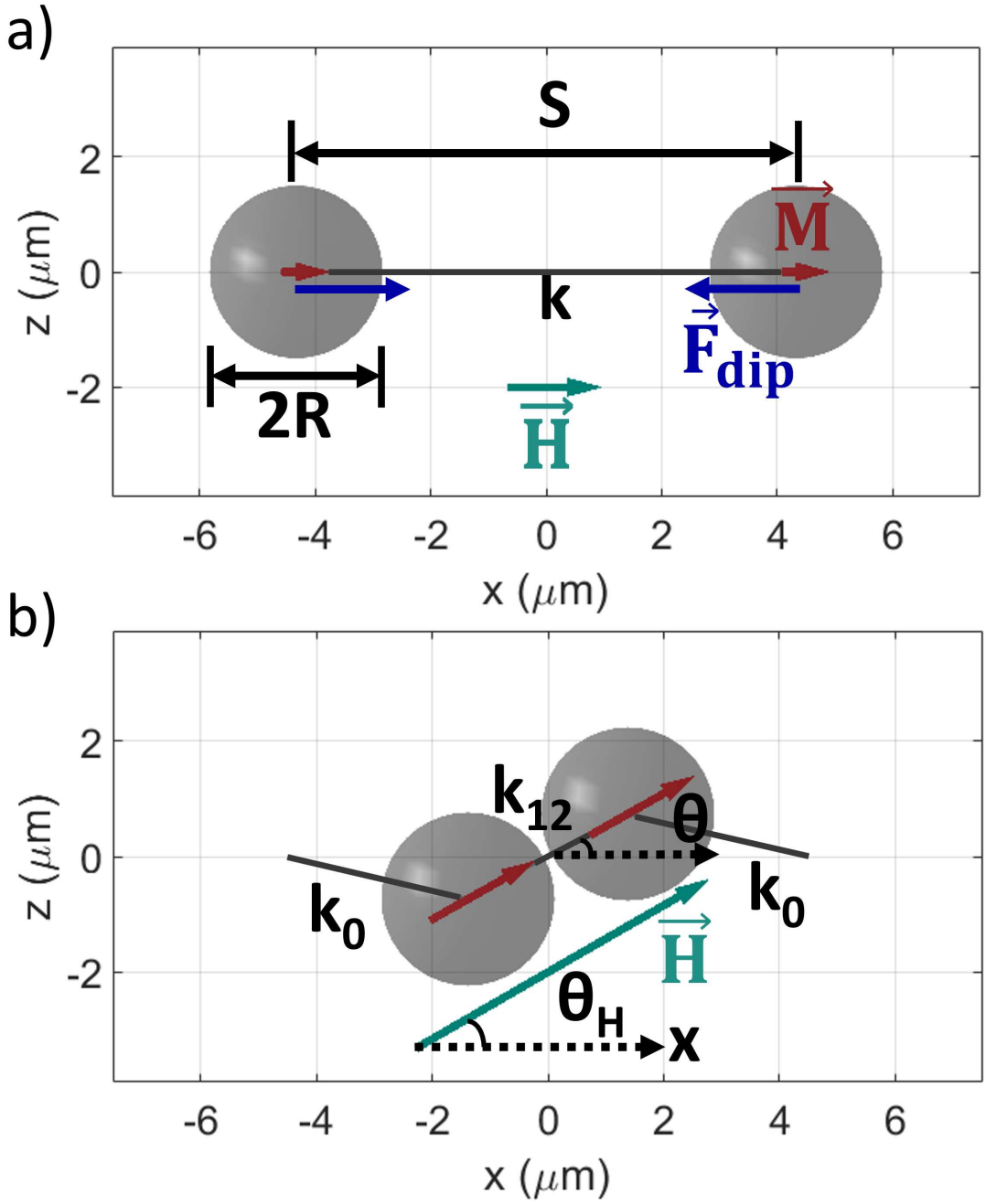

Figure 2.1: (a) Diagram of single-spring two-particle model, with particle diameter $2R$, separation S, and spring stiffness k. When the applied magnetic field $\vec{H}$ is along the axis connecting the particles, the particles are magnetized along $\vec{H}$ (dark red arrows) and the particles experience an attractive dipole force (blue arrows) (b) Diagram of three-spring two-particle model, with diameter $2R$, separation S, and spring stiffnesses k_0 and k_{12}. When $\vec{H}$ is applied at an angle θ_H relative to the x-axis, also the axis that connects the particles at $H = 0$, the two-particle unit will rotate such that $\theta \leq \theta_H$, where θ is the angle between the center-to-center vector connecting the particles and the x-axis.

field $\vec{H}_{\text{eff}}$ at the location of particle i. In terms of reduced magnetic fields $\vec{h}_\alpha = \vec{H}_\alpha/M_s$,

$$\vec{m}_i = \chi \vec{h}_{\text{eff}}(\vec{r}_j) = \chi \left(\vec{h} + \vec{h}_{\text{dip}}(\vec{r}_j) \right) \tag{2.1}$$

with the saturation restriction of $|\vec{m}_i| \leq 1$. In (2.1), $\vec{h} = \vec{H}/M_s$ is the reduced external magnetic field and, assuming that the magnetic field of the particles can be described as a point dipole at the center of the sphere, the dipole field due to particle j at the location of particle i is

$$\vec{h}_{\text{dip}} = \frac{V}{4\pi} \frac{3\hat{r}_{ij}(\vec{m}_j \cdot \hat{r}_{ij}) - \vec{m}_j}{r_{ij}^3} \tag{2.2}$$

where $r_{ij} = |\vec{r}_i - \vec{r}_j| = S$ is the distance between the two particles, also the separation, and $\hat{r}_{ij}$ is the unit vector that points from particle j to particle i.

The assumed linear relationship between the magnetization and effective field ((2.1)) is supported by micromagnetic simulations. Simulations performed using MuMax3 [38] for a $R = 1.5$ μm spherical iron particle, with $M_s = 1.4 \times 10^6$ A/m, exchange constant $A_{\text{ex}} = 2 \times 10^{-11}$ J/m, a spatially uniform magnetic field, and a cubic mesh size of 30 nm showed a linear magnetic response and, furthermore, the application of a rotating magnetic field of fixed magnitude showed no rotational hysteresis. These simulations assume no magnetocrystalline anisotropy, which is reasonable since the particles used in MREs are generally polycrystalline carbonyl iron with negligible anisotropy. The unsaturated spin distributions obtained in the simulations are complex multidomain and vortex states, but the stray fields obtained from the spin distributions are well described by the lowest order (dipole) term in the multipole expansion (to better than 0.01% at a distance of 100 nm from the particle edge in any direction). We note that the magnetic fields used in the simulations are uniform and the response may be more complex for the non-uniform magnetic fields found in a real MRE.

At equilibrium, the net force between the two spheres must be zero, and the forces that must be considered are the elastic and the magnetic dipole-dipole interaction forces. This was done in practice by minimizing the total energy of the system of particles using a nonlinear conjugate

gradient method. The total energy of the single spring system is

$$E_{\text{tot,1}} = -\mu_0 M_s^2 V \sum_{i=1}^{2} \vec{m}_i \cdot \vec{h} - \frac{\mu_0 M_s^2 V}{2} \sum_{i=1}^{2} \vec{m}_i \cdot \vec{h}_{\text{dip}} + \frac{1}{2} k (S - S_0)^2 + \sum_{i=1}^{2} \frac{\mu_0 M_s^2 V}{2\chi} m_i^2 \tag{2.3}$$

where the terms are, in order of appearance, the Zeeman energy, dipole-dipole energy, elastic energy, and a self-energy term. Our self-energy term is analogous to the self-energy term used for induced electric dipoles in molecular dynamics simulations, a derivation of which can be found in Ref. [57] Chapter 3, Polarization and Energy, section 15, equations (3.90) to (3.95). In micromagnetic simulations, this self-energy is constant as the magnitude of the moment for each cell is fixed, and the self-energy is orientationally invariant. The spring constant k and the elastic equilibrium separation S_0 can be adjusted to capture the behaviors of polymers with different stiffnesses and particle separations, respectively. For the three-spring model (Figure 2.1(b)) two additional elastic energy terms must be added and the total energy is

$$E_{\text{tot,3}} = E_{\text{tot,1}} + \frac{1}{2} k_0 [(\vec{r}_1 - \vec{r}_{1,0})^2 + (\vec{r}_2 - \vec{r}_{2,0})^2] \tag{2.4}$$

where $\vec{r}_{1,0}$ and $\vec{r}_{2,0}$ are the elastic equilibrium positions of particles 1 and 2, respectively, k_0 is the spring constant of the springs that connect each particle to their respective elastic equilibrium positions, and k_{12} is used in place of k in (2.3).

An additional energy term, an overlap penalty is introduced to prevent the particles from intersecting. For the single-spring model $E_{\text{ov}} = E_{\text{max}}(\tanh(u/\delta)+1)/2$ is used where $u = 1/r_{ij} - 1/2R$, and δ determines the width of the roll-on/roll-off of the tanh function. Here $E_{\text{max}} = 100$ and $\delta = 1 \times 10^{-2}$ 1/μm were used. For the three-spring model a Weeks-Chandler-Andersen potential,

a modified form of the Lennard-Jones potential, was used

$$E_{\text{WCA}} = \begin{cases} 0 & \text{for } S > r_{\text{cut}} \\ 4E_{\text{max}}((\frac{r_{\text{min}}}{S})^{12} - (\frac{r_{\text{min}}}{S})^{6} + \frac{1}{4}) & \text{for } S \leq r_{\text{cut}} \end{cases}$$

with $E_{\text{max}} = 0.01$, a minimum allowed separation $r_{\text{min}} = 2R$, and a cutoff separation of $r_{\text{cut}} = 2^{1/6} r_{\text{min}}$. Both functions increase rapidly with decreasing S when S is close to $2R$ and decrease rapidly to zero as S increases. Both overlap penalties produce similar results, however, the energy minimization was more reliable with the WCA roll-off for the three-spring model, whereas use of the tanh overlap penalty leads to some situations where the model is trapped in nonphysical local energy minima.

Hysteresis loops were obtained by stepping through a sequence of applied magnetic fields $\vec{H}$. At each step, the local minimum energy configuration was found starting from the previous particle configuration using an iterative nonlinear conjugate gradient method. At each step of the energy minimization procedure, the magnetization was determined based on $\vec{H}$ and the particle positions. The magnetizations of the particles were found by solving a system of linear equations [5] of the form $\mathbf{A}\vec{x} = \vec{b}$, subject to the restriction $|\vec{m}_i| \leq 1$. The system of linear equations is obtained by combining Eqs. (2.1) and (2.2) and rearranging, which yields

$$\vec{m}_i - \chi \frac{R^3}{3} \sum_{j \neq i}^{N} \left(\frac{3\hat{r}_{ij}(\vec{m}_j \cdot \hat{r}_{ij}) - \vec{m}_j}{r_{ij}^3} \right) = \chi \vec{h}.$$

This can be written as a matrix equation by defining

$$\boldsymbol{A} = \begin{bmatrix} \boldsymbol{I} & \boldsymbol{D_{12}} \\ \boldsymbol{D_{12}} & \boldsymbol{I} \end{bmatrix}, \tag{2.5}$$

where $\boldsymbol{I}$ is a 2×2 identity matrix, $\boldsymbol{D_{12}}$ is

$$\boldsymbol{D_{12}} = -\chi \frac{R^3}{r_{12}^3} \begin{bmatrix} (3n_{12,x}^2 - 1) & (3n_{12,z}n_{12,x}) \\ (3n_{12,x}n_{12,z}) & (3n_{12,z}^2 - 1) \end{bmatrix}, \tag{2.6}$$

and $n_{ij,k}$ is the k^{th} component of the unit vector $\hat{n}_{ij} = \vec{r}_{ij}/r_{ij} = \vec{r}_{ij}/S$. The vectors $\vec{x}$ and $\vec{b}$ are then made up of the magnetization components of the two particles and repeated units of $\vec{h}_{ext}$ multiplied by χ, respectively, and are

$$\vec{x} = \begin{bmatrix} m_{1,x} \\ m_{1,z} \\ m_{2,x} \\ m_{2,z} \end{bmatrix}, \text{ and } \vec{b} = \chi \begin{bmatrix} h_x \\ h_z \\ h_x \\ h_z \end{bmatrix}. \tag{2.7}$$

The particle positions are used to update $\boldsymbol{A}$ at each iteration, and then the magnetizations are obtained by solving for $\vec{x}$.

The simplicity of this modeling approach allows for straightforward interpretation of the results and, since the computational expense is minimal, it is possible to cover a wide range of parameters. Here we apply the model to two identical particles with radii of $R = 1.5$ μm and magnetic properties that are similar to those of carbonyl iron, $M_s = 1.4 \times 10^6$ A/m and a susceptibility $\chi = 2$. Stiffnesses of $k = 1 \times 10^{-3}$ to 9×10^{-1} N/m and elastic equilibrium separations S_0 of 3.2 to 13 μm were considered, which covers a range of behaviors from rubber-like to ultrasoft [45]. These values of k and S_0 roughly correspond to a range of MREs with Young's moduli of $E \approx 100$ Pa to 400 kPa, estimated by treating the material between the particles as a cylinder with cross-sectional area $A = \pi R^2$ and assuming that the stress-strain response is linear and that the modulus is constant under deformation, which yields $k = EA/S_0$. In an isotropic MRE the average separation between particles is $S_{0,\text{avg}} = (V/\Phi)^{\frac{1}{3}}$ where $\Phi = NV/V_{\text{MRE}}$ is the volume filling fraction, and N is the number of particles that reside within a volume V_{MRE}. For $\Phi = 0.03$ and $R = 1.5$ μm, realistic

parameters for an ultrasoft MRE, $S_{0,\text{avg}} = 7.8\ \mu$m.

For the three-spring model we use the method described in Ref. [50] to obtain realistic estimates for k_0 and k_{12} from the shear modulus G of the polymer, particle size, and initial separation of the particles using

$$k_0 = \frac{1}{M_0}\left[1 - \frac{3}{2}\frac{R}{S_0} + \frac{9}{4}\left(\frac{R}{S_0}\right)^2 - \frac{19}{8}\left(\frac{R}{S_0}\right)^3 + \frac{93}{16}\left(\frac{R}{S_0}\right)^4\right], \tag{2.8}$$

and

$$k_{12} = \frac{1}{M_0}\left[\frac{3}{2}\frac{R}{S_0} + \frac{19}{8}\left(\frac{R}{S_0}\right)^3\right], \tag{2.9}$$

where $M_0 = 1/6\pi GR$. The single-spring and three-spring models provide equivalent results for $\theta_H = 0^\circ$ and 90° when $k = k_0/2 + k_{12}$ is used for the single-spring model.

2.5 Results

2.5.1 Single-spring model and the relationship between particle motion and magnetic hysteresis

We will first concentrate on the single-spring two-particle model. Figure Figure 2.2(a) shows a hysteresis loop and the corresponding particle displacement for the case where $\vec{H}$ is aligned with the axis connecting the particles, also the x-axis, calculated for $k = 4 \times 10^{-2}$ N/m and $S_0 = 9\ \mu$m. When $\vec{H}$ is aligned with the axis, the magnetic interaction between the two particles is attractive. The field is first increased from 0 T to 1 T, then decreased to -1 T and increased back to 1 T in steps of 0.01 T. The magnetic response (Figure 2.2(a)) has a pinched loop shape where the response near $H = 0$ is linear with no hysteresis and the appearance of side lobes that open up as H is increased, which is qualitatively similar to what is observed experimentally for ultrasoft MREs [45]. Starting from $H = 0$, the particles have no magnetic moment and are at their elastic equilibrium positions with a normalized x-component of the magnetization of $M_x/M_s = (m_1 + m_2)/2 = 0$ and $S = S_0$.

As H is increased, M_x increases, the particles experience an attractive dipolar force that draws them together, and $S - S_0$ decreases as H increases at first gradually and then an abrupt change in separation is observed at a critical field H_{C2} where $S - S_0$ decreases to -6 μm and the particles are in surface contact ($S = D$). We will refer to the state where the particles are in contact as the clustered state. The particles remain clustered for $H > H_{C2}$. The particles also remain clustered as H is decreased from H_{C2} down to a second critical field H_{C1}, where $|H_{C1}| < |H_{C2}|$. H_{C1} corresponds to the field at which m_1 and m_2 are small enough that the elastic force is able to overcome the attractive dipolar interaction between the particles and pull them apart. As H is decreased further, $S - S_0$ increases gradually until the particles return to their elastic equilibrium positions at $H = 0$.

Bistability in the particle separation is observed over a range of H values from H_{C1} to H_{C2} in Figure 2.2, where the bistability arises due to the presence of two accessible energy minima. This can only occur if the magnetic interaction is strong enough to overcome the elastic restoring force that pulls the particles apart over some portion of the hysteresis loop. When this occurs a dumbbell/dimer pair will form. As shown in Figure 2.2, the fields at which pair formation occurs and bistability exists exactly correspond to the fields at which magnetic hysteresis occurs. The motional and magnetic hysteresis are hence linked. There are other possible sources of hysteresis, e.g., domain wall motion, anisotropies within a single particle that are neglected here but these are expected to be small for magnetically soft carbonyl spheres.

The magnetic response and displacement curves are markedly different when H is applied perpendicular to the axis that connects the particles, as shown in Figure 2.3 for the same k, S_0, and field range used for Figure 2.2. In Figure 2.3 the magnetic interaction is repulsive. Like the attractive case the particles are at the equilibrium separation with no magnetization when $H = 0$, however, $S - S_0$ increases as H is increased due to the repulsive dipolar interaction. The separation reaches a maximum of 0.4 μm when the particles reach magnetic saturation, where the motion is restricted by the elastic restoring force. The separation and magnetization retrace the up-going field

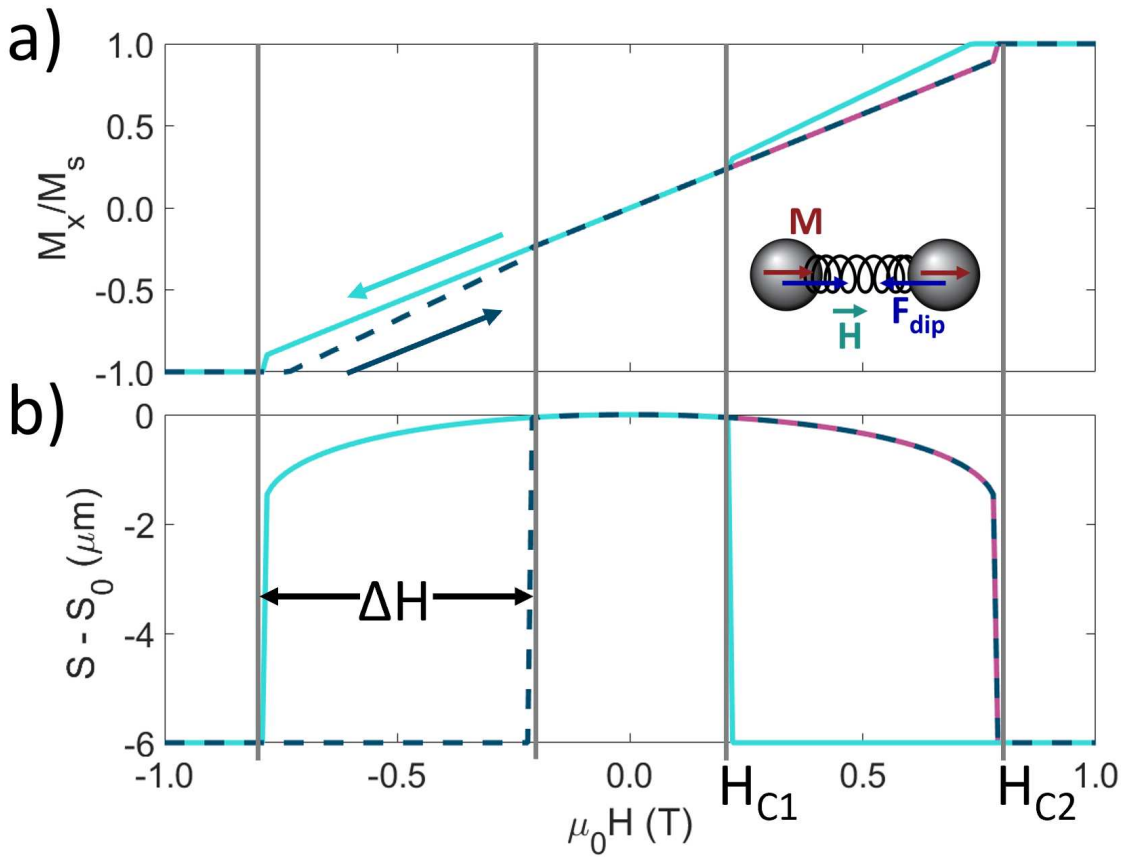

Figure 2.2: The (a) magnetization and (b) particle displacement ($S - S_0$) are shown as a function of H, calculated for $S_0 = 9$ μm and $k = 4 \times 10^{-2}$ N/m for the case where $\vec{H}$ is applied along the axis that connects the two particles. The inset to (a) shows the directions of $\vec{H}$ (teal arrow), the resultant particle magnetization $\vec{M}$ (dark red arrows), and the dipolar force $\vec{F}_{\text{dip}}$ (blue arrows), which is attractive in this case. The magenta solid lines show the legs increasing from 0 T to saturation, the cyan solid lines show the descending legs, and the blue dashed lines show the ascending leg. The solid arrows show the directions of the field sweep. The same line color/style convention will be used in hysteresis figures that follow. Vertical lines show the critical field values H_{C1} and H_{C2} between which the particle configuration is bistable. The field range over which there are two accessible states, also the field range over which hysteresis occurs is $\Delta H = H_{\text{C2}} - H_{\text{C1}}$.

curve as H is reduced. There is no region of bistability, no motional hysteresis, and no magnetic hysteresis.

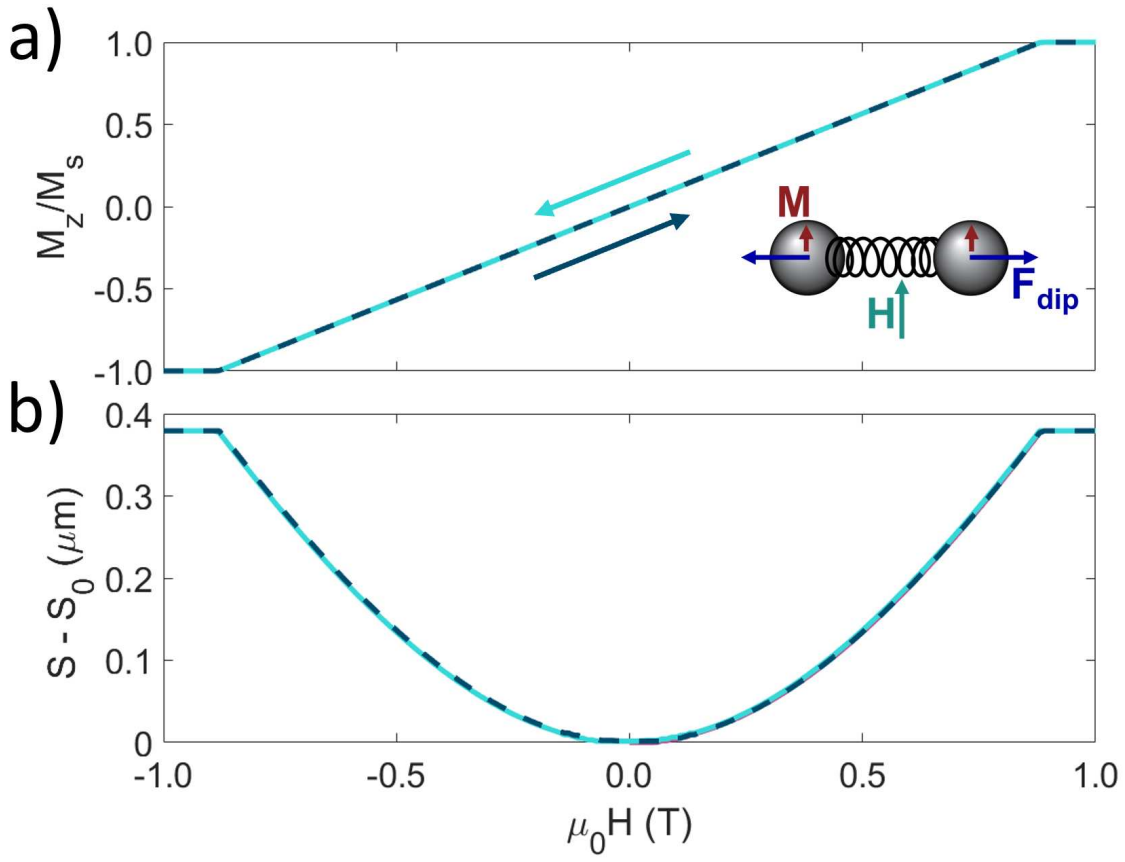

Figure 2.3: The (a) magnetization and (b) particle displacement ($S - S_0$) are shown as a function of H for case where $\vec{H}$ is applied perpendicular to the axis that joins the two particles for $S_0 = 9$ μm and $k = 4 \times 10^{-2}$ N/m. As illustrated in the inset to (a), the applied field $\vec{H}$ (teal arrow) magnetizes the particles in the direction perpendicular to the particle axis (dark red arrows), which leads to a repulsive $\vec{F}_{\text{dip}}$ (blue arrows).

Next we explore the attractive case in more detail. For the single-spring two-particle model, both k and S_0 affect the shape and characteristics of particle displacement. Figure Figure 2.4 shows the particle displacement vs. H curves for nine combinations of k and S_0. In all cases the field range of bistability corresponds to the field range over which hysteresis is observed. As shown in Figs. Figure 2.4(a-c), a stiff spring (large k) will inhibit pair formation and consequently hysteresis in the displacement and the magnetic response, and the magnitude of the particle displacement

decreases with increasing S_0 because the magnetic interaction is weaker when the particles are farther apart. In contrast, for lower k (Figure 2.4(d-f) and (g-i))) the particle motion increases with increasing S_0 for all but one of the S_0 values shown in these plots. In Figure 2.4(f), pair formation is inhibited by the large S_0 and intermediate k (0.04 N/m), whereas for Figs. Figure 2.4(d,e) and (g-i) the magnetic interactions are strong relative to the elastic forces and the particles form clusters. The trend of increasing particle motion with increasing S_0 occurs because the particles have a longer distance over which they can move before they touch and stop as S_0 increases, and this larger particle motion also corresponds to a larger field range over which the bistability occurs, ΔH. The magnetic interactions are weaker, however, for larger S_0, and these trends of increasing motion and increasing ΔH only continue if the magnetic interactions are sufficiently strong to promote cluster formation.

The trends observed in Figure 2.4 are examined in more detail in Figure 2.5, which shows the effect of k and S_0 on the critical fields associated with the cluster formation, H_{C1} and H_{C2}, as well as the field range associated with particle bistability ΔH over a three order of magnitude range of k values and for S_0 out to $8R$. The considered k range covers physically realizable polymer stiffnesses [45], and $S_0 = 8R$ corresponds approximately to the maximum value of S_0 that leads to bistability for this k range. Figures Figure 2.5(c) and (d) show that ΔH increases smoothly with S_0 until a critical point beyond which bistability and hysteresis are no longer observed, and the maximum ΔH increases for lower k, which occurs since particles in a matrix with lower stiffness will be able to move over longer distances. The stability ranges predicted using (2.10) agree well with the critical points extracted from the more detailed modeling (Figure 2.5(d)).

2.5.2 Threshold for hysteresis vs. no hysteresis

In Figure 2.5(d), ΔH increases with increasing S_0 at fixed k, but exhibits a steep drop off beyond a critical value where the combination of k and S_0 is such that pairs no longer form. The drop off is abrupt because of the simplicity of the model. Either the combination of stiffness and separation can result in the formation of pairs or it cannot. The critical S_0 value for a given k

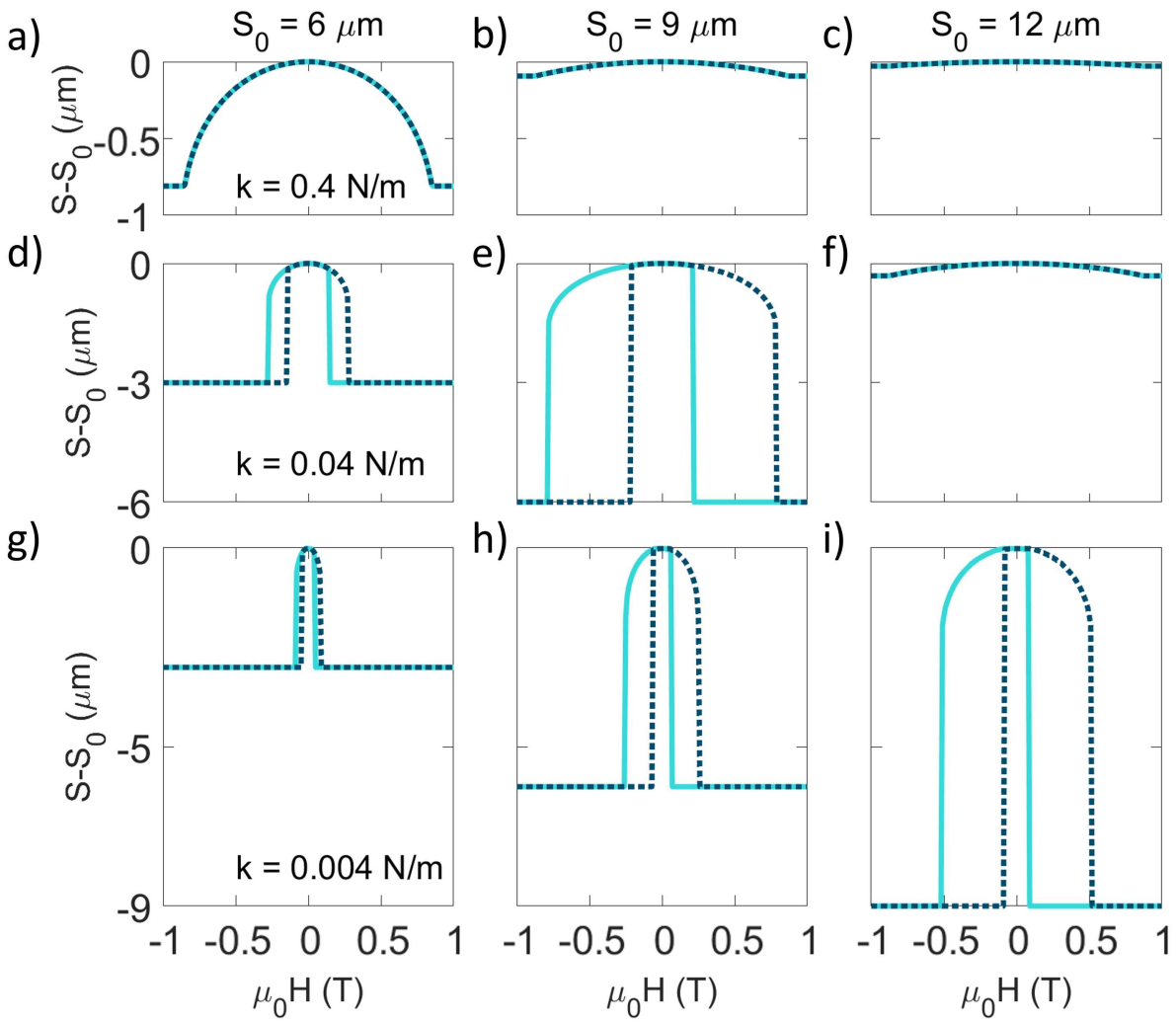

Figure 2.4: Plots of $S - S_0$ as a function of H for two particles with H along the particle axis for selected k and S_0 with $k = 0.4$ N/m (a,b,c), 0.04 N/m (d,e,f), and 0.004 N/m (g,h,i) and $S_0 = 6$ μm (a,d,g), 9 μm (b,e,h), and 12 μm (c,f,i). The x-axis limits are the same for all plots. The y-axis limits are different for each of the k values and the plot aspect ratios have been scaled to highlight the scale differences. The particle size limits the distance of closest approach.

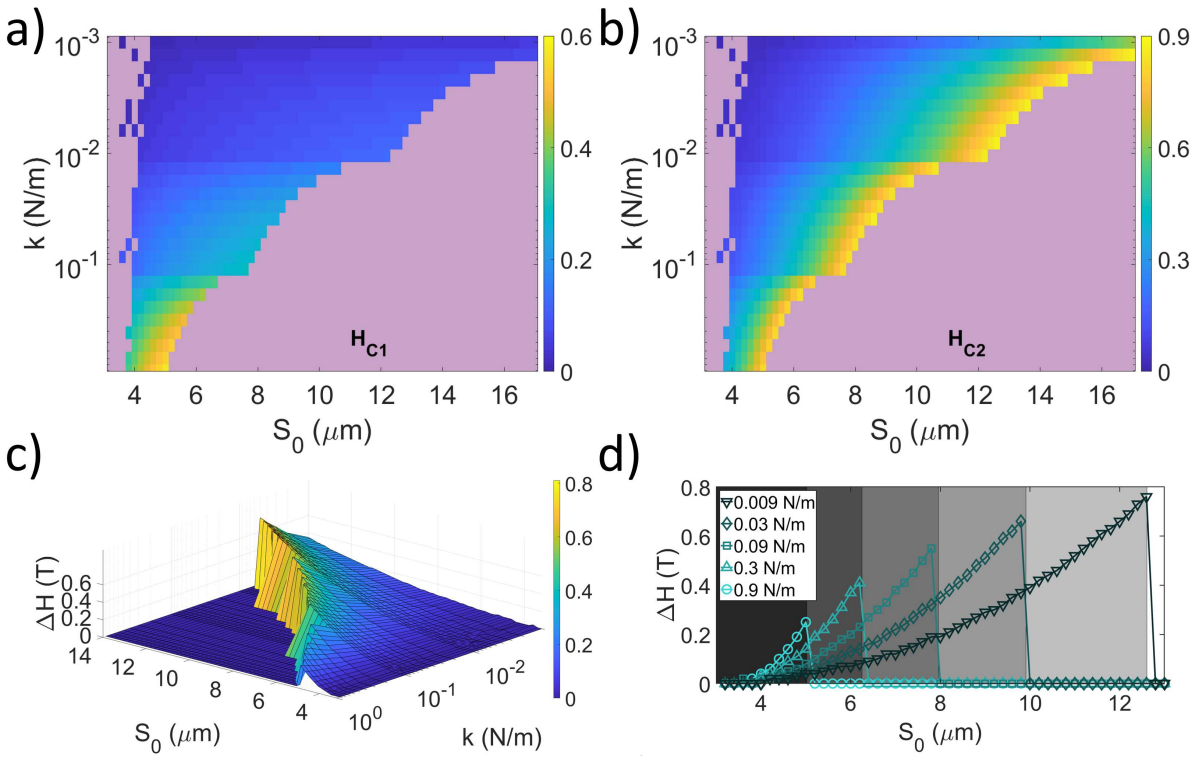

Figure 2.5: Critical fields (a) H_{C1} and (b) H_{C2} as a function of k and S_0 where H is applied along the axis connecting the particles. The taupe regions indicate parameter combinations that do not result in hysteresis. ΔH (c) as a function of k and S_0 and (d) as a function of S_0 for selected k values. In (d) the shaded regions show the range of S_0 values where hysteresis is expected, calculated using (2.10) for each of the k values shown in the legend. The darkest (lightest) grey corresponds to the largest (smallest) k, and in all cases the range of S_0 extends from $S_0 = 2R$ to the maximum shaded value.

can be estimated by considering the elastic and dipolar forces when the particles are saturated ($m_1 = m_2 = 1$). At saturation, and when $\vec{H}$ is along the axis that connects the two particles, the elastic force on dipole 1, where dipole 1 is on the left, is

$$\vec{F}_{\text{el,1}} = k(S - S_0)\hat{x}$$

and the magnetic force on dipole 1 is

$$\vec{F}_{\text{dip,1}} = \frac{6\mu_0 M_s^2 V^2}{4\pi S^4}\hat{x}.$$

The particles will cluster provided there is no energy barrier that prevents them from coming together. The condition for the disappearance of this energy barrier is when $\vec{F}_{\text{net,1}} = \vec{F}_{\text{el,1}} + \vec{F}_{\text{dip,1}} = 0$ and $dF_{\text{net,1}}/dS = 0$, i.e., when $\vec{F}_{\text{net,1}}$ has a minimum value of zero over the range $S \in [2R, S_0]$. The condition for clustering and for hysteresis is hence

$$S_0 < \frac{5}{4}\left(\frac{6\mu_0 M_s^2 V^2}{\pi k}\right)^{\frac{1}{5}}. \tag{2.10}$$

As shown in Figure 2.5(d), the critical S_0 values calculated using (2.10) agree well with the cutoff values obtained from the hysteresis calculations.

2.5.3 Three-spring model and the rotational response

A real MRE will contain many pairs of interacting particles, and the axes of the particle pairs will be at varying angles with respect to $\vec{H}$. Consequently, many of the particle pairs will experience non-axial forces that will lead to a rotation of the axis that connects the particle pair in addition to motion along the axis. The single-spring model provides no resistance to rotation and is hence only appropriate for the two cases considered thus far. The three-spring model (Figure 2.1(b)) provides the needed resistance to rotation. Here we use the three-spring model to examine the reversal behavior of a pair of magnetic spheres as a function of the field angle θ_H. In the discussion below,

the term “rotation" is used to refer to the rotation of the axis that connects the two particles and the rotation angle θ is measured with respect to the x-axis as shown in Figure 2.1(b).

Before we can proceed with examining the three-spring model we must address a technical detail – the overlap energy that prevents the particles from overlapping. The results shown thus far utilize the hyperbolic tangent overlap potential E_{ov}, which increases rapidly and then plateaus as the particles come into surface contact. This overlap potential works well for the simpler single-spring model but with the three-spring model, which has more degrees of freedom, the energy minimization algorithm sometimes fails when $\theta_H \neq 0$. To avoid numerical issues we use the Weeks-Chandler-Andersen potential (WCA), E_{WCA}, since it provides more reliable results for the three-spring model. The WCA potential is non-zero starting at $S = 2^{1/6}2R$ and increases as S decreases. For these results we will refer to the state where the particles are at separations near or below this cutoff as the clustered state. As shown in Figure 2.6, the more gradual WCA overlap penalty leads to a slight increase in $|H_{C1}|$, the field at which the clustered particles will separate, due to the fact that the minimum particle separation distance is slightly larger for the WCA penalty as compared to the tanh function. The responses are otherwise identical, and the magnetization and displacement of the particle pairs are identical for the single-spring and equivalent stiffness three-spring case with $\theta_H = 0$ when the same overlap penalty is used.

Calculations of the particle displacement, rotation, and magnetization as a function of H are shown for $\theta_H = 10^\circ$ in Figure 2.7, performed using $S_0 = 9$ μm, $k_0 = 3.133 \times 10^{-2}$ N/m and $k_{12} = 1.015 \times 10^{-2}$ N/m, which were chosen to correspond to a material with $G = 1375$ Pa, and the WCA overlap penalty. Like the attractive single-spring results (Figure 2.2, $\theta_H = 0$), the three-spring model shows hysteresis in the displacement and magnetization of the particles over the same field range, and the hysteretic region corresponds to a region of accessible bistability where one of the states is a clustered pair. In Figure 2.7, however, the particle pair also rotates. The rotation is such that θ increases with increasing H and is largest when the particles are magnetically saturated, but the elastic forces resist rotation so θ is always less than θ_H. The magnetization

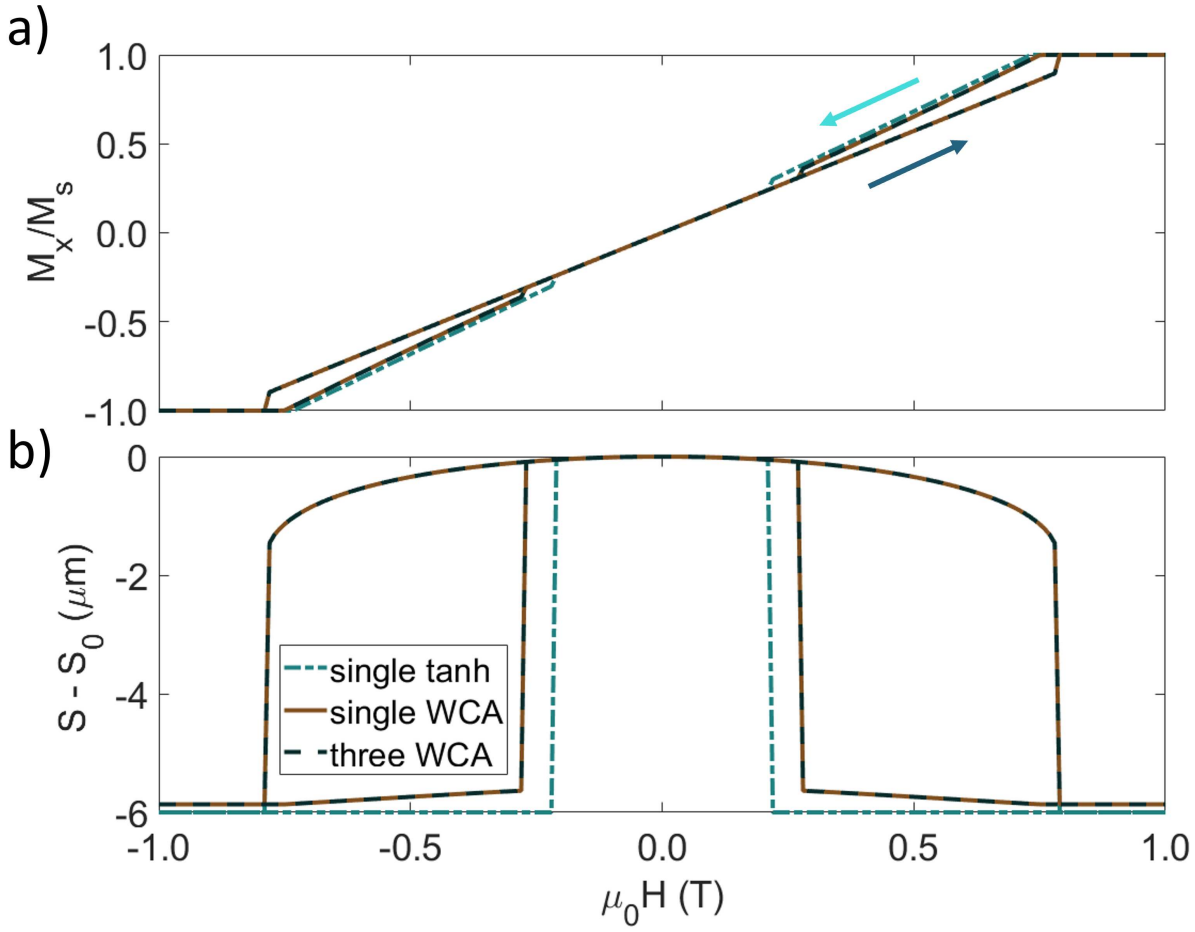

Figure 2.6: (a) Magnetization and (b) displacement as a function of H, with the field applied along the x-axis ($\theta_H = 0$) with $S_0 = 9$ μm. The dash-dotted dark cyan line and the solid brown line show results for the single-spring model with $k = 4 \times 10^{-2}$ N/m using the tanh and the WCA overlap penalties, respectively, and the equivalent three spring case is shown with a dark blue dashed line, with $k_0 = 4.855 \times 10^{-2}$ N/m and $k_{12} = 1.572 \times 10^{-2}$ N/m, calculated using the WCA overlap penalty.

angles, in contrast, are generally quite close to θ_H. The rotational response $\theta(H)$ is, similar to the displacement and magnetization responses, hysteretic over the region of bistability.

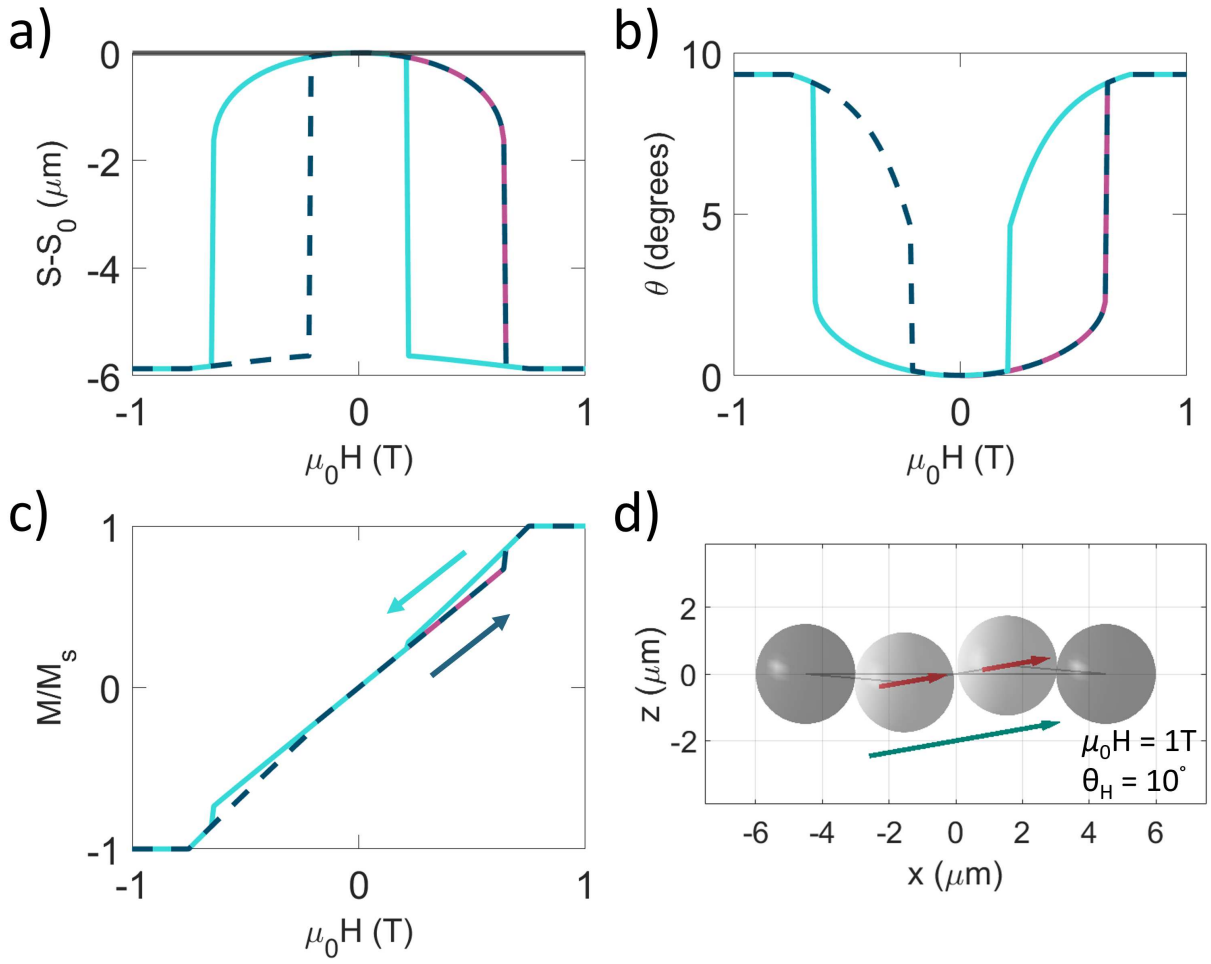

Figure 2.7: (a) Displacement, (b) rotation angle, and (c) magnetization as a function of H for $\theta_H = 10°$, measured with respect to the x-axis in the xz-plane, for $S_0 = 9$ μm, $k_0 = 3.133 \times 10^{-2}$ N/m, $k_{12} = 1.015 \times 10^{-2}$ N/m, which corresponds to G = 1375 Pa, and the WCA overlap penalty. (d) Plots of the particle configuration at $H = 0$ (equilibrium) and at 1 T (displaced and rotated).

Calculations of the particle displacement, rotation, and magnetization as a function of H are shown in Figure 2.8 for $\theta_H = 80°$. The magnetic interaction between particles is repulsive, no clustering occurs, and no hysteresis is observed. The system still rotates to align with $\vec{H}$ and to thereby reduce the magnetic energy of the system, in this case by almost 3°at saturation.

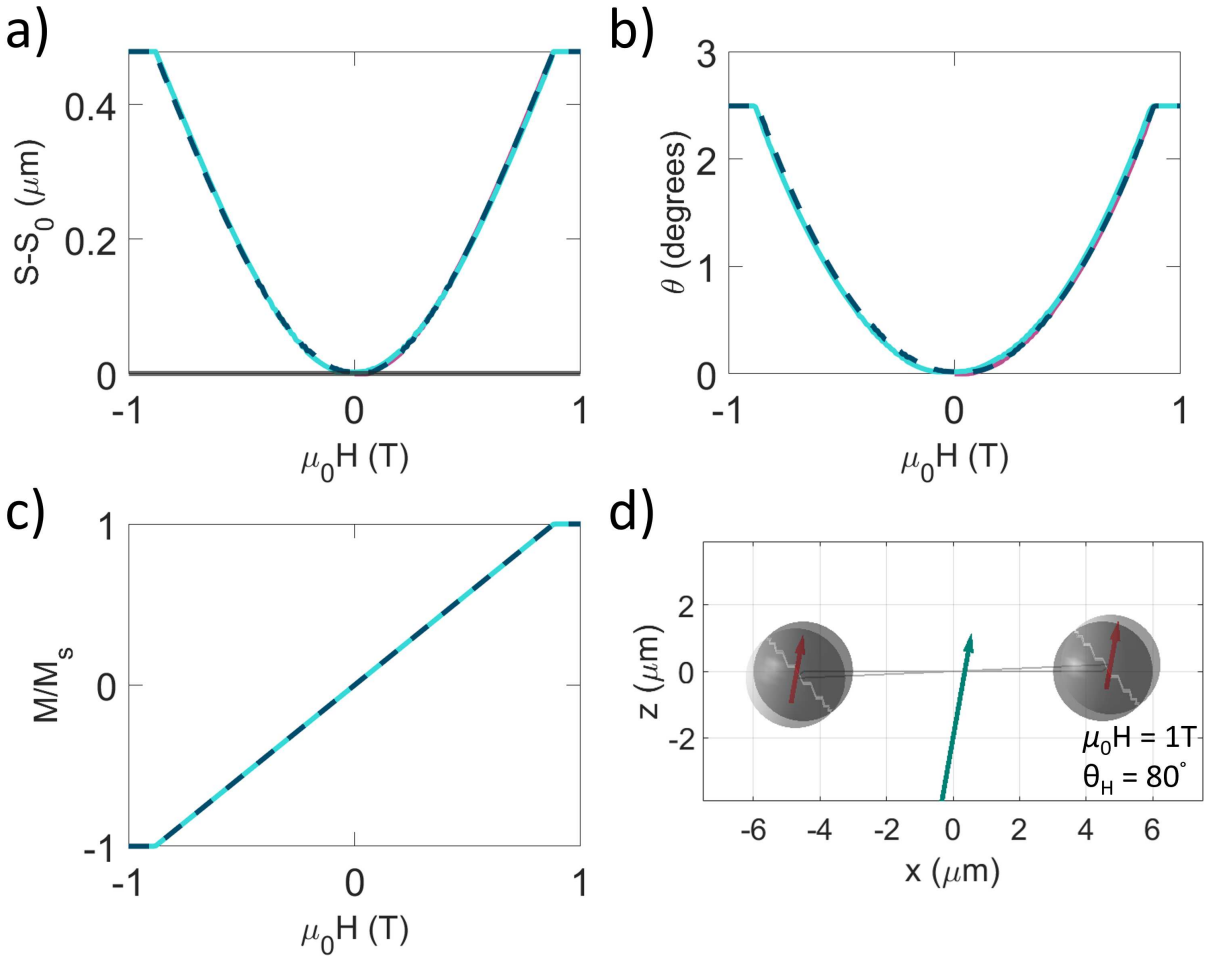

Figure 2.8: (a) Displacement, (b) rotation angle, and (c) magnetization as a function of H for $\theta_H = 80°$, calculated using the same parameters as Figure 2.7. (d) Plots of the particle configuration at $H = 0$ (equilibrium) and at 1 T (rotated and displaced).

Figure Figure 2.9 shows the effects of θ_H and S_0 on H_{C1}, H_{C2}, and the field range of bistability for θ_H of 0 to 90° and for S_0 out to $S_0 \approx 8R$. The stiffness constants k_0 and k_{12} used in Figure 2.9 were calculated using Eqs. (2.8) and (2.9), respectively, using $G = 1375$ Pa, the same G used for the three-spring calculations shown in Figs. Figure 2.7-Figure 2.8. The clustering effect that leads to hysteresis is present for $0 \leq |\theta_H| \leq \theta_{H,C}$, where the critical angle $\theta_{H,C} < 90°$, and the precise θ_H at which the clustering ceases depend on S_0, and k_{12}, and k_0. As shown in Figure 2.9(c) and (d), ΔH increases with increasing S_0 for a given θ_H and exhibits a steep drop off beyond a critical S_0 value above which pairs no longer form. ΔH increases more rapidly with increasing S_0 for larger θ_H, and the range of S_0 values that lead to clustering decrease with increasing θ_H. The maximum ΔH decreases, but only slightly, with increasing θ_H.

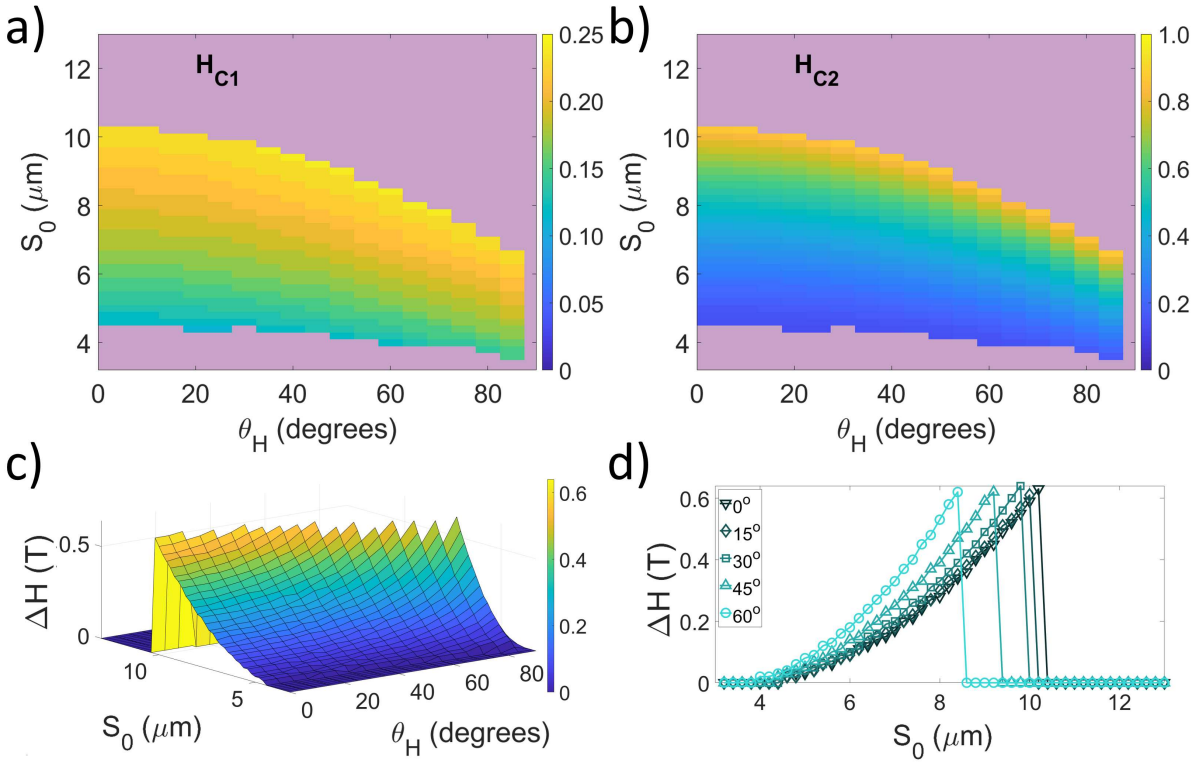

Figure 2.9: Critical fields (a) H_{C1} and (b) H_{C2} for three-spring system as a function of θ_H and S_0 with the same G value used in Figure 2.7 and Figure 2.8. The taupe regions indicate parameter combinations that do not result in hysteresis. ΔH is shown in (c) as a function of θ_H and S_0, and in (d) as a function of S_0 for selected θ_H values.

2.6 Discussion

The results presented above focus on the case of two interacting particles, whereas a real MRE is made up of many interacting particles. These simple two-particle models nevertheless show a hysteretic magnetic response at low stiffnesses that matches the pinched-loop shape observed experimentally for ultrasoft MREs [45,46], and these models also provide important insight into the hysteretic behavior of MREs. The modeling results presented here demonstrate that hysteresis in the displacement, the rotational, and magnetic responses of an MRE are linked to one another, and that clustering/bistability plays an important role in the hysteretic behavior observed for ultrasoft MREs.

The field range over which hysteretic behavior is observed (ΔH) increases with increasing S_0 since the particles have a larger distance over which they can respond to an attractive dipolar interaction but there is an abrupt cutoff S_0 value above which the clustered state is no longer accessible and hysteresis is absent. For example, the single-spring modeling results shows that for $k \leq 1 \times 10^{-1}$ N/m, the two particles will form clusters for a wide range of S_0 values, up to $8R$, and ΔH increases from 0.07 T for $S_0 = 6$ μm to 0.73 T for $S_0 = 12.2$ μm. The results for larger k show a cutoff separation that is inversely proportional to the k. These results suggest that MREs made of low stiffness polymers and smaller volume filling fraction under the percolation threshold will exhibit increased magnetic hysteresis, however, the dependence of the hysteretic field range on volume filling fraction will be non-monotonic. Increasing the volume filling fraction will lead to smaller average separations, constrained particle motion, and decreased ΔH, but decreasing the volume filling fraction to the point that the average separation between particles starts to exceed the critical S_0 value will also lead to a reduction in hysteresis.

Another important observation involves the applied field angle. The results from the three-spring model shown in Figure 2.9 indicate that particle pairs can form clusters and consequently exhibit hysteretic behavior at a wide range of applied field angles. The particle pairs not only move along the axis that connects them, but rotation of the axis of the particle pair is also observed for $|\theta_H| \neq 0$, which likely contributes to the field-dependent stiffening observed in experiments. The

modeling results show that the range of θ_H values for which hysteresis occurs depends on S_0. At small $S_0 < 4.4R$ the particles can cluster for θ_H of up to $85°$, which is larger than the so-called magic angle of $54.7°$ that corresponds to a change of the dipolar force from attractive to repulsive for the point dipole model used in Ref. [58]. For $3R < S_0 < 6R = 9$ μm, θ_H of up to $50°$ lead to hysteresis, while at slightly greater $S_0 = 10$ μm, clustering and hence hysteretic behavior is only observed for $\theta_H \leq 10°$.

Our two-particle modeling work expands on the spring method presented in Puljiz *et al*. [50] by exploring an expanded parameter space, though with a different linear magnetization model, and shows qualitative similarities to modelling done by Biller *et al*. [48] that included nonlinearities of the elastic response and non-uniform magnetization of the particles at small distances. Our results also agree well with Vaganov and Raikher's [51] work on two-particle systems for simulating first order reversal curves (FORCs), including field angle effects which we have explored here in more detail. We also formulate the two-particle problem in terms of energies rather than forces and explain the self-energy term that is critical to obtaining accurate results using an energy-based approach with a point dipole approximation. Although only two particles were considered, ensemble averaging of two-particle modeling results may provide a useful route to modeling experimental results. In our previous work [45] we demonstrate that weighted averaging of single-spring modelling results with the field along the particle axis ($\theta_H = 0$) qualitatively matches experimental hysteresis measurements made on ultrasoft MREs, and averaging of particle pairs weighted by a realistic field angle distribution is likely to provide a more realistic approximation of the MRE response. Discrete particle-based description can also be be extended to calculate the field-dependent mechanical properties of the system [49, 59, 60].

2.7 Conclusions

In summary, we have presented and analyzed calculations done using simple two-dipole models, and we show that these models reproduce the pinched magnetic hysteresis loop shape observed experimentally for ultrasoft MREs and provide insight into the connections between the particle

motion and magnetization that lead to this characteristic hysteresis loop shape. The model results show that particle clustering is closely linked to the appearance of hysteresis in the magnetic response of an ultrasoft MRE, and our results also show how the measurable hysteresis parameters, H_{C1}, H_{C2}, and ΔH, vary with the particle separation and applied field angle. The hysteretic behavior requires attractive inter-particle interactions. The attractive interactions are strongest when the magnetic field is aligned with the axis that connects the two particles, but attraction and hysteresis are observed for a range of field angles where the angle range over which hysteresis is observed increases with decreasing inter-particle separation. The two-dipole models, although simplistic, provide useful insight into the role of stiffness, field angle, and particle separation on magnetomechanical hysteresis. This discrete modeling approach has a lower computational cost as compared to finite element modeling approaches but still captures important behaviors of MREs. Modeling work in the field of MREs is essential to improving MRE design, and the dipole-spring models are an important tool that can be used to bridge between the micro-and the macro-scales to provide the physical insight that is necessary for improving MRE design.

2.8 Acknowledgments

We thank Marty Gelfand for helpful discussions. Work at CSU is supported by National Science Foundation DMR Grant Number 1709525. Work at BMC was supported by the Center for Engineering Mechanobiology (CEMB), an NSF Science and Technology Center, under grant agreement CMMI:15-48571.

Chapter 3

The effect of polymer stiffness on magnetization reversal of magnetorheological elastomers

Andy T. Clark, David Marchfield, Zheng Cao, Tong Dang, Nan Tang, Dustin Gilbert, Elise A. Corbin, Kristen S. Buchanan, and Xuemei M. Cheng, APL Mater. **10**, 041106 (2022)[1]; licensed under a Creative Commons Attribution (CC BY) license.

3.1 Context and Contributions

This chapter consists of the paper *The effect of polymer stiffness on magnetization reversal of magnetorheological elastomers*, which was published in APL Materials in 2022.

The supplemental material is shown in Section 3.8. This work aimed to demonstrate the effects of polymer stiffness and the role of magnetic particle motion on magnetization reversal in magnetorheological elastomers. Hysteresis loop measurements of samples composed of different polymers with varying stiffness, and temperature dependent measurements of a sample above and below a stiffness phase transition temperature, provide evidence that blocking particle rearrangement precludes magnetic hysteresis in these samples. Fluorescent confocal microscopy demonstrated significant displacement of the magnetic particles in an ultrasoft polymer matrix under the action of an applied magnetic field. Modeling results showed the importance of particle motion and clustering for the appearance of a characteristic pinched hysteresis loop.

Sample fabrication and room temperature magnetometry were performed by A. T. Clark(Bryn Mawr). Modeling work was performed by D. B. Marchfield(CSU). Confocal microscopy imaging was performed in collaboration with S. Le Marchan(UDel), Z. Cao(UDel), and E. Corbin(UDel). Indentation experiments were performed by Z. Cao(UDel). Temperature dependent major and minor hysteresis loops were measured by N. Tang(UTenn) in D. Gilbert's(UTenn) laboratory. Mi-

[1]https://doi.org/10.1063/5.0086761

cromagnetic simulations were performed by T. Dang(Bryn Mawr) and A. T. Clark. The paper was written by A. T. Clark and D. B. Marchfield in collaboration with K. S. Buchanan(CSU) and X. M. Cheng(Bryn Mawr).

3.2 Abstract

Ultrasoft magnetorheological elastomers (MREs) offer convenient real-time magnetic field control of mechanical properties that provides a means to mimic mechanical cues and regulators of cells *in vitro*. Here, we systematically investigate the effect of polymer stiffness on magnetization reversal of MREs using a combination of magnetometry measurements and computational modeling. Poly-dimethylsiloxanebased MREs with Young's moduli that range over two orders of magnitude were synthesized using commercial polymers Sylgard™ 527, Sylgard 184, and carbonyl iron powder. The magnetic hysteresis loops of the softer MREs exhibit a characteristic pinched loop shape with almost zero remanence and loop widening at intermediate fields that monotonically decreases with increasing polymer stiffness. A simple two-dipole model that incorporates magneto-mechanical coupling not only confirms that micrometer-scale particle motion along the applied magnetic field direction plays a defining role in the magnetic hysteresis of ultrasoft MREs but also reproduces the observed loop shapes and widening trends for MREs with varying polymer stiffnesses.

3.3 Introduction

Magnetorheological elastomers (MREs) are multifunctional materials that consist of a non-magnetic elastomeric matrix with embedded micro- or nano-sized magnetic particles. The elastic moduli [13, 14, 22, 42, 43, 61–63] and surface roughness [43, 64–67] of MREs can be tuned using an applied magnetic field, where mechanical changes of several orders of magnitude have been reported. In addition, the base elastic moduli at zero magnetic field of MREs can span across several orders of magnitude, depending on the constituent polymer types as well as the type and concentration of the embedded magnetic particles. [28] MREs have consequently become attractive

for a wide range of applications in the automotive industry, construction, electronics, biology, medicine, and robotics. [31]

Recently, ultrasoft MREs with a base Young's modulus (E) of several kPa have received great attention because they offer an innovative means to mimic biophysical mechanical cues and regulators of cells *in vitro*. [13,14,43] Ultrasoft MREs have shown much larger magnetic field-dependent changes in their moduli [13, 43] than what was predicted by the analytic models that consider stationary magnetic dipoles. [21, 68] Unlike rubber-like MREs, soft MREs have been shown to exhibit magnetic field-dependent motion of the constituent magnetic particles within the polymer matrix. [49,69] The magnetic hysteresis loops of soft MREs are also markedly different than those of stiffer MREs and exhibit a characteristic pinched loop shape with zero remanence and loop widening at intermediate fields. [5] Particle motion is thought to be an important contributing factor to this loop shape, [48, 50–52] and recent experiments on hysteresis loops in an MRE that is stiffened by lowering the temperature provide compelling evidence that the magnetic particle motion is, indeed, linked to the widening of the magnetic hysteresis loops. [46, 70, 71] However, the temperature dependent experiments to date [46, 70, 71] only examine two stiffnesses and a more comprehensive examination of the effect of stiffness that includes experiments and modeling is needed.

In this work, we investigate the effect of polymer stiffness on magnetization reversal of MREs where the elastic moduli are varied systematically over the range from ultrasoft to rubber-like by varying the polymer composition. While cooling an ultrasoft polymer [46, 70, 71] has the advantage that the measurements can be performed on the same sample, only two stiffnesses can be reliably accessed. Our measurements cover a wide range of MRE stiffnesses, and we further confirm that hysteresis loops measured in the same ultrasoft MRE at low temperatures where the polymer is rubber-like are identical to the room temperature hysteresis loops from rubber-like MREs synthesized with stiffer polymers. We also compare our measured hysteresis loops to theoretical hysteresis loops calculated using a simple two-dipole model that captures the magneto-mechanical coupling in MREs. Our modeling approach is similar to approaches used recently in

the field, [48, 50–52] using a simple description of the magnetic and elastic behavior. The modeling results reproduce the main features of the experimentally observed trends in the hysteresis measurements and provide insight into the physical mechanism of the MRE hysteresis. Our results provide evidence that the motion of magnetic particles, particularly along the direction of the applied field, plays a critical role in the magnetic hysteresis loop widening.

3.4 Experimental Details

Ultrasoft ($E \approx$ kPa) poly-dimethylsiloxane (PDMS)-based MREs were synthesized by mixing Sylgard™ 527 (Dow Corning™) polymer with carbonyl iron powder (BASF™) at volume fractions of $\Phi = 3\%$, 23%, 30% and 40%. To investigate the effect of stiffness on magnetic properties, harder MREs with E that range over two orders of magnitude were synthesized [72] by adding different amounts of a harder Sylgard™ 184 polymer, as shown in Table 3.1. We note that unless otherwise indicated, E refers to the Young's modulus at zero magnetic field. Samples for magnetometry measurements were cut from the center of the as-prepared MREs to a size of 4×4×1 mm^3. See supplementary material for more details. Major magnetic hysteresis loops of MRE samples at room temperature were measured using a Lakeshore Cyrotronics™ Micromag 3900 vibrating sample magnetometer (VSM) by decreasing the magnetic field H applied in the sample plane from 15 to -15 kOe and then increasing back to 15 kOe with a field sweep rate of 100 Oe/s, where 15 kOe is well above the saturation field for all the MRE samples. Temperature-dependent major magnetic hysteresis loops with H cycled between ± 15 kOe and minor hysteresis loops with H cycled between ± 5 kOe with a field sweep rate of 20 Oe/s for the MRE sample 1 were measured at selective temperatures between 300 K and 2 K by a Quantum Design™ PPMS VSM. In particular, the sample was field-cooled (FC) at 5 kOe for the minor loops measured at lower temperatures. The field sweep rates were chosen to provide sufficient time for iron particles within the MREs to respond to magnetic field change (see the supplementary material).

3.5 Magnetization Reversal of MREs

A characteristic pinched major hysteresis loop for an ultrasoft MRE ($E \approx 9$ kPa) sample is shown in Figure 3.1(a) and a zoomed-in view of the first quadrant is shown as the pink curve in Figure 3.1(b). While the remanence, i.e., the magnetization at zero field, is almost 0 [$M_r/M_s = (3.92 \pm 0.01) \times 10^{-3}$] and the coercive field is also small ($H_C = 14 \pm 1$ Oe), the loop opens up at intermediate fields and closes again near the saturation field, which is referred to as loop widening. We quantify the loop widening using $\Delta(M/M_s)$, which is defined as the magnetization difference of the two branches of the hysteresis loop at each H, as shown in the inset of Figure 3.1(b). The loop widening can also be highlighted by comparing the normalized differential susceptibility χ/M_s for the decreasing H and increasing H branches, where the differential magnetic susceptibility χ is defined as $\chi = dM/dH$, as shown in the inset of Figure 3.1(a). The observed characteristic loop widening is consistent with previous reports where the authors attributed the loop widening to the magnetic particle motion in the MREs. [5, 46, 70, 71]

If the observed loop widening, indeed, arises from magnetic field-dependent motion of magnetic particles within the polymer matrix, the widening should decrease with the increase in E of MREs, since the larger E will impede particle motion. To investigate the effect of polymer stiffness on magnetization reversal of MREs, we measured the major hysteresis loops for MREs with E ranging from ≈ 9 kPa (ultrasoft) to 2400 kPa (rubber-like). Figure 3.1(b) shows the zoomed-in view of the first quadrant of major hysteresis loops for MRE samples 1-4 with E as listed in Table I. The measured loop widening, characterized by $\Delta(M/M_s)$, indeed, monotonically decreases with increasing E. The peak value of $\Delta(M/M_s)$ for MRE sample 4 (stiffest) is about 10% of the peak value for MRE sample 1 (softest) as shown in Figure 3.1(c).

Temperature also provides a means to control the stiffness of an MRE since PDMS-based MREs undergo a phase transition at $T_P \approx 230$ K where the E increases by several orders of magnitude, [46, 70, 71, 73] which enables us to investigate the effects of polymer stiffness and iron particle motion on magnetization reversal in the same MRE sample. Figure 3.2(a) shows that while the major hysteresis loops of the MRE sample 1 with ultrasoft polymer A measured at 300

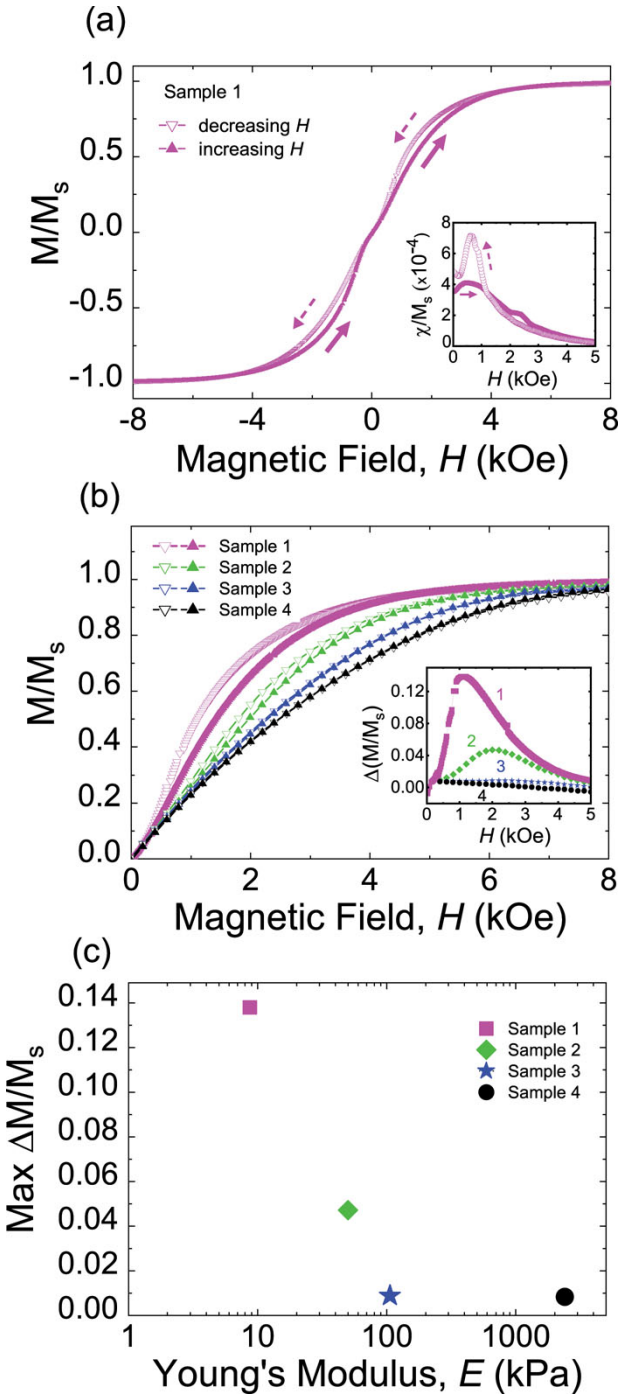

Figure 3.1: Room temperature magnetic reversal of MREs. (a) The major hysteresis loop of ultrasoft MRE sample 1 shows zero remanent magnetization and a characteristic loop widening at the intermediate fields. The inset compares the normalized differential susceptibility χ/M_s for the decreasing and increasing H branches, where a five-point average was applied to reduce random noise. (b) The zoomed-in view of the first quadrant of the major hysteresis loops for MRE samples 1–4 having polymer stiffnesses ranging from ultrasoft (1) to rubber-like (4). The inset shows the field dependence of $\Delta(M/M_s)$, the difference between the magnetizations for the increasing and decreasing branches at each H. (c) Maximum $\Delta(M/M_s)$ as a function of Young's modulus for MRE samples 1–4.

and 250 K (both above T_P) overlap and both show loop widening, the major loop of this MRE sample 1 at 200 K (below T_P, stiffer) has no characteristic loop widening and overlaps with the rubber-like MRE sample 4 (polymer D, 300K). Figure 3.2(b) shows the FC-minor hysteresis loops with H cycled between ± 5 kOe for the MRE sample 1 at selected temperatures between 300 and 2 K. Similarly, all the minor loops measured above T_P (softer) overlap and exhibit loop widening and those measured below T_P (stiffer) also overlap but show no loop widening, consistent with the effect of MRE stiffness on magnetization reversal shown in Figure 3.1(b).

Figure 3.2(c) compares the major loops and FC-minor loops of the same MRE sample 1 measured at 300 K (softer) and 200 K (stiffer). While the major and minor loops overlap at 300 K as expected, the normalized magnetization of the major loop at 200 K is significantly smaller than that of the FC-minor loops at the same field. As we explain below, this difference suggests that the magnetic particle spacing in MREs affects the magnetization reversal. Lowering the temperature increases the MRE stiffness so the particles are less movable at lower temperatures, and lowering the temperature from above to below T_P in $H = 5$ kOe freezes the particles at their locations from the previous FC-minor loop measured above T_P. The magnetic particles are consequently closer together on average, resulting in stronger dipolar interactions between neighboring particles, as compared to the zero-field cooling case at 200 K for the same H. The difference in the normalized magnetization between the major and FC-minor loops measured below T_P can be further highlighted by comparing the χ/M_s values near zero field. As shown in the insets of Figure 3.2, the χ/M_s near remanence for sample 1 below T_P is about 2.6 times larger for the minor loop as compared to the major loop, and the minor loop χ/M_s is larger than the corresponding value measured above T_P.

Another way to modify the inter-particle spacing in MREs is to change the iron particle concentration Φ. To confirm the effect of magnetic particle spacing, we measured room temperature major hysteresis loops of MREs with the same polymer (A) and Φ ranging from 3% to 40%, as shown in Figure 3.3(a). As Φ increases, the minimum and average inter-particle spacing both decrease so the particles have less available space to move, which results in a reduction of the loop widening

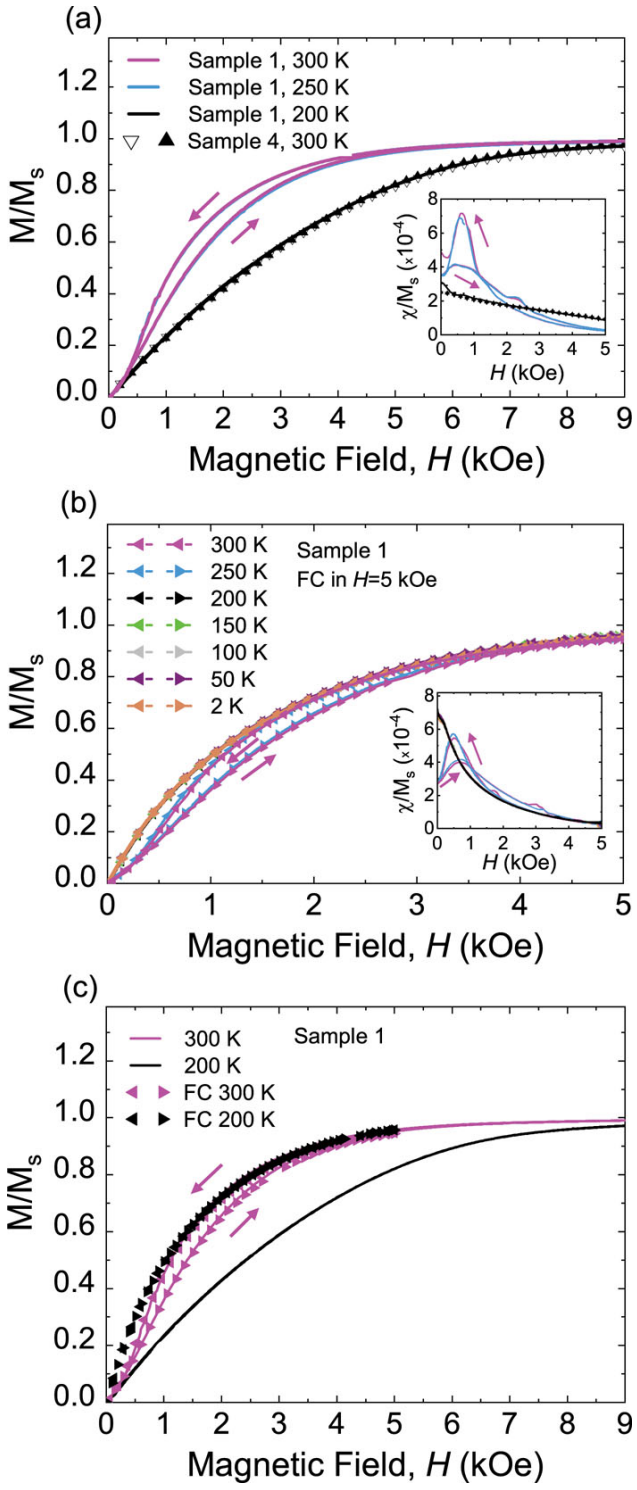

Figure 3.2: Temperature-dependent magnetic properties of MRE sample 1. (a) Zoomed-in view of the first quadrant of major hysteresis loops of MRE sample 1 measured at 300, 250, and 200 K as well as that of MRE sample 4 measured at 300 K. The inset shows the field dependence of χ/M_s. (b) Field-cooled minor hysteresis loop measurements of the same ultrasoft MRE sample 1. The inset shows χ/M_s at different temperatures. (c) Comparison of major loops and FC minor loops of MRE sample 1 at temperatures above (softer) and below (stiffer) T_P.

Table 3.1: Young's moduli E of MREs with volume fraction $\Phi = 3\%$ of iron particles synthesized using different ratios by weight of commercial polymers Sylgard™ 527 and Sylgard™ 184. The Young's moduli were measured by compressive indentation at zero magnetic field (see the supplementary material).

MRE Sample	Polymer type	Sylgard™ 527: Sylgard™184 (by w.t.)	E (kPa)
1	Polymer A	1:0	8.7± 0.6
2	Polymer B	10:1	50 ± 2
3	Polymer C	5:1	106 ± 1
4	Polymer D	0:1	2,400 ± 400

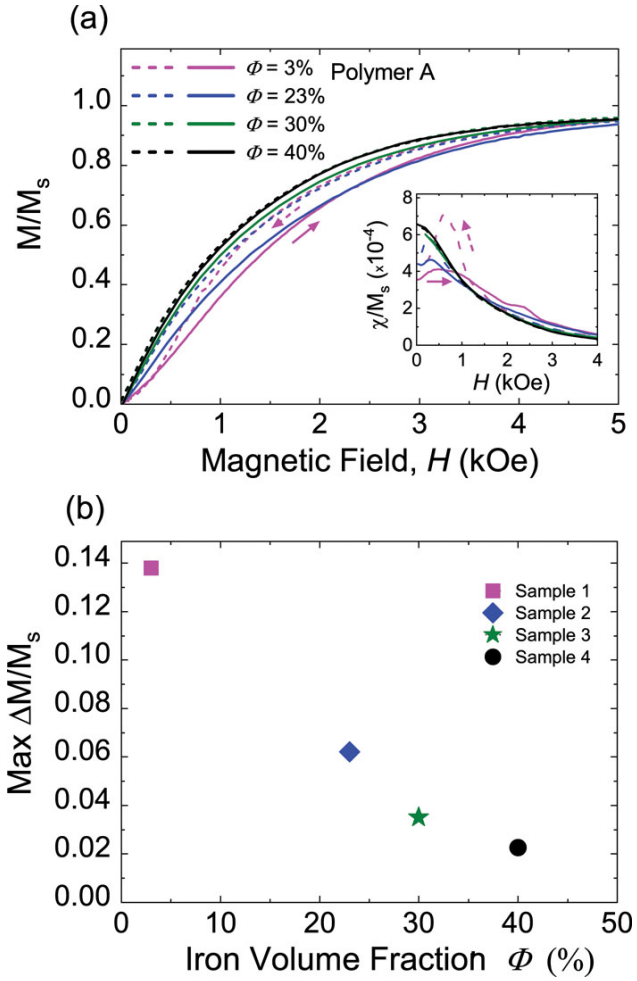

Figure 3.3: Effect of iron particle concentration on magnetic reversal of ultrasoft MREs. (a) Zoomed-in view of magnetic hysteresis loops for ultrasoft MREs containing $\Phi = 3\% - 40\%$ iron particles embedded in polymer A. The inset shows the field dependence of χ/M_s where a five-point averaging was applied to reduce random noise. (b) Maximum $\Delta(M/M_s)$ as a function of iron volume fraction.

[Figure 3.3(b)]. Additionally, the closer distances between the iron particles lead to larger stray magnetic fields and larger magnetic moments for each particle at a given H. As expected, χ/M_s at remanence is higher for MREs with larger Φ, as shown in the inset of Figure 3.3(a).

3.6 Two-Dipole Magneto-Mechanical Modeling

To further understand the effect of stiffness and particle spacing on the magnetic behavior of MREs, we used a simple two-dipole model, similar to the ball and spring modeling approach by Stepanov *et al*. [5] and Puljiz *et al*. [50], to model the MRE behaviors. As illustrated in the inset of Figure 3.4(d), two spherical particles of diameter D and saturation magnetization M_s are connected to each other by a single spring with a stiffness constant k, representing the elastic polymer. The net magnetic dipole moment of each sphere is $m = MV = \chi_{sph} H_{eff} V$ below magnetic saturation, and $m = M_s V$ at and above saturation, where χ_{sph} is the magnetic susceptibility of a single sphere, H_{eff} is the local effective field at the center of each particle that includes the applied field H and the stray field of the other sphere, and $V = \pi D^3/6$ is the particle volume. The particles are treated as point magnetic dipoles located at the center of each sphere, and the net force experienced by either one of the spheres for the case where **H** is applied parallel to the spring is

$$F = -k(S - S_o) - \frac{3\mu_o m^2}{2\pi S^4}, \tag{3.1}$$

where S is the inter-particle separation, and S_o is the elastic equilibrium separation (also $S = S_0$ at $H = 0$). A negative (positive) F represents an attractive (repulsive) net force. The first term in Eq. (1) is the elastic restoring force, and the second is the dipole-dipole interaction force, which is attractive when **H** is along the line connecting the two spheres. Hysteresis loops were obtained by finding the equilibrium ($F = 0$) for each H value where H was decreased from $+H_{max}$ to $-H_{max}$ then increased back to $+H_{max}$. In practice, a nonlinear conjugate gradient method was used to find S associated with the local energy minimum, where the force and energy (U) are related by $F = -\nabla U$, and m is calculated at each step based on χ_{sph} and the local H_{eff}. Modeling was

also conducted with **H** perpendicular to the spring, which leads to a repulsive magnetic force and consequently $S > S_o$. Modeling was conducted for selected k values for $S_o = 3.2 - 13.0$ μm in steps of 0.2 μm with particle diameter $D = 3$ μm, $M_s = 1.4 \times 10^6$ A/m, and $\chi_{sph} = 2$. To obtain more realistic estimates of the MRE hysteresis curves, averages of the magnetic response weighted by an estimated separation distribution (a Gaussian distribution with a mean and standard deviation of 4.8 and 6.5 μm, respectively) were calculated.

Figure 3.4 compares the particle motion and the corresponding hysteresis loops calculated for two dipoles with $S_o = 12$ μm connected by a spring of different stiffness constants: $k = 9 \times 10^{-3}$ N/m and $k = 9 \times 10^{-1}$ N/m, as shown in Figure 3.4(a) and (c) and Figure 3.4(b), and (d), respectively. The approximate equivalent E, obtained by considering the spring as a compressed cylinder, which yields $E = 2kS_o/\pi D^2$, are $E \approx 8$ kPa and ≈ 800 kPa, respectively; hence, Figure 3.4(a) and (c) and Figure 3.4(b) and (d) approximately correspond to the softest (sample 1) and stiffest (sample 4) MREs considered in the experiments, respectively. At large H where the particles are magnetically saturated, they are at their closest distance due to the attractive dipole-dipole forces. When the particles are touching, as in Figure 3.4(a), we refer to this as the clustered state. As H is reduced, m decreases since m is proportional to H_{eff} and, consequently, the magnitude of the dipole-dipole force decreases. For the ultrasoft case in Figure 3.4(a), the elastic force is small and the particles touch ($S = D$) at saturation. The particles remain in contact until H is reduced to a critical value H_{c1}, where the attractive magnetic force is sufficiently small that the elastic force can pull the particles apart, as the clustered state is no longer a local minimum energy state, resulting in a jump in S. As H is further decreased to zero, S increases gradually to a maximum S_o at $H = 0$. As H is further decreased below zero, **H** increases in magnitude but now in the opposite direction, the particles are attracted to each other and S decreases gradually at first until the particles touch once again at H_{c2} when the separated state is no longer an available minimum energy state. The corresponding magnetic response [Figure 3.4(c)] shows zero remanent magnetization within the uncertainty of the calculations and exhibits a pinched loop shape that is qualitatively similar to what is observed in the experiments (Figure 3.1) and also to recent modeling

results for a similar system. [51] The particle motion is reversible when H is removed, which is expected based on recent experiments. [50] The field range associated with the hysteretic magnetic response ($H_{c1} < |H| < H_{c2}$) corresponds to the region of bistability of particle spacings where one of the stable states corresponds to the particles touching. For larger k [Figure 3.4(b) and (d)], the stronger elastic force inhibits particle contact, and there is no hysteresis in the particle motion or the magnetic response. When **H** is applied perpendicular to S instead of parallel to S, the dipole-dipole interactions are repulsive and no hysteresis is observed.

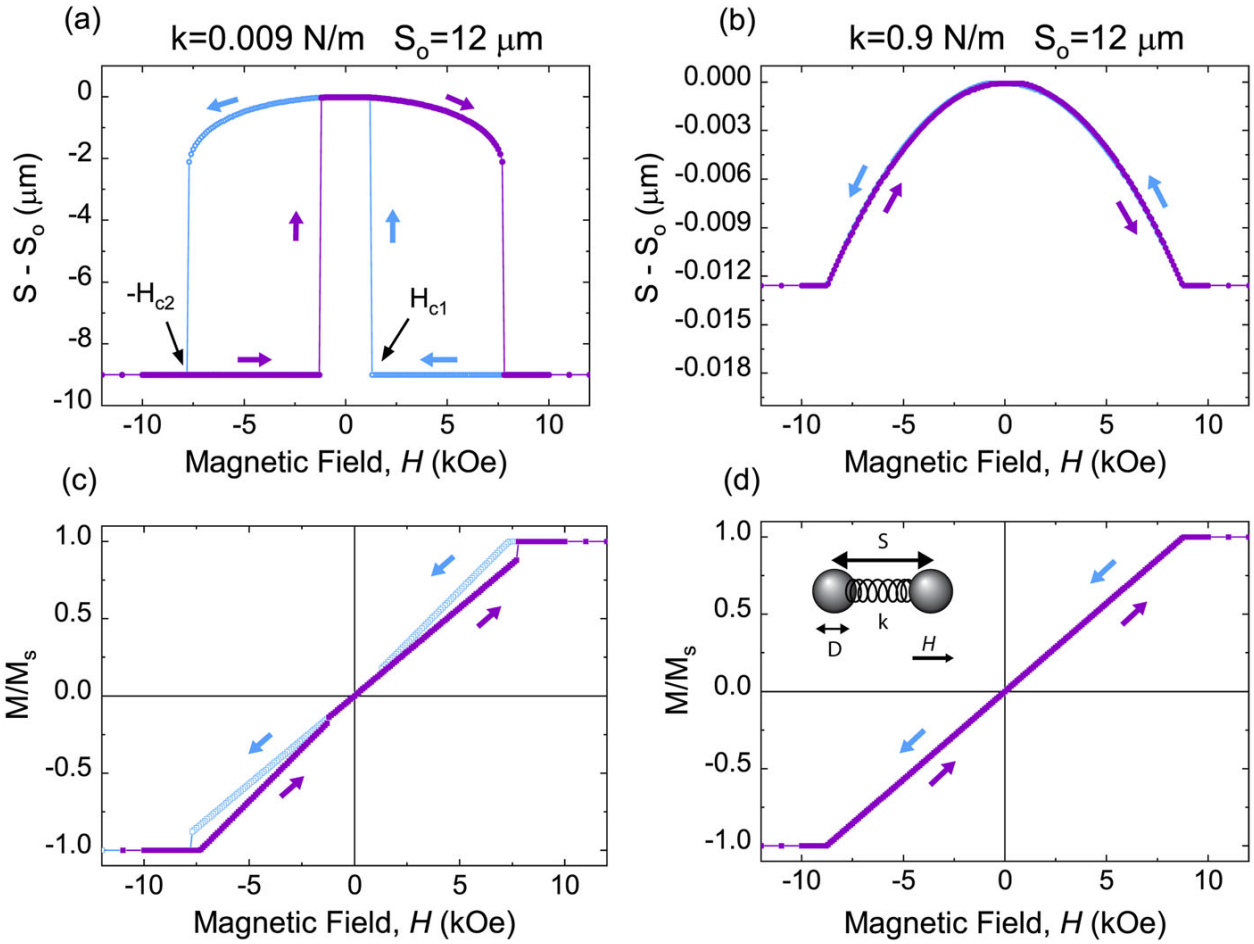

Figure 3.4: Two-dipole modeling results for two stiffness constants: $k = 9 \times 10^{-3}$ N/m [(a) and (c)] and $k = 9 \times 10^{-1}$ N/m [(b) and (d)]. In both cases, the elastic equilibrium particle separation (at zero magnetic field) is $S_o = 12$ μm. The inter-particle displacement (S - So) and the corresponding magnetic hysteresis loops are shown in (a) and (b) and (c) and (d), respectively. The inset of (d) shows a schematic diagram of the two-dipole model.

The two-dipole modeling results highlight the role of attractive inter-particle interactions in the hysteretic magnetic response. To better account for the effects of the collective behavior of an ensemble of particles, we consider a distribution of equilibrium positions, which leads to a smoother magnetic response and that is more representative of a real sample. Figure 3.5(a) shows the zoomed-in view of the first quadrant for the weighted average of hysteresis loops calculated for $k = 9 \times 10^{-1}$, 9×10^{-2}, and 9×10^{-3} N/m using a weighted average of hysteresis loops with $S_o = 3.2 - 13$ μm. Increasing k leads to a smaller loop widening, also evident in Figure 3.5(b), which matches the experimentally observed trend in Figure 3.1(b). Modeling also shows that increasing k and decreasing S_0 leads to an increase in the zero-field susceptibility. Since higher k and lower S_0 is the expected result of the "locking in" of particles at close positions under FC conditions, this is consistent with the increase in χ/M_s at $H = 0$ observed in Figure 3.2(b) as compared to Figure 3.2(a) for MRE sample 1 below T_P. A linear magnetic response is used for each sphere, which may lead to a larger H_{c1} as compared to the nonlinear response used by Biller *et al*. [48] and this may in part account for the lower $\Delta M/M_s$ values observed in the model as compared to the experiment.

The model of two dipoles connected by a single spring, which was used to obtain the results shown in Figure 3.4 and Figure 3.5, has limitations. Similar to many other models, [48, 50–52] the hysteretic losses from individual particles are not included although these losses should be small [2, 5, 46] (see the supplementary material). Additionally, this single-spring model does not allow consideration of fields at an angle, which would cause rotation in addition to attraction/repulsion. To assess the role of off-axis fields applied at intermediate angles, we carried out additional modeling runs using a three-spring approach similar to what was reported by Puljiz *et al*. [50] with $S_0 = 9$ μm and $k = 4 \times 10^{-3}$ N/m for all three springs with **H** at an angle of 19° (see supplementary material). The particle response, although combined with rotation, still shows a pinched loop shape with bistability similar to what is observed in Figure 3.4(a) and (b), and clustering is still the mechanism that leads to hysteresis. More complicated models that include additional field angles, allow particle rotation, add more particles sizes, and allow clusters of more than two

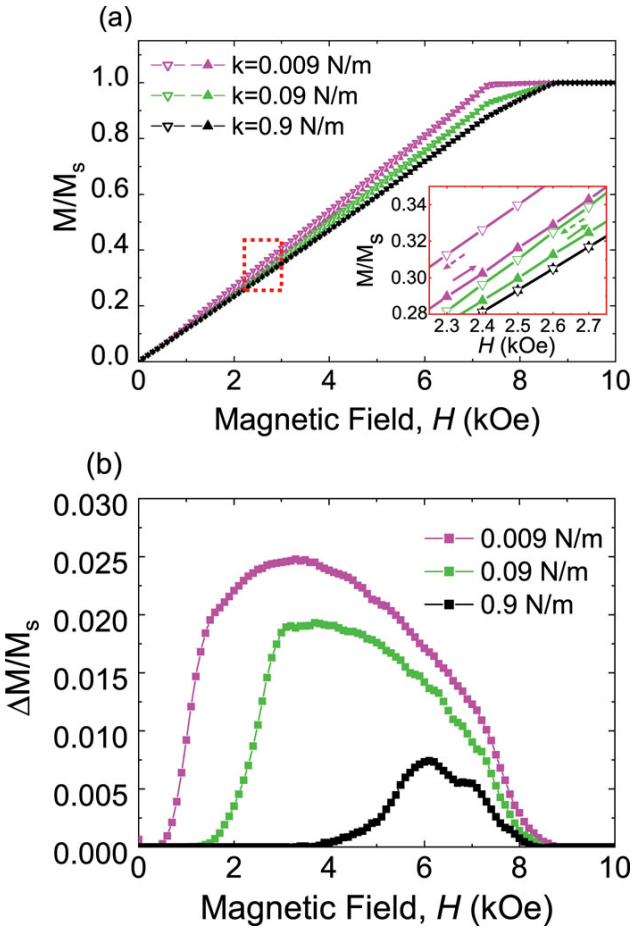

Figure 3.5: The effect of stiffness constants ($k = 9 \times 10^{-1}, 9 \times 10^{-2}$, and$9 \times 10^{-3}$ N/m) on magnetic hysteresis loops calculated from the two-dipole model by taking weighted average of a collection of hysteresis loops calculated using a distribution of S_o values ranging from 3.2to13.0 μm. (a) The first quadrant of the calculated weighted average hysteresis loops; the inset shows a zoomed-in view. (b) Calculated $\Delta(M/M_s)$ vs H for different k's, where a five-point averaging was applied.

particles could be important for capturing a more realistic picture of the particle motion in the MREs and for refining the shape of the hysteresis loops. However, our simple model highlights the fundamental role of the competition between the elastic and magnetic forces and the resultant local particle motion, especially the motion along the applied field direction, in the magnetization reversal of MREs. Furthermore, confocal microscopy imaging confirms that the iron particle motion in the polymer matrix is, indeed, primarily along the direction of applied magnetic field (see supplementary material).

3.7 Conclusion

In conclusion, we have investigated the effect of the polymer stiffness and magnetic particle spacing on the magnetization reversal of MREs experimentally and with modeling. MREs with Young's moduli that range over two orders of magnitude were synthesized using mixtures of two polymers, Sylgard™ 527 and Sylgard™ 184, and carbonyl iron powder. Magnetometry measurements for MREs of systematically varied stiffness from ultrasoft to rubber-like show a characteristic pinched loop shape that is consistent with previous measurements on ultrasoft MREs. Our results reveal that the loop widening monotonically decreases with increasing MRE stiffness. Furthermore, we confirm that hysteresis loops measured in the same ultrasoft MRE at low temperatures ($T < T_P$) where the polymer is rubber-like are identical to the room temperature hysteresis loops from rubber-like MREs synthesized with stiffer polymers and the same magnetic particle volume fraction Φ. A two-dipole model shows that the observed loop widening arises from a bistability of inter-particle displacements along the applied magnetic field direction. This model, while simple, produces calculated magnetic hysteresis loops that show a widening trend that qualitatively matches the experimental results for MREs with varying polymer stiffnesses. Our results provide guidance for magnetic field control of MREs with a wide range of stiffnesses in biomedical and other applications.

3.8 Supplementary Material

3.8.1 MRE synthesis and magnetometry sample preparation

Ultrasoft ($E \approx$ kPa) PDMS-based MREs were fabricated using Sylgard™ 527 (Dow Corning™), prepared by mixing equal parts by weight of monomer with crosslinker and then mixing in magnetically soft carbonyl iron powder (BASF™) at volume fractions of $\Phi = 3, 23, 30$ and 40%. After mixing, the MREs were poured into 35-mm diameter culture dishes to a thickness of ≈ 5 mm and cured in a vacuum oven at 65 °C for four hours.

Smaller samples were sectioned from the middle of the MREs and cut to a size of 4x4x1 mm^3. To prevent changes in shape anisotropy due to magnetic field-dependent deformation of the MRE sample, the samples were volume-constrained by placing each sample on a silicon wafer and encasing it with a 2-part epoxy (Gorilla™).

3.8.2 Young's modulus measurements by compressive indentation

The experimental Young's modulus values listed in Table 3.1 were obtained by compressive indentations performed using a custom built micro-indenter similar to that described by Rennie *et al*. [74] and Schulze *et al*. [75] A spherical indenter 1.8 mm in diameter connected to a cantilever with a spring constant of $k = 1200$ N/m was brought into contact with the MRE surface and then immediately retracted. The Young's modulus was calculated by fitting the unloading portion of the indentation vs. force curves with the JKR adhesive contact model. [76] A plot of E as a function of Sylgard 184 percentage is shown in Figure 3.6. The measurements were all done with no magnetic field applied.

3.8.3 Additional results of magnetometry measurements

M-H Loop of Carbonyl Iron Powder

The magnetic hysteresis of carbonyl iron powder was measured by magnetometry. Figure 3.7(a) shows the major magnetic hysteresis loop for carbonyl iron powder with a zoomed-in

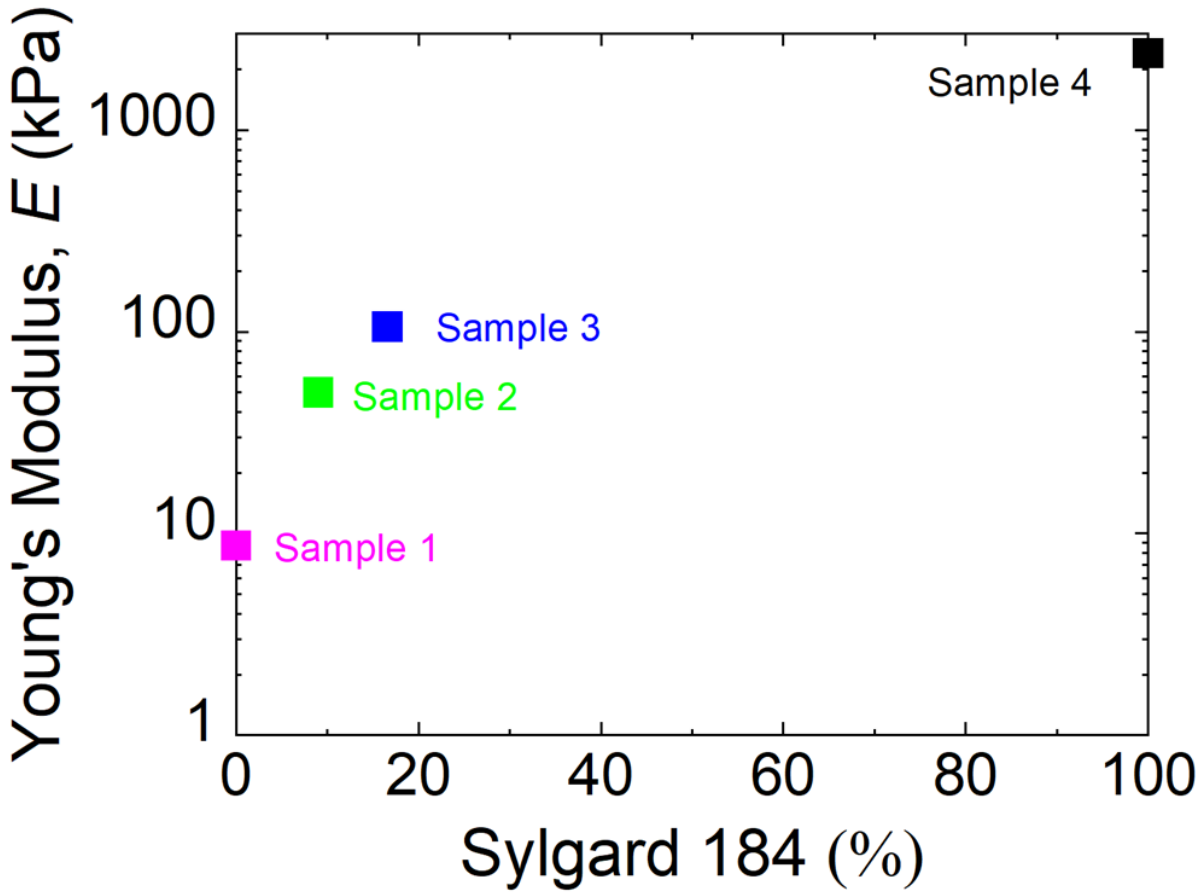

Figure 3.6: Young's modulus E of MRE samples 1-4 synthesized using commercial polymer Sylgard™ 527 with different amounts of added harder Sylgard™ 184 polymer by weight measured at $H = 0$.

view of the first quadrant in Figure 3.7(b). The hysteresis loop shows no loop widening, confirming that the individual iron particles have negligible hysteresis loss.

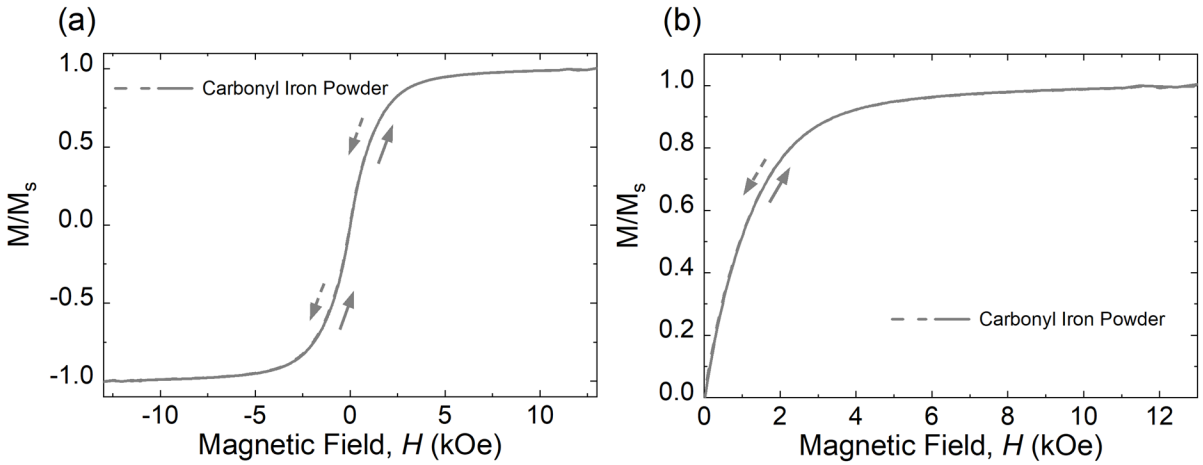

Figure 3.7: Magnetic hysteresis of carbonyl iron powder. (a) Major magnetic hysteresis loop of carbonyl iron powder. (b) Zoomed-in view of the first quadrant of the major magnetic hysteresis loop of carbonyl iron powder.

M-H Loops of unconstrained vs. constrained MREs

Ultrasoft MREs exhibit magnetic field-dependent changes in sample shape upon application of an external magnetic field. To determine whether macroscopic sample deformation and the resultant shape anisotropy changes affect the hysteresis loop of the ultrasoft MREs considered in this study, major magnetic hysteresis loop measurements were made on the ultrasoft MRE sample 1 before and after the sample shape was constrained. Figure 3.8 shows a zoomed-in view of the first quadrant of the major magnetic hysteresis loops which are identical, hence constraining the shape of the MRE and thereby restricting changes in shape anisotropy, has no effect on the observed loop widening.

Effect of Magnetic Field Sweep Rate on M-H Loops of MREs

The effect of field sweep rate on the observed widening in the hysteresis loops of ultrasoft MREs was investigated by magnetometry. Major magnetic hysteresis loops for MRE sample 1

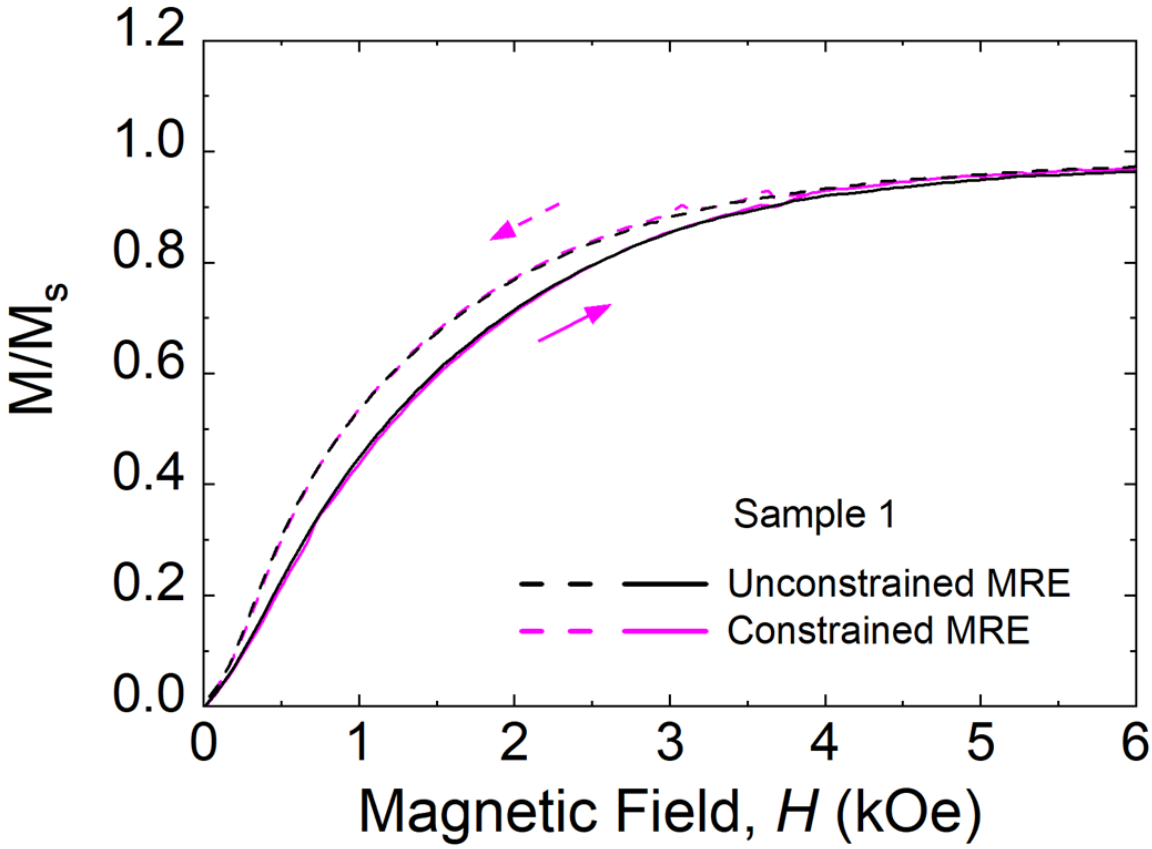

Figure 3.8: Zoomed-in view of the first quadrant of the major magnetic hysteresis loops for the MRE sample 1 before and after the sample shape was constrained.

were measured for varying magnetic field sweep rates ranging from 500 – 20 Oe/s as shown in Figure 3.9(a). A zoomed-in view of the first quadrant displayed in Figure 3.9(b) where the inset shows the field-dependence of $\Delta(M/M_s)$. The hysteresis loops show a 35% decrease in the peak $\Delta(M/M_s)$ as the sweep rate is decreased from 500 Oe/s down to 100 Oe/s, after which minimal difference is observed.

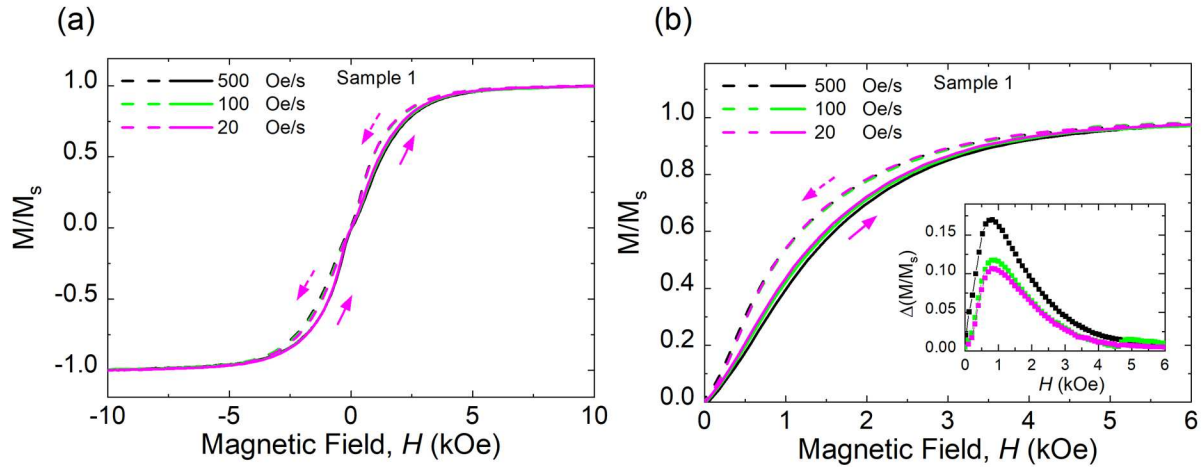

Figure 3.9: Comparison of the major magnetic hysteresis loops for the MRE sample 1 measured with varying magnetic field sweep rates. (a) Major magnetic hysteresis loop for varying magnetic field sweep rate. (b) Zoomed-in view of the first quadrant of the magnetic hysteresis loops with inset showing the field-dependence of the calculated $\Delta(M/M_s)$ for each sweep rate.

3.8.4 3D Particle Tracking by Magnetic Field-Dependent Confocal Microscopy

The magnetometry and modeling results in the main paper indicate that local particle motion is important in the magnetization reversal process in ultrasoft MREs. To probe the particle motion directly, a 3D particle tracking experiment was conducted using field-dependent confocal microscopy. To enable the particle tracking, the surface of the carbonyl iron particles was modified prior to synthesizing an otherwise identical version of the ultrasoft MRE sample 1. The modification process consisted of three major stages (Figure 3.10). First, carbonyl iron powder (CIP) was covered with a silica layer prepared via tetra-ethoxysilane (TEOS) hydrolysis. Next, the

particles (CIP/SiO2, CIP-TEOS) were coated with a second layer formed through hydrolysis and condensation of (3-Aminopropyl)-triethoxysilane (APTES). Finally, a fluorophore was attached to the CIP-TEOS-APTES particles through a bioconjugation of Atto 488 NHS ester.

In the first step of the magnetic particle modification, a silica precursor consisting of anhydrous ethanol, TEOS, and hydrochloric acid were mixed in a molar ratio of 7.6:1:0.05, where hydrochloric acid was added as a catalyst [77]. The mixture was stirred for 2 h at room temperature. The resulting TEOS hydrolysate was kept for 24 h for sol aging at room temperature. We then combined 20 g of CIP with 50 mL anhydrous ethanol and homogenized the mixture in a water bath using ultrasonic vibration for 10 min. Then, the pre-prepared TEOS hydrolysate was dropwise added using a dropping funnel into CIP mixture with mechanical stirring at room temperature for 3 h. Additionally, the dispersion was homogenized mid-reaction and post-reaction for 10 min, respectively. The resulting particles were collected using a permanent magnet and washed 3 times with anhydrous ethanol, to remove organic residues and prevent the particles from agglomerating. The product (CIP-TEOS) was dried at 60 °C for 24 h and collected.

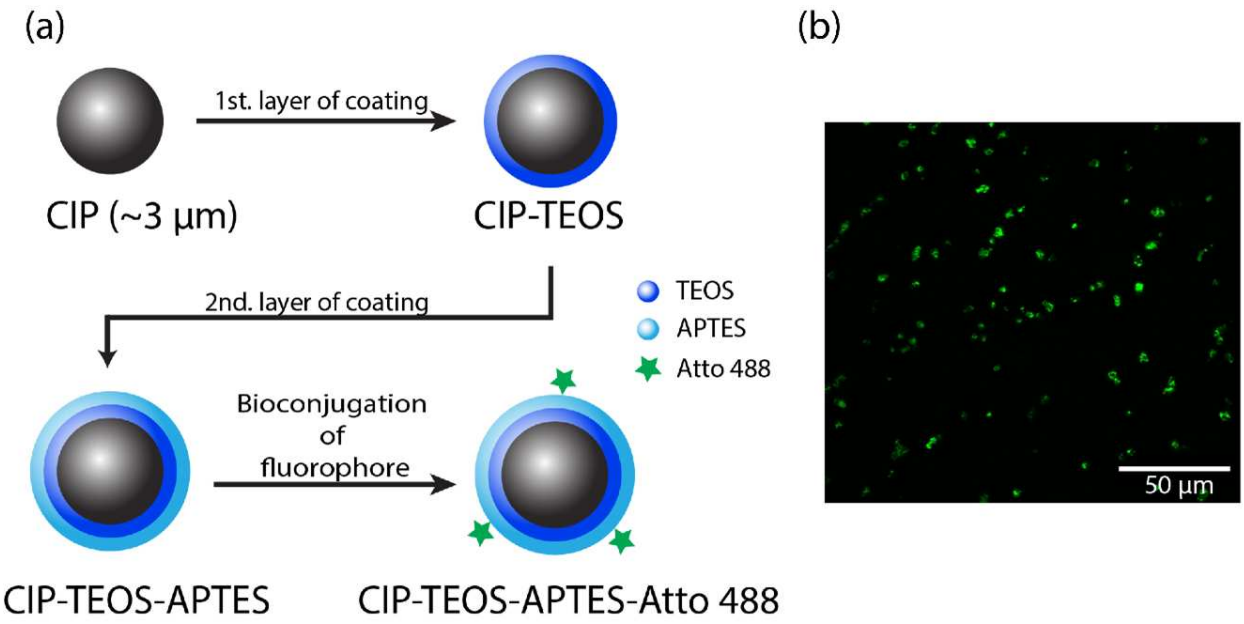

Figure 3.10: (a) Schematic of fluorescent labelling process of iron particles. (b) Fluorescent image of fluorescently labeled iron particles.

To cover the CIP-TEOS with APTES, we first equipped a 100 mL, three-neck, round bottom flask with an overhead mechanical stir through the middle neck, cold water condenser and thermometer through the outer necks. 10 g of prepared CIP-TEOS was combined with 80 mL dry toluene and pre-homogenized using ultrasonic vibration in water bath for 30 min. The mixture was poured in the three-neck, round bottom flask followed by injecting a solution of 1.2 mL of APTES in 5 mL dry toluene via syringe under vigorous mechanical stirring. The reaction mixture was heated to 105 °C for 6 h. Aluminum foil was used to cover the flask and heat block to maintain the insulation during the reaction. The powder was collected by using a permanent magnet upon cooling to room temperature. The APTES coated CIP-TEOS (CIP-TEOS-APTES) was washed three times with anhydrous ethanol. The product (CIP-TEOS-APTES) was dried at 60 °C for 24 h and collected.

Finally, we used the primary amine reactive Atto 488 NHS ester to label CIP-TEOS-APTES through conjugation with the amine group on APTES. The stock solution of Atto 488 NHS ester was prepared by dissolving 1 mg of Atto 488 NHS ester in 100 μL of anhydrous DMSO. To bind fluorophores on the surface of CIP, 500 mg of CIP-TEOS-APTES were dispersed in 9.99 mL of anhydrous DMSO followed by adding 10 μL of stock solution of Atto 488 NHS ester. To prevent photobleaching, the reaction was completed in the dark for 6 h at room temperature. The Atto 488 NHS ester labeled CIP-TEOS-APTES was magnetically separated and washed five times with anhydrous ethanol to remove non-conjugated fluorophores. The final product (CIP-TEOS-APTES-Atto 488) was dried at 60 °C for 24 h in the dark and collected.

Figure 3.11 shows the experimental setup used for the 3D particle tracking confocal microscopy measurements. The volume constrained fluorescently labeled MRE sample was placed above the confocal microscope objective. An electromagnet (from GMW) was connected to an Agilent 6553A power supply operating in constant current mode. The current was tuned to apply fixed magnetic fields of 0, 250 and 500 Oe to the MRE sample, measured using a gaussmeter (Lakeshore®-410). Z-stack images were taken at each magnetic field using a Zeiss LSM880 confocal microscope with a 20x/1.0 water immersion objective lens. The resolution of each z-stack

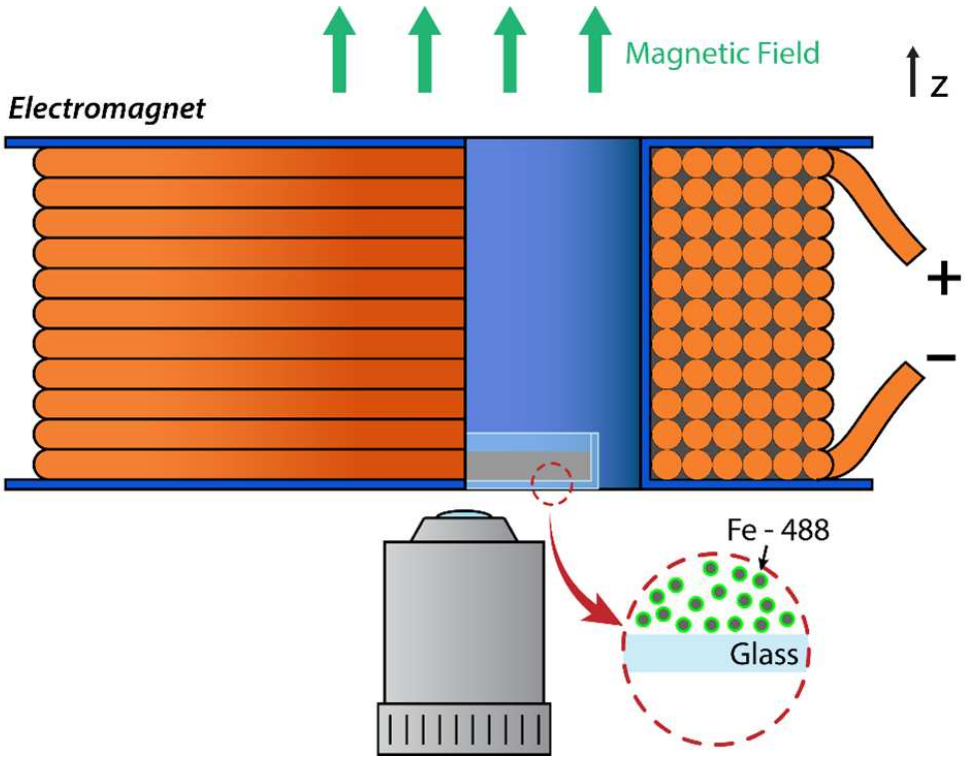

Figure 3.11: Experimental setup for the magnetic-field dependent confocal microscopy of an MRE containing fluorescently labeled iron particles.

was 1772x1772x28 pixels^3 with a voxel size of 200x200x410 nm^3 and the acquisition time for a full stack was thirty seconds.

The trajectories of six particles were tracked as the magnetic field was increased from 0 to 500 Oe and back to 0 Oe in steps of 250 Oe. First, an in-focus image was obtained prior to applying any magnetic field, and images cropped around each particle were selected. A set of 2D cross correlation were performed using the cropped in-focus images of each of the selected particles as inputs to determine the in-focus 3D position of each particle at every magnetic field. The magnetic field-dependent motion for one of the particles is shown in Figure 3.12. The particle moves primarily along the applied magnetic field direction, and the magnitude of the particle motion is larger when the H is increased from 250 to 500 Oe than it is for the 0 to 250 Oe field step, and the motion is several microns in magnitude, all of which are in qualitative agreement with the modeling results. The microscopy results hence confirm by direct observation that the iron particles exhibit micron-scale motion primarily along the applied magnetic field direction within the polymer. In addition,

Figure 3.12 indicates that the field-induced particle motion is reversible within the measurement uncertainty.

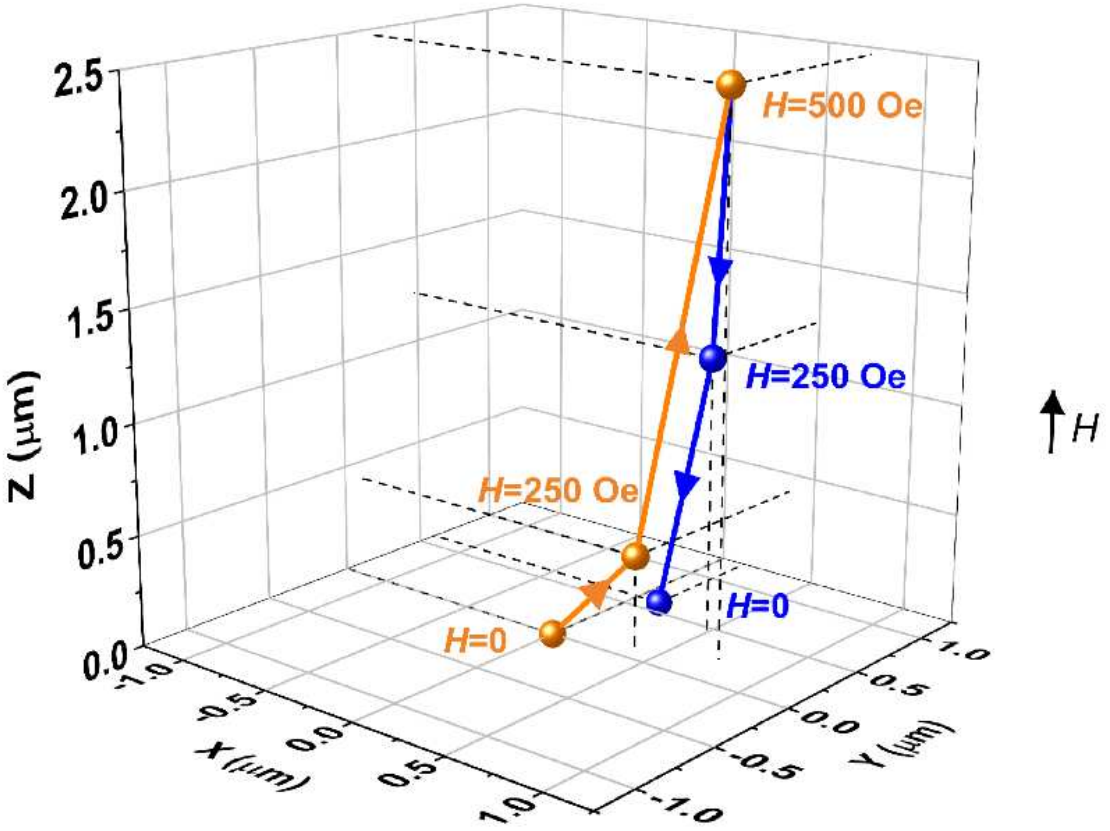

Figure 3.12: Trajectory of an iron particle within the polymer matrix of an ultrasoft MRE extracted using confocal microscopy. The measurements were done on the fluorescently labeled MRE sample1, and H was applied along the Z direction. The uncertainty for the z-position is ± 0.4 μm and that for the x- or y-position is ± 1 μm.

3.8.5 Modeling for field applied at an intermediate angle

The model of two dipoles connected by a single spring, which was used to obtain the results shown in Figure 3.4 and Figure 3.5, is suitable for studying the response of magnetic dipoles to a magnetic field that is applied along or perpendicular to the line that connects the centers of the two particles. We refer to the above case as the on-axis case. To capture the restoring force in response

to a rotational motion, we employed a three-spring model, as demonstrated by Puljiz *et al.* [50] and illustrated in the inset of Figure 3.13, where the gray regions that the two end springs attached to are the equilibrium positions of the spheres at zero magnetic field. Figure 3.13 shows modeling results done using this three-spring approach with the field applied at an angle of $\theta = 19°$ to the particle axis with $k = 4 \times 10^{-3}$ N/m, $S_0 = 9$ μm, and otherwise the same parameters as used in Figure 3.4 and Figure 3.5. We note that Puljiz *et al.* [50] describe a method to modify the k values for the two additional end springs to capture the shear modulus magnitude more accurately. Here we use the same k to provides a reasonable qualitative picture of the response. As shown in Figure 3.13, at this angle ($\theta = 19°$), the net force is attractive and the particles consequently move towards each other at intermediate fields and also rotate towards the applied field direction. As in the on-axis case, the hysteretic region shown in Figure 3.13(b) corresponds to the region of bistability.

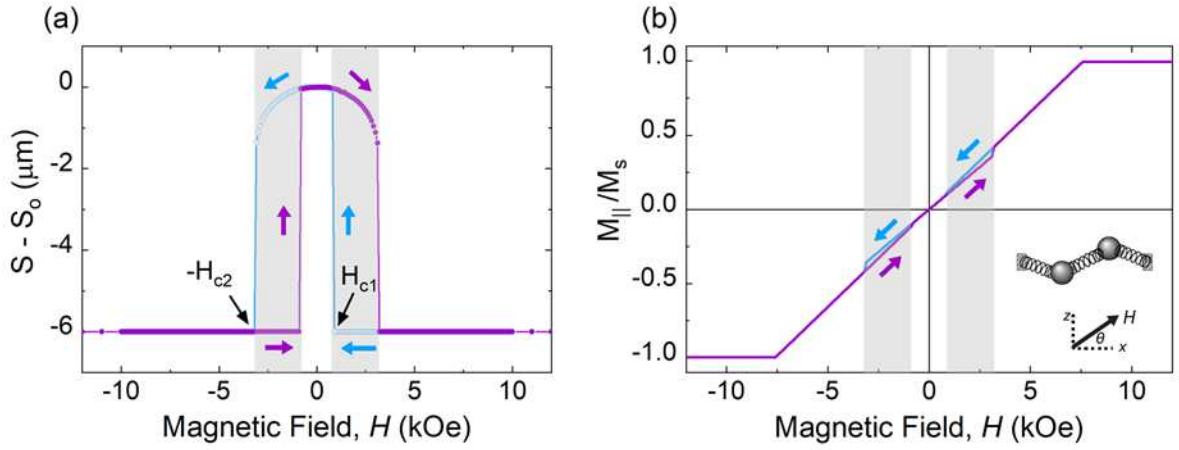

Figure 3.13: Modeling results for a field angle of $\theta = 19°$, $k = 4 \times 10^{-3}$ N/m for the three springs, $S_0 = 9$ μm for the spring that connects the two dipoles, $R = 1.5$ μm ($\chi = 2, M_s = 1.4 \times 10^6$ A/m). As shown in the inset, one spring connects the particles and two additional springs connect each particle to its equilibrium position. The magnetic response parallel to the applied field and the particle displacement magnitude ($S - S_0$) are shown in (a) and (b), respectively. The field ranges over which the particle bistability occurs are shaded in (a) and (b), and in (b) the bistability field range (shaded in gray) corresponds to the field range over which magnetic hysteresis is observed.

3.9 Acknowledgements

The work at BMC was supported by the Center for Engineering Mechanobiology (CEMB), an NSF Science and Technology Center, under Grant Agreement No. CMMI:15-48571. The work at CSU was supported by Grant No. NSF-DMR 1709525. The work at UD was supported by the Delaware INBRE program, with a grant from the National Institute of General Medical Science—NIGMS (Grant No. P20 GM103446) from the National Institutes of Health and the State of Delaware. Low-Temperature magnetometry was supported by the U.S. Department of Energy, Office of Basic Energy Sciences, under Award No. DE-SC0021344. The authors thank Dr. Sylvain Le Marchand and Dr. Jeffrey Caplan from the University of Delaware's Bio-Imaging Center for their expertise and support performing confocal microscopy. We also thank Dr. Marty Gelfand for helpful discussions on modeling.

Chapter 4

Magnetic hysteresis and field dependent shear modulus of magnetoactive-polymers as 3D mass-spring models

4.1 Introduction

Magnetoactive polymers have complicated behaviors in response to mechanical loading, and are responsive to an external magnetic field. Modeling those behaviors requires making assumptions about what the important aspects of these systems are. It also requires us to clearly state the problem we are interested in, and to simplify the problem until we have something that can be solved numerically. The mathematical treatment of a magnetoactive polymer depends on the length scale, time scale, and properties that are of interest.

The model used in Chapter 2 and Chapter 3 massively simplifies the magnetic and elastic parts of the problem, allowing us to explore the interplay between the elastic and magnetic forces at the expense of being less realistic. The linear magnetic response is appropriate for small magnetic fields or for paramagnetic particles, but not for ferromagnetic materials. The treatment of the elastic part of the problem by single springs connecting magnetic particles results in no resistance to shearing forces or twisting. The interfacial bonding between the magnetic particle and polymer is ignored, the deformation of the surrounding polymer isn't resolved, and shape changes or magnetostriction can't be captured. We are going to move beyond this dipole-spring model to something that is able to capture more physically realistic problems.

The behavior of magnetoactive polymers depends on the details of the particle arrangement within the polymer matrix, so we would like to model the magnetorheological elastomer on a length scale that resolves the micron sized particles, but not their domain structure, or the polymer chains. These length scales are still large enough that the polymer matrix can be treated as

a continuous medium. We treat the polymer matrix as isotropic, linearly elastic, and not quite incompressible. We will model the elastic part of the problem using a modified mass-spring system. For the magnetic part of the problem, we treat the magnetic particles as spherical, identical in size, rigid, and with an anhysteretic but nonlinear and saturable magnetization response. The magnetic particle interactions are treated as magnetic dipoles sitting at the center of each particle, using the standard dipole-dipole interaction energy and force expressions, the Zeeman energy, magnetostatic self-energy terms, and a volume exclusion energy and force that prevents particle overlap.

The system is discretized into a collection of uniformly distributed nodes connected by linearly elastic springs, and volume elements that exert forces on the nodes to preserve their volume. Internodal distances are kept small compared to particle size, and volume elements are initially cubic. Dirichlet boundary conditions are applied to the nodes on the surface of the system, defining the displacement of those nodes, $\vec{u}_i(\vec{x}_i, t)$. External magnetic fields, $H_{ext} = B_{ext}/\mu_0$ are applied to the system, which are uniform throughout the volume of the system. By evaluating the forces acting on all nodes and numerically integrating the system of ODEs through time, the equilibrium configuration of the nodes are found. From the equilibrium nodal positions the system magnetization and energy can be determined, and the magnetization response and effective modulus of the system can be analyzed.

With this description in place, we find that even for simple systems there are a huge number of potential situations to explore: varying particle size, susceptibility, magnetization saturation, number of particles, particle density, and particle arrangement, as well as considering variations of the elastic modulus and Poisson ratio, boundary conditions, and the direction of the applied magnetic field.

The results presented will focus on a small subset of potential problems that can be explored with the model. We will focus on a small number of particles, and values for the elastic modulus and Poisson ratio that are similar to experimentally realized ultrasoft polymer based magnetorheological elastomers. We will focus on studies of the magnetic hysteresis of the system with only

two particles, and on the effective shear modulus for systems with two particles, four particle chain like structures, and eight particle helical chain like structures.

The modeling work done here is an extension of the model presented in [1]. This is a hybrid mass spring system (HMSS) approach, presented in [1] as an option for real-time simulation of soft materials with near incompressibility, $\nu \approx 0.5$, such as biological tissues and polymers. The modification to the traditional mass spring system is an additional bulk modulus parameter and volume correction force that acts to preserve the volume of cubic volume elements which make up the simulated system. The freedom of choice of Poisson ratio makes this an interesting option for modeling the polymer matrix in magnetoactive polymer composites while preserving the utility of mass-spring based approaches to modeling elasticity. The HMSS approach was extended through the addition of rigid magnetic spheres, allowing the method to be used for simulating MRE systems, which we will refer to as a magnetic elastomer spring system, or MESS.

4.1.1 Spring Models

Spring based models [5, 49, 50, 59, 60, 78–81] are simple, easy to implement, and straightforward to interpret. These models work best in the small strain limit where the approximation to a linearly elastic response is still accurate. More realistic models that incorporate nonlinear material responses, viscous effects, and incompressibility require alternate approaches. This can mean describing the system in terms of systems of partial differential equations and tensor fields. For complicated system shapes, analytical solutions may not be possible, and numerical methods need to be used.

Methods like the finite difference method, finite element method (FEM), and finite volume method, turn the continuous partial differential equation (PDE) problem into a discrete representation that can be stored in computer memory [82]. For FEM, this allows finite dimensional function spaces to be used to approximate the solution. Variations on the finite element method are powerful tools, and have been used to great success for structural analysis, studying static and dynamic responses to mechanical loading, electromagnetic phenomena, fluid dynamics, and MREs [33].

So called multi-physics problems combining mechanical, electromagnetic, and thermodynamic problems can also be tackled using these approaches.

There is a tradeoff in the use of more complex methods, like FEM, and more more complex mathematical descriptions of systems like continuum magnetomechanics. The user needs to ensure they have properly set up the problem, including discretizing and representing the system of interest, chosen an appropriate solver, type of volume element and function space, and used boundary conditions that reflect what would be experienced by the real system. Care needs to be taken in choosing the problem to be solved and its setup. Even when done correctly, it is necessary to visualize the results and analyze them to provide useful feedback. Along with this additional conceptual complexity is increased demand for computational power, and the problem needs to fit within available memory.

With spring based methods some of the same pitfalls remain, like the limitations of memory, the need to properly discretize your system, apply appropriate boundary conditions, and visualize and analyze the results in a way that provides insight. One benefit to spring based models is lower computational expense as compared to FEM. Spring based models are used in computer graphics to create real-time physically based models of deformation. The response may not be as accurate as a full FEM simulation, but these models are based on a physically realistic mathematical description of the response to deformation.

Spring based models of magnetoactive polymers have been explored by other authors. These models use different assumptions and different approaches to representing the polymer matrix, the behavior of the magnetic particles, and the arrangement of the magnetic particles.

Ref. [60] uses fixed identical magnetic moments with lattice particle arrangements, with and without additional randomization in position, where magnetic particles are treated as point dipoles connected by linearly elastic springs. The model is 2D, and results are restricted to cases where the lattice of particles does not collapse into clusters. Results are shown for tensile, compressive, and shear moduli while allowing only affine deformations of the system, and while allowing non-affine deformations where the dipoles can rearrange with 2 degrees of freedom each, except for

those on the boundaries. Ref. [59] has a 3D model with permanent identical magnetic dipoles and linearly elastic spring connections for neighboring particles, but does not assume periodic particle distributions. It reports on static and dynamic moduli through normal mode analysis of the system. Ref. [49] has a 3D model with identical magnetization, but variation in particle size and neglects mutual magnetization. The model includes mesh nodes which are not magnetic particles. Nodes are initially face centered cubic with nearest neighbor connecting edges between nodes being linearly elastic springs. Experimentally measured particle configurations are laid over the lattice spring network and nearby nodes are shifted to match particle positions. Mean squared displacement of particle nodes is used to stochastically shift non-particle nodes in a way which produces the same mean squared displacement, except for boundary nodes that are shifted less to maintain a roughly cubic shape for the system. Results are shown for dynamic moduli and particle rearrangement.

Ref. [78] includes orientational memory and particle rotations, as well as linearly elastic spring connections between magnetic particles. The model is 3D, with three positional degrees of freedom for each magnetic particle, and two degrees of freedom for the magnetic moment orientation. Each particle has an identical magnetic moment magnitude. Ref. [78] specifically studies situations where the particles do not collapse or cluster. Ref. [79] is a 1D model of magnetic particles with identical magnetic moment magnitudes with orientational degrees of freedom. The particles are connected by linearly elastic springs, and have a steric repulsion term to prevent particle overlap. The results show that a hardening transition occurs in the system when the particles cluster under the effect of an applied magnetic field.

Ref. [5] uses mutually magnetizing magnetic particles with linear magnetization responses so that the magnetic moments are found by solving a linear system of equations. Magnetic particles are connected with linearly elastic springs. Results are shown for particle rearrangement under the effect of an applied magnetic field in 2D and 3D systems with hexagonal lattices. Ref. [80] has a 2D model of a chain of magnetic particles with a network of springs. This work uses a regular hexagonal mesh that includes additional nodes that do not carry a magnetic dipole moment

to represent the polymer matrix. The particles are made up of multiple nodes in the mesh, and the spring connections within a particle are stiffer to reflect rigidity of the magnetic particles. Results are shown for the case where the spring connections between particle nodes and nodes in the surrounding polymer are stiffened, and the case where these spring connections are not stiffened. Stiffening those connections recreates buckling behavior seen experimentally, suggesting the volume immediately surrounding magnetic particles is stiffened in these soft gel systems.

Ref. [81] studies dynamic shear moduli of cubic networks of magnetic dipoles connected by springs in 3D with point like dipole interactions and identical magnetization. Rearrangement of the particles into clusters is not considered in the study. Ref. [50] models a system of two paramagnetic particles that mutually magnetize and takes into account the self-demagnetizing field of the particles. The elastic response of the polymer is handled using a Neo-Hookean model and FEM. They also map a linear elasticity theory model to a three-spring and one-spring model. They then do a comparison of these models with an experimental setup consisting of two paramagnetic nickel particles with size $D \approx 170$ μm, and this comparison justifies the use of a linear elasticity model in the regime before particle collapse.

Dipole-spring models have been useful for theoretical studies of the behavior of magnetoactive polymers, with different restrictions on their applicability to real systems and situations. Using constant magnetization, or neglecting mutual magnetization makes problems easier computationally, but these are often not physically realistic assumptions. Similarly, the rearrangement of particles into clusters is an important aspect of MRE behavior. Aspects of the model used in this thesis, dubbed the magnetic elastomer spring system (MESS) model, increased the complexity of the problem and the systems that can be studied, with the goal of having a more physically realistic model and actionable predictions, while preserving some of the simplicity of dipole models and the ease of evaluating spring forces. This increase in complexity does come with an increased computational expense. As per Golec *et al*. [1], "Mass-spring systems simulating elastic materials obey constraints known...as the *Cauchy relations*, restricting the Poisson ratio of isotropic systems to be exactly $\nu = 1/4$." This is a strong restriction on the types of materials that can be modeled using

spring systems. The approach taken by Golec *et al.* and adopted here allows for simulating systems with $-1 \leq \nu \leq 1/2$, so that incompressible or nearly incompressible materials like elastomers, which have ν close to 0.5, can be more accurately modeled. Treating three dimensional problems greatly increases the memory costs, but by treating the surrounding polymer matrix explicitly we can more accurately reproduce the behavior of the composite and the effect of the rearrangement of the particles on the polymer matrix. We gain the advantage of relating material properties such as the bulk, shear, or Young's modulus to the spring stiffness constants of the system. These relationships are established by equating the strain-energy density of the spring mass system with the strain-energy density of an isotropic, homogeneous, linearly elastic medium in the framework of continuum mechanics. This in turn allows us to make quantitative statements about the effective moduli for comparison to experimental results.

4.2 Methods

Modeling magnetoactive polymer systems requires descriptions of the mechanical and magnetic parts of the problem, the coupling between them, and appropriate boundary conditions. It also requires methods for discretizing the system, methods for solving the resulting systems of equations to determine the configuration of the system under the influence of external magnetic fields and strains, and a framework for analysis of the resulting solutions.

4.2.1 Determining Stiffness Constants

Relating stiffness constants to material parameters like the Young's modulus and Poisson's ratio allows us to make quantitative predictions about the systems being studied. Here we closely follow [1] in deriving expressions for the spring stiffness constants in terms of the Young's modulus, E, and Poisson ratio, ν, as well as the discretization length, l_e. The discretization length is the size of the edges of the cubic volume elements making up the system, and can be considered a lattice constant. In order to model systems with values besides $\nu = 1/4$, an additional non-central force proportional to a bulk modulus κ is included in the model, whose value depends on E and ν.

Energy Density Equivalence

To determine the spring stiffness constant expressions, the energy density of a linearly elastic system experiencing a homogeneous deformation is written in terms of a continuum mechanics framework, and for a system with the same properties modeled as a cubic volume element with discrete springs connecting nodes at the element vertices.

By assuming homogeneous deformations, and using approximations to relate the applied strain, ε, the nodal positions, $\vec{x}$, and the displacement field, $\vec{u}$, relationships among the spring stiffness constants, k, and the polymer parameters are found. Except for a scant few additional explanatory comments of my own to increase understandability, the following derivations are taken from work presented in [1].

Continuum Mechanics and Linear Elasticity

In linear elasticity the strain-energy density can be written as

$$W = \frac{1}{2}\boldsymbol{\varepsilon} : \mathsf{C} : \boldsymbol{\varepsilon} \tag{4.1}$$

or, in component form, as

$$W = \frac{1}{2}\mathsf{C}_{ijkl}\varepsilon_{ij}\varepsilon_{kl}. \tag{4.2}$$

This quadratic form implies symmetry of the fourth order stiffness tensor $\mathsf{C}_{ijkl} = \mathsf{C}_{klij}$. This symmetry of the tensor plus additional symmetries reduce the number of independent components from 81 components to 21, with further reductions based on the symmetries of the underlying system.

Discrete Linear Spring Model

For our system of springs, the energy density is calculated while considering the energy stored in the springs under a homogeneous deformation of a unit cell. The cell is a cubic volume element, composed of 4 springs spanning the cube diagonals with stiffness constant k_c and length $\sqrt{3}l_e$, 12 springs along the edges with stiffness constant k_e and length l_e, and 12 springs along the face

diagonals with stiffness constant k_f and length $\sqrt{2}l_e$, see Figure 4.1. The energy per unit volume of the cell is

$$W^{(s)} = \frac{1}{2V_c} \sum_{\alpha \in cell} k_\alpha (l'_\alpha - l_\alpha)^2. \tag{4.3}$$

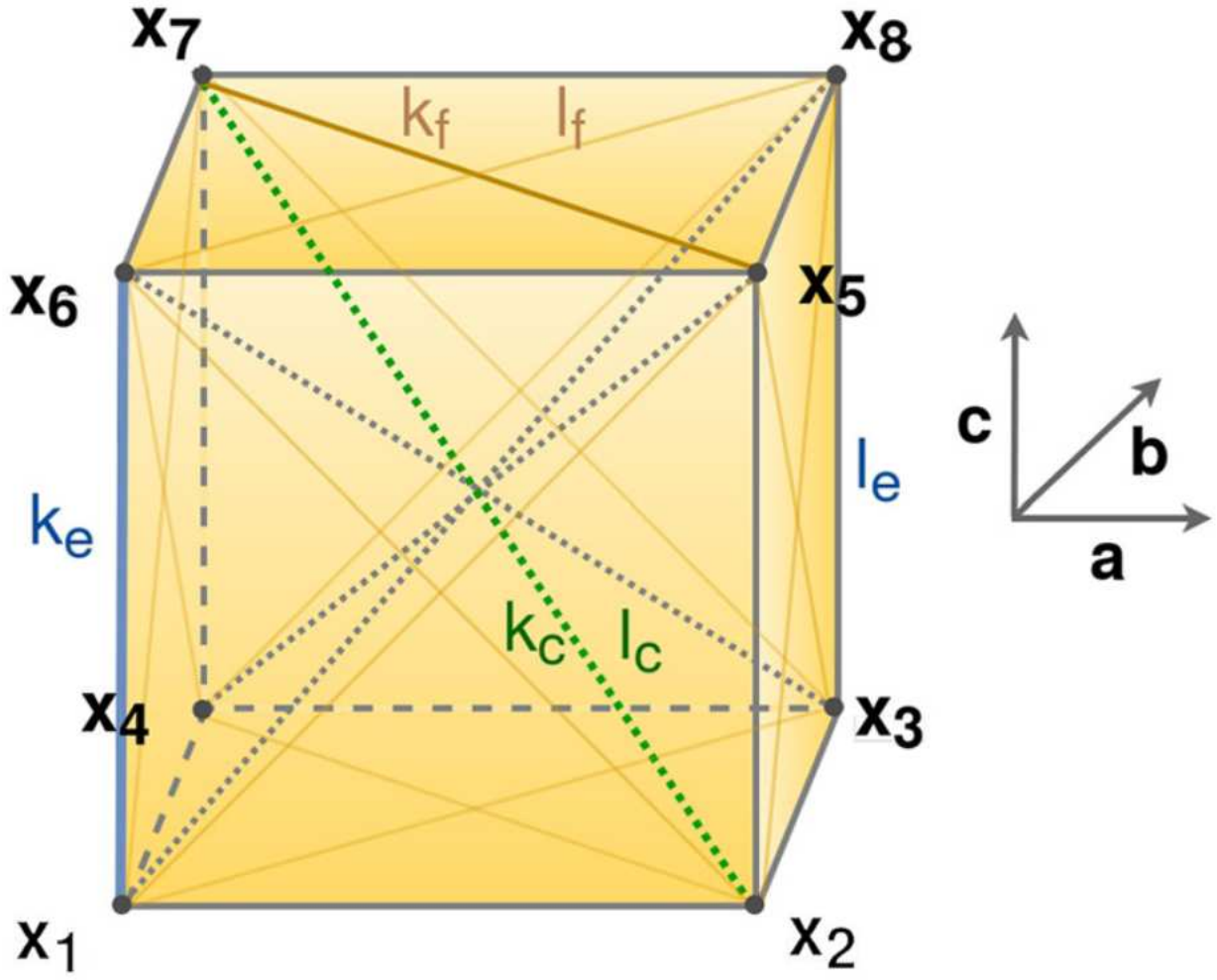

Figure 4.1: An element of our hybrid mass spring system composed of 12 edge springs, 12 face diagonal and 4 inner-diagonal springs interconnecting the particles. Figure and figure caption reproduced directly from [1]. The four inner-diagonal springs are represented by dotted lines. The x_i are the nodes, k_e and l_e are the spring stiffness constant and equilibrium length of edge springs, k_f and l_f the same for the face springs, k_c and l_c the same for the center diagonal springs.

If the dimension of the cell is small compared to the deformation on a macroscopic scale we can assume a homogeneous deformation over the length of the cell, $\vec{u}(\vec{x}) = (\nabla\vec{u})^T \cdot \vec{x}$ with a uniform deformation gradient $\nabla\vec{u}$ imposed on the boundaries. The springs will deform affinely, with the end-to-end vector $\vec{r}_\alpha \to \vec{r}'_\alpha = \vec{r}_\alpha + (\nabla\vec{u})^T \cdot \vec{r}_\alpha$. The length changes from $l_\alpha = \sqrt{\vec{r}_\alpha^{\,2}}$ to

$$l'_\alpha = \sqrt{\vec{r}'^{\,2}_\alpha} = \sqrt{(\vec{r}_\alpha + (\nabla\vec{u})^T \cdot \vec{r}_\alpha) \cdot (\vec{r}_\alpha + (\nabla\vec{u})^T \cdot \vec{r}_\alpha)} \tag{4.4}$$

$$= \sqrt{\vec{r}_\alpha^2 + 2\vec{r}_\alpha \cdot ((\nabla\vec{u})^T \cdot \vec{r}_\alpha) + ((\nabla\vec{u})^T \cdot \vec{r}_\alpha)^2} \tag{4.5}$$

$$= l_\alpha \sqrt{(1 + 2\frac{\vec{r}_\alpha}{l_\alpha^2} \cdot ((\nabla\vec{u})^T \cdot \vec{r}_\alpha) + \frac{1}{l_\alpha^2}((\nabla\vec{u})^T \cdot \vec{r}_\alpha)^2} \tag{4.6}$$

$$\approx l_\alpha + \frac{1}{l_\alpha}\nabla_i u_j r_{\alpha i} r_{\alpha j} = l_\alpha + \frac{1}{l_\alpha}\varepsilon_{ij} r_{\alpha i} r_{\alpha j} \tag{4.7}$$

where the binomial approximation was used, keeping only terms first order in $\nabla\vec{u}$. Substituting (4.7) into (4.3) yields

$$W^{(s)} = \frac{1}{2V_c}\sum_{\alpha\in cell} k_\alpha (\frac{1}{l_\alpha}\varepsilon_{ij} r_{\alpha i} r_{\alpha j})^2 \tag{4.8}$$

$$= \frac{1}{2V_c}\sum_{\alpha\in cell} \frac{k_\alpha}{l_\alpha^2}\varepsilon_{ij}\varepsilon_{kl} r_{\alpha i} r_{\alpha j} r_{\alpha k} r_{\alpha l}. \tag{4.9}$$

Comparing to (4.2), the energy also depends on the strain squared, $\frac{1}{2}\mathsf{C}_{ijkl}\varepsilon_{ij}\varepsilon_{kl}$, so for a spring system

$$\mathsf{C}^{(s)}_{ijkl} = \frac{1}{V_c}\sum_{\alpha\in cell} \frac{k_\alpha}{l_\alpha^2} r_{\alpha i} r_{\alpha j} r_{\alpha k} r_{\alpha l} \tag{4.10}$$

For an isotropic material, which can be characterized by two parameters like the Lamé constants λ and G, where G is the shear modulus, we have

$$\mathsf{C}^{(iso)}_{ijkl} = \lambda\delta_{ij}\delta_{kl} + G(\delta_{ik}\delta_{jl} + \delta_{il}\delta_{jk}) \tag{4.11}$$

with the following deformation energy

$$\mathsf{W}^{(iso)} = \frac{\lambda}{2} Tr(\varepsilon)^2 + GTr(\varepsilon^2) = \frac{\lambda}{2}(\varepsilon_{kk})^2 + G\varepsilon_{ij}\varepsilon_{ij}. \tag{4.12}$$

In the rari-constant theory of elasticity, which assumes only pairwise central forces between atoms or molecules on a lattice the symmetric fourth order stiffness tensor is reduced from 21 independent components to 15 due to the 6 Cauchy relations. In a cubic system this reduces to 3 independent elastic constants. In an isotropic material the rari-constant elastic model of the system is described by a single elastic constant, and $\lambda = G$. Then

$$\mathsf{C}_{ijkl}^{(s+iso)} = G(\delta_{ij}\delta_{kl} + \delta_{ik}\delta_{jl} + \delta_{il}\delta_{jk}). \tag{4.13}$$

The rari-Young modulus and Poisson ratio become

$$E = \frac{5G}{2} \tag{4.14}$$

$$\nu = 1/4 \tag{4.15}$$

For a useful discussion of the relationship between microscopic and macroscopic elasticity theories, and the distinction between rari-constant and multi-constant theories of elasticity, the reader is directed to [83].

The Modified Approach

In order to create a multi-constant model of elasticity that behaves like a real world material, a non-central force has to be introduced. The underlying spring system is a rari-constant model with only central forces. The modified system contains a new energy term quadratic in the relative volume change of a cubic volume element. V_c is the volume of the undeformed cell, and V_c' is the volume of the deformed cell. The volume density of the energy is then

$$W^{'} = W^{(s)} + W^{(v)} = \frac{1}{2V_c}\sum_{\alpha \in cell} k_\alpha (l_\alpha^{'} - l_\alpha)^2 + \frac{\kappa}{2}\left(\frac{V_c^{'} - V_c}{V_c}\right)^2 \tag{4.16}$$

where the relative volume change is $(V_c^{'} - V_c)/V_c = \varepsilon_{kk}$ and Einstein summation is implied by the repeated indices. The constant κ is an additional bulk modulus. We then have

$$W^{'} = \frac{1}{2}\mathsf{C}_{ijkl}^{'}\varepsilon_{ij}\varepsilon_{kl} \tag{4.17}$$

$$\text{with } \mathsf{C}_{ijkl}^{'} = \frac{1}{V_c}\sum_{\alpha \in cell}\frac{k_\alpha}{l_\alpha^2} r_{\alpha i} r_{\alpha j} r_{\alpha k} r_{\alpha l} + \kappa \delta_{ij}\delta_{kl} \tag{4.18}$$

where $\mathsf{C}_{ijkl}^{'}$ is the sum of the spring stiffness tensor and a compression term proportional to κ.

For an isotropic system

$$W^{'(iso)} = \frac{1}{2}(G + \kappa)(\varepsilon_{kk})^2 + G\varepsilon_{ij}\varepsilon_{ij}. \tag{4.19}$$

Considering a uniaxial strain characterized by $\sigma_{xx} \neq 0, \sigma_{yy} = \sigma_{zz} = 0$ with $\varepsilon_{yy} = \varepsilon_{zz}$, the Young's modulus is given by $E = \sigma_{xx}/\varepsilon_{xx}$ and Poisson's ratio by $\nu = -\varepsilon_{yy}/\varepsilon_{xx}$. Thus in the modified system they are defined in terms of G and κ by

$$E = G\frac{3\kappa + 5G}{\kappa + 2G} \quad \text{and} \quad \nu = \frac{1}{2}\frac{\kappa + G}{\kappa + 2G} \tag{4.20}$$

and the bulk modulus becomes

$$K = \kappa + \frac{5}{3}G. \tag{4.21}$$

We can then solve for the additional bulk modulus κ in terms of the parameters E and ν, which yields

$$\kappa = \frac{E(4\nu - 1)}{2(1 + \nu)(1 - 2\nu)}\,. \tag{4.22}$$

Our modified mass-spring model is now a multi-constant model of elasticity described by two independent elastic constants, but we need to determine the spring stiffness constants in our spring

model. If we consider a 3D space with a lattice of cubic cells as described earlier and seen in Figure 4.1, we can write down the vectors spanning the edges, face diagonals, and center diagonals in the undeformed cell. We then consider the contribution of the springs in a cubic cell to $\mathsf{C}^{(s)}$, and then arrive at expressions for the spring stiffness constants in our system in terms of G and l_e, our lattice constant.

Since each edge belong to four adjacent volume elements, only one spring should be counted in each direction. That is, the four edge springs each contribute only $1/4$ of their stiffness to the single cubic cell considered, so we need only consider one edge spring vector along each axis. Edge springs span the following vectors

$$\vec{r}_1 = (l_e, 0, 0), \quad \vec{r}_2 = (0, l_e, 0), \quad \vec{r}_3 = (0, 0, l_e), \tag{4.23}$$

and inner-diagonal springs span the following vectors with length $l_c = \sqrt{3} l_e$

$$\vec{r}_4 = (l_e, l_e, l_e) \quad \vec{r}_5 = (l_e, l_e, -l_e) \tag{4.24}$$

$$\vec{r}_6 = (l_e, -l_e, l_e) \quad \vec{r}_7 = (-l_e, l_e, l_e). \tag{4.25}$$

Since each face belongs to two cells, similar to the argument above concerning edges, we only count one of each type of face spring. Face diagonal springs span the following vectors with length $l_f = \sqrt{2} l_e$

$$\vec{r}_8 = (l_e, l_e, 0) \quad \vec{r}_9 = (l_e, -l_e, 0) \quad \vec{r}_1 0 = (0, l_e, l_e) \tag{4.26}$$

$$\vec{r}_{11} = (0, l_e, -l_e) \quad \vec{r}_{12} = (l_e, 0, l_e) \quad \vec{r}_{13} = (l_e, 0, -l_e). \tag{4.27}$$

Considering an element of the stiffness tensor, with $V_c = l_e^3$

$$\mathsf{C}^{(s)}_{ijkl} = l_e^{-3}\Big\{ \sum_{\alpha=1}^{3} l_e^{-2} k_e r_{\alpha i} r_{\alpha j} r_{\alpha k} r_{\alpha l} \tag{4.28}$$

$$+ \sum_{\alpha=4}^{7} l_c^{-2} k_c r_{\alpha i} r_{\alpha j} r_{\alpha k} r_{\alpha l} \tag{4.29}$$

$$+ \sum_{\alpha=8}^{13} l_f^{-2} k_f r_{\alpha i} r_{\alpha j} r_{\alpha k} r_{\alpha l} \Big\} \tag{4.30}$$

$$= l_e^{-5}\Big\{ k_e \sum_{\alpha=1}^{3} r_{\alpha i} r_{\alpha j} r_{\alpha k} r_{\alpha l} \tag{4.31}$$

$$+ \frac{k_c}{3} \sum_{\alpha=4}^{7} r_{\alpha i} r_{\alpha j} r_{\alpha k} r_{\alpha l} + \frac{k_f}{2} \sum_{\alpha=8}^{13} r_{\alpha i} r_{\alpha j} r_{\alpha k} r_{\alpha l} \Big\}. \tag{4.32}$$

By symmetry, components of the stiffness tensor having an odd number of identical indices vanish. Since the directions 1, 2 and 3 are equivalent, the nonzero components of $\mathsf{C}^{(s)}$ are

$$\mathsf{C}^{(s)}_{1111} = l_e^{-5}\Big\{ k_e \sum_{\alpha=1}^{3} r_{\alpha 1}^4 + \frac{k_c}{3} \sum_{\alpha=4}^{7} (r_{\alpha 1})^4 + \frac{k_f}{2} \sum_{\alpha=8}^{13} (r_{\alpha 1})^4 \Big\} \tag{4.33}$$

$$= l_e^{-1} \left(k_e + \frac{4}{3} k_c + 2k_f \right) \tag{4.34}$$

$$= \mathsf{C}^{(s)}_{2222} = \mathsf{C}^{(s)}_{3333} \tag{4.35}$$

and

$$\mathsf{C}^{(s)}_{1122} = l_e^{-5}\Big\{ k_e \sum_{\alpha=1}^{3} (r_{\alpha 1} r_{\alpha 2})^2 + \frac{k_c}{3} \sum_{\alpha=4}^{7} (r_{\alpha 1} r_{\alpha 2})^2 + \frac{k_f}{2} \sum_{\alpha=8}^{13} (r_{\alpha 1} r_{\alpha 2})^2 \Big\} \tag{4.36}$$

$$= l_e^{-1} \left(\frac{4}{3} k_c + k_f \right) \tag{4.37}$$

$$= \mathsf{C}^{(s)}_{1133} = \mathsf{C}^{(s)}_{2233} = \mathsf{C}^{(s)}_{1212} = \mathsf{C}^{(s)}_{1313} = \mathsf{C}^{(s)}_{2323} \tag{4.38}$$

To ensure elastic isotropy, the stiffness constants need to be chosen in such a way that the spring stiffness tensor can be cast into the form (4.13) which can only happen if

$$\mathsf{C}^{(s)}_{1111} = 3\mathsf{C}^{(s)}_{1122}. \tag{4.39}$$

This leads to the condition

$$k_e = \frac{8}{3}k_c + k_f \tag{4.40}$$

and the shear modulus is then

$$G = \mathsf{C}^{(s)}_{1122} = l_e^{-1}\left(\frac{4}{3}k_c + k_f\right). \tag{4.41}$$

With G specified, we introduce a parameter $A = k_f/k_c$ that sets the ratio of the center diagonal and face diagonal spring stiffness constants. We can rewrite equations (4.40), (4.41), and (4.15) to obtain the following expressions for the spring stiffness constants in terms of the Young's modulus, E, and the lattice constant l_e.

$$k_c = \frac{6}{5}\frac{E\, l_e}{4+3A} \tag{4.42}$$

$$k_f = Ak_c \tag{4.43}$$

$$k_e = \frac{2\, E\, l_e}{5}\frac{8+3A}{4+3A} \tag{4.44}$$

There is freedom to choose the value of A, and we set the value $A = 1$ in practice.

4.2.2 Discretization and Sphere Voxelization

Any system we want to study needs to be discretized in order to solve for the configuration of the magnetic particles and the deformation of the polymer matrix. The simplest choice is to have uniformly separated nodes connected by springs, and cubic volume elements with nodes at each of the eight vertices, as described in the previous section. A unit cell of this system is shown in

Figure 4.1. This grid of spring-connected nodes allows us to model the elastic part of the problem. The magnetic particles will be contained within the boundaries of the system. Magnetic particles are placed on the grid of nodes and volume elements. We require that the center of the particle sit at the center of a volume element. Based on the particle size and the discretization factor, the particle has a diameter of $(2n_d+1)$ voxels, where n_d is the discretization factor. This constrains the potential arrangements of the particles within the system. We also require some interstitial volume elements between particles that have elastic properties of the polymer. A finer discretization is needed if more precise control over particle placement is desired.

The Problem Domain: Nodes, Springs, and Volume Elements

The volume of interest is discretized into nodes and cubic volume elements. The nodes belong to one of the following categories based on their position: corner, edge, surface, interior, and particle. The interior and particle nodes are connected to their 26 nearest neighbors by linearly elastic springs, while fewer connections exist for surface, edge, and corner nodes. Those springs are either edge, face diagonal, or center diagonal springs. The value of the spring stiffness constants is weighted by the number of cubic volume elements whose faces or edges touch the respective face or edge of the associated spring. If there is no material present it should not contribute to the stiffness of the connection. For nodes on the surface of the volume the face diagonal spring stiffness constant will be 1/2 that of other face diagonal spring connection, and edge spring stiffness constants will also be halved. For corner-edge node connections, and edge-edge connections, the edge spring stiffness will be 1/4 that of interior-interior node connections.

Springs are represented in the implementation by a 2D array of 4 element row vectors. The first two columns contain the node indices, which are the indices of the 2D positions, velocities, and accelerations arrays corresponding to the nodes. Those node indices can be mapped to their initialized positions. The third column of the springs array contains the stiffness constant of the spring, the fourth contains the equilibrum length of the spring.

Volume elements are represented in the implementation by a 2D array of 8 element row vectors. The entries in each row correspond to node indices which make up the vertices of the volume

element. The volume of the elements can be estimated by taking the vector triple product of the average of the vectors which define the edges of the element. There are twelve edges to the cube, so the four edge vectors which point along each of the Cartesian coordinates are averaged to make the three average edge vectors.

$$\vec{a} = \frac{1}{4}(\vec{x}_2 - \vec{x}_1 + \vec{x}_3 - \vec{x}_4 + \vec{x}_5 - \vec{x}_6 + \vec{x}_8 - \vec{x}_7) \tag{4.45}$$

$$\vec{b} = \frac{1}{4}(\vec{x}_3 - \vec{x}_2 + \vec{x}_4 - \vec{x}_1 + \vec{x}_8 - \vec{x}_5 + \vec{x}_7 - \vec{x}_{6h}) \tag{4.46}$$

$$\vec{c} = \frac{1}{4}(\vec{x}_6 - \vec{x}_1 + \vec{x}_8 - \vec{x}_3 + \vec{x}_5 - \vec{x}_2 + \vec{x}_7 - \vec{x}_4) \tag{4.47}$$

Here $\vec{x}_i$ are the nodal positions of the vertices of the volume element, and

$$V_{element} = \vec{a} \cdot (\vec{b} \times \vec{c}) \tag{4.48}$$

when the deformation of the volume element is homogeneous, (4.48) is exact.

The discretization length, l_e, of the problem domain are chosen with respect to the magnetic particle size, R. This ensures that the voxelization of the spheres matches the desired particle size as well as possible given the discrete nature of the representation.

$$l_e = \frac{2R}{2n_d + 1} \tag{4.49}$$

The size of the system can be determined in the code either by specifying the size directly or by providing the desired volume fraction of magnetic particles and the desired number of particles. In both cases the exact dimensions may vary slightly from expectation based on the discretization length, since only integer values of volume elements and nodes are possible, so the system size and volume fraction of magnetic particles may vary slightly.

If the system size and particle positions are given, the particle volume fraction Φ is

$$\Phi = \frac{V_{particles}}{V_{total}}. \tag{4.50}$$

If there is a particle volume fraction of Φ, and N_p particles in the simulation, the total simulation volume is

$$V_{total} = \frac{N_p \frac{4}{3}\pi R^3}{\Phi}. \tag{4.51}$$

If there is only one particle in the volume, we can use that to determine the side length of a cube that would contain one magnetic particle assuming a uniform distribution of particles through the volume

$$L = V^{1/3} = \left(\frac{\frac{4}{3}\pi R^3}{\Phi}\right)^{1/3}. \tag{4.52}$$

Using the particle size R, the desired number of particles N_p, and Φ we can determine the volume of the system. With additional information about the manner in which the particles are supposed to be distributed, uniformly or along certain directions, the exact dimensions can be determined.

Discrete Spheres

The translation of the spherical particles to the discrete system is called voxelization, as a 3D analog to rasterization onto a 2D array of pixels for displays. From the origin of the sphere, any voxels (cubic volume elements) that fall within the radius, in voxels, of the sphere will be part of that sphere. We then identify the nodes which belong to those voxels for future use in both setting spring stiffness constants during initialization and distributing forces during simulation. Increasing the value of n_d results in a better approximation to the spherical shape, at the cost of increasing the computational power required to simulate the system. The results of voxelization with different n_d values is shown in Figure 4.2. Choice of n_d comes down to a tradeoff between improving the approximation of a spherical shape and precision in magnetic particle placement with increasing memory demands and runtime.

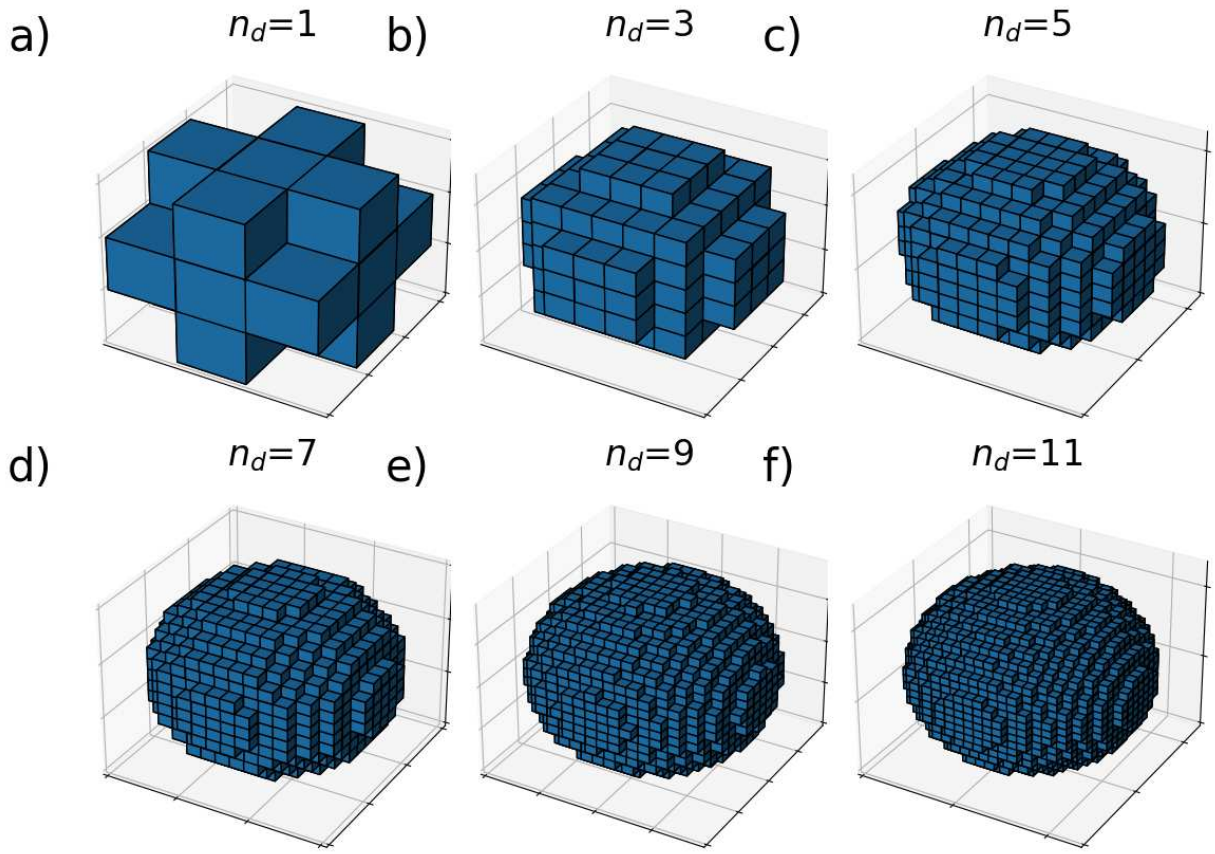

Figure 4.2: Rendered images of a single magnetic particle for a variety of n_d values. a-f) $n_d = 1, 3, 5, 7, 9, 11$.

The elastic response of the particles is modeled by setting the spring stiffness coefficients among nodes that belong to the same particle to be $10000\times$ the stiffness of the polymer constants, or based off the same expressions, but using the properties of iron, whichever is smaller. This is for the sake of numerical stability, as springs which are too stiff can lead to divergence due to truncation error in the numerical integration method.

Nodal Mass

A mass is assigned to each of the nodes in order to relate the forces acting on the nodes to their resulting accelerations. The density of the magnetic particles is set to that of iron, and is greater than that of the polymer matrix. The mass of the nodes belonging to the particle are all set to the same value:

$$m_{Fe,node} = \rho_{Fe} V_{particle} / N_{particle\ nodes} \tag{4.53}$$

where $m_{Fe,node}$ is the mass assigned to a single node belonging to a magnetic particle, $\rho_{Fe} = 7.86 \times 10^3$ kg/m^3 is the mass density of iron[2], $V_{particle}$ is the volume of the magnetic particle, and $N_{particle\ nodes}$ is the number of nodes that make up the particle.

The mass of the polymer nodes is set in a similar manner, but with the additional considerations that were used when assigning spring stiffness constants. For nodes in the interior volume of the system, each node belongs to eight cubic volume elements, and has mass assigned to it equal to that of a volume element. Nodes on the surface, on an edge, or on a corner, have a mass value equal to $1/8 N_{elements} m_{polymer\ node}$ where $N_{elements}$ is the number of elements which have the node as a vertex.

$$m_{polymer\ node} = \rho_{polymer} l_e^3 \tag{4.54}$$

where $\rho_{polymer} = 0.965 \times 10^3$ kg/m^3 to match the value for polydimethylsiloxane[3].

[2]https://www.americanelements.com/carbonyl-iron-powder-7439-89-6

[3]https://www.chemicalbook.com/ChemicalProductProperty_EN_CB3696473.htm

4.2.3 Solving for Magnetization

We treat the magnetic particles as magnetically isotropic, with a nonlinear, saturable anhysteretic magnetization response. The particles are polycrystalline, resulting in randomized magnetocrystalline anisotropies and a negligible net anisotropy. The lack of magnetocrystalline anisotropy results in minimal coercivity and no hysteresis. We treat the magnetic particles as point dipoles at the center of each particle for the purpose of calculating magnetic fields, interaction energies and inter-particle forces. The magnetic particles are assumed to magnetize in response to the local effective field at the center of the particle, and are mutually magnetizable, which means including the effects of all other magnetic particles in the system.

Froehlich-Kennelly Law

The nonlinear, anhysteretic, saturable Froehlich-Kennelly magnetization law is used to model the magnetization response of the carbonyl iron particles (Section 1.3.3), with

$$\vec{M} = \frac{M_s \chi \vec{H}}{M_s + \chi |H|}. \tag{4.55}$$

This expression can be rearranged and written in component form to obtain a system of nonlinear equations for the components of the magnetization of the particles as

$$(M_s + \chi |H_\alpha|) M_{\alpha q} - M_s \chi H_{\alpha q} = 0 \tag{4.56}$$

where α is the particle number, $|H_\alpha|$ is the norm and $H_{\alpha q}$ is the qth component of the total magnetic field at the center of particle α, and $M_{\alpha q}$ is the qth component of the magnetization of particle α.

The total magnetic field is the sum of the external magnetic field and the dipole fields of all other magnetic dipoles. The dipole magnetic field $\vec{H}_{\text{dip}}(\vec{r}_{ij})$ is the magnetic field at $\vec{r}_i$ due to the dipole at $\vec{r}_j$ takes the standard form

$$\vec{H}_{\text{dip}}(\vec{r}_{ij}) = \frac{V_{particle}}{4\pi} \left(\frac{3\hat{r}_{ij}(\vec{M}_j \cdot \hat{r}_{ij}) - \vec{M}_j}{r_{ij}^3} \right) \tag{4.57}$$

where $\vec{r}_{ij} = \vec{r}_i - \vec{r}_j$ is the vector pointing from particle j to particle i.

Combining equations (4.56) and (4.57) leads to a nonlinear system of equations

$$\left(M_s + \chi \left| \left(\vec{H}_{ext} + \sum_{\beta \neq \alpha}^{N_{particles}} \vec{H}_{dip}(\vec{r}_{\alpha\beta}, \vec{M}_\beta) \right) \right| \right) M_{\alpha q} - M_s \chi \left(H_{ext,q} + \sum_{\beta \neq \alpha}^{N_{particles}} H_{dip,q}(\vec{r}_{\alpha\beta}, \vec{M}_\beta) \right) = 0 \, . \quad (4.58)$$

For a given H_{ext}, χ, and set of particle positions, the magnetization of each particle is found by solving this system of equations.

Iterative Method for Nonlinear System of Equations

Finding the magnetization of the particles, while taking into account the external magnetic field and the dipolar fields of all other particles, amounts to finding the roots of this nonlinear system of equations (4.58). It is possible that there are multiple solutions or no solutions for a nonlinear system of equations, and failing to find a solution numerically does not mean one does not exist. An iterative method begins by making an initial guess as to the solution. We use a fixed-point iteration method, which can be used to solve systems of equations of the form

$$\vec{x} + \vec{F}(\vec{x}) = 0, \quad (4.59)$$

which matches the form of Eq. (4.55). We use the solutions found for previous time steps and magnetic field as initial solutions for the next time or magnetic field step since these are often close to the true solutions and are more likely to converge, and to converge more quickly.

When we begin a simulation and have no magnetization history to draw from, the first step for finding the magnetization uses only the external magnetic field to determine the magnetization response. This magnetization is then used as the initial guess. For each future time step the most recently calculated solution is used as the ansatz, giving historical continuity as the simulation pro-

gresses. Similarly, as the simulation progresses and the boundary conditions or external magnetic field are altered the magnetization solution is carried forward.

The algorithm for the iterative method is as follows.

1. Get $\vec{H}_{total}(\vec{r_\alpha})$. Use the ansatz magnetization to calculate the resulting $\vec{H}_{dip}$ at the center of each particle, and the total magnetic field by summing those dipolar field contributions with $\vec{H}_{ext}$.

2. Calculate the difference between the previous magnetization solution and the most recently calculated magnetization. $\Delta\vec{M} = \vec{M}_{p+1} - \vec{M}_p$, where p is the iteration number.

3. If $\forall\ q,\ |(\Delta M)_q| \leq a_{tol} + r_{tol}|M_{p,q}|$, where $|(\Delta M)_q|$ is the q component of a vector of magnetization differences:

   (a) Then all components of the difference vector are below the tolerance, the system is assumed to have converged, the solution is accepted, and we move to step 4)

   (b) Or else some component of the magnetization difference does not match the tolerance and the most recent solution is used to begin the process again at step 1).

4. Once convergence is achieved, record $\vec{M}$ for reuse as the initial magnetization guess for the next time step, and for calculating magnetic forces.

In practice the normalized magnetization M/M_s is used, and typical values of the tolerances are $a_{tol} = 1 \times 10^{-3}$, meaning an absolute tolerance of 0.1% of M_s, and $r_{tol} = 5 \times 10^{-3}$. At each time step the previous magnetization is passed forward to be reused in the fixed-point iterative method for magnetization solving. When a final configuration of the nodes of the system is found, the magnetization is saved out, and reused for the next step in the simulation. The next step may be for a different external magnetic field vector, or a different applied boundary condition value for the same external magnetic field vector.

In this manner, the magnetization history of the system is used as the system evolves, both within simulated time in a simulation step, and from simulation step (external magnetic field and

boundary condition value). While the particles themselves have an anhysteretic magnetization response, the total response of the composite system can demonstrate hysteresis. In order to capture that hysteretic response the configuration of the nodes of the system, the particle positions, and the particle magnetizations need to be recorded and used to represent the initial state of the system as it continues to evolve under new applied magnetic fields and boundary conditions.

4.2.4 Energy and Forces

To do an analysis of the effective modulus of a system we write down its total energy by separately considering the mechanical and magnetic energies. The forces acting on the nodes of the system are derived from the energy terms using

$$\vec{F} = -\nabla U, \tag{4.60}$$

where $\vec{F}$ is the force, U is the energy, and the derivative is taken with respect to the position of the node. The net force acting on a node is used with its mass to calculate its acceleration

$$\vec{a} = \vec{F}_{net}/m. \tag{4.61}$$

From the acceleration the nodal velocities are updated, and from the velocities the nodal positions are updated. Integrating over a long enough period of time and including a drag term proportional to the velocity the system to settles into an equilibrium.

Elastic Energy and Force

The elastic energy of the system is the sum of the energy of the linearly elastic springs of the system.

$$U_{el} = \frac{1}{2} \sum_{\alpha \in springs} k_\alpha (l'_\alpha - l_\alpha)^2 \tag{4.62}$$

where the summation is over all the springs in the system, k_α is the stiffness constant of the spring, l'_{alpha} is the current spring length, and l_α is the equilibrium spring length.

The classic spring force term is used.

$$\vec{F}_{el} = -k\left(\|\vec{r}_{ij}\| - r_{ij,0}\right)\hat{r}_{ij} \tag{4.63}$$

where $r_{ij,0}$ is the equilibrium length of the spring, and $\vec{r}_{ij}$ is the vector connecting the two nodes spanned by the spring.

Volume Element Energy and Force

The additional bulk modulus κ is used to relate the relative volume change of the cubic volume elements to the energy

$$U_{VE} = \frac{1}{2}\sum_{\alpha \in elements} \kappa\left(\frac{V_\alpha^{'} - V_\alpha}{V_\alpha}\right)^2, \tag{4.64}$$

where the summation is over all the volume elements of the system, $V_\alpha^{'}$ is the current volume given by Eq. (4.48), and V_α is the volume of the element at initialization, so that $V_\alpha = l_e^3$.

The volume element force uses the average edge vectors, $\vec{a}, \vec{b},$ and $\vec{c}$, defined in Eq. (4.47) and relative volume change to find the force acting on the nodes

$$\vec{F}_a = -\frac{\partial U_{VE}}{\partial \vec{x}_a} = -\kappa(l_e^{-3}\vec{a}\cdot(\vec{b}\times\vec{c}))\frac{\partial V_c^{'}}{\partial \vec{x}_a}, \tag{4.65}$$

where the gradients of $V_c^{'}$ with respect to the positions $\vec{x}_a$of the eight nodes of the volume element are

$$\frac{\partial V_c^{'}}{\partial \vec{x}_1} = \frac{\partial V_c^{'}}{\partial \vec{x}_8} = -(\vec{b}\times\vec{c}) - (\vec{c}\times\vec{a}) - (\vec{a}\times\vec{b}) \tag{4.66}$$

$$\frac{\partial V_c^{'}}{\partial \vec{x}_2} = \frac{\partial V_c^{'}}{\partial \vec{x}_7} = (\vec{b}\times\vec{c}) - (\vec{c}\times\vec{a}) - (\vec{a}\times\vec{b}) \tag{4.67}$$

$$\frac{\partial V_c^{'}}{\partial \vec{x}_3} = \frac{\partial V_c^{'}}{\partial \vec{x}_6} = (\vec{b}\times\vec{c}) + (\vec{c}\times\vec{a}) - (\vec{a}\times\vec{b}) \tag{4.68}$$

$$\frac{\partial V_c^{'}}{\partial \vec{x}_4} = \frac{\partial V_c^{'}}{\partial \vec{x}_5} = -(\vec{b}\times\vec{c}) + (\vec{c}\times\vec{a}) - (\vec{a}\times\vec{b}). \tag{4.69}$$

Since each node can belong to more than one volume element, the net force on the node depends on the contribution of each element it belongs to, in addition to each elastic spring connection.

Magnetic Energies and Force

The magnetic energies of the system are due to the magnetic particles, as the polymer is non-magnetic. By treating the magnetic particles as magnetic dipoles we can use the usual expressions for the energy of a magnetic dipole interacting with an external magnetic field, and for the interaction between magnetic dipoles. The magnetic particles are not permanently magnetized, so some work must be done by the source generating the external magnetic field. We derive an appropriate expression for the magnetostatic self-energy that describes the energy stored in the process of magnetizing the particles.

Zeeman Energy The Zeeman energy is the interaction of the magnetic dipole moment with an external magnetic field, given by

$$U_{Zeeman} = -\mu_0 \sum_{\alpha \in dipoles} \vec{m}_\alpha \cdot \vec{H}_{ext} \tag{4.70}$$

where the summation is over all the dipoles in the system, and $\vec{m}_\alpha$ is the magnetic moment of particle α.

Dipole-Dipole Energy The dipole-dipole energy is the interaction of the magnetic particle dipole moment with other magnetic particles

$$U_{dip-dip} = -\frac{\mu_0}{2} \sum_i \sum_{j \neq i} \vec{m}_i \cdot \vec{H}_{dip,j}(\vec{r_{ij}}) \tag{4.71}$$

where $\vec{r}_{ij} = \vec{r}_i - \vec{r}_j$ points from magnetic particle j to i, the summation is over all the dipoles, and $\vec{H}_{dip,j}$ is the usual magnetic dipole field due to particle j, see Eq. (2.2).

Magnetostatic Self-Energy The magnetic self-energy of the dipoles is derived by following along with Ref. [57] for the energy necessary to polarize a linear dielectric, with the necessary adjustments for the use of the Frohlich-Kenelly law to describe the magnetization response of the magnetic particles using a field dependent magnetic susceptibility, $\chi_{eff}(H)$. While the particles are mutually magnetizing, it is assumed that the work done to magnetize the particles is done by the source of the external magnetic field. The particles are treated as being linearly magnetizable while having an effective magnetic susceptibility given by the term

$$\chi_{eff} = \frac{M_s \chi_0}{M_s + \chi_0 |H_{ext}|} \tag{4.72}$$

This results in the following expression for the magnetic self-energy:

$$U_{self} = \sum_{particles} \frac{\mu_0 \vec{m}_i \cdot \vec{m}_i}{2\chi_0 V M_s} (M_s + \chi_0 |H_{ext}|). \tag{4.73}$$

This expression is analogous to the term used in Chapter 2 for the saturable linear magnetization response. The magnetostatic self-energy term is self-consistent with the dipole-dipole interaction force. When considering the magnetic force as the negative gradient of the magnetic energies, $\vec{F}_{mag} = -\nabla U_{mag} = -\nabla(-\vec{m} \cdot \vec{B}) = \vec{m} \cdot \nabla \vec{B} + \vec{B} \cdot \nabla \vec{m}$, including the Zeeman, dipole-dipole, and magnetostatic self energy terms, the dipole-dipole interaction force is recovered. This expression for magnetostatic self-energy is an approximation that was derived by assuming we could treat the particle as linearly magnetizable despite using the Froehlich-Kenelly magnetization law. An additional assumption is that the magnetic field is uniform over the volume of the particle, and that the resulting magnetization is also uniform. This assumption breaks down when there are multiple magnetic particles with center-to-center separations on the order of the particle diameter. Still, the response of a single particle is anhysteretic, so no energy losses occur. This makes it possible to express the energy stored in the magnetization of the particle as the work done to magnetize it, using Eq. (4.74) and Eq. (4.75).

$$\delta W = \vec{H} \cdot \delta \vec{B} \tag{4.74}$$

$$\vec{B} = \mu_0(\vec{H} + \vec{M}) \tag{4.75}$$

The following expression for the self-energy of the dipoles results in the Froelich-Kennelly law when optimizing the energy of a single magnetic particle in an external field with respect to the particle magnetization.

$$U_{self} = \sum_{particles} \frac{\mu_0 M_s V}{\chi_0} \left[-M + M_s \log\left(\frac{M_s}{M_s - M}\right)\right] \tag{4.76}$$

The author thanks Dr. Martin Gelfand for the discussion regarding this expression for the self-energy term. Solving for the particle magnetization from an energy optimization framework would require the use of (4.76).

Gradient of the Magnetic Field A spatial gradient in the net magnetic field due to external sources and dipolar fields due to other particles results in a force on a magnetic dipole

$$\vec{F} = \vec{m} \cdot \nabla \vec{B}. \tag{4.77}$$

Magnetic Dipole-Dipole Interaction Force The interaction forces among magnetic particles are calculated as the interaction between magnetic dipoles located at the particle centers.

$$\vec{F_{ij}} = \frac{3\mu_0}{4\pi r_{ij}^5}\left[(\vec{m_i}\cdot\vec{r_{ij}})\vec{m_j} + (\vec{m_j}\cdot\vec{r_{ij}})\vec{m_i} + (\vec{m_i}\cdot\vec{m_j})\vec{r_{ij}} - \frac{5(\vec{m_i}\cdot\vec{r_{ij}})(\vec{m_j}\cdot\vec{r_{ij}})}{r_{ij}^2}\vec{r_{ij}}\right] \tag{4.78}$$

Volume Exclusion Energy and Force The volume exclusion energy is used as a steric repulsion term to keep the magnetic particles' volumes from overlapping. The purely repulsive Weeks-Chandler-Andersen potential is used, which is a modification of the Lennard-Jones potential.

$$E_{\text{WCA}} = \begin{cases} 0 & \text{for } S > r_{\text{cut}} \\ 4E_{\text{max}}((\frac{r_{\text{min}}}{S})^{12} - (\frac{r_{\text{min}}}{S})^{6} + \frac{1}{4}) & \text{for } S \leq r_{\text{cut}} \end{cases} \tag{4.79}$$

This results in a force given by,

$$\vec{F}_{\text{WCA}} = -\nabla E_{\text{WCA}} = \begin{cases} 0 & \text{for } S > r_{\text{cut}} \\ 4E_{\text{max}}(12(\frac{r_{\text{min}}^{12}}{S^{13}}) - 6(\frac{r_{\text{min}}^{12}}{S^{7}})) & \text{for } S \leq r_{\text{cut}} \end{cases} \tag{4.80}$$

where $E_{max} = \mu_0 \pi M_s^2 R_{particle}^3/72$ (maximum dipole-dipole interaction energy assuming the particles are magnetically saturated, their magnetizations are aligned parallel, and the center to center separation is $2R_{particle}$. We use $r_{min} = 2R_{particle} + 100$ nm and $r_{cut} = 2^{\frac{1}{6}} r_{min}$. This force acts to repel the particles from one another, and can be considered the elastic term associated with the interaction between particles that come into contact with one another.

Force on a Magnetic Particle

When the dipole-dipole interaction force or volume exclusion force is calculated for a magnetic particle, the net force is distributed among all nodes that are part of that magnetic particle to ensure rigid body translation. The magnetic isotropy of the particles ensures that the magnetization is what rotates to align with the external magnetic field, and not the particle itself. The elastic and volume element forces are not distributed across all particle nodes in the same way. By allowing the elastic forces to maintain the rigidity of the magnetic particles, rotation of the particle can occur due to interaction with the surrounding medium.

Viscous Force

To allow the system to settle into a minimum energy configuration a drag term needs to be included to remove kinetic energy from the system as it evolves to a lower energy configuration. The drag force is

$$\vec{F}_{drag} = -\eta \vec{v}. \tag{4.81}$$

The drag coefficient η is not related to any physical properties or constants, and is set such that the value after scaling will be unity.

4.2.5 Numerical Integration

The system is simulated to find the minimum energy configuration given the applied magnetic field and boundary conditions. This is done by writing down a system of ordinary differential equations (ODEs) using Newton's second law and numerically solving for the nodal positions at a discrete sequence of times from some starting configuration. This is an initial value problem (IVP). Over a long enough sequence of time steps the system will settle into a stable configuration that is a local energy minimum. In classical mechanics, Newton's second law states that the acceleration of a particle is proportional to the net force and inversely proportional to the mass.

$$\vec{F}_{net} = m\vec{a} = m\frac{\partial^2 \vec{x}}{\partial t^2}. \tag{4.82}$$

Netwon's second law is a second order differential equation. By introducing a helper function, it is possible to convert (4.82) into a set of 6N first order differential equations, where N is the number of particles in the system, 3N for the positions and 3N for the velocities, with

$$\frac{\partial \vec{x}}{\partial t} = \vec{v} \tag{4.83}$$

$$\frac{\partial \vec{v}}{\partial t} = \frac{\vec{F}_{net}}{m}. \tag{4.84}$$

This problem can then be handled by numerically solving a system of first order differential equations for the nodal positions and velocities. To determine the time-evolution of the problem, we simply need to know the nodal positions and velocities at a time $t = t_0$, and the forces acting on the nodes must be calculated. The solution to the ordinary differential equations can be approximated in the area around the current known solution by a Taylor series expansion.

Discretizing Time: Taylor Series Approach to ODE Solvers

The following sections discussing numerical integration methods are drawn in part from Ref. [84], but any texts regarding general numerical methods should cover these topics.

One method for approximating the time dependent position of the nodes of the system is to write down a Taylor series expansion of the position around some time t. The Taylor series is a power series expansion and representation of a continuously differentiable function.

$$f(x) = \sum_{n=0}^{\infty} \frac{(x-a)^n}{n!} f^{(n)}(a) = f(a) + (x-a)f^{'}(a) + \frac{(x-a)^2}{2!} f^{''}(a) + ...$$

This expansion approximates the value of a function at x, in a neighborhood around a, in terms of the value of the function and its derivatives at a. Keeping many terms will decrease the truncation error, but increase the number of functions which will need to be evaluated. Higher order methods should reduce this source of error and allow for the use of larger time steps, and there are methods available which use adaptive time steps to reduce the runtime of simulations.

Euler's Method Euler's method is the simplest method of numerical integration for an ordinary differential equation. It can be derived as a truncated Taylor expansion with only two terms into which the ODE is inserted

$$f(t + \Delta t) = f(t) + \Delta t \cdot \partial_t f(t) + \mathcal{O}(\Delta t^2), \tag{4.85}$$

where ∂_t is the partial derivative with respect to time, $f(t)$ is the solution at time t, $f(t + \Delta t)$ is the solution at the next time we want to find, Δt is the time step, and $\mathcal{O}(\Delta t^2)$ are terms with Δt^2 and higher.

The Euler method is first order in time, and so the local error is on the order of the size of the time step. This means that if we halve the time step size the error should go down by a factor of two. If the time step is too large, the method will not be stable. In terms of our nodal positions and velocities we have

$$x(t + \Delta t) = x(t) + v(t)\Delta t \tag{4.86}$$

$$v(t + \Delta t) = v(t) + a(t)\Delta t. \tag{4.87}$$

Leapfrog Method The leapfrog method updates velocity and position with the same time step size but offset from one another by $\Delta t/2$.

$$x(t + \Delta t) = x(t) + \Delta t \cdot v(t + \Delta t/2) \tag{4.88}$$

$$v(t + \Delta t/2) = v(t - \Delta t/2) + \Delta t \cdot a(x(t), t) \tag{4.89}$$

The leapfrog method is globally second-order accurate [84]. This can be seen by substituting Eq. (4.89) into Eq. (4.88), which yields

$$\begin{aligned} x(t + \Delta t) &= x(t) + \Delta t \cdot [v(t - \frac{\Delta t}{2}) + \Delta t \cdot a(x(t), t)] && (4.90)\\ &= x(t) + \Delta t \cdot [v(t) - \frac{\Delta t}{2} \cdot a(x(t), t) + \Delta t \cdot a(x(t), t)] && (4.91)\\ &= x(t) + \Delta t \cdot v(t) + \frac{\Delta t^2}{2} \cdot a(x(t), t)\ . && (4.92) \end{aligned}$$

This is the Taylor expansion truncated after the third term. This works because of time reversibility of the Taylor series expansion

$$f(t + \Delta t) = f(t) + \Delta t \cdot \partial_t f(t) \quad \text{and} \quad f(t - \Delta t) = f(t) - \Delta t \cdot \partial_t f(t). \tag{4.93}$$

The leapfrog method improves the global error bound, giving a second order method without having to increase the number of function evaluations from what is required with the explicit Euler method. To kickstart the leapfrog method, an explicit Euler step is made to update the velocity and get $v(t + \Delta t/2)$, at which point the leapfrog updates for position and velocity can alternate. The leapfrog method was used for numerical integration in the modeling results presented in this chapter.

Convergence Criteria

To determine when to stop the numerical integration, some check must be done on the state of the system to see if it is still evolving. The accelerations and velocities of the nodes are the objects of interest. The rigid particle springs are ignored when considering the convergence of the system, as the nodes comprising the particle may oscillate with strong accelerations about their equilibrium separation without causing significant changes to the positions of the particles or the deformation of the surrounding polymer. If the magnitudes of the velocity components are below some threshold, the system will be considered to have converged to a solution. To calculate this threshold, we consider the limitations of working with floating point representations, which are discrete, of real numbers, which are continuous.

Floating Point Precision and Convergence Checking Floating point numbers represent real numbers with a finite number of binary digits. Due to the finite number of digits it is not possible to encode the continuous range of real numbers. Instead, only discrete values are possible. There is a finite difference between the current number represented via floating point, and the next or previous representable floating point number. Round-off error is the difference between the machine representation of the number and the actual number. This error can creep into every non-trivial floating point instruction [84]. Care has to be taken when working with floating point arithmetic, as different representations of the same analytical expression can give different results. Floating point arithmetic can suffer from a lack of associativity, so that the order in which you add terms in a sum can effect the end result. Subtraction of two numbers close in magnitude can result in large errors due to loss of significant bits. Finally, accumulation stagnation is the addition of two numbers, one large and one small, where the result is just the large number. We use the existence of accumulation stagnation to determine what the smallest acceleration or velocity of a node could be, given the fixed time step size, such that the product of the two would not result in an update to the position or velocity of the node upon addition to the current position or velocity. This is estimated

by considering the initialized positions of the nodes, and the average difference between that value and the next largest representable floating point number for the entire set of nodal positions.

4.2.6 Computation

The implementation is done in Python[4], using Python 3.10.12 in a virtual environment for package management. Cython[5] is an "optimising static compiler" using a superset of Python to generate code with performance similar to C, and was used early on the development process for calculating forces, and for initializing the system, and is still used for the initialization process. CuPy[6] is a package that provides an interface for implementing CUDA code within a Python program with lower friction. CUDA, compute unified device architecture, is an API developed by Nvidia[7] for general purpose GPU computing on their GPU devices. CuPy was used to write functions to handle the entirety of the simulation process, except for the check on convergence of the system, initialization, and input and output. CUDA kernels were written to calculate the elastic, volume element, dipole-dipole, and volume exclusion forces. CUDA kernels were also written to handle the numerical integration, determine the positions of particles, and the algorithm for magnetization solving. CUDA kernels were also written for the analysis, to calculate the different energies of the system. The use of general purpose GPU (GPGPU) computing was important in achieving reasonable run time for simulations of systems of reasonable size. Matplotlib[8] was used to generate the figures in this chapter.

Parallelization and GPGPU Computing

In order to achieve reasonable runtimes and make best use of the available computing hardware the model implementation was moved from CPU bound to GPU based computations. While

[4]https://www.python.org/

[5]https://cython.org

[6]https://cupy.dev/

[7]https://developer.nvidia.com/cuda-toolkit

[8]https://matplotlib.org/

parts of the program are sequential in nature, the update of nodal positions and velocities is parallelizable, as well as the calculation of the forces associated with each spring and each volume element. The act of summing those forces to get the net forces on the nodes does require the use of atomic functions. Atomic operations are used to prevent race conditions, and are used to handle the accumulation of the sum of forces. A race condition is when one part of the program accesses a value stored in memory and updates it, while another thread simultaneously accesses the value and updates it, overwriting the first update. For the parts of the program that are mostly sequential it was still necessary to port the functionality onto the GPU. While the architecture may not be best suited to those sequential operations, the act of moving memory between CPU and GPU imposes significant overhead. By moving the majority of the program onto the GPU, the speedups from the parts of the problem that can be done in parallel are preserved.

Scaling

Scaling of length and time quantities occurs in the implementation to improve numerical stability and performance. The characteristic length of the system is $x_c = l_e$, and the characteristic time, t_c is given by considering the period of simple harmonic oscillation for a polymer node in the interior volume displaced slightly from equilibrium

$$t_c = T = 1/f = 2\pi/\omega = 2\pi\sqrt{m/k_{eff}}. \tag{4.94}$$

So that the characteristic time is determined by the nodal mass of a polymer node, and the effective stiffness it experiences for a displacement along one of the axes, considering the contributions from the 26 spring connections the node has and their orientations relative to the direction of displacement

$$k_{eff} = 2k_e + 8k_f/\sqrt{2} + 4k_c\ . \tag{4.95}$$

The time step size reported in the results section is given in units of the characteristic time. Accelerations are scaled by $\beta = t_c^2/l_e$. The drag coefficient is set to equal unity after scaling.

4.2.7 Simulation Types

There are different simulation types which differ in terms of the application of magnetic fields and the boundary conditions used. There are three main categories of simulations: hysteresis, stress, and strain simulations. While stress based simulations were implemented, none of the results in this chapter are from stress simulations.

Hysteresis

Hysteresis simulations begin at zero field and apply a sequence of magnetic fields. The nodal positions and particle magnetization are passed forward at the end of one simulation step, which has a fixed magnetic field vector, to the next in the sequence.

Strain

Strain simulations are defined by the strain type, strain values, and boundary conditions. For a sequence of applied magnetic fields, the system starts with zero applied strain and at the lowest magnetic field value and passes the nodal positions and magnetization forward to the next when the system has converged to a stable state. For a sequence of applied strains at a given field, the system starts from the configuration found at that field with zero strain, using both the nodal positions and particle magnetization.

Tension and Compression Tension and compression have similar boundary conditions, such that for tension or compression along an axis, the surfaces which have surface normals in the direction of that axis are held fixed. For example, if a 1% tensile strain is applied along the x-axis, the surface nodes with $x = 0$ are held fixed, and the nodes at $x = L_x$ are moved and held fixed at $x = Lx(1 + 0.01)$. The other surface nodes are free.

Simple Shear Under the simple shear boundary conditions, all surfaces are held fixed. When a non-zero shear strain is applied, the appropriate surface nodes experience a translation related to

their height relative to the relevant surface and the shearing angle.

$$|\vec{u}| = h(\vec{x}) \tan(\gamma) \tag{4.96}$$

As seen in (4.96), the magnitude of the displacement of the surface node depends on the tangent of the shearing angle γ and the height h of the node. For example, a shear strain applied to the top surface of the system at $z = L_z$ in the $\hat{x}$ direction has a height defined by the surface node's z position, and is displaced in the positive $\hat{x}$ direction and then held fixed. Meanwhile, the bottom surface at $z = 0$ is held fixed.

Stress

Stress based simulations have a stress boundary condition which means an additional force is prescribed on one or more surfaces of the system. The motion of the magnetic particles within the elastic matrix due to an applied magnetic field lead to uneven forces distributed over the stressed surface, and non-uniform displacement of the nodes of the stressed surface. This produces some ambiguity in defining the strain on the system, but allows magnetostriction to be observed, as well as the impact of particle rearrangement on the surface. Analysis of stress based simulations based on changes in energy density is possible, though the fit to the stress-energy density curve would provide the compliance of the material, which is the inverse of the stiffness.

Boundary Conditions

For any simulation, boundary conditions must be defined. The boundary conditions applied will significantly affect the outcome of a simulation and the results of any analysis. Strain based boundary conditions are Dirichlet boundary conditions, and fix the value of the displacement of surface nodes. In all results in this chapter, Dirichlet boundary conditions are used.

Strain boundary conditions for tension, compression, and simple shearing cases are implemented. Torsion boundary conditions are also implemented, but not explored. Boundary conditions for hysteresis simulations hold all surface nodes fixed. If surface nodes are not held fixed, or

if only one surface has nodes held fixed, then magnetostriction is observed as a result of particle motion.

4.2.8 Analysis

Field Dependent Effective Modulus

Analysis of the effective modulus of the system is done by applying a series of strain values as Dirichlet boundary conditions and finding the equilibrium configuration of the system. To calculate the total energy of the system, we need to consider the elastic and volume element energies, as well as the particle-particle volume exclusion energy (WCA), the interaction of the particles' magnetic moments with the external field, the dipole-dipole interactions, and the self energy of the induced magnetic moments.

$$U_{total} = U_{elastic} + U_{VE} + U_{Zeeman} + U_{dipole-dipole} + U_{self} + U_{WCA}$$

For a fixed applied magnetic field, the energy density of the system is calculated by considering the volume element, spring, dipole, Zeeman, self and WCA energies.

We assume that the strain-energy density of the system is at a minimum when the applied strain is zero, for any applied magnetic field, and convex with respect to the applied strain. For small perturbations about that equilibrium the response of the system is analogous to a simple harmonic oscillator, and well approximated by a quadratic expression. The error in the strain-energy density is on the order of $O(\varepsilon^3)$. The coefficient of the first order term is taken to be zero, as the strain-energy density is at a minimum. This leaves us with an expression of the form

$$u(\varepsilon) = \frac{1}{2} E_{eff} \varepsilon^2 + c$$

where we assume the quadratic coefficient is the effective modulus of the system, in analogy to the strain-energy density of a uniformly strained, isotropic homogeneous linear elastic medium.

By calculating the total energy of the simulated system as a function of the applied strain for a fixed field, the resulting (strain-energy density, strain) points can be plotted. We determine the effective modulus by a nonlinear least squares fitting procedure to the quadratic expression. In this way, we seek to study the magnetic field dependence of the effective modulus of particular strain types, and the dependence on particle microstructure.

4.3 Results

The work presented in the following sections covers two distinct aspects of magnetoactive polymers: their magnetic hysteresis, and their field responsive stiffness. We first explore magnetic hysteresis in simple systems. Magnetoactive polymers made of ultrasoft polymers with magnetically soft filler have a characteristic pinched loop hysteresis shape, which can be qualitatively captured under certain dipole based models. In contrast to this, our model demonstrates qualitatively different magnetic hysteresis, demonstrating significant remanent magnetization and magnetization switching, suggesting that other mechanisms besides reversible particle clustering can occur and play a role in the macroscopic magnetic hysteresis of MAPs. The second section discusses the field responsive stiffness changes in MAP-like systems experiencing shear strains. A dependence on the volume fraction of magnetic particles, Φ, for the size of the field stiffening effect is observed. Additionally, the dependence on applied magnetic field orientation is explored for a chain of four magnetic particles. Finally, a 3D helical arrangement of eight magnetic particles is studied, which demonstrates complex dependence of field stiffening effect size on the radius of the helix, as well as the importance of the details of particle rearrangement on the micro-scale in the field stiffening effect.

4.3.1 Two Particle Hysteresis Hybrid Mass Spring System

We begin with a simple system, two magnetically soft particles embedded in a linearly elastic matrix. While real systems are composed of large numbers of particles (for example, in a 3% volume fraction sample with a volume of 1 mm^3, there would be roughly 1 mm$^3 \times 0.03/V_{particle} \approx$

2×10^6 particles), the clustering of magnetically soft particles demonstrated here is the source of the characteristic shape of the magnetic hysteresis of ultrasoft polymers with magnetically soft filler. The major reason to focus on small numbers of magnetic particles and small system dimensions are the demands on computational resources like RAM, and GPU VRAM, as well as the runtime. These smaller systems can be run, analyzed, and used to provide feedback for future directions of exploration in time scales on the order of hours. Additionally, focusing on small systems provides a test case to compare against our intuition for expected behavior of simple problems, and demonstrates the behavior and capabilities of the model.

The simulation parameters used are as follows: $E = 9$ kPa, which corresponds to the softest MRE sample used in Chapter 3, $\nu = 0.47$, a Poisson ratio for a nearly incompressible material, $D = 3$ μm, the same magnetic particle size used in Chapter 2 and Chapter 3, $\Phi = 1\%$, $S = 11.1818$ μm, $l_e = 0.2727$ μm, $L_x = L_y = 11.1818$ μm, $L_z = 22.3636$ μm, $\delta t = 5 \times 10^{-3}$.

The external magnetic field is applied along the z-axis. For all hysteresis results presented, the chosen boundary conditions hold the surfaces of the systems fixed, $\vec{u} = 0$, where $\vec{u}$ is the displacement field. The system is composed of 146,412 nodes, $(42\times42\times83)$, and 137,842 volume elements, $(41 \times 41 \times 82)$, the particle diameter is 11 volume elements, and the discretization order is $n_d = 5$. The edge length of the volume elements is determined by the discretization order, n and particle diameter in SI units, through the expression $l_e = D/(2n + 1)$. A 3D view of the outer surfaces of the system can be seen in Figure 4.3a, along with visualization of the initial configuration of particles and particle nodes in Figure 4.3b-d.

In Figure 4.4a the particles move closer together as the external magnetic field is increased, but do not cluster. In Figure 4.4b the overall magnetization response is a smoothly increasing magnetization along the external field direction, with the slope decreasing as the particle magnetization approaches saturation. As the external field strength is decreased the magnetization decreases and the particles stay slightly closer together compared to the upward leg until the external field strength is reduced to zero. The particle separation shows some hysteresis that is not visible in the magnetization with these axis limits, but which must also be present.

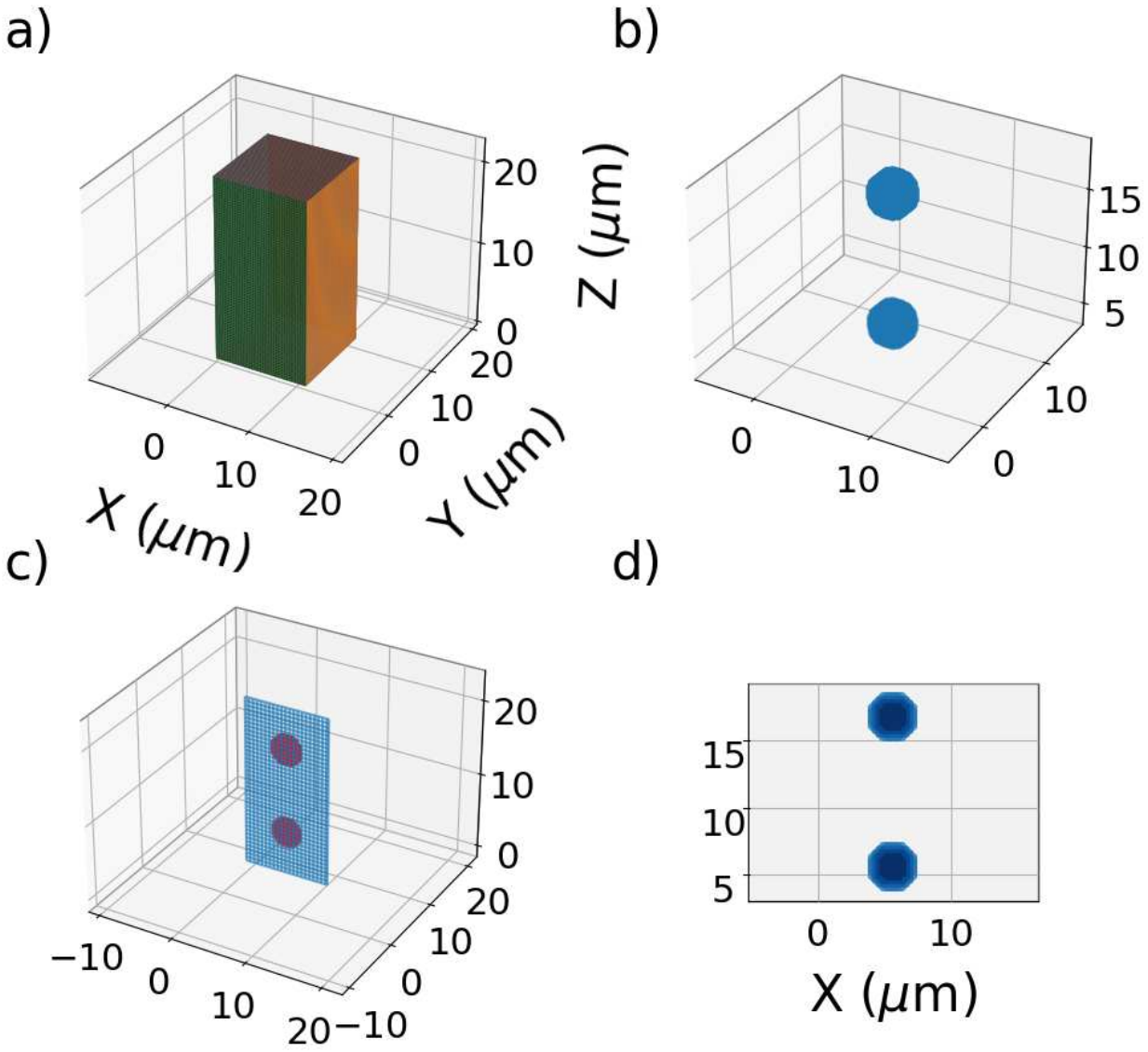

Figure 4.3: a) Outside view of initial system configuration for $\Phi = 1\%$, b) scatter plot of the nodes that belong to the magnetic particles within the system, c) wireframe of a cut at constant y at a position approximately halfway through the thickness of the system, with red markers denoting the nodes within the magnetic particles, d) scatter plot of particle nodes where the shade indicates depth, with the darker shade meaning the node is closer to the viewer.

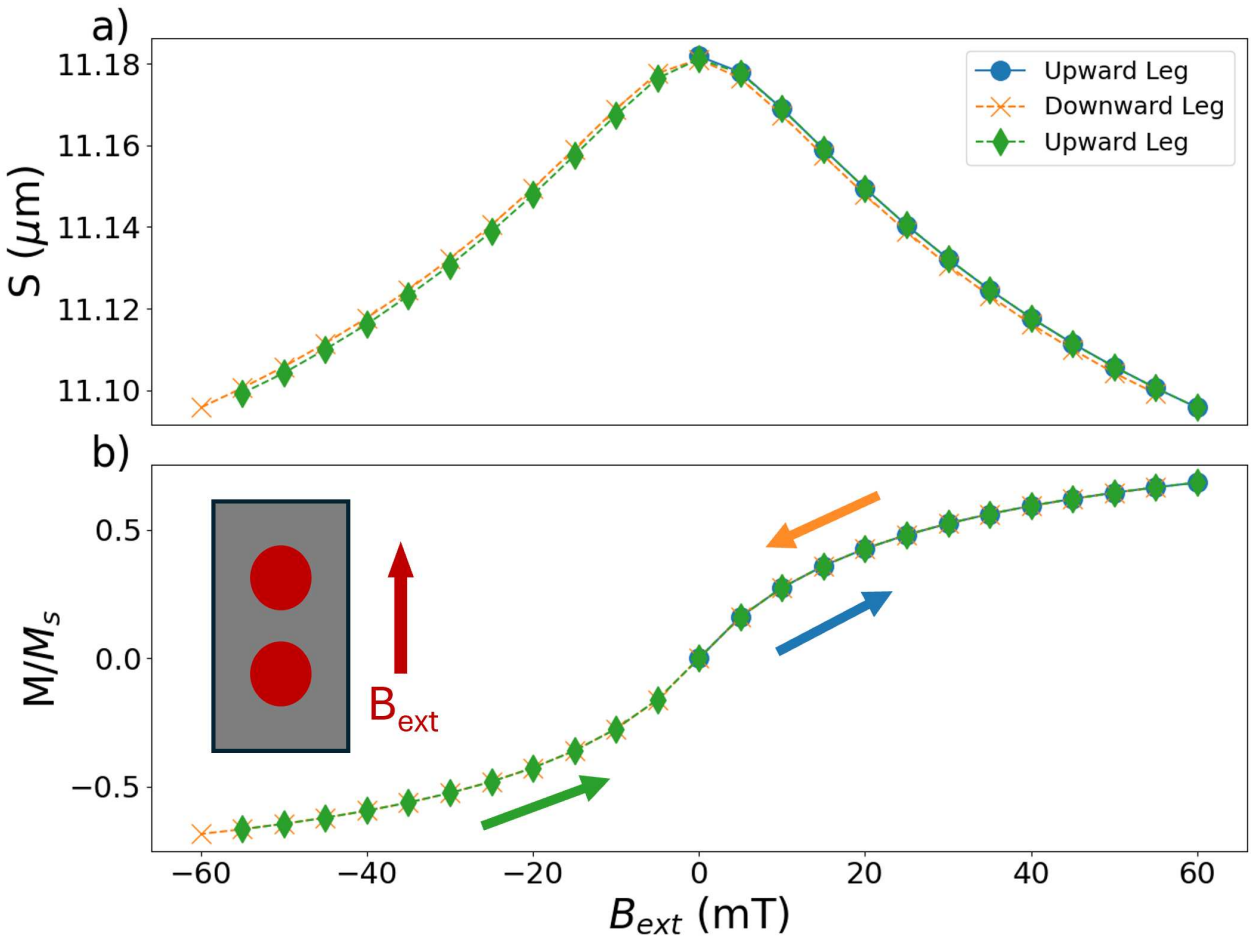

Figure 4.4: (a) Center-to-center particle separations and (b) normalized magnetization of the two particle system versus external field, shown for the case of $E = 9$ kPa, $\nu = 0.47$, $\chi = 70$, $M_s = 1.6 \times 10^6$ A/m, $D = 3$ μm, $n_d = 5$, $\Phi = 1\%$, $S = 11.18$ μm, with the external field applied along the axis connecting the particles. The solid arrows in b) illustrate the initial (blue), downward (orange), and upward (green) legs of the hysteresis loop, and the inset of b) shows a diagram of the particle arrangement and the direction of $\vec{B}_{ext}$.

If we increase Φ, we first observe minor changes. Simulation parameters are as follows: $E = 9$ kPa, $\nu = 0.47$, $D = 3\ \mu$m, $\Phi = 3\%$, $S = 7.909\ \mu$m, $l_e = 0.2727\ \mu$m, $L_x = L_y = 7.909\ \mu$m, $L_z = 15.5454\ \mu$m, $\delta t = 5 \times 10^{-3}$. The system is composed of 52,200 nodes, $(30 \times 30 \times 58)$, and 47,937 volume elements, $(29 \times 29 \times 57)$, the particle diameter is 11 volume elements, and the discretization order is $n_d = 5$.

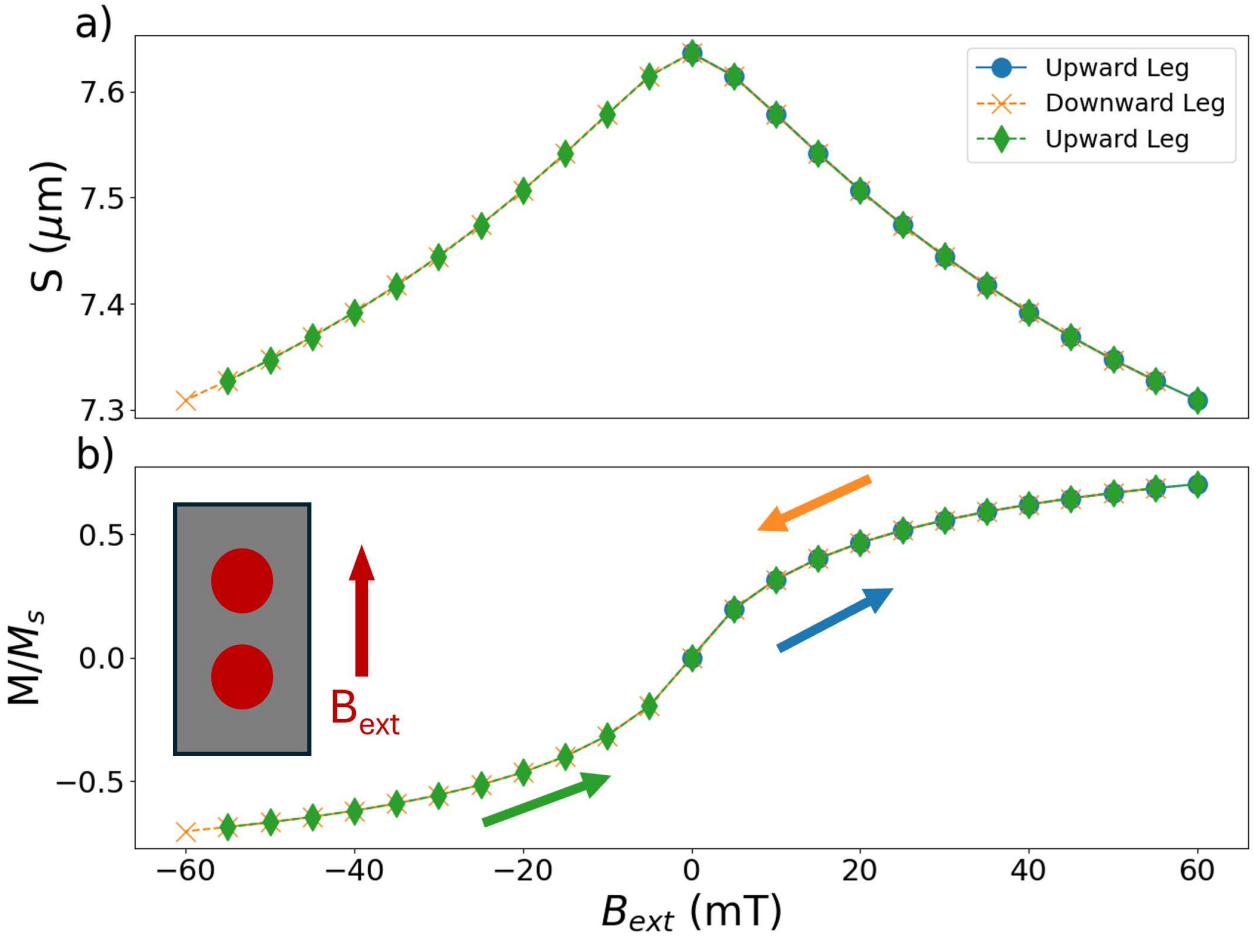

Figure 4.5: (a) Center-to-center particle separations and (b) normalized magnetization of the two particle system versus external field, shown for the case of $E = 9$ kPa, $\nu = 0.47$, $\chi = 70$, $M_s = 1.6 \times 10^6$ A/m, $D = 3\ \mu$m, $n_d = 5$, $\Phi = 3\%$, $S = 7.909\ \mu$m, with the external field applied along the axis connecting the particles. The solid arrows in b) illustrate the initial (blue), downward (orange), and upward (green) legs of the hysteresis loop, and the inset of b) shows a diagram of the particle arrangement and the direction of $\vec{B}_{ext}$.

In Figure 4.5, the particles approach as the external magnetic field is increased, and move further than when $\Phi = 1\%$. The overall magnetization response shows a smoothly increasing

magnetization along the external field direction, with a steeper initial slope. As the external field strength is decreased the magnetization slowly decreases and the particles separate as the external field strength is reduced to zero. The particle motion shows less, if any hysteresis compared to $\Phi = 1\%$.

If we increase Φ to 5% the particles travel further, but do not cluster. Simulation parameters are as follows: $E = 9$ kPa, $\nu = 0.47$, $D = 3$ μm, $\Phi = 5\%$, $S = 6.5454$ μm, $l_e = 0.2727$ μm, $L_x = L_y = 6.5454$ μm, $L_z = 13.0909$ μm, $\delta t = 5 \times 10^{-3}$. The time step, δt, and material parameters have remained constant, while Φ increases, and the system dimensions, and S, have decreased. The system is composed of 30,625 nodes, $(25 \times 25 \times 49)$, and 27,648 volume elements, $(24 \times 24 \times 48)$, the particle diameter is 11 volume elements, and the discretization order is $n_d = 5$.

In Figure 4.6, the particles approach as the external magnetic field is increased, and move further than when $\Phi = 3\%$. The overall magnetization response shows a smoothly increasing magnetization along the external field direction, with a steeper initial slope. As the external field strength is decreased the magnetization slowly decreases and the particles separate as the external field strength is reduced to zero.

When we increase Φ to 7% we observe a categorical shift in the behavior of the system. Simulation parameters are as follows: $E = 9$ kPa, $\nu = 0.47$, $D = 3$ μm, $\Phi = 7\%$, $S = 5.7272$ μm, $l_e = 0.2727$ μm, $L_x = L_y = 6$ μm, $L_z = 11.7272$ μm, $\delta t = 5 \times 10^{-3}$. The system is composed of 23,276 nodes, $(23 \times 23 \times 44)$, and 20,812 volume elements, $(22 \times 22 \times 43)$, the particle diameter is 11 volume elements, and the discretization order is $n_d = 5$. A 3D view of the outer surfaces of the system for $\Phi = 7\%$ can be seen in Figure 4.7a, along with visualization of the initial configuration of particles and particle nodes in Figure 4.7b-d.

As seen in Figure 4.8, the particles approach as the external magnetic field is increased, and at a critical field value somewhere between 35 and 40 mT come as close together as possible given volume exclusion. The overall magnetization response shows a smoothly increasing magnetization along the external field direction, with a jump when the particles collapse onto one another. As the external field strength is decreased, the magnetization slowly decreases, and the particles stay in

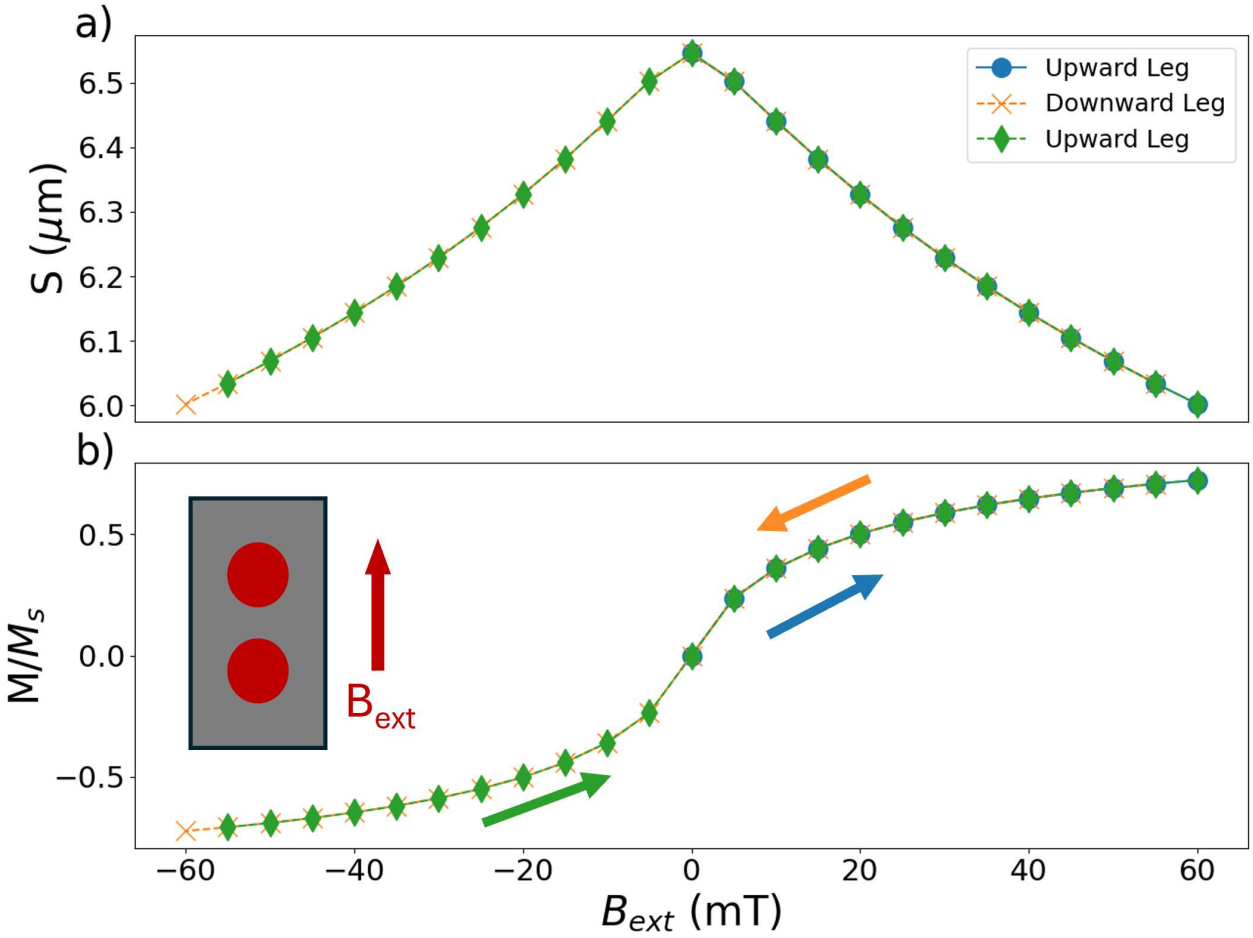

Figure 4.6: (a) Center-to-center particle separations and (b) normalized magnetization of the two particle system versus external field, shown for the case of $E = 9$ kPa, $\nu = 0.47$, $\chi = 70$, $M_s = 1.6 \times 10^6$ A/m, $D = 3$ μm, $n_d = 5$, $\Phi = 5\%$, $S = 6.5454$ μm, with the external field applied along the axis connecting the particles. .The solid arrows in b) illustrate the initial (blue), downward (orange), and upward (green) legs of the hysteresis loop, and the inset of b) shows a diagram of the particle arrangement and the direction of $\vec{B}_{ext}$. The particles remain well separated for all B_{ext}.

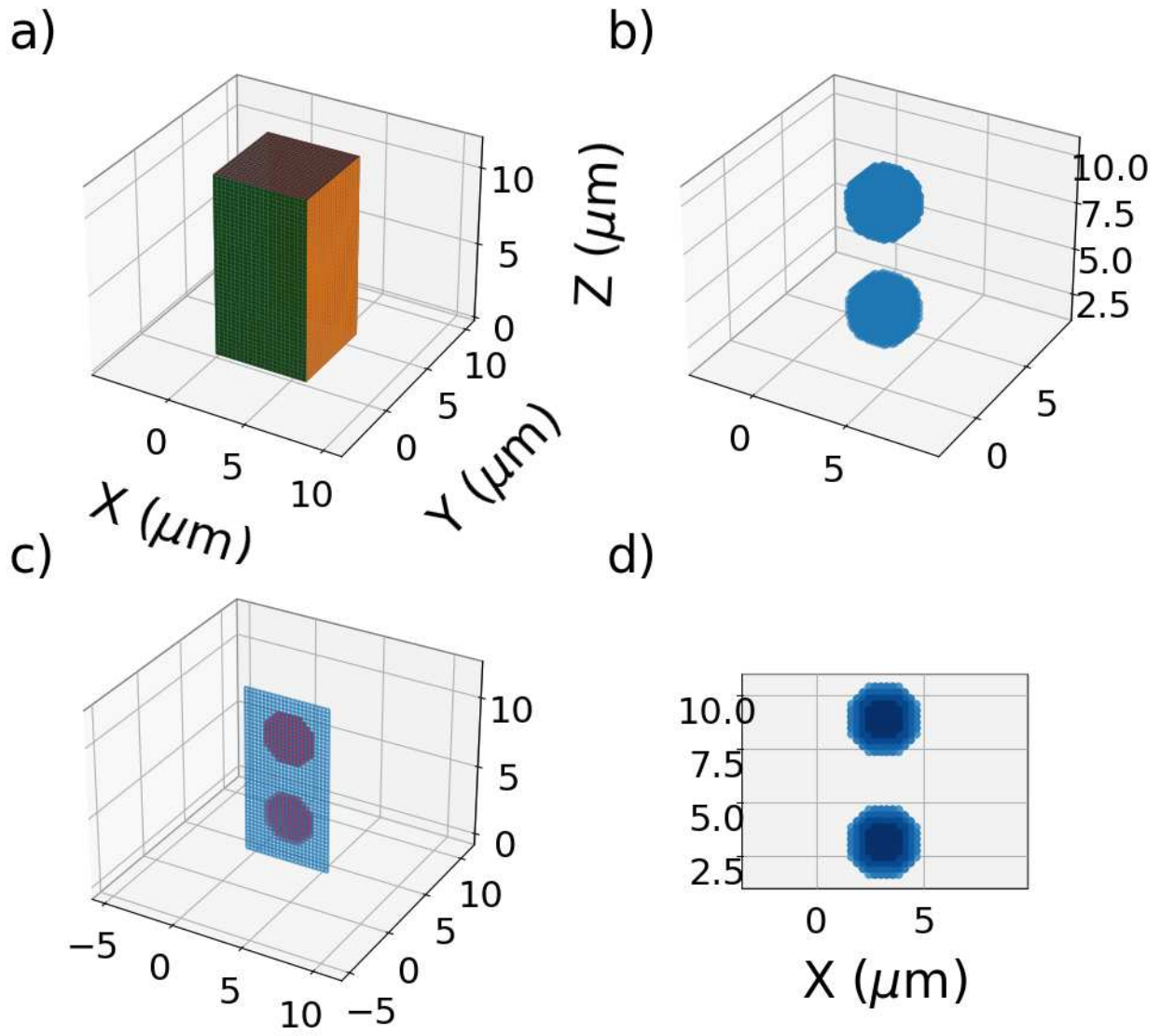

Figure 4.7: a) Outside view of initial system configuration for $\Phi = 7\%$, b) scatter plot of the nodes that belong to the magnetic particles within the system, c) wireframe of a cut at constant$y$at a position approximately halfway through the thickness of the system, with red markers denoting the nodes within the magnetic particles, d) scatter plot of particle nodes where the shade indicates depth, with the darker shade meaning the node is closer to the viewer.

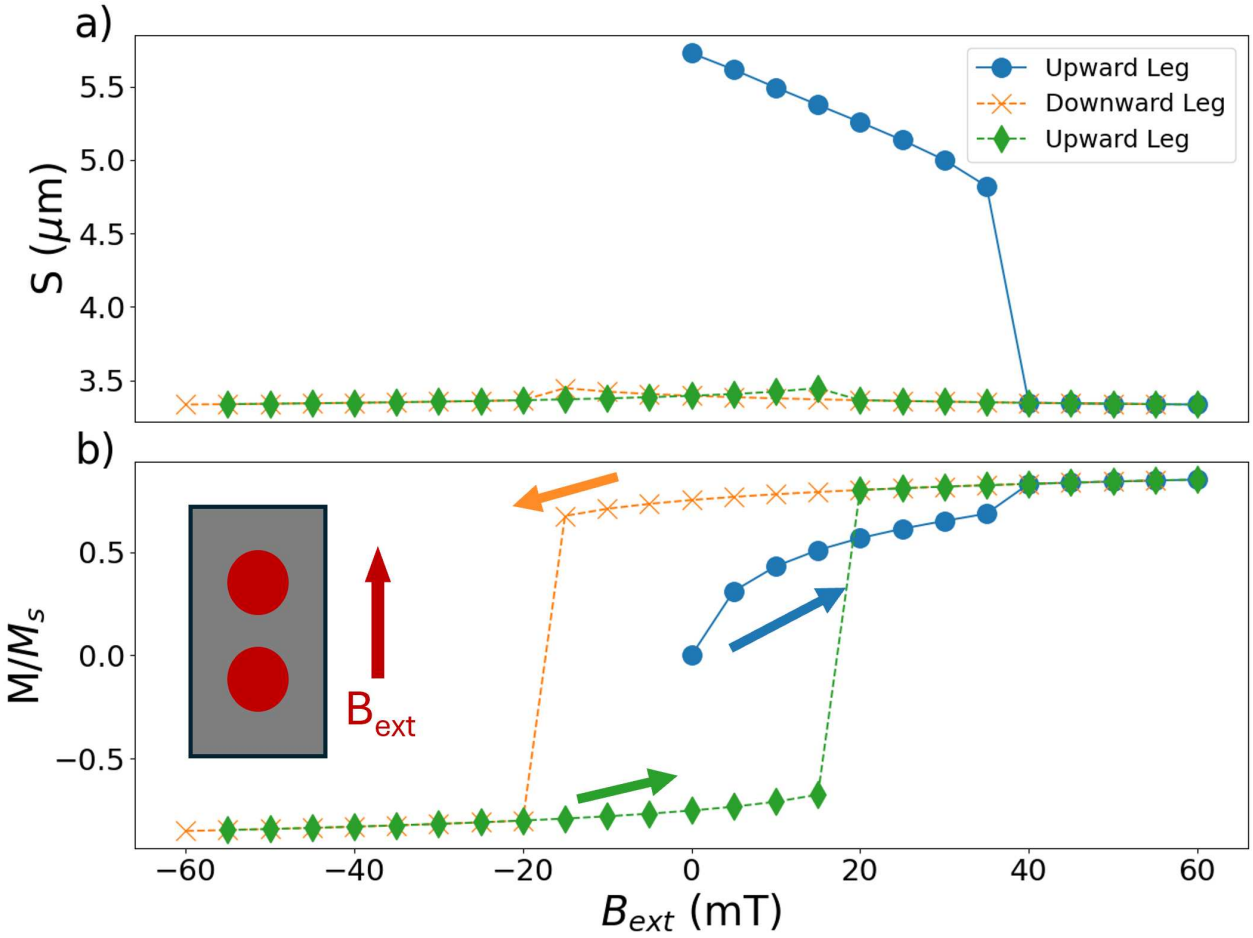

Figure 4.8: (a) Center-to-center particle separations and (b) normalized magnetization of the two particle system versus external field, shown for the case of $E = 9$ kPa, $\nu = 0.47$, $\chi = 70$, $M_s = 1.6 \times 10^6$ A/m, $D = 3$ μm, $n_d = 5$, $\Phi = 7\%$, $S = 5.7272$ μm, with the external field applied along the axis connecting the particles. The solid arrows in b) illustrate the initial (blue), downward (orange), and upward (green) legs of the hysteresis loop, and the inset of b) shows a diagram of the particle arrangement and the direction of $\vec{B}_{ext}$. The particles initially cluster together at 40 mT, with a separation around 3.35 μm.

their collapsed configuration even as the external field strength is reduced to zero, and continues to $-B_{ext,max}$. The particle pair remains magnetized as the external field is reduced to zero, displaying strong remanence, and a switching field (similar to the Stoner-Wohlfarth model of hysteresis) somewhere between 15 and 20 mT. This behavior is symmetrically reproduced in the upward leg from $-B_{ext,max}$ to $+B_{ext,max}$. The particle motion, and the particles achieving the collapsed configuration, results in magnetic hysteresis that is not present when the anhysteretic Froehlich-Kennelly magnetization law is used to model the magnetic response of each particle individually, see Figure 1.6. The magnetization response is also different from a macroscopic hard ferromagnet, where the magnetization would appear to smoothly pass through $M = 0$, which would define the coercive field. Instead, the pair of particles have their magnetization flip orientation at some critical field in a behavior similar to that seen in the Stoner-Wohlfarth model of hysteresis.

We will turn now to the same $\Phi = 5\%$ system, now with the external magnetic field applied in the $\hat{x}$ direction, perpendicular to the vector from one particle to the other. All other simulation parameters are the same as before. Figure 4.9 shows that the particles move to be farther apart, as expected of two magnetic dipoles with parallel dipole moments placed side-by-side. The initial slope of the magnetization curve is lower than for the attractive condition, Figure 4.6, because the dipolar field of each magnetic particle that acts on the other is in the direction opposite to the external magnetic field. This leads to a reduction in the magnetization of each particle as compared to the attractive condition where the dipole fields add to the external field.

Varying Φ while keeping the number of particles fixed altered the overall size of the system. Since the boundary conditions were chosen such that the outer surface nodes remain fixed in place, there could be an impact on the effective stiffness the particles experience while moving within the polymer matrix due to proximity to a fixed surface or surfaces. To control for this effect, a series of two particle simulations with a fixed system size and varying particle separation were performed, with particle separations closely matching those of the earlier results where Φ was varied with the field oriented parallel to the axis joining the particles.

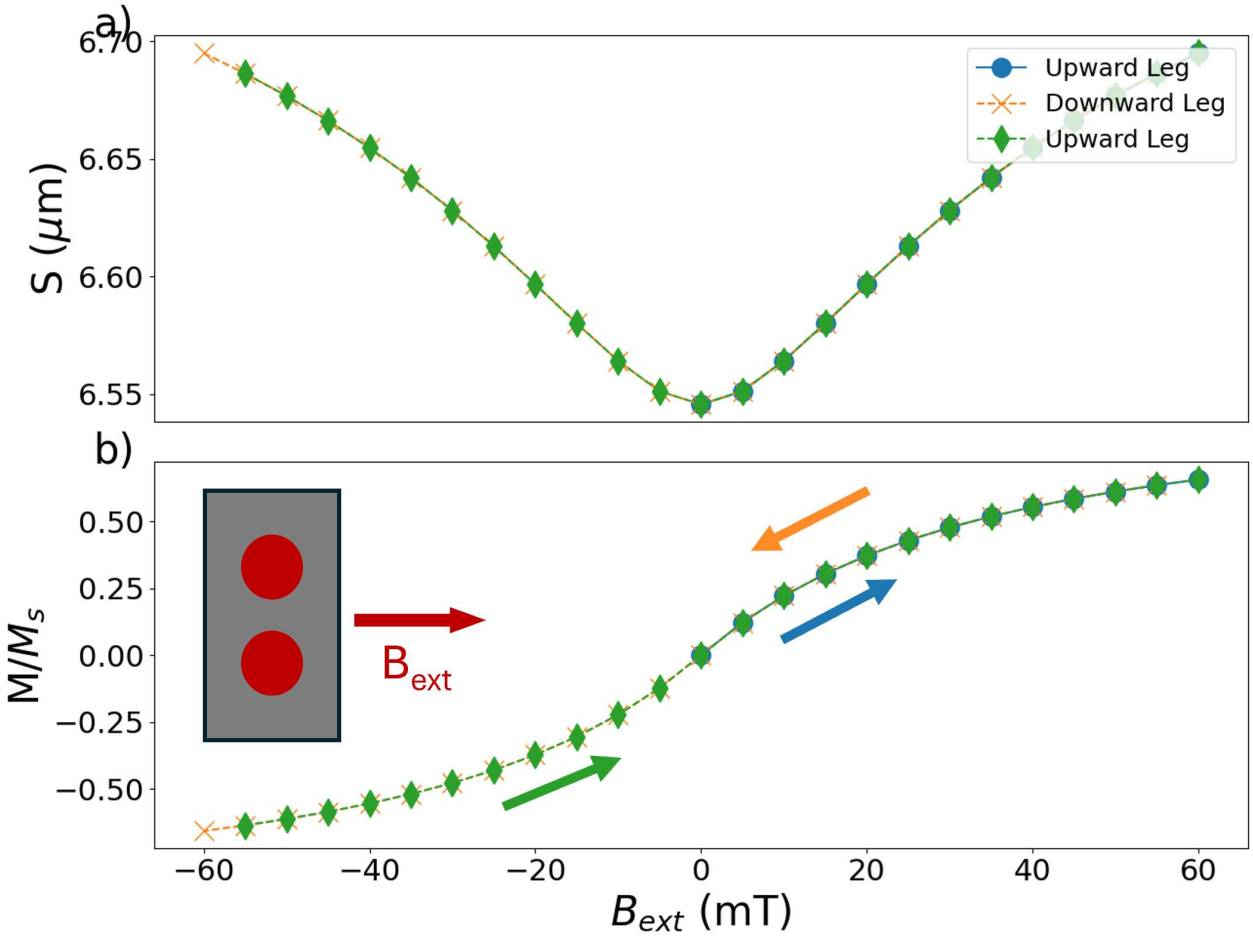

Figure 4.9: (a) Center-to-center particle separations and (b) normalized magnetization of the two particle system versus external field, shown for the case of $E = 9$ kPa, $\nu = 0.47$, $\chi = 70$, $M_s = 1.6 \times 10^6$ A/m, $D = 3$ μm, $n_d = 5$, $\Phi = 5\%$, $S = 6.5454$ μm, with the $\vec{B}_{ext}$ applied perpendicular to the axis connecting the particles. The solid arrows in b) illustrate the initial (blue), downward (orange), and upward (green) legs of the hysteresis loop, and the inset of b) shows a diagram of the particle arrangement and the direction of $\vec{B}_{ext}$.

We now present results for the two particle case with a larger overall system size. An initial separation of $S = 6.5454$ μm, comparable to that present in the $\Phi = 5\%$ case was used. A 3D view of the outer surfaces of the system can be seen in Figure 4.10a, along with visualization of the initial configuration of particles and particle nodes in Figure 4.10b-d. When we run the equivalent separation for the $\Phi = 5\%$ case, we find some significant differences with a larger system and more distance from any fixed surfaces.

The simulation parameters are as follows: $E = 9$ kPa, $\nu = 0.47$, $D = 3$ μm, $\Phi = 0.516\%$, $S = 6.5454$ μm, $l_e = 0.2727$ μm, $L_x = L_y = 11.7272$ μm, $L_z = 39.8181$ μm, $\delta t = 5 \times 10^{-3}$. The system is composed of 284,592 nodes, $(44 \times 44 \times 147)$, and 269,954 volume elements, $(43 \times 43 \times 146)$, the particle diameter is 11 volume elements, and the discretization order is $n_d = 5$.

As seen in Figure 4.11, as B_{ext} is initially increased from zero, the particles cluster between 25 and 30 mT, have remanent magnetization when the field is returned to 0 mT and stay clustered together, and flip their magnetization between -20 and -25 mT. When compared to Figure 4.6 for the $\Phi = 5\%$ with $S = 6.5454$ μm case, which lacks particle clustering and magnetic hysteresis, this result highlights the importance in the choice of boundary conditions and the size of the simulation in the effective stiffness experienced by the magnetic particles as they rearrange within the polymer matrix. With greater distances from the fixed surfaces in the $\Phi \approx 0.5\%$ and $S = 6.5454$ μm case, the effective stiffness is lowered in a manner which should be asymptotic to the value achieved in an infinite elastic medium, and the particles are more free to move. It is reasonable to expect that additional magnetic particles would also act to constrain the rearrangement of the particles due to volume exclusion.

Figure 4.12a shows the configuration of particles and the resulting deformation of the surrounding polymer matrix for a plane of nodes whose initial positions are at a constant y value, about halfway through the system, at +25 mT. Figure 4.12b shows the same at +30 mT when the particles are strongly clustered. The particles are constrained by the surrounding polymer matrix, and their motion deforms the polymer matrix in the surrounding volume, stretching in some places, and compressing in others, dragging along some portions on the sides in a shearing motion. When

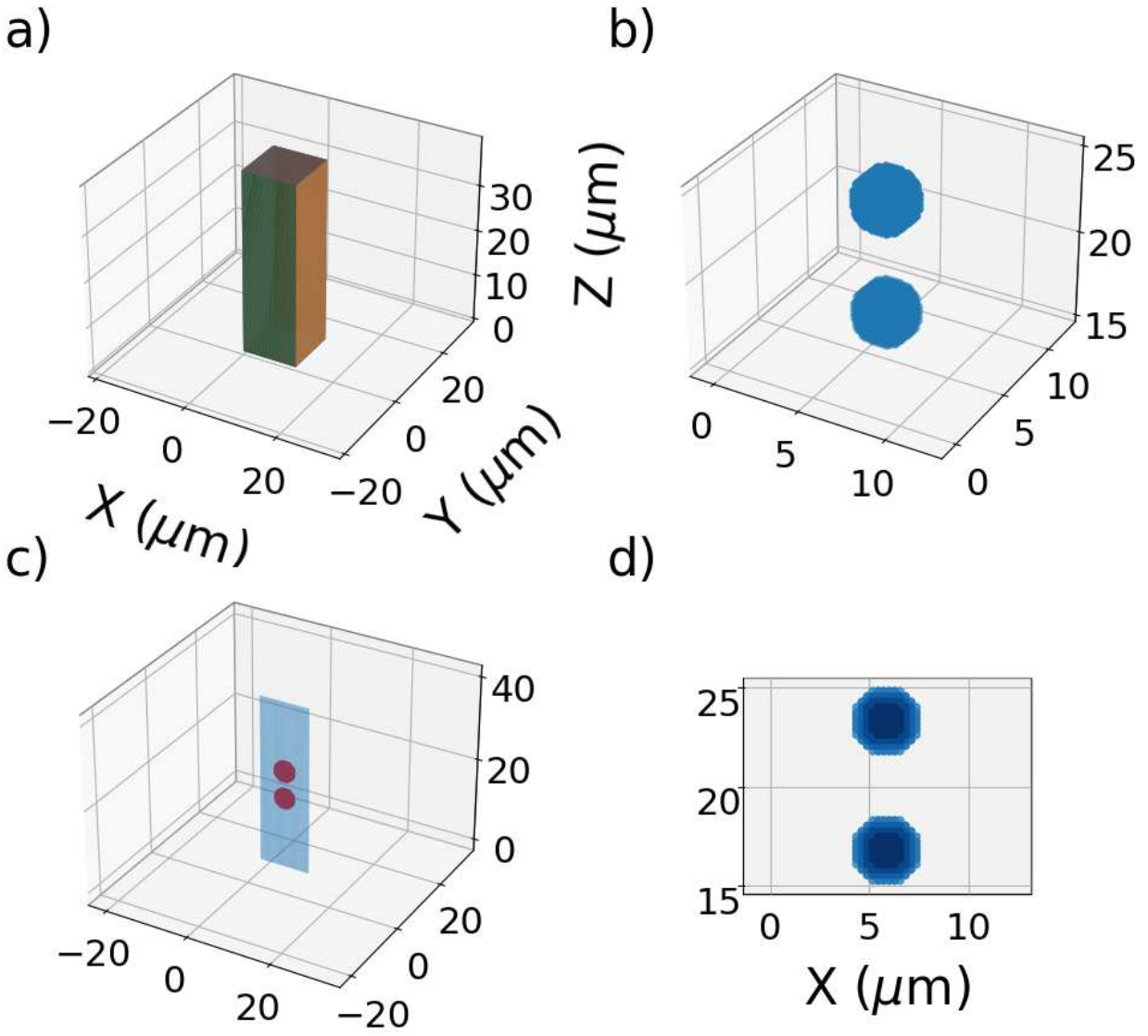

Figure 4.10: a) Outside view of initial system configuration, b) scatter plot of the nodes that belong to the magnetic particles within the system, c) wireframe of a cut at constant$y$at a position approximately halfway through the thickness of the system, with red markers denoting the nodes within the magnetic particles, d) scatter plot of particle nodes where the shade indicates depth, with the darker shade meaning the node is closer to the viewer.

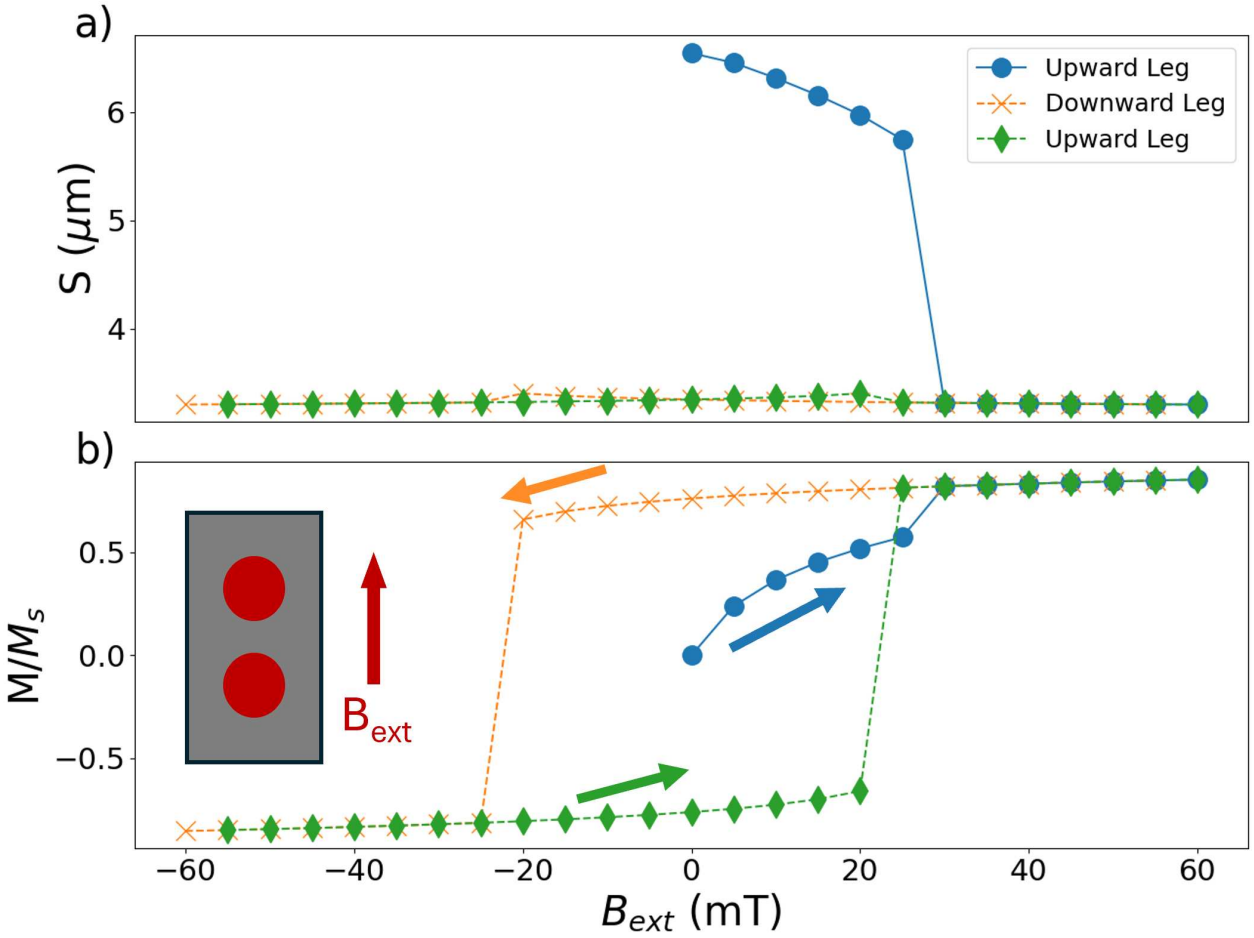

Figure 4.11: (a) Center-to-center particle separations and (b) normalized magnetization of the two particle system versus external field, shown for the case of $E = 9$ kPa, $\nu = 0.47$, $\chi = 70$, $M_s = 1.6 \times 10^6$ A/m, $D = 3$ μm, $n_d = 5$, $\Phi = 0.516\%$, $S = 6.5454$ μm, with the external field applied along the axis connecting the particles. The solid arrows in b) illustrate the initial (blue), downward (orange), and upward (green) legs of the hysteresis loop, and the inset of b) shows a diagram of the particle arrangement and the direction of $\vec{B}_{ext}$.

the particles cluster, the polymer matrix between them is strongly compressed. In this model, the strongly compressed interstitial volume deforms in a way that distorts the volume elements from their initially cubic shape. This breakdown is one limitation of the model approach, which uses an approximation to calculate the volume change of the elements. Future work would seek to capture the nonlinear response of the material to compressive strains that should diverge as the strain values approach 100%.

When we run an almost equivalent separation for the $\Phi = 7\%$ case ($S = 5.4545$ μm instead of $S = 5.7272$ μm), we find some significant differences with a larger system and more distance from any fixed surfaces. Simulation parameters are as follows: $E = 9$ kPa, $\nu = 0.47, D = 3$ μm, $\Phi = 0.516\%, S = 5.4545$ μm, $l_e = 0.2727$ μm, $L_x = L_y = 11.7272$ μm, $L_z = 39.8181$ μm, $\delta t = 5 \times 10^{-3}$. The system is composed of 284,592 nodes, $(44 \times 44 \times 147)$, and 269,954 volume elements, $(43 \times 43 \times 146)$, the particle diameter is 11 volume elements, and the discretization order is $n_d = 5$.

Figure 4.13a shows that the particles cluster as soon as there is a non-zero magnetic field, and the switching field at which the particle magnetizations flip is between -25 and -30 mT in Figure 4.13b, compared to the -15 to -20 mT observed in the $\Phi = 7\%$ case, Figure 4.8. When comparing to Figure 4.11, where the overall system size is the same, but the initial particle separation is larger, an increase in particle separation shifts the field at which clustering occurs upward in magnitude, and the switching field is larger for smaller separations. The requirement for a stronger B_{ext} when the initial separation increases was expected, but the existence of switching behavior was unpredicted, as was the dependence of the switching field on initial separation.

Work by Gundermann *et al*. [69] using x-ray computed microtomography showed irreversible particle clustering in an MRE after the removal of the external magnetic field. The results shown in Figure 4.8, Figure 4.11 and Figure 4.13 seem to demonstrate a similar phenomenon. So how does this sort of irreversible clustering and the appearance of remnant magnetization fit into the experimentally measured macroscopic pinched magnetic hysteresis loop shape? It seems plausible that there are some configurations of particles, separations, and local effective stiffness that

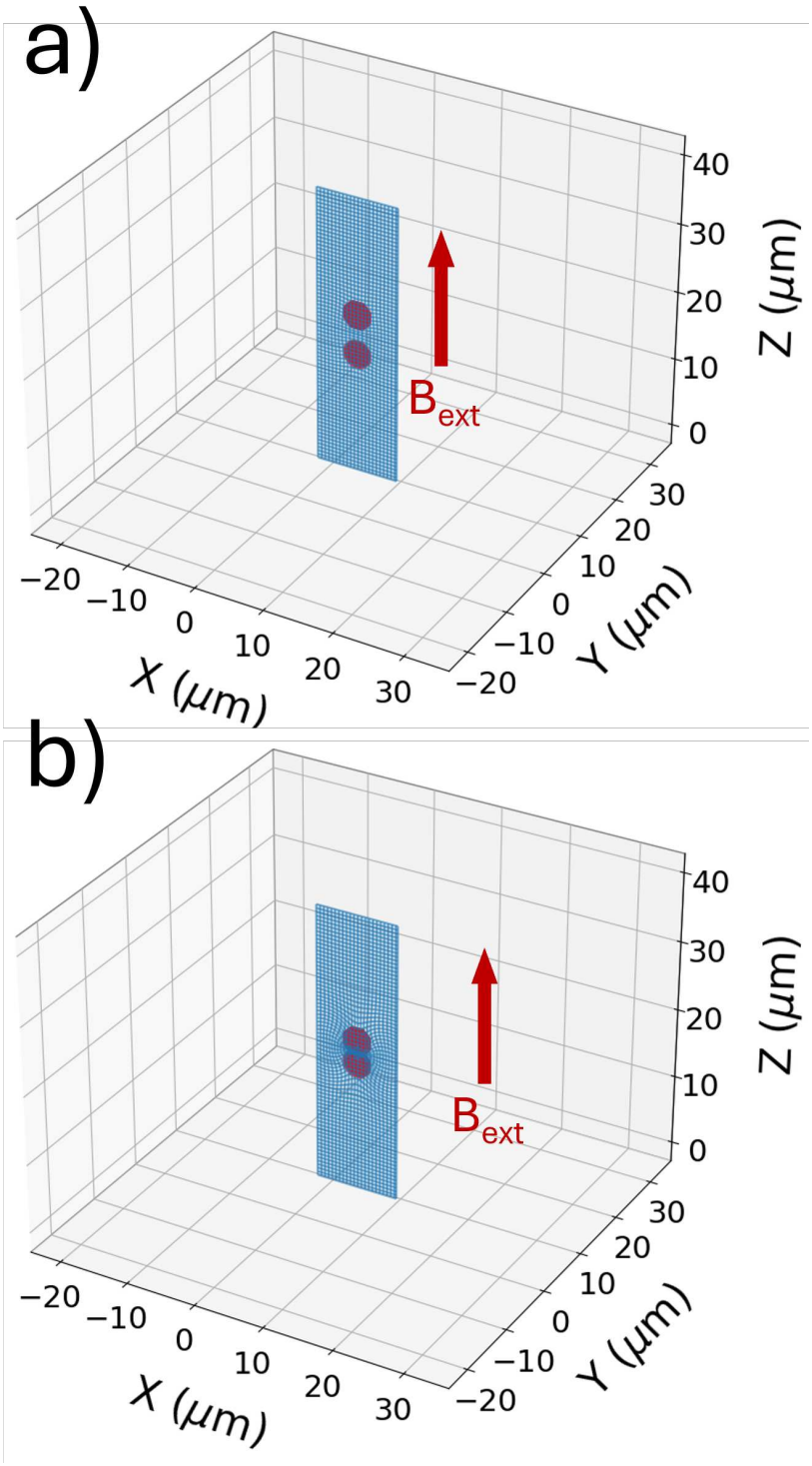

Figure 4.12: Wireframe plots of a cut of the system for nodes initialized at a constant y at a position approximately halfway through the thickness of the system at a) +25 mT and b) +30 mT of the first upward leg, with red markers denoting the nodes within the magnetic particles, shown for the case of $E = 9$ kPa, $\nu = 0.47$, $\chi = 70$, $M_s = 1.6 \times 10^6$ A/m, $D = 3$ μm, $n_d = 5$, $\Phi = 0.516\%$, $S = 6.5454$ μm, with the external field applied along the axis connecting the particles.

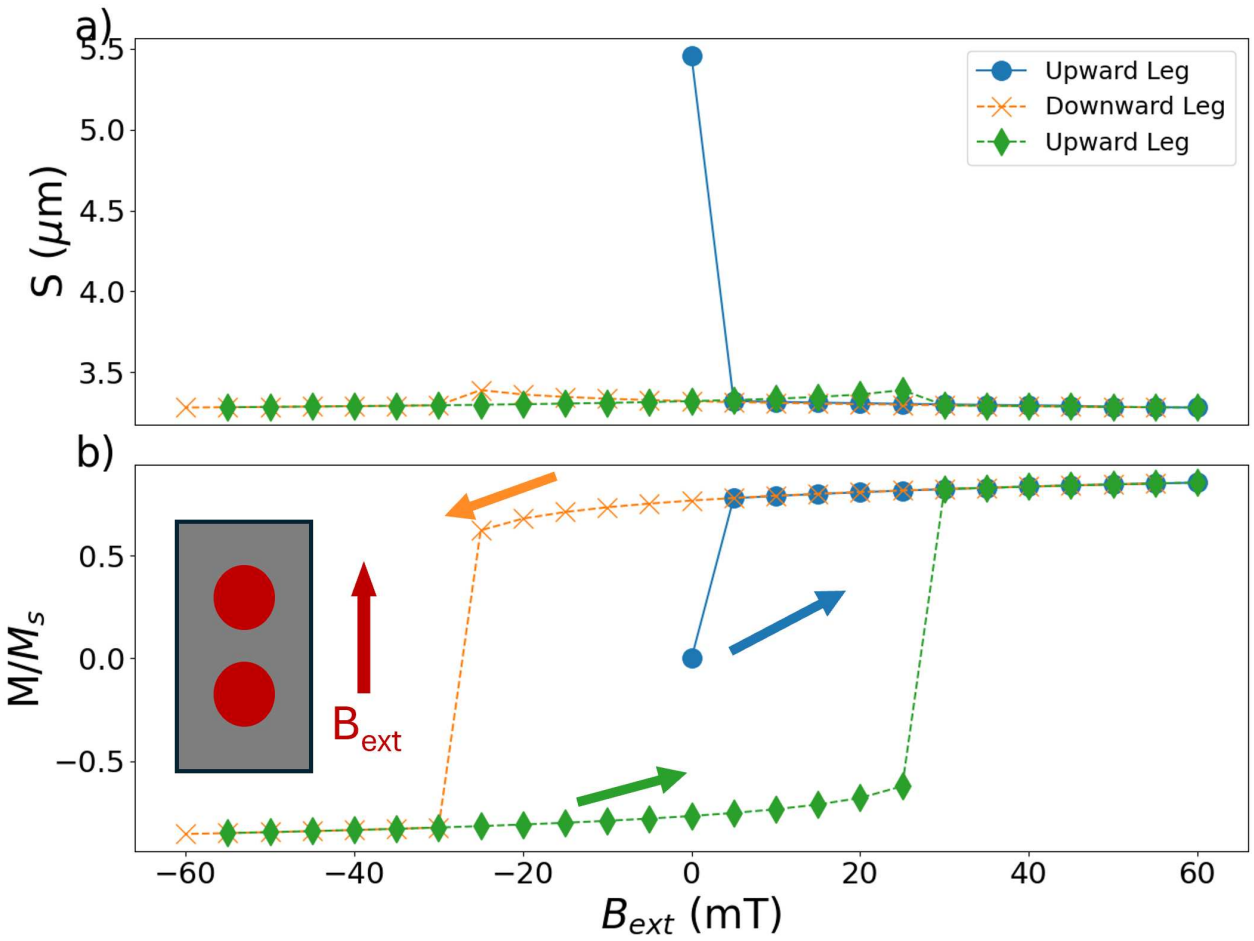

Figure 4.13: a) Center-to-center particle separations and b) normalized magnetization of the two particle system versus external field, shown for the case of $E = 9$ kPa, $\nu = 0.47$, $\chi = 70$, $M_s = 1.6 \times 10^6$ A/m, $D = 3$ μm, $n_d = 5$, $\Phi = 0.516\%$, $S = 5.4545$ μm, with the external field applied along the axis connecting the particles. The solid arrows in b) illustrate the initial (blue), downward (orange), and upward (green) legs of the hysteresis loop, and the inset of b) shows a diagram of the particle arrangement and the direction of $\vec{B}_{ext}$.

do allow the particles to cluster, but also under a weakened or removed external magnetic field to reversibly separate. The magnetization of these clusters could also rotate with the particle clusters as the field is weakened, maintaining the magnetization due to shape anisotropy and mutual magnetizing effects, but reoriented as the polymer matrix relaxes into a less stressed/deformed state as the external field weakens. Future work is necessary to explore this hypothesis.

4.3.2 Effective Shear Modulus

Magnetoactive polymers and magnetorheological elastomers experience changes in stiffness under the effect of an applied magnetic field. The increase in the effective modulus of the material may be referred to as the magnetorheological effect, or MR effect, and given in terms of a percentage increase compared to the original value. Anisotropic MREs with the external magnetic field applied along the direction of anisotropy, and with a shear strain applied perpendicular to the chain direction, are expected to show large changes in effective stiffness. We begin by studying a two particle system for the sake of simplicity in interpreting the results, and to limit computational expense.

Two Particle Model

The behavior of a pair of magnetic particles is investigated under the effect of an external magnetic field applied parallel to the particle placement, while the system undergoes a simple shear. Under the simple shear boundary conditions, all surfaces are held fixed. When a non-zero shear strain is applied, all surface nodes experience a translation related to their height relative to the relevant surface and the shearing angle, see Eq. (4.96) and Figure 1.8c.

For all cases shown here, unless noted otherwise, the external magnetic field is applied in the $\hat{z}$ direction, and the particles are aligned along the $\hat{z}$ direction.

Volume Fraction and the Field Stiffening Effect

One important question for designing MREs for engineering applications is how the volume fraction of magnetic particles, Φ, impacts the effective stiffness of the MRE. To address this ques-

tion, we begin by looking at the field dependence of the stiffness of the simulated volume for $\Phi = 3, 4$ and 6%, and then move to studying the effect of Φ on the field-dependent stiffness and the magnitude of the magnetorheological effect over a broader range of values from $\Phi \approx 1\%$ to 20% at external magnetic fields $B_{ext} = 0$ mT and $B_{ext} = 140$ mT.

The simulation parameters are as follows: $E = 9$ kPa, $\nu = 0.47, D = 3\ \mu$m, $\Phi = 3\%, S = 7.909\ \mu$m, $l_e = 0.2727\ \mu$m, $L_x = L_y = 7.909\ \mu$m, $L_z = 15.5454\ \mu$m, $\delta t = 5 \times 10^{-3}$. The system is composed of 52,200 nodes, $(30 \times 30 \times 58)$, and 47,937 volume elements, $(29 \times 29 \times 57)$, the particle diameter is 11 volume elements, and the discretization order is $n_d = 5$. The shear strain was applied by applying Eq. (4.96) to update the positions of surface nodes based on the applied shear strain, γ, those surface nodes are then held fixed.

Figure 4.14a-f shows the individual energies of the $\Phi = 3\%$ system when $B_{ext} = 0$ mT. Only the volume element and spring energies vary with the applied strain, and strictly increase. Figure 4.14g shows the energy density of the system as a function of applied strain when $B_{ext} = 0$ mT, as well as a fit line using the parameters from fitting the dataset to Eq. (4.2.8). The fit shows good agreement with the dataset, and G_{eff} is found to be ≈ 4 kPa. The value of G for the polymer itself can be found in terms of E and ν as $G = E/(2(1+\nu)) = 3.061$ kPa. The inclusion of rigid magnetic particles reinforces the system even in the absence of a magnetic field.

Figure 4.15a-f shows the individual energies of the $\Phi = 3\%$ system when $B_{ext} = 80$ mT. The volume element and spring energies vary with the applied strain, but in this case the volume element energy decreases with increased shear strain and deviates from a quadratic shape around $\gamma = 0.1$. The rearrangement of the particles compresses the polymer between the particles, and the shearing seems to relieve some of the deformation associated with volume changes of the volume elements. The Zeeman, dipole-dipole, and magnetic self energies all maintain a quadratic-looking dependence on shear strain, where the Zeeman and dipole-dipole energies increase with increasing strain, and the magnetic self energy decreases with increasing applied strain. The decrease in magnetic self energy is proportional to a decrease in the squared magnitude of the magnetizations of the particles. The increase in Zeeman energy can be due to a decrease in the magnetization

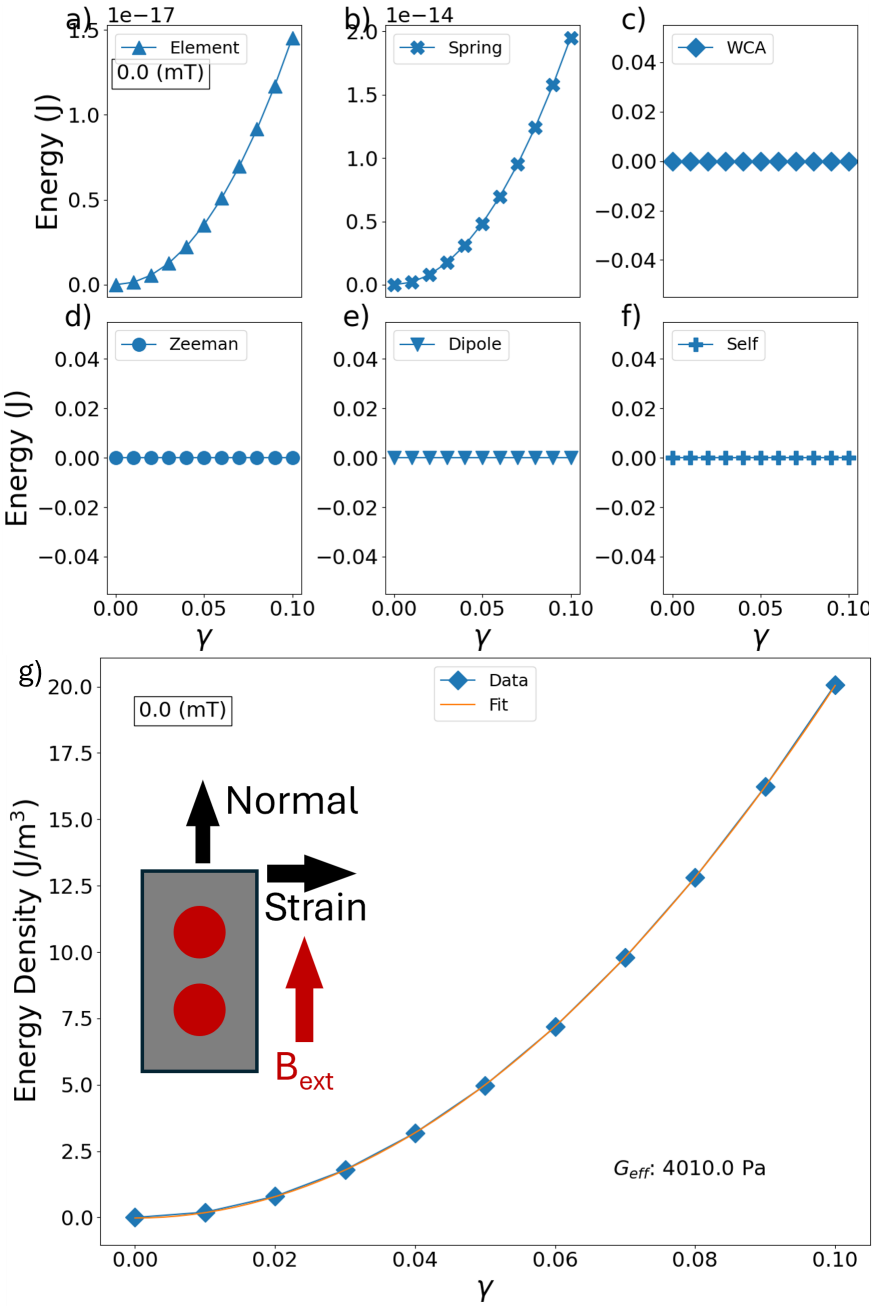

Figure 4.14: Plots of individual energies (a-f) and total energy density (g) versus applied strain when $B_{ext} = 0$ mT. a) Energy associated with volumetric strain of the volume elements, b) energy associated with the deformation of linear springs, c) energy associated with particle-particle elastic interactions, or volume exclusion energy, d) Zeeman energy due to the particle magnetization interaction with the external magnetic field, e) dipole-dipole energy due to the interaction of the particle magnetization with the dipolar field of the other particle, f) magnetic self energy related to the work done to magnetize the particles, g) the total energy density curve, with the approximate effective modulus, and a fit curve made from using the parameters found by fitting the energy density versus strain data. Results shown for the case of $E = 9$ kPa, $\nu = 0.47$, $\chi = 70$, $M_s = 1.6 \times 10^6$ A/m, $D = 3$ μm, $n_d = 5$, $\Phi = 3\%$, $S = 7.909$ μm, with the external field applied along the axis connecting the particles.

magnitude, and deviation from alignment with B_{ext}. Decrease in the dipole-dipole energy is due to weaker dipole fields proportional to the magnetization magnitude and alignment of the magnetizations with those fields. Figure 4.15g shows the energy density of the system as a function of applied strain when $B_{ext} = 80$ mT, as well as a fit line using the parameters from fitting the dataset to Eqn. (4.2.8). The fit shows good agreement with the dataset, and G_{eff} is found to be ≈ 5 kPa. The energy density curve maintains a quadratic-looking dependence on the shear strain, despite the additional magnetic energies, and the magnetic field has had a stiffening effect on the system.

For the $\Phi = 4\%$ simulation, the parameters that were used are as follows: $E = 9$ kPa, $\nu = 0.47, D = 3\ \mu$m, $\Phi = 4\%, S = 7.0909\ \mu$m, $l_e = 0.2727\ \mu$m, $L_x = L_y = 7.0909\ \mu$m, $L_z = 14.1818\ \mu$m, $\delta t = 5 \times 10^{-3}$. The system is composed of 38,637 nodes, $(27 \times 27 \times 53)$, and 35,152 volume elements, $(26 \times 26 \times 52)$, the particle diameter is 11 volume elements, and the discretization order is $n_d = 5$.

For the $\Phi = 6\%$ simulation, the parameters that were used are as follows: $E = 9$ kPa, $\nu = 0.47, D = 3\ \mu$m, $\Phi = 6\%, S = 6.2727\ \mu$m, $l_e = 0.2727\ \mu$m, $L_x = L_y = 6.2727\ \mu$m, $L_z = 12.2727\ \mu$m, $\delta t = 5 \times 10^{-3}$. The system is composed of 26,496 nodes, $(24 \times 24 \times 46)$, and 23,805 volume elements, $(23 \times 23 \times 45)$, the particle diameter is 11 volume elements, and the discretization order is $n_d = 5$.

Figure 4.16a-f shows the individual energies of the $\Phi = 6\%$ system when $B_{ext} = 0$ mT. Only the volume element and spring energies vary with the applied strain, and strictly increase, in the same manner as the $\Phi = 3\%$ case. Figure 4.16g shows the energy density of the system as a function of applied strain when $B_{ext} = 0$ mT, as well as a fit line using the parameters from fitting the dataset to Eq. (4.2.8). The fit shows good agreement with the dataset, and G_{eff} is found to be ≈ 4.5 kPa, showing an enhancement in the stiffness of the system with the increase in Φ of $\approx 12.5\%$ when compared to $G_{eff} = 4$ kPa for the $\Phi = 3\%$ case.

Next we observe the response for an applied magnetic field. Figure 4.17a-f shows the individual energies of the $\Phi = 6\%$ system when $B_{ext} = 80$ mT. The volume element and spring energies vary with the applied strain, but in this case the volume element energy still increases with increased

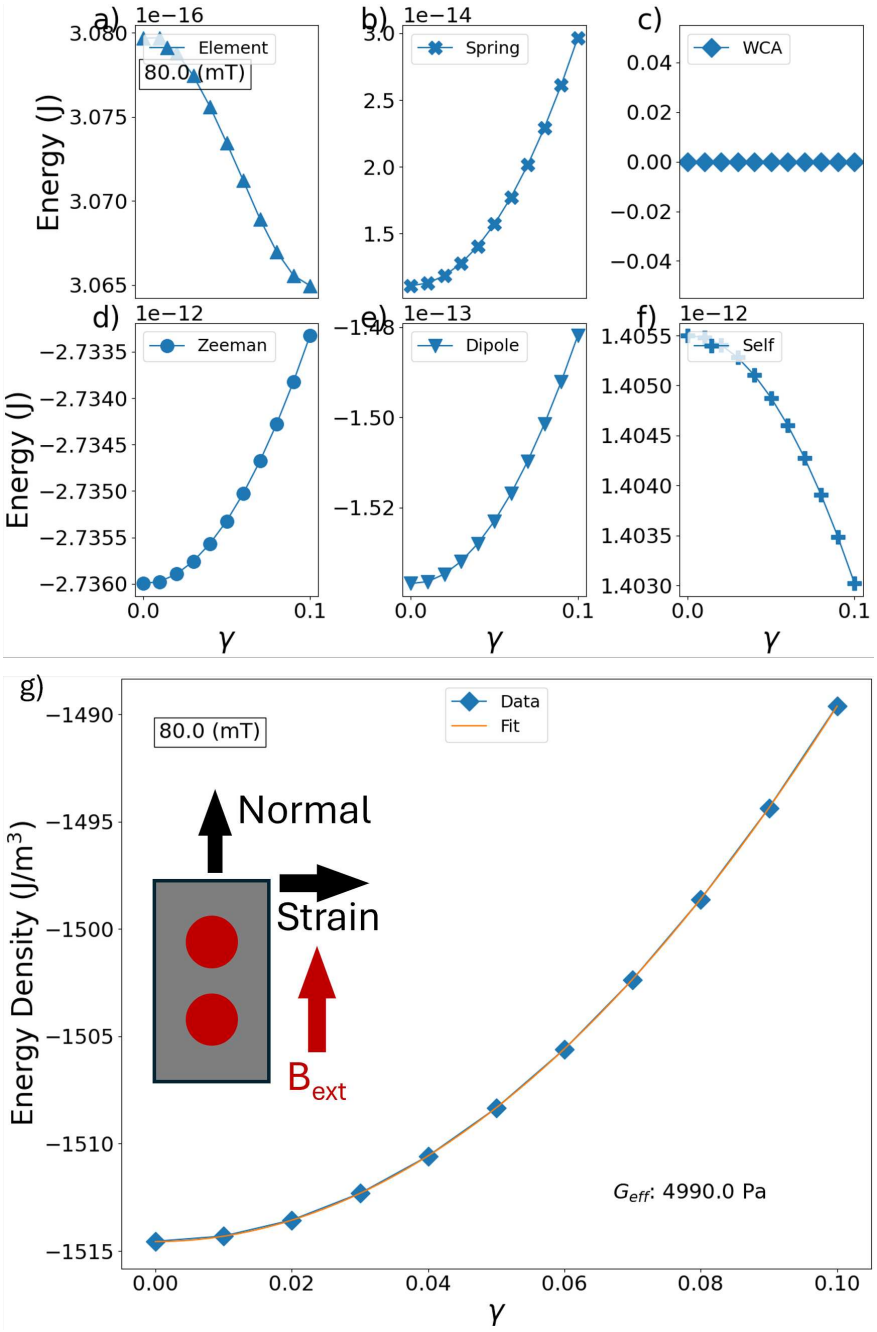

Figure 4.15: Plots of individual energies (a-f) and total energy density (g) versus applied strain when $B_{ext} = 80$ mT. a) Energy associated with volumetric strain of the volume elements, b) energy associated with the deformation of linear springs, c) energy associated with particle-particle elastic interactions, or volume exclusion energy, d) Zeeman energy due to the particle magnetization interaction with the external magnetic field, e) dipole-dipole energy due to the interaction of the particle magnetization with the dipolar field of the other particle, f) magnetic self energy related to the work done to magnetize the particles, g) the total energy density curve, with the approximate effective modulus, and a fit curve made from using the parameters found by fitting the energy density versus strain data. Results shown for the case of $E = 9$ kPa, $\nu = 0.47$, $\chi = 70$, $M_s = 1.6 \times 10^6$ A/m, $D = 3$ μm, $n_d = 5$, $\Phi = 3\%$, $S = 7.909$ μm, with the external field applied along the axis connecting the particles.

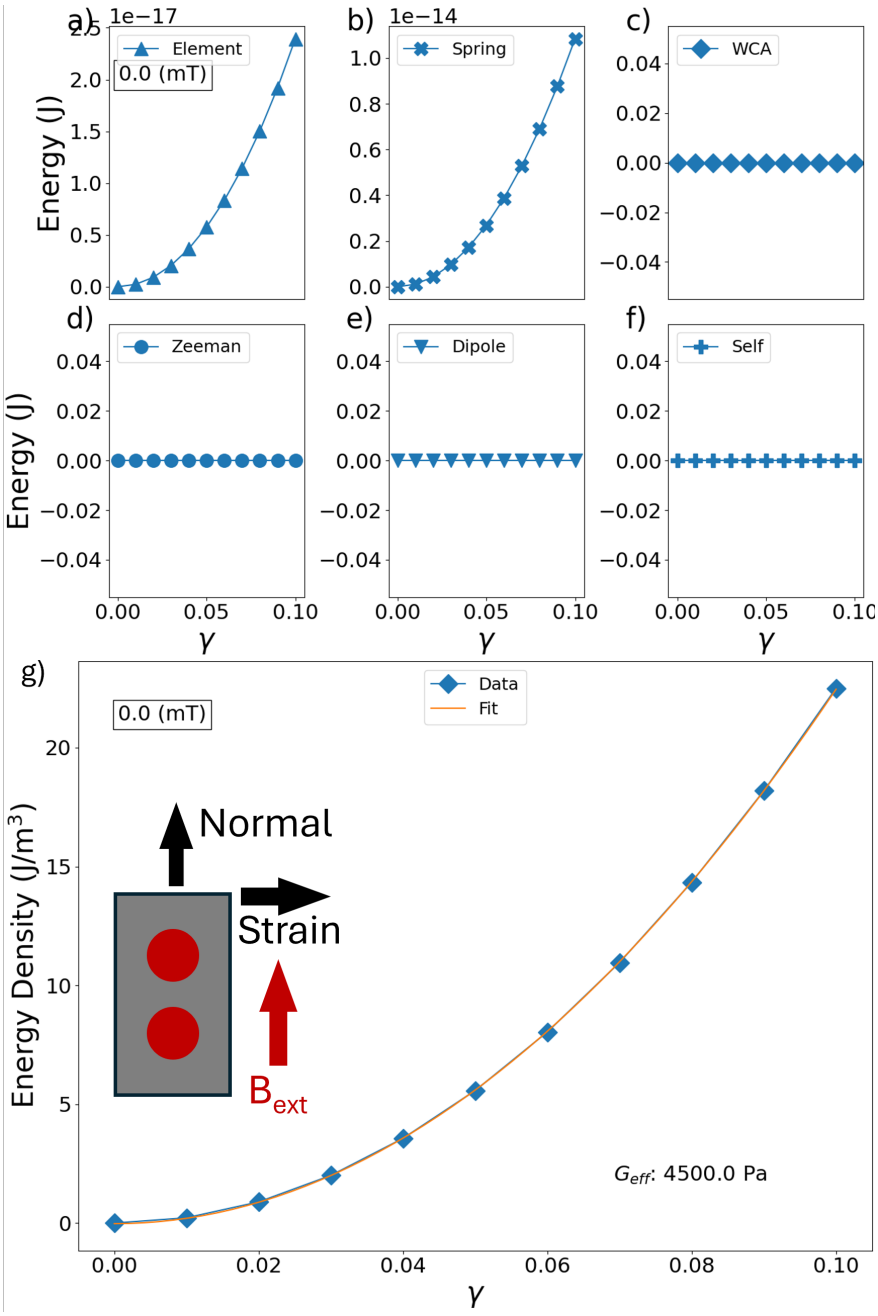

Figure 4.16: Plots of individual energies (a-f) and total energy density (g) versus applied strain when $B_{ext} = 0$ mT. a) Energy associated with volumetric strain of the volume elements, b) energy associated with the deformation of linear springs, c) energy associated with particle-particle elastic interactions, or volume exclusion energy, d) Zeeman energy due to the particle magnetization interaction with the external magnetic field, e) dipole-dipole energy due to the interaction of the particle magnetization with the dipolar field of the other particle, f) magnetic self energy related to the work done to magnetize the particles, g) the total energy density curve, with the approximate effective modulus, and a fit curve made from using the parameters found by fitting the energy density versus strain data. Results shown for the case of $E = 9$ kPa, $\nu = 0.47$, $\chi = 70$, $M_s = 1.6 \times 10^6$ A/m, $D = 3$ μm, $n_d = 5$, $\Phi = 6\%$, $S = 6.2727$ μm, with the external field applied along the axis connecting the particles.

shear strain compared to the $\Phi = 3\%$ case. The Zeeman, dipole-dipole, and magnetic self energies all maintain a quadratic-looking dependence on shear strain. As for $\Phi = 3\%$, the Zeeman and dipole-dipole energies increase, and the magnetic self energy decreases with increasing applied strain. In comparison to the $\Phi = 3\%$ case, Figure 4.15, here the WCA energy is non-zero and decreasing with shear strain. The WCA energy is non-zero only when particles become close together, with separations approaching the diameter of a particle, which we consider to be clustered states. In this case the shear strain is separating the clustered particles, and reducing the WCA energy, though the particles remain in a clustered state. Figure 4.17g shows the energy density of the system as a function of applied strain when $B_{ext} = 80$ mT, as well as a fit line using the parameters from fitting the dataset to Eqn. (4.2.8). The fit shows good agreement with the dataset, and G_{eff} is found to be ≈ 16.8 kPa. The energy density curve maintains a quadratic looking dependence on the shear strain, despite the additional magnetic energies and the clustered particle state, and the magnetic field has had a stiffening effect on the system.

Figure 4.18 shows G_{eff} as a function of B_{ext} for the cases of $\Phi = 3, 4$ and 6%. The systems show smooth, but saturating increases in G_{eff} with increasing B_{ext} for $\Phi = 3$ and 4%. The maxmimum value of G_{eff} increases with increasing Φ. For the case of $\Phi = 6\%$ the dependence of G_{eff} on B_{ext} seems almost quadratic, in line with experimental results [43]. When $B_{ext} = 60$ mT there is a sharp increase in G_{eff} which is associated with the formation of the clustered state for the magnetic particles. For fields beyond $B_{ext} = 60$ mT there is an increase in G_{eff} but the effect levels off, in line with the magnetic saturation of the particles.

Figure 4.19a shows the impact of varying Φ on the zero-field G_{eff}, which shows an increase in G_{eff} with slight upward curvature. The general trend of increasing stiffness of the system with increasing proportion of relatively rigid magnetic filler matches intuition for composite materials. Figure 4.19b shows the value of G_{eff} when $B_{ext} = 140$ mT as Φ varies. A general increase in G_{eff} is observed with increasing Φ, however, G_{eff} increases sharply at around $\Phi = 5\%$. Figure 4.19c shows the magnetorheological effect as a function of Φ. The magnetorheological effect is defined as the percent increase in the G_{eff} at $B_{ext} = 140$ mT from the value when $B_{ext} = 0$ mT.

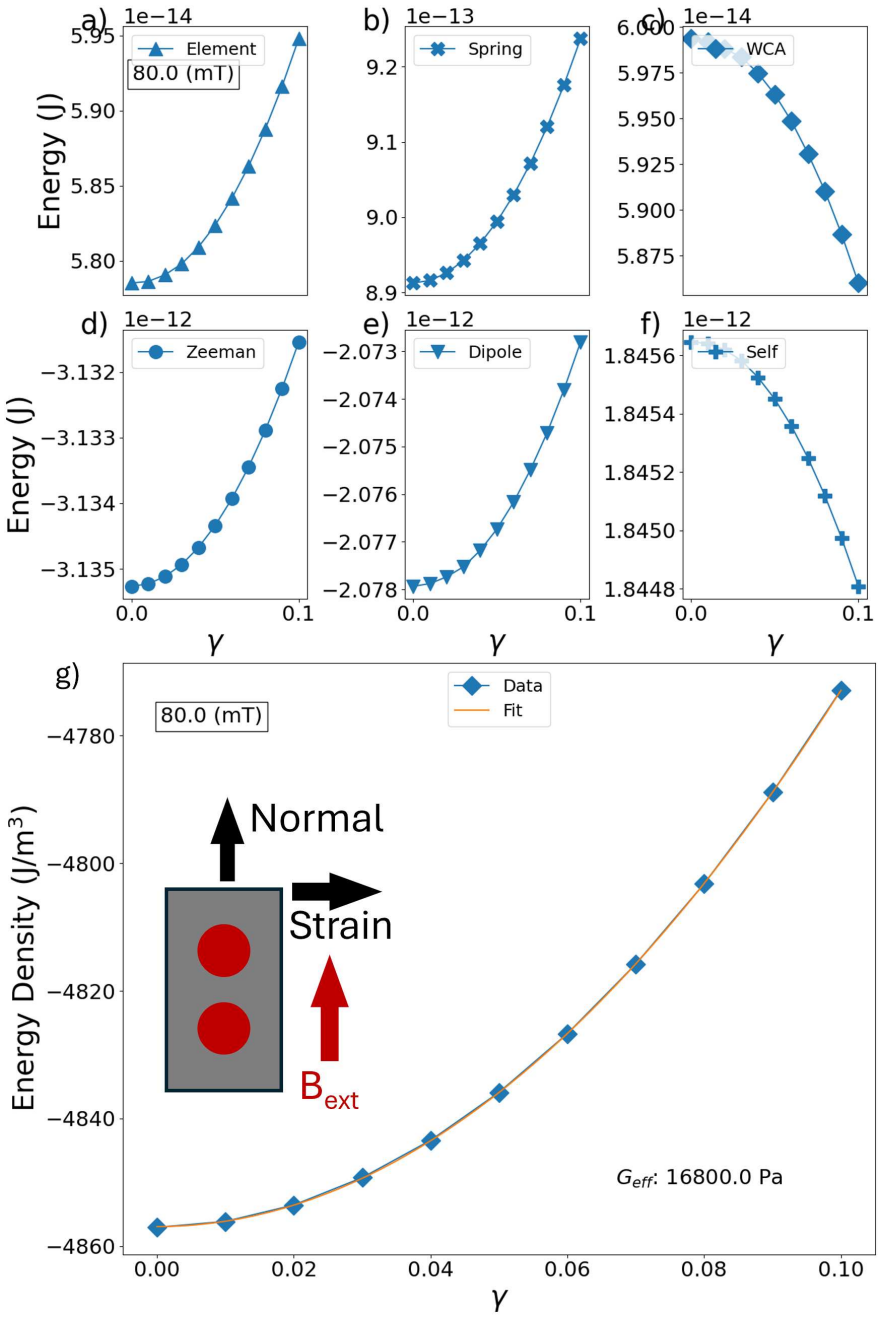

Figure 4.17: Plots of individual energies (a-f) and total energy density (g) versus applied strain when $B_{ext} = 80$ mT. a) Energy associated with volumetric strain of the volume elements, b) energy associated with the deformation of linear springs, c) energy associated with particle-particle elastic interactions, or volume exclusion energy, d) Zeeman energy due to the particle magnetization interaction with the external magnetic field, e) dipole-dipole energy due to the interaction of the particle magnetization with the dipolar field of the other particle, f) magnetic self energy related to the work done to magnetize the particles, g) the total energy density curve, with the approximate effective modulus, and a fit curve made from using the parameters found by fitting the energy density versus strain data. Results shown for the case of $E = 9$ kPa, $\nu = 0.47$, $\chi = 70$, $M_s = 1.6 \times 10^6$ A/m, $D = 3$ μm, $n_d = 5$, $\Phi = 6\%$, $S = 6.2727$ μm, with the external field applied along the axis connecting the particles.

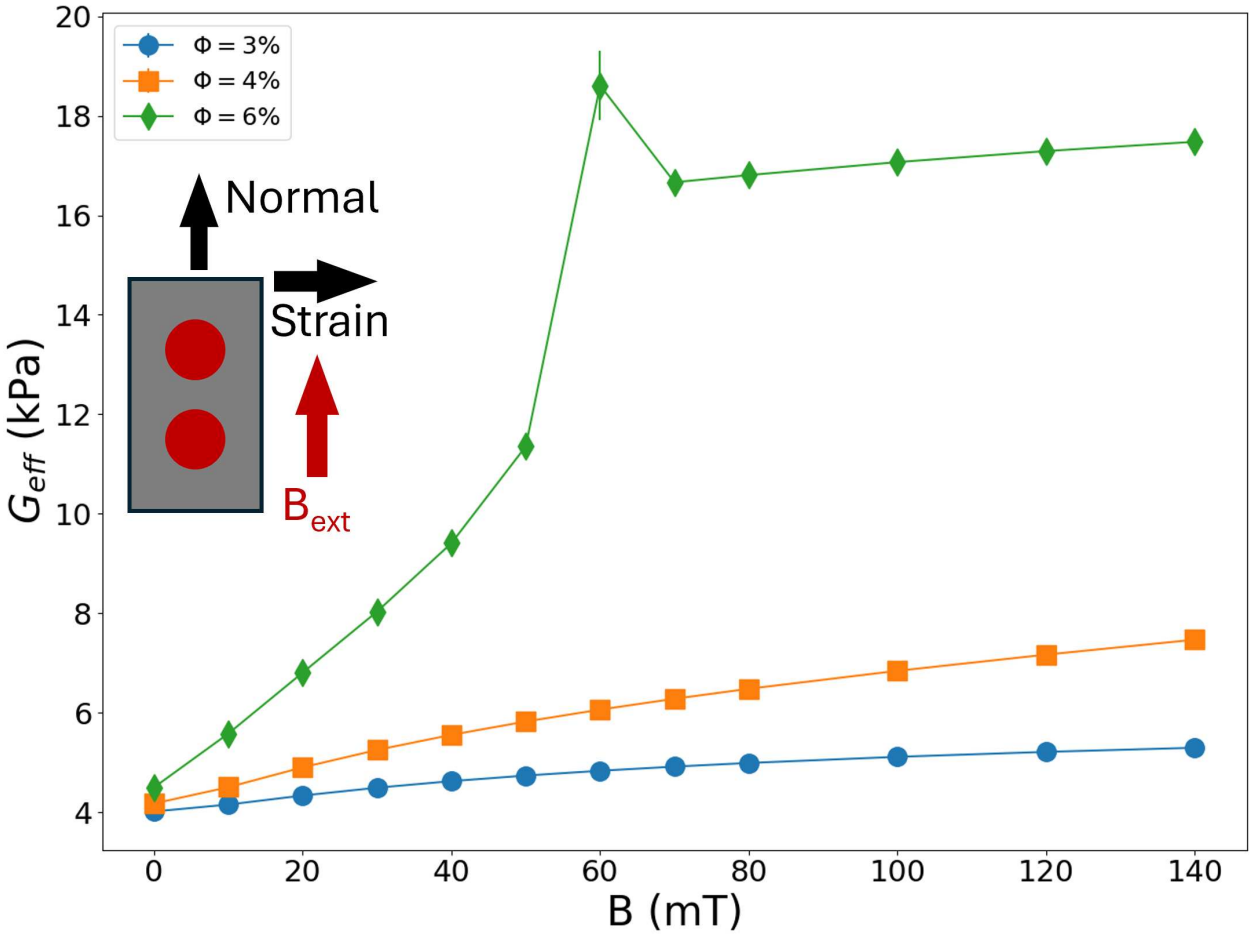

Figure 4.18: Effective shearing modulus versus external magnetic field for $\Phi = 3, 4$, and 6%. Results shown for the case of $E = 9$ kPa, $\nu = 0.47$, $\chi = 70$, $M_s = 1.6 \times 10^6$ A/m, $D = 3$ μm, $n_d = 5$, with the external field applied along the axis connecting the particles.

$$MR = \frac{G_{eff,B} - G_{eff}}{G_{eff}}$$

The same sharp increase is also observed in Figure 4.19c around $\Phi = 5\%$. Near $\Phi = 5\%$ the magnetic particles are spaced close enough that they are able to enter clustered states under the effect of B_{ext} at 140 mT. When $B_{ext} = 140$ mT the particles are approaching magnetic saturation. Larger values of B_{ext} may show slightly different results, but the general trends should be similar to what is shown in Figure 4.19.

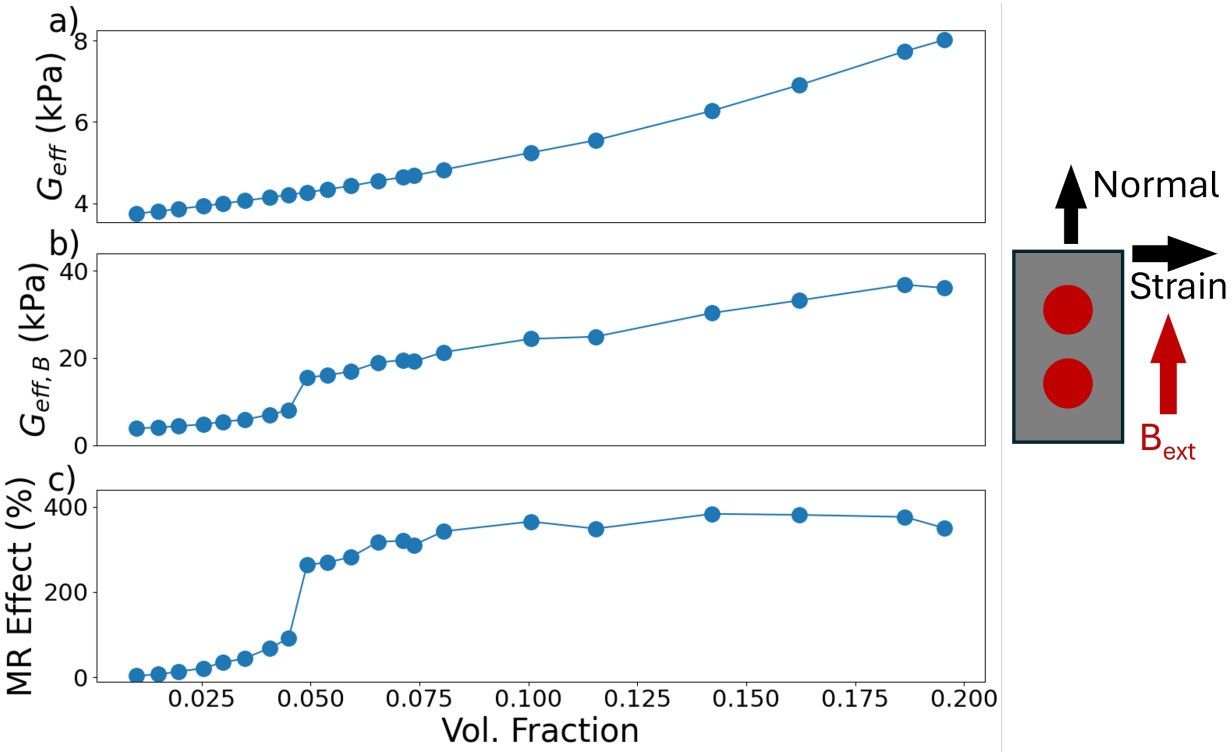

Figure 4.19: a) Effective shearing modulus when $B_{ext} = 140$ mT versus Φ. b) when $B_{ext} = 140$ mT versus Φ. c) Magnetorehological effect expressed as a percentage increase in stiffness at $B_{ext} = 140$ mT compared to $B_{ext} = 0$ mT versus Φ. Results shown for the case of $E = 9$ kPa, $\nu = 0.47$, $\chi = 70$, $M_s = 1.6 \times 10^6$ A/m, $D = 3$ μm, $n_d = 7$, with the external field applied along the axis connecting the particles.

The results show that the presence of magnetic particles can lead to a field stiffening effect, even for dilute systems of magnetic particles. Furthermore, it is apparent that the formation of clusters of particles in a sample can create larger increases in effective stiffness. Even in dilute

systems, inhomogeneity in the magnetic particle distribution will alow for some regions of the sample to achieve clustered states.

The treatment of non-dilute systems is beyond this dissertation due to the difficulties associated with solving the non-linear system of equations with $N > 2$ particles in close proximity with low symmetry, and the importance of non-uniform magnetization in accurately describing the forces and energies of such systems. Additional difficulties arise in dealing with closely packed particles' interaction with the surrounding elastic medium, and the crossing of percolation thresholds, values of Φ such that the magnetic medium would extend continuously across the sample, and the strong restrictions on particle rearrangement that would exist.

Four Particle Chain

Thus far we have focused on two particle systems, but it is instructive to look at larger collections of particles. Next, the behavior of an evenly spaced, straight, four particle chain is investigated under the effect of an external magnetic field applied parallel and perpendicular to the chain, while the system undergoes a simple shear. This system provides a simplified representation of an anisotropic MRE.

Simulation parameters are as follows: $E = 9$ kPa$, \nu = 0.47, D = 3\ \mu$m$, \Phi \approx 1\%, S = 6\ \mu$m$, l_e = 0.2727\ \mu$m$, L_x = L_y = 11.7272\ \mu$m$, L_z = 39.8181\ \mu$m$, \delta t = 5 \times 10^{-3}$. The system is composed of 284,592 nodes, $(44 \times 44 \times 147)$, and 269,954 volume elements, $(43 \times 43 \times 146)$, the particle diameter is 11 volume elements, and the discretization order is $n_d = 5$. The initial configuration of the system can be seen in Figure 4.20.

Figure 4.21 shows the effective shearing modulus when the strain is applied to the top surface in the $\hat{x}$ direction, with the field along $\hat{z}$ and the chain axis, and with the field perpendicular along $\hat{x}$ and perpendicular to the chain axis. The zero-field G_{eff} value is approximately 3.75 kPa. With the field parallel to the chain axis, the value of G_{eff} reaches 5.5 kPa at 140 mT, or $\approx 46.7\%$ increase in G_{eff}. With the field perpendicular to the chain axis and parallel to the strain direction, the value of G_{eff} reaches 2.77 kPa at 140 mT, representing an $\approx 26.13\%$ decrease.

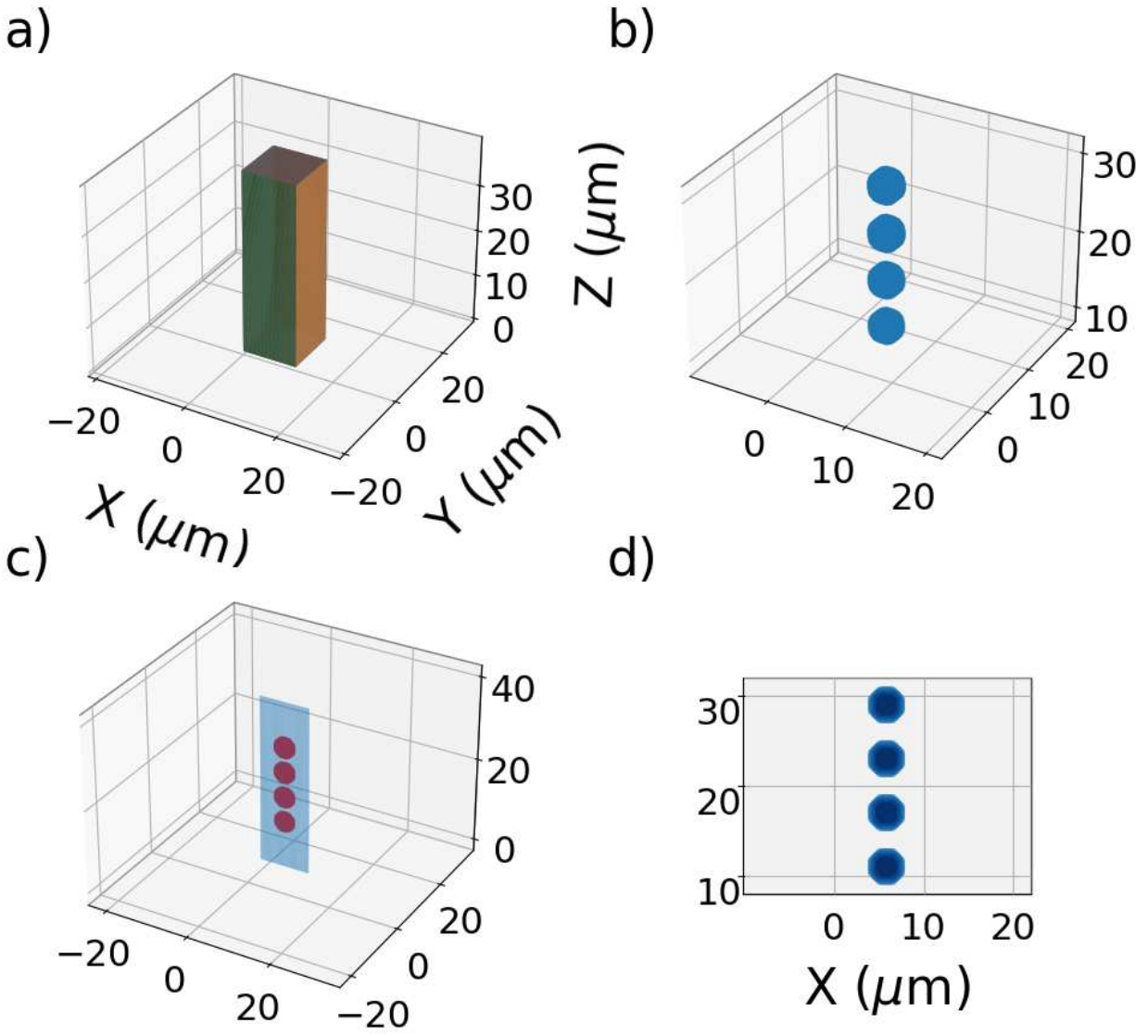

Figure 4.20: a) Outside view of initial system configuration of a four particle chain with interparticle spacing $S = 6$ μm, b) scatter plot of the nodes that belong to the magnetic particles within the system, c) wireframe of a cut at constant$y$at a position approximately halfway through the thickness of the system, with red markers denoting the nodes within the magnetic particles, d) scatter plot of particle nodes where the shade indicates depth, with the darker shade meaning the node is closer to the viewer.

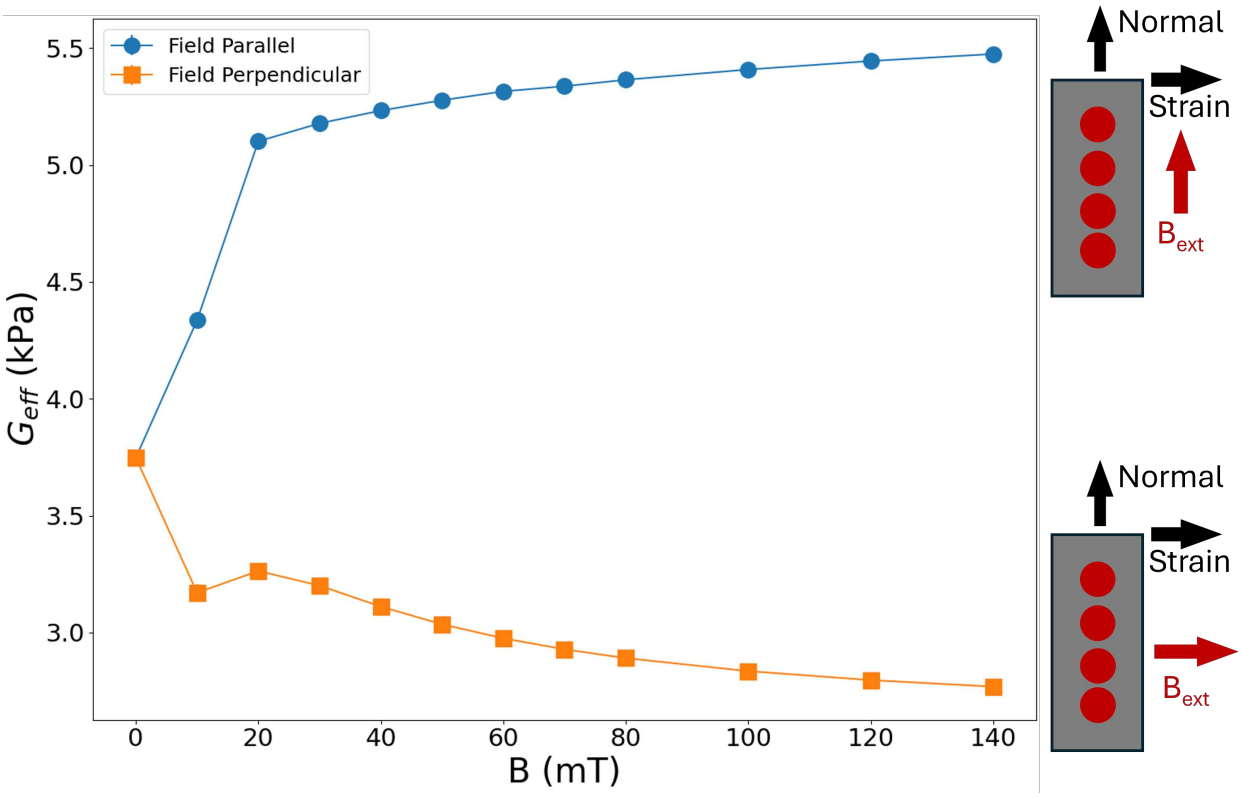

Figure 4.21: Effective shearing modulus for an evenly spaced four particle chain (Figure 4.20) when the magnetic field is applied along and perpendicular to the chain. Results shown for the case of $E = 9$ kPa, $\nu = 0.47$, $\chi = 70$, $M_s = 1.6 \times 10^6$ A/m, $D = 3$ μm, $n_d = 5$, $S = 6$ μm.

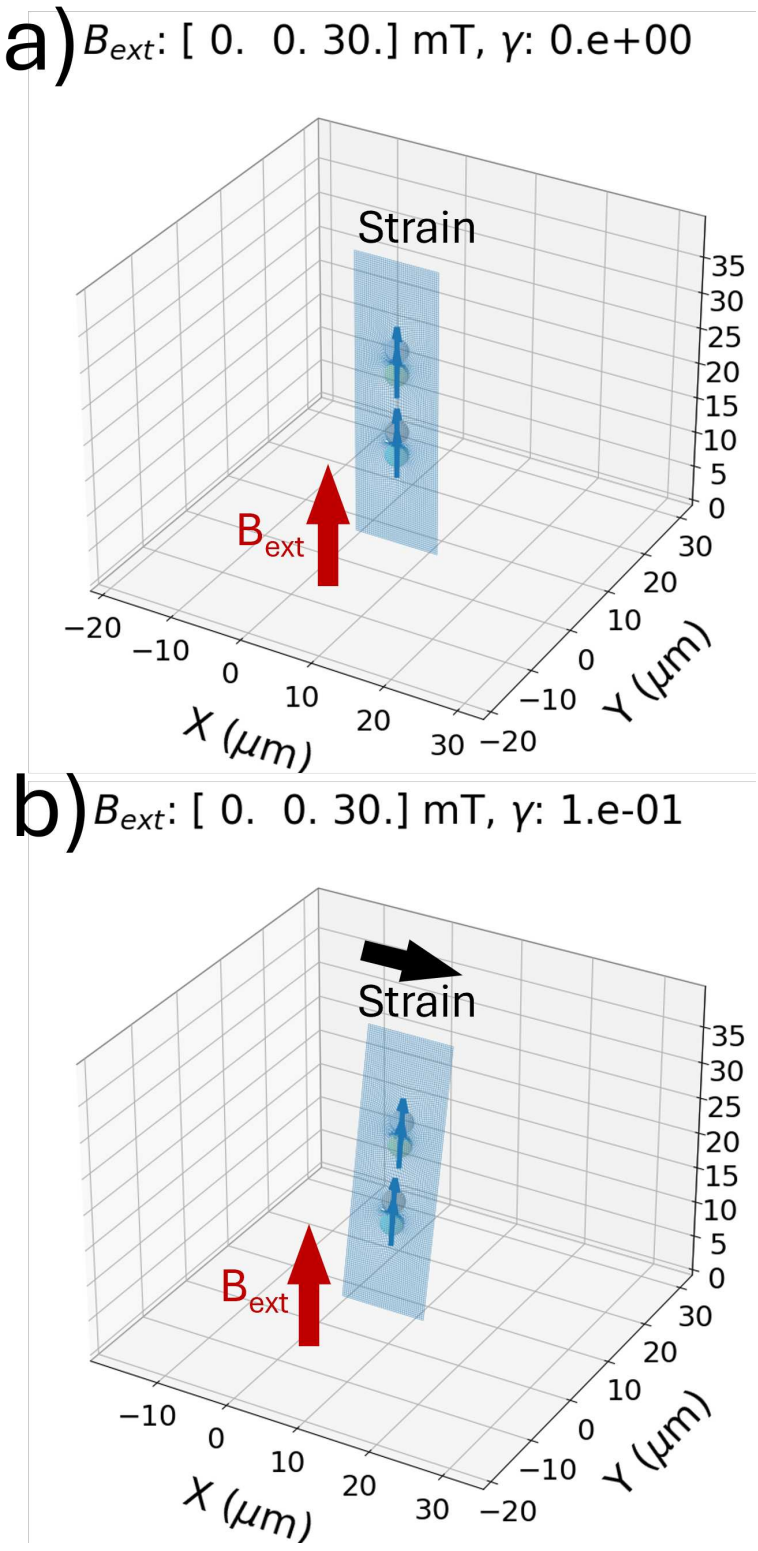

Figure 4.22: Four particle chain (Figure 4.20) with the field applied along the particle chain along $\hat{z}$ with $B_{ext} = 30$ mT and with the shear strain perpendicular to the particle chain along $\hat{x}$ with shear strain values 0 and 1×10^{-1}.

When the external magnetic field is aligned with the magnetic particle chain, and perpendicular to the shear strain direction, there is a field stiffening effect. This is a very similar situation to the two particle results seen earlier, where the rearrangement of the particles under the influence of the shear strain tends to reduce the tip-to-tail alignment of the magnetic particle magnetization vectors, leading to an increase in the dipole-dipole energy terms, along with decreasing mutual magnetization between the magnetic particles as their separation increases. This shift in the particle arrangement and magnetization vector canting is visible in Figure 4.22. When the external magnetic field and the shear strain direction coincide, there is a field softening effect. The shearing causes particle rearrangement such that the particles are no longer side-by-side. The particles are instead shifted slightly in front of or behind one another, with a corresponding shift in the orientation of the individual magnetization vectors of each particle. This reduces the dipole-dipole energy penalty of the side-by-side arrangement of the magnetic particles. Both the rearrangement of the particles and the change in the orientation of the magnetization vectors contribute to this reduction in energy, and are visible in Figure 4.23.

Eight Particle Helices

Moving up to a more complex system, next we consider the behavior of an eight particle helix-like distribution of particles under the effect of an external magnetic field applied parallel to the chain, while the system undergoes simple shear, for a range of values for the radius of the helix.

The simulation parameters used are as follows: $E = 9$ kPa$, \nu = 0.47, D = 3$ μm$, \Phi \approx 2\%, S_z = 5$ μm$, l_e = 0.2727$ μm$, L_x = L_y = 17.7272$ μm$, L_z = 61.9090$ μm$, \delta t = 4 \times 10^{-3}$. S_z is the vertical separation of the magnetic particles. The system is composed of 993,168 nodes, $(66 \times 66 \times 228)$, and 959,075 volume elements, $(65 \times 65 \times 227)$, the particle diameter is 11 volume elements, and the discretization order is $n_d = 5$. The initial configuration of two systems can be seen in Figure 4.24. The helices stop shy of forming one full twist from top to bottom magnetic particle, with an angular difference, $\Delta\phi$, between adjacent magnetic particles of $\pi/4$. The radii of the helices vary from $R_{helix} = 0.5$ μm, seen in Figure 4.24a-c, to $R_{helix} = 3.5$ μm, seen in Figure 4.24d-f.

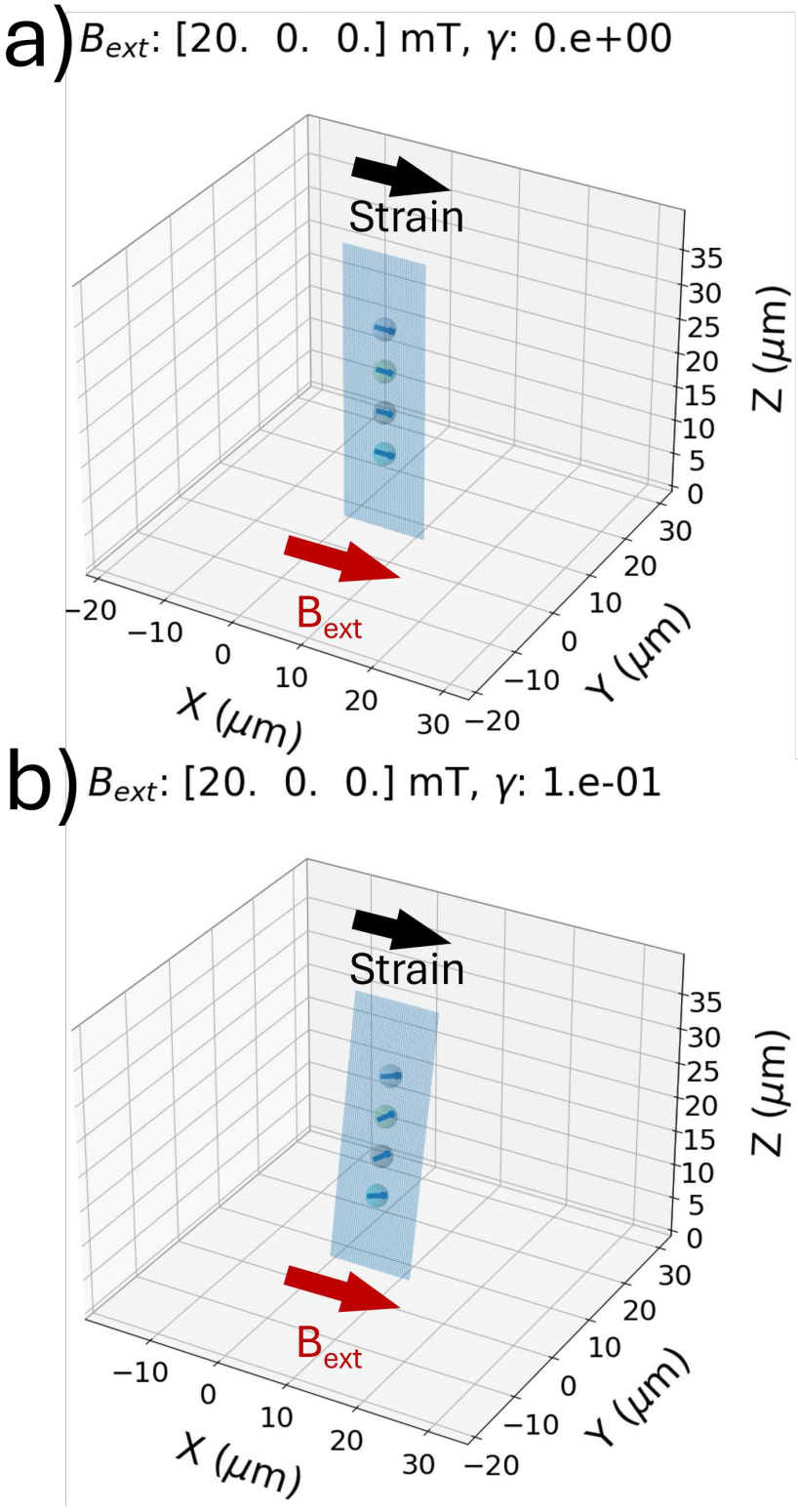

Figure 4.23: Four particle chain (Figure 4.20) with the field applied perpendicular to the particle chain along $\hat{x}$ with $B_{ext} = 20$ mT and with the shear strain perpendicular to the particle chain along $\hat{x}$ with shear strain values 0 and 1×10^{-1}.

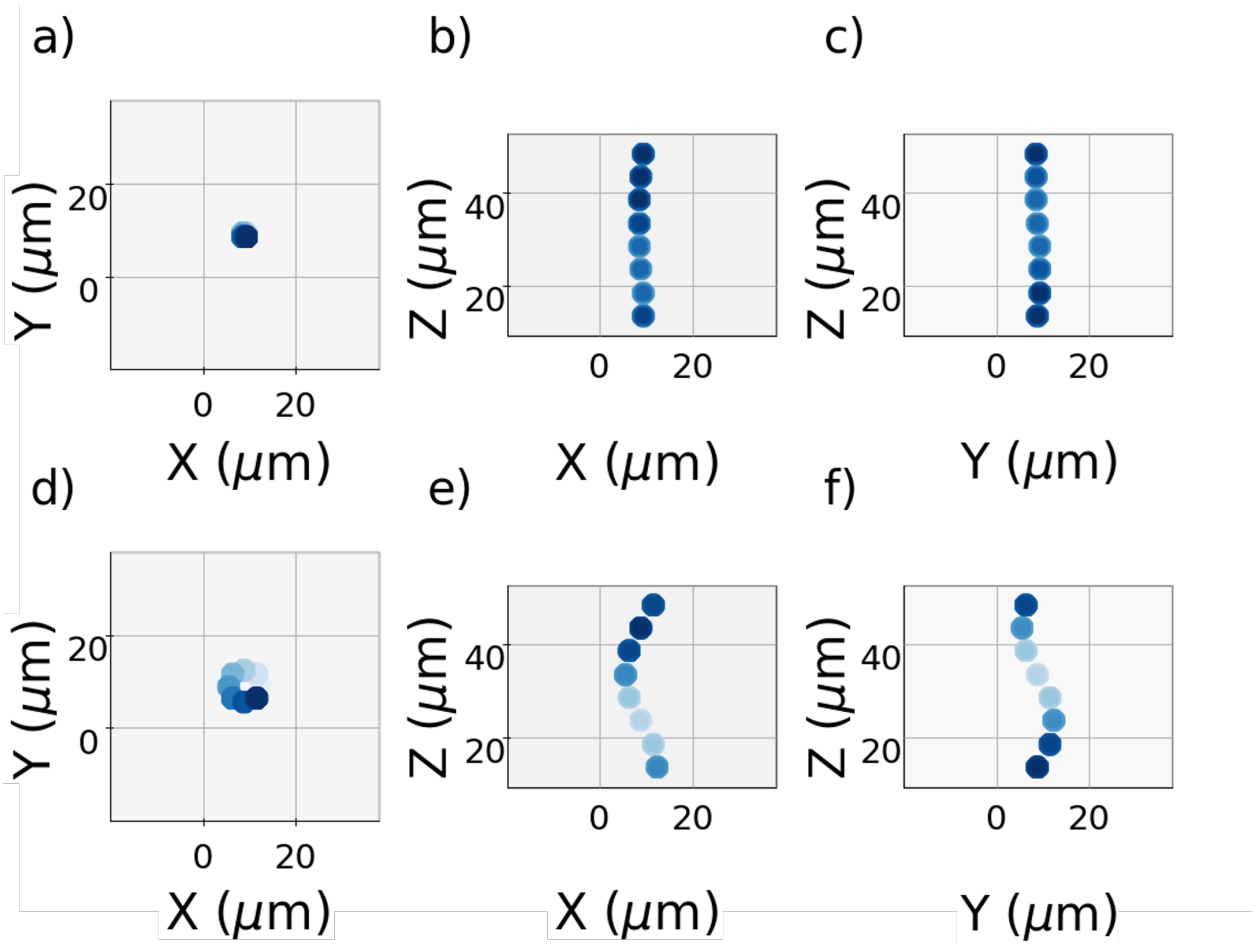

Figure 4.24: Orthographic views showing scatter plot of particle nodes where the shade indicates depth into the page. The darker shade means the node is closer to the viewer, and lighter shades being further away. (a-c) Correspond to a helix with a radius of 0.5 μm, (d-f) correspond to a helix with a radius of 3.5 μm.

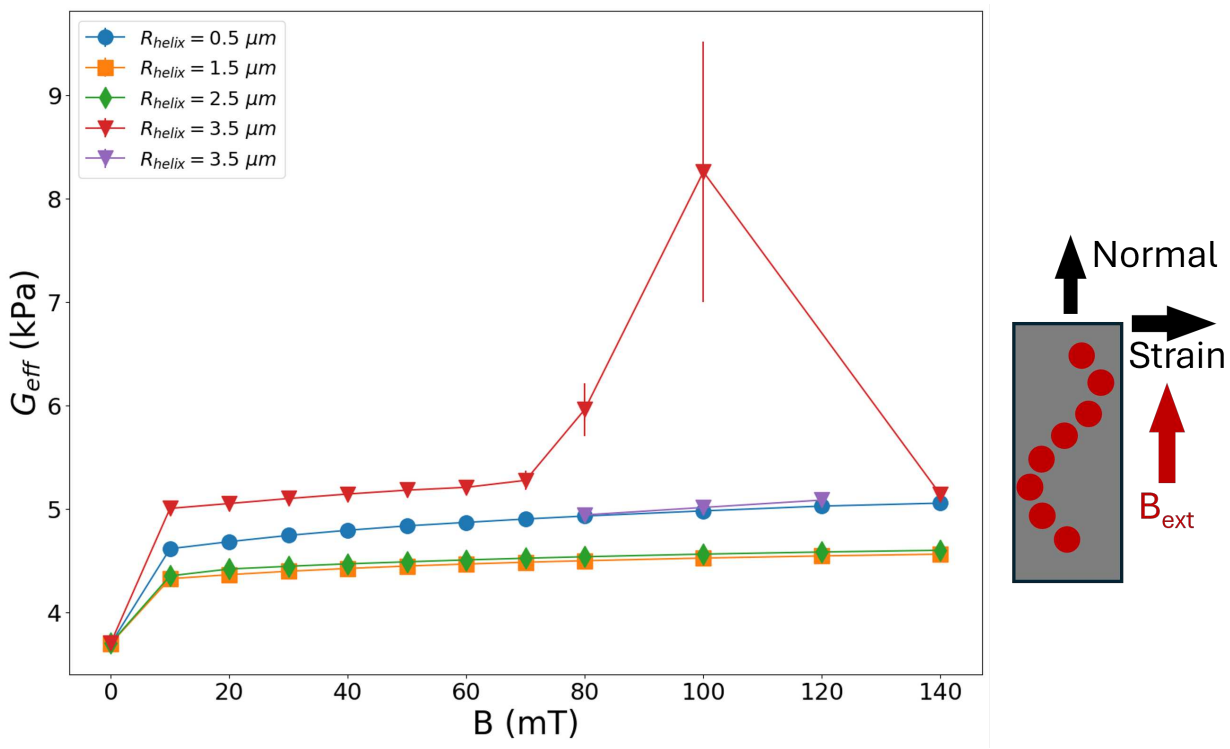

Figure 4.25: Effective shear modulus for four systems of eight magnetic particle helices with radius of 0.5 to 3.5 μm. $R_{helix} = 3.5\mu$m appears twice in the legend due to the discontinuity in the strain energy density that appears due to particle clustering under the effect of the applied shear strain, as seen in Figure 4.26 and Figure 4.27. Results shown for the case of $E = 9$ kPa, $\nu = 0.47$, $\chi = 70$, $M_s = 1.6 \times 10^6$ A/m, $D = 3$ μm, $n_d = 5$.

For each of the helical particle arrangements, effective moduli were extracted by fitting the total energy density vs strain curves as was done in Section 4.3.2 and Section 4.3.2. Figure 4.25 shows the effective shear moduli as a function of B_{ext}. There is a general trend of increasing G_{eff} with increasing $B + ext$. However, these results show an unexpected nonmonotonic dependence of the field stiffening effect on the helix radius. The original hypothesis was that an increase in R_{helix} would generate states that are less anisotropic and more isotropic in terms of the effective anisotropy of the particle distribution, and that this should lead to a decrease in the magnitude of field stiffening effect with increasing radius. This does not appear to be the case for the range of values explored in this work. This may also be due to the limited size of the system, both in dimensions and number of magnetic particles. Even for this relatively small system, the behavior is complex.

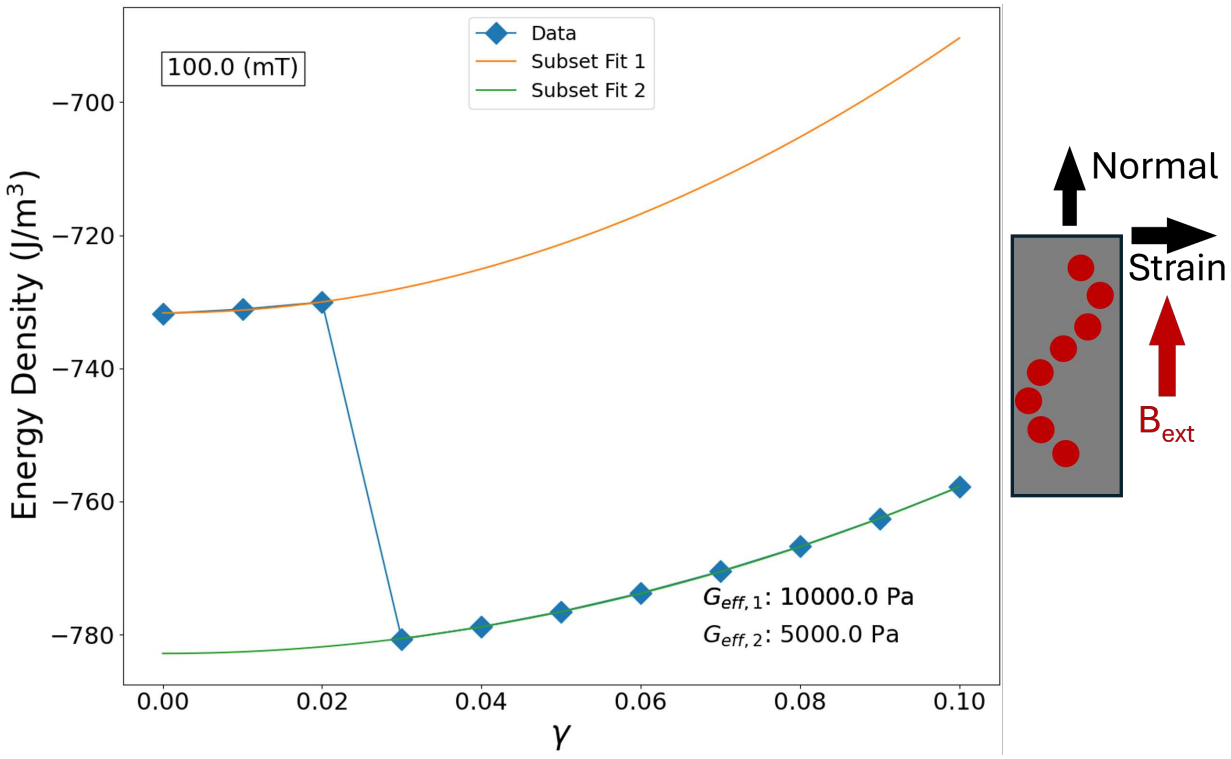

Figure 4.26: Strain energy density for a system of eight magnetic particles with a helical arrangement with $R_{helix} = 3.5$ μm. Results shown for the case of $E = 9$ kPa, $\nu = 0.47$, $\chi = 70$, $M_s = 1.6 \times 10^6$ A/m, $D = 3$ μm, $n_d = 5$, $S_z = 5\mu$m, $\Delta\phi = \pi/4$.

For the case where $R_{helix} = 3.5\mu$m, two curves are shown in Figure 4.26. Large jumps in the field-dependent effective modulus are seen in Figure 4.25 for $B_{ext} = 80, 100,$ and 120 mT. Closer examination of the energy density of the system at a fixed magnetic field as a function of shear strain curves shows discontinuities at $B_{ext} = 80,\ 100$ and 120 mT, as can be seen in Figure 4.26 for $B_{ext} = 100$ mT. As shown in Figure 4.27, the application of the shear strain allows clustering of a magnetic particle that had previously not been part of a cluster. This kind of behavior is important for understanding the microscopic and macroscopic response of magneto-active polymers with magnetically soft filler. The formation of clusters of magnetic particles is important as a mechanism for magnetic hysteresis in these kinds of systems, and should play a role in field stiffening effects. When a magnetic particle cluster pair or tuple forms it is a low magnetic energy state, and perturbing it from that state by straining the system adds an additional energy penalty that appears experimentally as an increase in effective stiffness. In a similar line of thought, high strains that can cause clusters of magnetic particles to break apart may play a role in strain softening effects that are seen experimentally, as the energy penalty for breaking those clustered states only needs to be paid once.

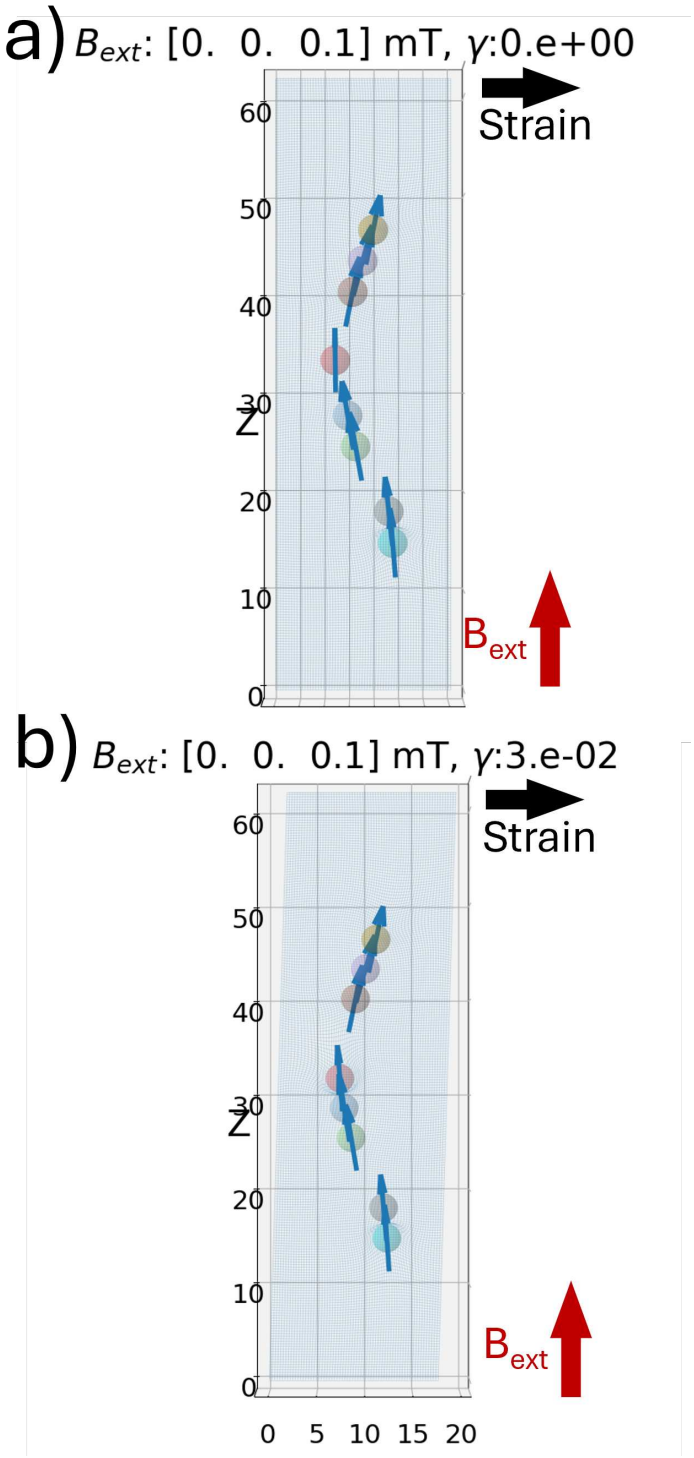

Figure 4.27: Visualization of magnetic particles, their magnetization, and the deformation of the surrounding polymer for system of eight magnetic particle helix with $R_{helix} = 3.5$ μm when a) $\gamma = 0$ and b) $\gamma = 3 \times 10^{-2}$ where an additional particle joins an existing two particle cluster to form a three particle cluster. Results shown for the case of $E = 9$ kPa, $\nu = 0.47$, $\chi = 70$, $M_s = 1.6 \times 10^6$ A/m, $D = 3$ μm, $n_d = 5$, $S_z = 5\mu$m, $\Delta\phi = \pi/4$.

4.4 Discussion

Compared to the dipole-spring model in Chapter 2 the magnetic hysteresis results shown here are dramatically different. The large remanent magnetization and the presence of switching fields instead of smoothly passing through zero magnetization was an unexpected result. The dipole-spring model shown in Chapter 2 managed to qualitatively recreate the pinched hysteresis loop shape observed experimentally in soft MREs. The dipole-spring model used a linearly susceptible magnetization response, which allowed the magnetization components to be solved by solving a linear system of equations.

$$\mathbf{A}\vec{x} = \vec{b}. \tag{4.97}$$

When the external magnetic field was zero, the right hand was zero, and the answer for the magnetizations was trivially zero, and the magnetic particles are unclustered. At low magnetic fields, the response of a magnetically soft carbonyl iron is well approximated by a linear model, and the Froehlich-Kennelly magnetization law is approximately linear for small magnetic fields. However, the behavior of mutually magnetizing magnetically soft particles at distances small compared to the particle size is not well approximated by point-dipole like interactions due to non-uniform magnetization, and the approach to solving the nonlinear system of equations used in this chapter used the magnetization histories of the particle systems. When the external magnetic field was reduced to zero from some non-zero value, and the particles already had some non-zero magnetization and were clustered together, the fixed point iteration converged to a solution that was not trivially zero. The dipolar field expression had not changed from Chapter 2, but the numerical method and the model used for the magnetic response of a single particle have both changed. The method for solving the linear system of equations returned the trivial zero solution, but it was not necessarily the only solution. In practice the author found that when using the linear magnetization response, in a two particle system with a small external magnetic field aligned with particles, a large value of χ, and a separation close to $2R$, numerical solutions for the linear system of equations can result in particle magnetization anti-parallel to the external magnetic field. The choice of model for the

magnetization response of the magnetic particles and the numerical methods used can both have significant impact on the results.

Considering the experimentally measured magnetization curve for carbonyl iron presented in Chapter 3, it does seem reasonable that the magnetization of the particles would go to zero when the external magnetic field is removed. It also seems reasonable that the magnetic particles, once magnetized, and in a configuration that creates an effective shape anisotropy, could maintain some magnetization when the external magnetic field is removed. However, this is ignoring the microscopic details of the magnetic domains, magneto-crystalline anisotropy, and exchange interactions.

In a real system, even if clusters of particles have only a few magnetic particles each, there will be a distribution of relative angles between the axis connecting particles in the cluster and the direction of the external magnetic field. When the external magnetic field is removed, alignment with that field is less energetically favorable, and so the cluster could rotate away from that axis, or separate entirely.

Ref. [69] used x-ray micro-computed tomography and found irreversible particle motion within an isotropic MRE with 2% by weight carbonyl iron (CIP) content, where after the removal of the magnetic field particles remained aggregated with small changes in their position and orientation. It should be noted that the mean particle size was $D = 35$ μm, and a mean displacement of around the same distance. The elastic modulus of the PDMS matrix was not provided, but the use of silicon oil softeners suggests a low stiffness. Ref. [69] also suggests that the elastic properties of the matrix are not homogeneous, and that the area around the magnetic particles is not sufficiently polymerized or cross-linked. This stands in contrast to the interpretations presented in Ref. [80] that there is a stiffer layer of polymer surrounding magnetic particles. As a counterpoint to irreversibility of particle clustering, ref. [48] presents a two particle model using nonlinear elasticity for the polymer matrix and nonlinear magnetization response for the magnetic particles. It presents results demonstrating bistability that is qualitatively similar to the results in Chapter 2, where particle clustering is reversible, and particles separate as the magnetic field decreases.

There is an open question of how the hysteresis observed in two particle systems in this chapter can correspond to the pinched hysteresis loop shape. Changes in the properties of the elastic matrix, the magnetic particles, and the particle placement in the model of Chapter 4 could result in magnetomechanical hysteresis so that the particles uncluster at sufficiently low fields, or in the absence of an external magnetic field. The use of a nonlinear model of elasticity might also impact the formation and maintenance of clustered states. Some form of homogenization across many simulations could reproduce the pinched hysteresis loop shape. The combination of conflicting experimental evidence and theoretical results for reversible and irreversible particle motion makes this an interesting question which the author had initially thought was clearly settled in favor of reversibility.

Simulation results for the field dependent moduli show that increasing volume fraction of magnetic filler increased the field dependent effective shearing modulus when the magnetic particles and magnetic field were aligned, and the shearing was perpendicular to that axis, which is a trend that qualitatively matches experimental results. The jump in MR effect at a critical value of $\Phi \approx 5\%$ makes sense, as the particle separation becomes small enough for clustering to occur. The clustering of the magnetic particles creates a significant energy penalty for separating them, resulting in a large increase in stiffness. The maximal MR effect for the combination of polymer modulus $E = 9$ kPa and the magnetic field $H_{ext} = 140$ mT was under 400%. While large, this is significantly smaller than the increases seen in Ref. [43], which reports shearing modulus for up to ≈ 125 mT, which reported an over $10\times$ increase in shearing modulus for $\Phi = 23\%$.The point-dipole interaction seems an insufficient approximation for the magnetic energies when inter-particle distances are close to the size of the magnetic particles.

It was interesting to observe that applied strain impacts the magnetization magnitude and orientation in this model, resulting in changes to the magnetic energies. It was similarly interesting to observe that applied strains could result in either increasing or decreasing volume element and elastic energy based on the clustering of particles and type and direction of strain.

The field softening effect seen for the 4 particle chain with the shear strain and magnetic field direction parallel to one another and perpendicular to the chain direction matches other theoretical predictions. The reorientation of the particle magnetization due to the effect of shearing is observed. For the four particle chain with the magnetic field parallel to the chain, the observed stiffening effect was slightly greater than what was observed for the two particle case at a similar volume fraction of $\Phi = 1\%$.

An applied strain caused a clustering of particles in the presence of an external magnetic field for the helical particle arrangement, when the magnetic field alone did not produce the clustering. This behavior makes sense, and implies a behavior that helps explain strain softening observed experimentally. While there are other mechanisms for strain softening behavior, it seems that sufficiently large strains can separate particle clusters, reducing the energy of their magnetic interactions, resulting in a reduction in stiffness.

The helical chain systems deserve further investigation. Changes in the vertical separation, as well as the rate of angular change, chain length, and overall system size are all worth pursuing. The effective shearing modulus did not follow an obvious trend when varying helix radius. However, so-called wavy chain arrangements have been assumed to be more realistic, and the source of both positive magnetostriction (elongation along applied magnetic field direction) and field stiffening effects, and are worth investigating. In anisotropic MREs, columnar structures can form, rather than simple straight chains. Those sorts of particle arrangements with many particles in close proximity may require different tools to model the magnetization response and magnetic interactions, such as the use of multipole expansions or FEM approaches to solving the magnetostatic problem. Those more complicated models may be necessary to help explain the discrepancies between theoretical predictions of the size of MR effects and those experimentally measured for ultrasoft polymers.

One final but important note on the numerical approach is that during the course of this research, it was found that the fixed point iteration method for finding the particle magnetization could fail for arrangements with low symmetry when the magnetic field is small and the separa-

tions of the magnetic particles was close to the size of the particles. This suggests that new methods for solving for the magnetization, or new models for the magnetization response are necessary to study these situations. Methods like FEM may be necessary in those situations, and could inform simpler models for the magnetic response of the particles.

Chapter 5

Conclusion

Magnetorheological elastomers display complex viscoelastic behavior that changes with an applied magnetic field, and ultrasoft MREs have a distinct pinched hysteresis loop shape. We began in Chapter 2 with a simple two particle dipole-spring model that qualitatively captured the pinched shape hysteresis loop when the applied magnetic field lead to attraction between the magnetic particles that could overcome the elastic force and result in clustering. In Chapter 3 we saw how polymer stiffness could prevent this clustering and with it the magnetic hysteresis, whether by cooling a soft MRE below the glassy transition temperature of the polymer, or by using a stiff polymer at room temperature.

In Chapter 4 a more complicated 3D model was presented using a cubic spring mass network whose constants were determined by experimentally measurable moduli and Poisson's ratio, modified with an additional volume preserving force. In addition, a nonlinear magnetization response was included for the magnetic particles whose magnetic interactions were treated as point dipoles at the center of rigid spheres. Those magnetic particles' elastic properties were also modeled with the cubic spring mass network, allowing for polymer mediated elastic interactions between the magnetic particles, and for rotation as well as translation of the particles due to elastic forces. Simulations performed with this model demonstrated magnetic hysteresis that was quite different from the pinched shape hysteresis loop, with strong remanent magnetization, and magnetic switching at critical fields for particle pairs in attractive configurations. Simulations of systems of magnetic particles under simple shear strain demonstrated that the zero-field and field-on effective shearing modulus increased with increasing volume fraction of the magnetic particles. The magnetorheological effect, the percentage change in effective modulus with the magnetic field on, showed a leveling off just below 400% for the two particle system with the magnetic field aligned with the chain axis and perpendicular to the shear direction. Results with 4 particle chains demonstrated the dependence of efffective shear modulus on the orientation of the magnetic field relative to the

applied strain and chain direction, as well as demonstrating some dependence on the number of particles in a chain for the size of the magnetorheological effect. The results of helical chains demonstrated the sensitivity of the response to the details of the particle configuration, as well as the potential for applied strains to create and break particle clusters.

Creating accurate models of MRE systems at different length and time scales is critical for moving these materials out of the laboratory and into application, as soft actuators, vibration isolators, sensors, and more.

Appendix A

Appendix

This appendix provides a high level overview of how the software used for this dissertation works, and some examples for running simulations. The code base is publicly available at https://github.com/mre-cong/MRE_Golec. The examples can be found in sim_runner.py. Additionally, the function batch_job_runner() can be used to run series of simulations with variations in particle arrangement, material properties, and magnetic field configuration. The function jumpstart_sim() can be used to continue a simulation which was interrupted, picking up from the most recently available checkpoint file, or output file.

This code base was written to run on a particular workstation, with specific hardware. That includes an Nvidia GPU, which is required for this software to run. For the GPU kernels, the choice of grid and block size were made by considering the specifications of the QuadroP4000. Moving this software onto another platform could be done by updating the functions which call GPU kernels to take the grid and block sizes (and/or the number of streaming multiprocessors (SM)) as arguments, and to pass appropriate values based on the available hardware. While the software should run with the current grid and block sizes, optimal runtime performance can be achieved by considering the specifications of the available GPU (number of streaming multiprocessors, and number of threads per SM). Please see simulate.py for the source code of the kernels, and the functions which call them.

This GPU implementation of the model requires the use of one Cython file, which can be compiled by invoking the following command at the command line:

```
python3 springs_setup.py build_ext --inplace
```

This will generate files necessary for the initialization process in the current working directory.

Several modules are used to organize different aspects of the simulation: initialize.py, analyze.py, and sphere_rasterization.py are used while running the simulation. analyze is also where most, but not all functions related to the post-simulation analysis are stored. initialize handles

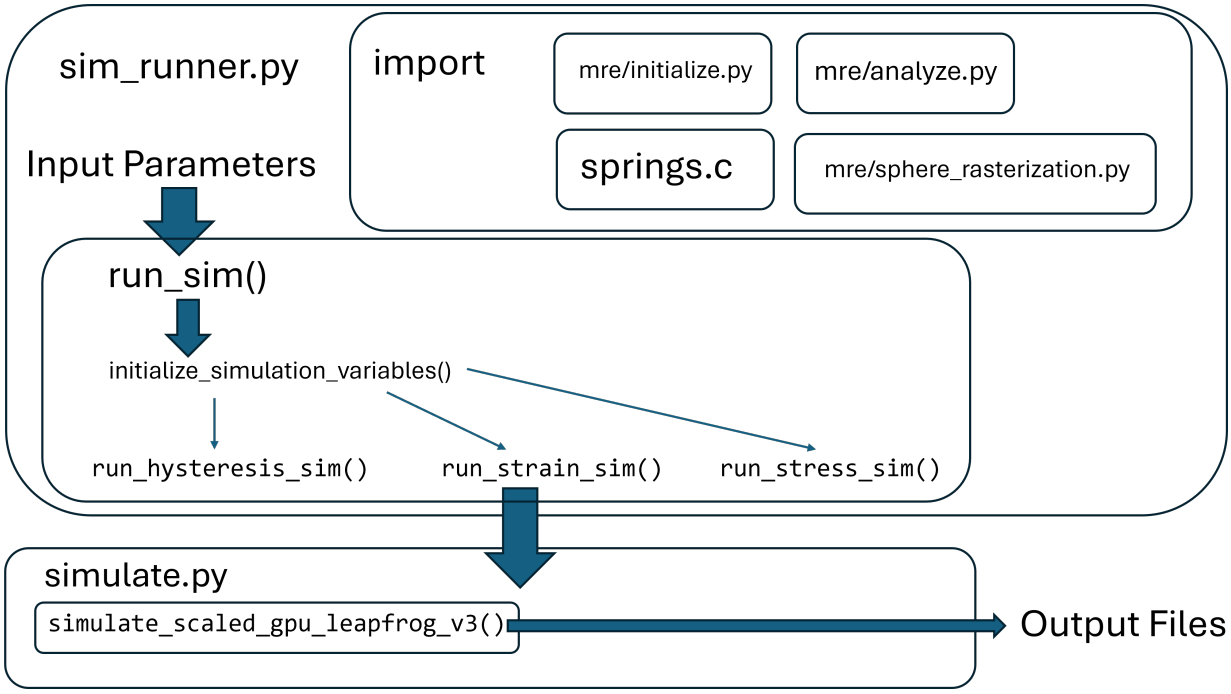

Figure A.1: A diagram showing program flow when running a simulation in sim_runner.py.

most but not all of the intialization procedure, the other parts of which are handled by springs, and sphere_rasterization, which handles the creatino of the spring and volume element variables, and the process of identifying which nodes are particle nodes, respectively.

To generate figures, refer to analysis_workflows.py. plot_particle_magnetization_vectors() generates figures like Figure 4.22. plot_energy_figures() is used to generate figures like Figure 4.14. temp_hysteresis_analysis() generates figures like Figure 4.4. Additional functions exist to generate visualizations of cuts through the system, the outside of the system, and calculation and visualization of strain tensor components.

To generate animations, refer to animation_practice.ipynb, and quiver_surface_animation.ipynb.

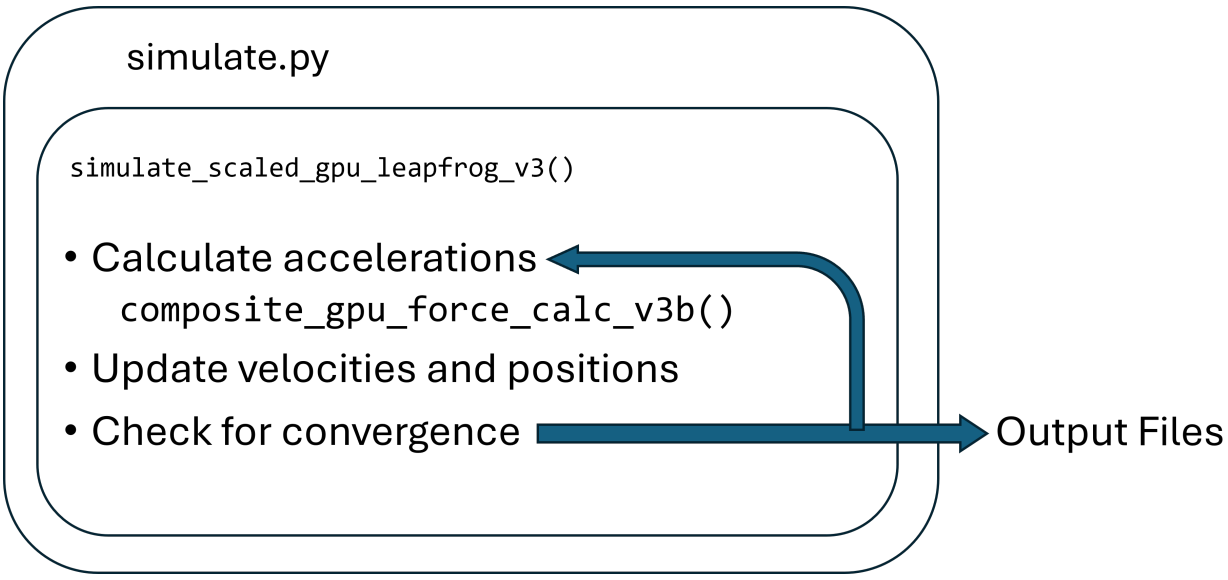

Figure A.2: A diagram showing the program flow inside the call to simulate_scaled_gpu_leapfrog_v3() when running a simulation.

A.1 Running a Simulation

A complete set of parameters defining the system and simulation type are required to run any simulation. These parameters are stored in a Python dictionary, whose keys are particular strings. This is eventually passed to a function initialize_simulation_variables(). These parameters include:

- Young's modulus, e.g. 9000 Pa
- Poisson ratio, e.g. 0.47
- discretization order, e.g. 5
- boundary condition direction, e.g. ('x','z')
- simulation type (which is also boundary condition type), e.g. 'strain_simple_shear'
- time step size, e.g. 5×10^{-3}
- number of integration steps (time steps in an integration round), e.g. 5000
- number of integration rounds (convergence checks are done at the end of integration rounds), e.g. 20

- drag coefficient, e.g. 1
- particle radius in meters, e.g. 1.5×10^{-6} m
- number of particles in the system, e.g. 2
- number of particles along each Cartesian direction, e.g. [1,1,2]
- particle placement type, e.g. 'regular'

See also the examples below for typical values of these parameters. Simulation types are: 'hysteresis', 'strain_simple_shearing', 'strain_compression', 'strain_tension', 'strain_torsion', 'strain_magnetostriction'. Stress based simulations have been implemented, 'simple_stress_shearing', 'simple_stress_compression', 'simple_stress_tension', which hold one surface fixed and apply the stress to the opposite surface, and 'special_stress_*', which apply forces to both opposing surfaces. However, these methods do not have a corresponding analysis of effective modulus. Programmatic particle placement options are 'regular', 'regular_noisy', 'anisotropic_regular', 'anisotropic_regular_noisy'. When passing particle positions, particle placement is 'by_hand'. Depending on the type of particle placement, other parameters need to be provided:

- volume fraction of particles (if not placing particles by hand), e.g. 0.03

  OR

- particle positions (if not using a programmatic placement),

  AND

- the system dimensions in meters ('dimensions'), e.g. [20×10^{-6},20×10^{-6},20×10^{-6}]

Anisotropy factor is necessary if either anisotropic particle placement is used. It is a three element array, with the relative size of the system along each Cartesian direction, x,y, and z respectively. Noisy particle placement adds some small noise in the particle placement, up to one

volume element shifted along each Cartesian direction for each particle. This can be modified in sim_runner.py, place_n_particles_normalized(), but is currently hard coded to be a maximum of one volume element for the shift in placement.

Additionally, the external magnetic fields and boundary conditions need to be defined:

The magnetic field can be provided in one of two ways:

- the magnetic field can be provided as an array of vectors, providing the H-field vector in the order to be applied. ('Hext_series'),

  OR

- the maximum magnetic field value in Tesla, and the number of magnetic field steps,

  AND

- the polar and azimuthal angles of the magnetic field direction are required ('field_angle_theta', 'field_angle_phi', respectively), e.g. (π/2,0)

- the boundary condition values can be provided as an array,

  OR

- the maximum value and number of boundary condition steps can be provided,

Finally, certain flags need to be set. Many of the flags are deprecated for the current GPU based implementation. Some code cleanup is necessary to remove them, but until then, these need to be initialized with some value.

- GPU flag set to True,
- plotting flag,
- criteria flag,
- persistent checkpointing flag

Particle properties are currently hard coded in sim_runner.py, initialize_simulation_variables().

Convergence checks are hard coded to require a minimum of 4 integration rounds, as well as meeting convergence criteria, and the solution vector difference norm (vector of node positions currently compared to last recorded set of node positions at the end of the prior integration round) must be decreasing compared to the last calculated value. These could be altered to reduce runtime by relaxing these requirements. See simulate.py, simulate_scaled_gpu_leapfrog_v3(). Snapshots of criteria from the simulation during the integration are recorded, plotted as a function of simulation time, t, and saved out. These can be useful diagnostics to understand how the simulation has progressed, and judge whether or not convergence was properly achieved, or if unusual or unexpected behaviors are occurring. Snapshots are recorded every 200 time steps, a hard coded value that can be adjusted (again see simulate_scaled_gpu_leapfrog_v3()) either in the function, or by adding a keyword argument with a default value to the function signature. These snapshots have some runtime performance impact, but were found worth retaining regardless.

Checkpoint files are saved out at the end of integration rounds, unless the system has converged, in which case an output file is generated. These checkpoint and output files are used for creating animations.

```
def hysteresis_example():
    youngs_modulus = 9e3
    E = youngs_modulus
    discretization_order = 5
    poisson_ratio = 0.47
    volume_fraction = 5e-2
    bc_direction = ('z','z')
    Hext_angle = (0,0)
    sim_type = 'hysteresis'
    bc_type = sim_type

    step_size = np.float32(5e-3)
    integration_steps = 5000
```

```
num_particles = 2
particle_arrangement = [1,1,2]
particle_posns = []

parameters = dict({})
parameters['max_integrations'] = 40
parameters['max_integration_steps'] = integration_steps
parameters['step_size'] = step_size
parameters['gpu_flag'] = True
parameters['particle_rotation_flag'] = True
parameters['persistent_checkpointing_flag'] = True
parameters['plotting_flag'] = False
parameters['criteria_flag'] = False
parameters['particle_radius'] = 1.5e-6
parameters['youngs_modulus'] = E
parameters['poisson_ratio'] = poisson_ratio
parameters['drag'] = 1
parameters['discretization_order'] = discretization_order
parameters['particle_placement'] = 'regular'
parameters['num_particles_along_axes'] = particle_arrangement
parameters['num_particles'] = parameters['num_particles_along_axes'][0]*
parameters['num_particles_along_axes'][1]*parameters['
num_particles_along_axes'][2]

parameters['anisotropy_factor'] = np.array([1.0,1.0,1.0])
parameters['anisotropy_factor'][:2] = 1/np.sqrt(parameters['
anisotropy_factor'][2])
parameters['volume_fraction'] = volume_fraction
first_leg = np.linspace(0,5e-1,51,dtype=np.float32)
hysteresis_loop_series = np.concatenate((first_leg,first_leg[-2::-1],
first_leg[1::]*-1,first_leg[-2::-1]*-1,first_leg[1::]))
field_angle_theta = Hext_angle[0]
field_angle_phi = Hext_angle[1]
```

```
    #if this entry exists in the parameters dict, it will be used over the set
    of parameters 'max_field','field_angle_*', and 'num_field_steps' that
   would otherwise construct the applied magnetic field series
    parameters['Hext_series'] = convert_field_magnitude_to_vector_series((1/
   mu0)*hysteresis_loop_series,field_angle_theta,field_angle_phi)
    parameters['max_field'] = 0.06
    parameters['field_angle_theta'] = Hext_angle[0]
    parameters['field_angle_phi'] = Hext_angle[1]
    parameters['num_field_steps'] = 15
    parameters['boundary_condition_max_value'] = 0
    parameters['num_boundary_condition_steps'] = 0
    parameters['boundary_condition_type'] = bc_type
    parameters['boundary_condition_direction'] = bc_direction
    print(f'sim type = {sim_type}\nbc_direction = {bc_direction}\n')
    print(f"Young's modulus = {E} Pa\nPoisson Ratio = {poisson_ratio}\
   ndiscretization order = {discretization_order}\n")
    print(f"N particles = {parameters['num_particles']}\nField angle theta = {
   Hext_angle[0]}\nField angle phi = {Hext_angle[1]}\n")
    print(f"gpu based calculation {parameters['gpu_flag']}")
    run_sim(parameters,sim_type)
```

Listing A.1: An example running a two particle hysteresis simulation. Shows off placing particles automatically based on volume fraction and particle_arrangement variables.

```
def shear_strain_example():
    youngs_modulus = 9e3
    E = youngs_modulus
    discretization_order = 5
    poisson_ratio = 0.47
    volume_fraction = 5e-2
    bc_direction = ('z','x')
    Hext_angle = (0,0)
    sim_type = 'strain_simple_shearing'
    bc_type = sim_type
```

```
step_size = np.float32(5e-3)
integration_steps = 5000
num_particles = 2
particle_arrangement = [1,1,8]
num_particles = 8
particle_posns = np.zeros((num_particles,3))

horizontal_spacing = 3.5e-6
#helical chain
Lx, Ly, Lz = (18e-6,18e-6,62e-6)
vertical_spacing = 5e-6
particle_posns[:,0] = 9e-6
particle_posns[:,1] = 9e-6
angle_increment = 2*np.pi/num_particles
for i in range(num_particles):
    particle_posns[i,2] = 13.5e-6 + i*vertical_spacing
    particle_posns[i,0] += horizontal_spacing*np.cos(i*angle_increment)
    particle_posns[i,1] += horizontal_spacing*np.sin(i*angle_increment)

parameters = dict({})
parameters['max_integrations'] = 40
parameters['max_integration_steps'] = integration_steps
parameters['step_size'] = step_size
parameters['gpu_flag'] = True
parameters['particle_rotation_flag'] = True
parameters['persistent_checkpointing_flag'] = True
parameters['plotting_flag'] = False
parameters['criteria_flag'] = False
parameters['particle_radius'] = 1.5e-6
parameters['youngs_modulus'] = E
parameters['poisson_ratio'] = poisson_ratio
parameters['drag'] = 1
```

```
 parameters['discretization_order'] = discretization_order
 parameters['particle_placement'] = 'by_hand'
 parameters['num_particles_along_axes'] = particle_arrangement
 parameters['num_particles'] = parameters['num_particles_along_axes'][0]*
parameters['num_particles_along_axes'][1]*parameters['
num_particles_along_axes'][2]
 if parameters['num_particles'] == 0 or 'hand' in parameters['
particle_placement']:
     #dimensions in normalized units, the number of elements in each
direction
     particle_diameter = 2*parameters['particle_radius']
     l_e = (particle_diameter/2) / (discretization_order + 1/2)
     parameters['dimensions'] = np.array([np.floor_divide(Lx,l_e),np.
floor_divide(Ly,l_e),np.floor_divide(Lz,l_e)])
     parameters['particle_posns'] = particle_posns
 parameters['anisotropy_factor'] = np.array([1.0,1.0,1.0])
 parameters['anisotropy_factor'][:2] = 1/np.sqrt(parameters['
anisotropy_factor'][2])
 parameters['volume_fraction'] = volume_fraction
 tmp_field_var = np.array([0.0,1e-2,2e-2,3e-2,4e-2,5e-2,6e-2,7e-2,8e-2,1e
-1,1.2e-1,1.4e-1])
 tmp_field_vectors = np.zeros((tmp_field_var.shape[0],3),dtype=np.float32)
 if np.isclose(Hext_angle[0],np.pi/2):
     tmp_field_vectors[:,0] = (1/mu0)*tmp_field_var
 else:
     tmp_field_vectors[:,2] = (1/mu0)*tmp_field_var
 #if this entry exists in the parameters dict, it will be used over the set
  of parameters 'max_field','field_angle_*', and 'num_field_steps' that
would otherwise construct the applied magnetic field series
 parameters['Hext_series_magnitude'] = (1/mu0)*tmp_field_var
 parameters['max_field'] = np.max(tmp_field_var)
 parameters['field_angle_theta'] = Hext_angle[0]
 parameters['field_angle_phi'] = Hext_angle[1]
```

```
 parameters['num_field_steps'] = 15
 parameters['boundary_condition_value_series'] = np.linspace(0,1e-1,11)
 #if 'boundary_condition_value_series' is defined, '
boundary_condition_max_value' and 'num_boundary_condition_steps' values
won't be used, but must be initialized with dummy values
 parameters['boundary_condition_max_value'] = 0.01
 parameters['num_boundary_condition_steps'] = 11
 parameters['boundary_condition_type'] = bc_type
 parameters['boundary_condition_direction'] = bc_direction
 print(f'sim type = {sim_type}\nbc_direction = {bc_direction}\n')
 print(f"Young's modulus = {E} Pa\nPoisson Ratio = {poisson_ratio}\
ndiscretization order = {discretization_order}\n")
 print(f"N particles = {parameters['num_particles']}\nField angle theta = {
Hext_angle[0]}\nField angle phi = {Hext_angle[1]}\n")
 print(f"gpu based calculation {parameters['gpu_flag']}")
 run_sim(parameters,sim_type)
```

Listing A.2: An example running a shear strain simulation. Shows off placing particles by hand.

Bibliography

[1] K. Golec, J. F. Palierne, F. Zara, S. Nicolle, and G. Damiand, *Hybrid 3d mass-spring system for simulation of isotropic materials with any poisson's ratio*, Visual Comput. **36**, 809 (2020), https://doi.org/10.1007/s00371-019-01663-0.

[2] S. Abramchuk, E. Kramarenko, G. Stepanov, L. V. Nikitin, G. Filipcsei, A. R. Khokhlov, and M. Zrínyi, *Novel highly elastic magnetic materials for dampers and seals: Part i. preparation and characterization of the elastic materials*, Polym. for Adv. Technol. **18**, 883 (2007), https://doi.org/10.1002/pat.924.

[3] G. Glavan, I. A. Belyaeva, I. Drevenšek-Olenik, and M. Shamonin, *Experimental study of longitudinal, transverse and volume strains of magnetoactive elastomeric cylinders in uniform magnetic fields*, J. Magn. Magn. Mater. **579** (2023), https://doi.org/10.1016/j.jmmm.2023.170826.

[4] G. V. Stepanov, S. S. Abramchuk, D. A. Grishin, L. V. Nikitin, E. Y. Kramarenko, and A. R. Khokhlov, *Effect of a homogeneous magnetic field on the viscoelastic behavior of magnetic elastomers*, Polymer **48**, 488 (2007), https://doi.org/10.1016/j.polymer.2006.11.044.

[5] G. V. Stepanov, D. Y. Borin, Y. L. Raikher, P. V. Melenev, and N. S. Perov, *Motion of ferroparticles inside the polymeric matrix in magnetoactive elastomers*, J. Phys. Condens. Matter **20**, 204121 (2008), https://doi.org/10.1088/0953-8984/20/20/204121.

[6] P. Testa, R. W. Style, J. Cui, C. Donnelly, E. Borisova, P. M. Derlet, E. R. Dufresne, and L. J. Heyderman, *Magnetically addressable shape-memory and stiffening in a composite elastomer*, Adv. Mater. **31**, 1900561 (2019), https://doi.org/10.1002/adma.201900561.

[7] N. Kchit, P. Lancon, and G. Bossis, *Thermoresistance and giant magnetoresistance of magnetorheological elastomers*, J. Phys. D: Appl. Phys. **42**, 105506 (2009), https://doi.org/10.1088/0022-3727/42/10/105506.

[8] J. M. Ginder, M. E. Nichols, L. D. Elie, and S. M. Clark, *Controllable-stiffness components based on magnetorheological elastomers*, in N. M. Wereley (Ed.), *Smart Structures and Materials 2000: Smart Structures and Integrated Systems*, vol. 3985, pp. 418 – 425, International Society for Optics and Photonics (SPIE, 2000).

[9] L. Fischer and A. M. Menzel, *Towards a soft magnetoelastic twist actuator*, Phys. Rev. Research **2**, 23383 (2020), https://doi.org/10.1103/PhysRevResearch.2.023383.

[10] V. Q. Nguyen, A. S. Ahmed, and R. V. Ramanujan, *Morphing soft magnetic composites*, Adv. Mater. **24**, 4041 (2012), https://doi.org/10.1002/adma.201104994.

[11] A. Alkhalaf, A. Hooshiar, and J. Dargahi, *Composite magnetorheological elastomers for tactile displays: Enhanced mr-effect through bi-layer composition*, Compos. Part B: Eng. **190**, 107888 (2020), https://doi.org/10.1016/j.compositesb.2020.107888.

[12] Ubaidillah, J. Sutrisno, A. Purwanto, and S. A. Mazlan, *Recent progress on magnetorheological solids: Materials, fabrication, testing, and applications*, Adv. Eng. Mater. **17**, 563 (2015), https://doi.org/10.1002/adem.201400258.

[13] E. A. Corbin, A. Vite, E. G. Peyster, M. Bhoopalam, J. Brandimarto, X. Wang, A. I. Bennett, A. T. Clark, X. Cheng, K. T. Turner, K. Musunuru, and K. B. Margulies, *Tunable and reversible substrate stiffness reveals a dynamic mechanosensitivity of cardiomyocytes*, ACS Appl. Mater. Interfaces **11**, 20603 (2019), https://doi.org/10.1021/acsami.9b02446.

[14] K. A. Tran, E. Kraus, A. T. Clark, A. Bennett, K. Pogoda, X. Cheng, A. C. Bers, P. A. Janmey, and P. A. Galie, *Dynamic tuning of viscoelastic hydrogels with carbonyl iron microparticles reveals the rapid response of cells to three-dimensional substrate mechanics*, ACS Appl. Mater. Interfaces **13**, 20947 (2021), https://doi.org/10.1021/acsami.0c21868.

[15] M. Chanda, *Introduction to Polymer Science and Chemistry: A Problem Solving Approach* (CRC Press, 2006).

[16] U. W. Gedde and M. S. Hedenqvist, *Fundamental Polymer Science (Second Edition)* (Springer Cham, 2019).

[17] O. V. Stolbov and Y. L. Raikher, *Magnetostriction effect in soft magnetic elastomers*, Arch. Appl. Mech. **89**, 63 (2019), https://doi.org/10.1007/s00419-018-1452-0.

[18] O. V. Stolbov, Y. L. Raikher, and M. Balasoiu, *Modelling of magnetodipolar striction in soft magnetic elastomers*, Soft Matter **7**, 8484 (2011), https://doi.org/10.1039/c1sm05714f.

[19] Z. Rigbi and L. Jilken, *The response of an elastomer filled with soft ferrite to mechanical and magnetic influences*, J. Magn. Magn. Mater. **37**, 267 (1983), https://doi.org/.

[20] Z. Rigbi and J. E. Mark, *Effects of a magnetic field applied during the curing of a polymer loaded with magnetic filler.*, J. Polym. Sci. Part A-2, Polym. Phys. **23**, 1267 (1985), https://doi.org/10.1002/pol.1985.180230618.

[21] M. R. Jolly, J. D. Carlson, and B. C. Muñoz, *A model of the behaviour of magnetorheological materials*, Smart Mater. Struct. **5**, 607 (1996), https://doi.org/10.1088/0964-1726/5/5/009.

[22] M. R. Jolly, J. D. Carlson, B. C. Muñoz, and T. A. Bullions, *The magnetoviscoelastic response of elastomer composites consisting of ferrous particles embedded in a polymer matrix*, J. Intell. Mater. Syst. Struct. **7**, 613 (1996), https://doi.org/10.1177/1045389X9600700601.

[23] L. C. Davis, *Model of magnetorheological elastomers*, J. Appl. Phys. **85**, 3348 (1999), https://doi.org/10.1063/1.369682.

[24] Y. Li, J. Li, W. Li, and H. Du, *A state-of-the-art review on magnetorheological elastomer devices*, Smart materials structures **23**, 123001 (2014), https://doi.org/10.1088/0964-1726/23/12/123001.

[25] M. T. Lopez-Lopez, J. D. G. Durán, L. Y. Iskakova, and A. Y. Zubarev, *Mechanics of magnetopolymer composites: A review*, J. Nanofluids **5**, 479 (2016), https://doi.org/10.1166/jon.2016.1233.

[26] M. A. Cantera, M. Behrooz, R. F. Gibson, and F. Gordaninejad, *Modeling of magneto-mechanical response of magnetorheological elastomers (MRE) and MRE-based systems: A review*, Smart Mater. Struct. **26**, 023001 (2017), https://doi.org/10.1088/1361-665X/aa549c.

[27] R. Weeber, M. Hermes, A. M. Schmidt, and C. Holm, *Polymer architecture of magnetic gels: A review*, J. Phys. Condens. Matter **30**, 063002 (2018), https://doi.org/10.1088/1361-648X/aaa344.

[28] A. K. Bastola and M. Hossain, *A review on magneto-mechanical characterizations of magnetorheological elastomers*, Compos. Part B: Eng. **200**, 108348 (2020), https://doi.org/10.1016/j.compositesb.2020.108348.

[29] A. K. Bastola, M. Paudel, L. Li, and W. Li, *Recent progress of magnetorheological elastomers: A review*, Smart Mater. Struct. **29**, 123002 (2020), https://doi.org/10.1088/1361-665X/abbc77.

[30] J. R. Morillas and J. D. Vicente, *Magnetorheology: a review*, Soft Matter **16**, 9614 (2020), https://doi.org/10.1039/d0sm01082k.

[31] M. A. Hafeez, M. Usman, M. A. Umer, and A. Hanif, *Recent progress in isotropic magnetorheological elastomers and their properties: A review*, Polymers **12**, 1 (2020), https://doi.org/10.3390/polym12123023.

[32] T. A. Nadzharyan, M. Shamonin, and E. Y. Kramarenko, *Theoretical modeling of magnetoactive elastomers on different scales: A state-of-the-art review*, Polymers **14** (2022), https://doi.org/10.3390/polym14194096.

[33] J.-P. Pelteret and P. Steinmann, *Magneto-active Polymers: Fabrication, Characterisation, Modelling and Simulation at the Micro- and Macro-scale* (Walter de Gruyter GmbH, Berlin/-Boston, 2020).

[34] B. D. Cullity and C. D. Graham, *Introduction to Magnetic Materials* (John Wiley & Sons, Ltd, 2008).

[35] B. D. Cullity and C. D. Graham, *Introduction to Magnetic Materials, Diamagnetism and Paramagnetism*, chap. 3, pp. 87–114 (John Wiley & Sons, Ltd, 2008).

[36] B. D. Cullity and C. D. Graham, *Introduction to Magnetic Materials, Magnetic Anisotropy*, chap. 7, pp. 197–239 (John Wiley & Sons, Ltd, 2008).

[37] F. Preisach, *Über die magnetische Nachwirkung*, Z. Phys. **94**, 277 (1935), https://doi.org/10.1007/BF01349418.

[38] A. Vansteenkiste, J. Leliaert, M. Dvornik, M. Helsen, F. Garcia-Sanchez, and B. Van Waeyenberge, *The design and verification of MuMax3*, AIP Adv. **4**, 107133 (2014), https://doi.org/10.1063/1.4899186.

[39] M. E. Gurtin, *An Introduction to Continuum Mechanics* (Elsevier, 1981).

[40] C. Truesdell and W. Noll, *The Non-Linear Field Theories of Mechanics* (Springer-Verlag Berlin Heidelberg GmbH, 2004).

[41] A. Bertram, *Elasticity and Plasticity of Large Deformations* (Springer Nature Switzerland AG, 2021).

[42] M. Mayer, R. Rabindranath, J. Börner, E. Hörner, A. Bentz, J. Salgado, H. Han, H. Böse, J. Probst, M. Shamonin, G. J. Monkman, and G. Schlunck, *Ultra-soft PDMS-based magnetoactive elastomers as dynamic cell culture substrata*, PLoS ONE **8**, e76196 (2013), https://doi.org/10.1371/journal.pone.0076196.

[43] A. T. Clark, A. Bennett, E. Kraus, K. Pogoda, A. Cebers, P. Janmey, K. T. Turner, E. A. Corbin, and X. Cheng, *Magnetic field tuning of mechanical properties of ultrasoft PDMS-based magnetorheological elastomers for biological applications*, Multifunct. Mater. **4**, 035001 (2021), https://doi.org/10.1088/2399-7532/ac1b7e.

[44] T. Gundermann, P. Cremer, H. Löwen, A. M. Menzel, and S. Odenbach, *Statistical analysis of magnetically soft particles in magnetorheological elastomers*, Smart Mater. Struct. **26**, 045012 (2017), https://doi.org/10.1088/1361-665X/aa5f96.

[45] A. T. Clark, D. Marchfield, Z. Cao, T. Dang, N. Tang, D. Gilbert, E. A. Corbin, K. S. Buchanan, and X. M. Cheng, *The effect of polymer stiffness on magnetization reversal of magnetorheological elastomers*, APL Mater. **10**, 41106 (2022), https://doi.org/10.1063/5.0086761.

[46] A. V. Bodnaruk, A. Brunhuber, V. M. Kalita, M. M. Kulyk, A. A. Snarskii, A. F. Lozenko, S. M. Ryabchenko, and M. Shamonin, *Temperature-dependent magnetic properties of a magnetoactive elastomer: Immobilization of the soft-magnetic filler*, J. Appl. Phys. **123**, 115118 (2018), https://doi.org/10.1063/1.5023891.

[47] A. M. Menzel, *Mesoscopic characterization of magnetoelastic hybrid materials: magnetic gels and elastomers, their particle-scale description, and scale-bridging links*, Arch. Appl. Mech. **89**, 17 (2019), https://doi.org/10.1007/s00419-018-1413-7.

[48] A. M. Biller, O. V. Stolbov, and Y. L. Raikher, *Mesoscopic magnetomechanical hysteresis in a magnetorheological elastomer*, Phys. Rev. E **92**, 023202 (2015), https://doi.org/10.1103/PhysRevE.92.023202.

[49] G. Pessot, M. Schümann, T. Gundermann, S. Odenbach, H. Löwen, and A. M. Menzel, *Tunable dynamic moduli of magnetic elastomers: From characterization by x-ray micro-*

computed tomography to mesoscopic modeling, J. Phys. Condens. Matter **30**, 125101 (2018), https://doi.org/10.1088/1361-648X/aaaeaa.

[50] M. Puljiz, S. Huang, K. A. Kalina, J. Nowak, S. Odenbach, M. Kästner, G. K. Auernhammer, and A. M. Menzel, *Reversible magnetomechanical collapse: virtual touching and detachment of rigid inclusions in a soft elastic matrix*, Soft Matter **14**, 6809 (2018), https://doi.org/10.1039/c8sm01051j.

[51] M. V. Vaganov and Y. L. Raikher, *Effect of mesoscopic magnetomechanical hysteresis on magnetization curves and first-order reversal curve diagrams of magnetoactive elastomers*, J. Phys. D: Appl. Phys. **53**, 405002 (2020), https://doi.org/10.1088/1361-6463/ab9674.

[52] A. Y. Zubarev, D. N. Chirikov, D. Y. Borin, and G. V. Stepanov, *Hysteresis of the magnetic properties of soft magnetic gels*, Soft Matter **12**, 6473 (2016), https://doi.org/10.1039/c6sm01257d.

[53] M. Puljiz, S. Huang, G. K. Auernhammer, and A. M. Menzel, *Forces on rigid inclusions in elastic media and resulting matrix-mediated interactions*, Phys. Rev. Lett. **117**, 238003 (2016), https://doi.org/10.1103/PhysRevLett.117.238003.

[54] E. C. Stoner and E. P. Wohlfarth, *A Mechanism of Magnetic Hysteresis in Heterogeneous Alloys*, Philos. Trans. R. Soc. A **240**, 599 (1948), https://doi.org/10.1098/rsta.1948.0007.

[55] B. D. Cullity and C. D. Graham, *Domains and the Magnetization Process*, chap. 9, pp. 275–333 (John Wiley & Sons, Ltd, 2008).

[56] I. Mayergoyz, *Mathematical Models of Hysteresis* (Springer, New York, 1991).

[57] C. J. F. Böttcher, O. C. v. Belle, P. Bordewijk, and A. Rip, *Theory of electric polarization* (Elsevier Scientific Pub. Co., Amsterdam, 1973), 2d ed. com ed.

[58] A. M. Biller, O. V. Stolbov, and Y. L. Raikher, *Modeling of particle interactions in magnetorheological elastomers*, J. Appl. Phys. **116**, 114904 (2014), https://doi.org/10.1063/1.4895980.

[59] G. Pessot, H. Löwen, and A. M. Menzel, *Dynamic elastic moduli in magnetic gels: Normal modes and linear response*, J. Chem. Phys. **145**, 104904 (2016), https://doi.org/10.1063/1.4962365.

[60] G. Pessot, P. Cremer, D. Y. Borin, S. Odenbach, H. Löwen, and A. M. Menzel, *Structural control of elastic moduli in ferrogels and the importance of non-affine deformations*, J. Chem. Phys. **141**, 124904 (2014), https://doi.org/10.1063/1.4896147.

[61] G. Y. Zhou, *Shear properties of a magnetorheological elastomer*, Smart Mater. Struct. **12**, 139 (2003), https://doi.org/10.1088/0964-1726/12/1/316.

[62] M. Lokander and B. Stenberg, *Improving the magnetorheological effect in isotropic magnetorheological rubber materials*, Polym. Test. **22**, 677 (2003), https://doi.org/10.1016/S0142-9418(02)00175-7.

[63] L. Chen, X. L. Gong, and W. H. Li, *Microstructures and viscoelastic properties of anisotropic magnetorheological elastomers*, Smart Mater. Struct. **16**, 2645 (2007), https://doi.org/10.1088/0964-1726/16/6/069.

[64] V. V. Sorokin, B. O. Sokolov, G. V. Stepanov, and E. Y. Kramarenko, *Controllable hydrophobicity of magnetoactive elastomer coatings*, J. Magn. Magn. Mater. **459**, 268 (2018), https://doi.org/10.1016/j.jmmm.2017.10.074.

[65] G. Glavan, P. Salamon, I. A. Belyaeva, M. Shamonin, and I. Drevenšek-Olenik, *Tunable surface roughness and wettability of a soft magnetoactive elastomer*, J. Appl. Polym. Sci. **135**, 46221 (2018), https://doi.org/10.1002/app.46221.

[66] S. Chen, R. Li, X. Li, and X. Wang, *Magnetic field induced surface micro-deformation of magnetorheological elastomers for roughness control*, Front. Mater. **5**, 76 (2018), https://doi.org/10.3389/fmats.2018.00076.

[67] G. Glavan, W. Kettl, A. Brunhuber, M. Shamonin, and I. Drevenšek-Olenik, *Effect of material composition on tunable surface roughness of magnetoactive elastomers*, Polymers **11**, 594 (2019), https://doi.org/10.3390/polym11040594.

[68] L. Chen and S. Jerrams, *A rheological model of the dynamic behavior of magnetorheological elastomers*, J. Appl. Phys. **110**, 013513 (2011), https://doi.org/10.1063/1.3603052.

[69] T. Gundermann and S. Odenbach, *Investigation of the motion of particles in magnetorheological elastomers by X-μCT*, Smart Mater. Struct. **23**, 105013 (2014), https://doi.org/10.1088/0964-1726/23/10/105013.

[70] A. V. Bodnaruk, A. Brunhuber, V. M. Kalita, M. M. Kulyk, P. Kurzweil, A. A. Snarskii, A. F. Lozenko, S. M. Ryabchenko, and M. Shamonin, *Magnetic anisotropy in magnetoactive elastomers, enabled by matrix elasticity*, Polymer **162**, 63 (2019), https://doi.org/10.1016/j.polymer.2018.12.027.

[71] A. V. Bodnaruk, V. M. Kalita, M. M. Kulyk, A. F. Lozenko, S. M. Ryabchenko, A. A. Snarskii, A. Brunhuber, and M. Shamonin, *Temperature blocking and magnetization of magnetoactive elastomers*, J. Magn. Magn. Mater. **471**, 464 (2019), https://doi.org/10.1016/j.jmmm.2018.10.005.

[72] R. N. Palchesko, L. Zhang, Y. Sun, and A. W. Feinberg, *Development of polydimethylsiloxane substrates with tunable elastic modulus to study cell mechanobiology in muscle and nerve*, PLoS ONE **7**, e51499 (2012), https://doi.org/10.1371/journal.pone.0051499.

[73] J. Osicka, M. Mrlik, M. Ilcikova, B. Hanulikova, P. Urbanek, M. Sedlacik, and J. Mosnacek, *Reversible actuation ability upon light stimulation of the smart systems with controllably*

grafted graphene oxide with poly (glycidyl methacrylate) and PDMS elastomer: Effect of compatibility and graphene oxide reduction on the photo-actuation performance, Polymers **10**, 832 (2018), https://doi.org/10.3390/polym10080832.

[74] A. C. Rennie, P. L. Dickrell, and W. G. Sawyer, *Friction coefficient of soft contact lenses: Measurements and modeling*, Tribol. Lett. **18**, 499 (2005), https://doi.org/10.1007/s11249-005-3610-0.

[75] K. D. Schulze, A. I. Bennett, S. Marshall, K. G. Rowe, and A. C. Dunn, *Real area of contact in a soft transparent interface by particle exclusion microscopy*, J. Tribol. **138**, 041404 (2016), https://doi.org/10.1115/1.4032822.

[76] K. L. Johnson, *Perspectives talks*, Proc. Inst. Mech. Eng. Part J: J. Eng. Tribol. **223**, 235 (2009), https://doi.org/10.1243/13506501JET223J3Persp.

[77] P. Małecki, K. Kolman, J. Pigłowski, J. Kaleta, and J. Krzak, *Sol–gel method as a way of carbonyl iron powder surface modification for interaction improvement*, J. Solid State Chem. **226**, 224 (2015), https://doi.org/10.1016/j.jssc.2015.03.002.

[78] M. Tarama, P. Cremer, D. Y. Borin, S. Odenbach, H. Löwen, and A. M. Menzel, *Tunable dynamic response of magnetic gels: Impact of structural properties and magnetic fields*, Phys. Rev. E **90**, 042311 (2014), https://doi.org/10.1103/PhysRevE.90.042311.

[79] M. A. Annunziata, A. M. Menzel, and H. Löwen, *Hardening transition in a one-dimensional model for ferrogels*, J. Chem. Phys. **138** (2013), https://doi.org/10.1063/1.4807003.

[80] S. Huang, G. Pessot, P. Cremer, R. Weeber, C. Holm, J. Nowak, S. Odenbach, A. M. Menzel, and G. K. Auernhammer, *Buckling of paramagnetic chains in soft gels*, Soft Matter **12**, 228 (2015), https://doi.org/10.1039/c5sm01814e.

[81] D. Ivaneyko, V. Toshchevikov, and M. Saphiannikova, *Dynamic moduli of magneto-sensitive elastomers: a coarse-grained network model*, Soft matter **11**, 7627 (2015), https://doi.org/10.1039/c5sm01761k.

[82] H. Elman, D. Silvester, and A. Wathen, *Finite Elements and Fast Iterative Solvers: with Applications in Incompressible Fluid Dynamics* (Oxford University Press, 2014).

[83] J. Etxebarria, *Surprises in the theory of elasticity: pairwise atomic interactions, central forces, and cauchy relations*, Eur. J. Phys. **45**, 065502 (2024), https://doi.org/10.1088/1361-6404/ad6e45.

[84] T. Weinzierl, *Principles of Parallel Scientific Computing* (Springer Cham, 2022).